Fabrication of Polyaniline-Based Nano Materials for the Application in Energy Harvesting and Sensing Devices

A thesis submitted

in partial fulfilment of the requirements

for the degree of

Doctor of Philosophy

by

Shatrudhan Palsaniya

Centre for Nanotechnology

Indian Institute of Technology Guwahati

Assam, India

June 2020

Dedicated to my Parents

Choudhary Bhom Singh Palsaniya, Smt. Phooli Devi, and

Respected Brothers and Sisters

भारतीय प्रौद्योगिकी संस्थान गुवाहाटी

Indian Institute of Technology Guwahati

Certificate

It is certified that the thesis entitled "**Fabrication of Polyaniline-Based Nano Materials for the Application in Energy Harvesting and Sensing Devices**" submitted by Shatrudhan Palsaniya (146153010), a research scholar in the Centre for Nanotechnology, Indian Institute of Technology Guwahati, for the award of the degree of Doctor of Philosophy, is a record of an original research work carried out by him under my supervision and guidance. The thesis has fulfilled all requirements as per the regulations of the institute and in our opinion has reached the standard needed for submission. The results embodied in this have not been submitted to any other university or institute for the award of any degree or diploma.

Guwahati, Assam

Dated: 11/06/2020

Prof. Ashok Kumar Dasmahapatra
Department of Chemical Engineering, Indian Institute of Technology Guwahati 781039, Guwahati, Assam

Prof. Harshal B. Nemade
Department of Electronics and Electrical Engineering, Indian Institute of Technology Guwahati 781039, Assam

Declaration

This is to declare that the thesis entitled "**Fabrication of Polyaniline-Based Nano Materials for the Application in Energy Harvesting and Sensing Devices**" submitted by me to the Indian Institute of Technology Guwahati for the award of the degree of Doctor of Philosophy is a bonafide record of research work carried out by me under the supervision of Prof. Ashok Kumar Dasmahapatra and Prof. Harshal B. Nemade. Hereby I declare that the contents of this thesis, in full or in parts, have not been submitted to any other University or Institute for the award of any degree or diploma.

Dated: 11-06-2020

Guwahati

Shatrudhan Palsaniya

Abstract

Conducting polymers are usually good candidates for electrode materials for the numerous applications, which can further improve by combining with suitable nanofillers**.** This thesis begins with an insight into the fascinating world of multifunctional nanomaterials. It traces back to the developmental intersection of energy storage, and the sensing domain discusses the most recent progress in the field. Some of the landmark findings have focused on energy storage, and biosensing applications conveyed the importance of functional nanomaterials in various areas of research. Thesis work report about the development of novel nanocomposites in the applications of energy storage and sensing of the polyaniline (PANI) based nanomaterials.

The first major contribution of the thesis is the fabrication of functionalized PANI with graphene (G) and MoS_2 based binary and ternary nanocomposites using *in-situ* chemical oxidative polymerization for the supercapacitor application. The improved cyclic stability of ternary composite has contributed significantly to recovering the capacitance retention in comparison with pure PANI and PANI-G binary composites. Further, PANI-G-MoS_2 symmetric electrode exhibits a high energy density at a power density, which validates as a promising composite for the supercapacitors.

The second major contribution of this research work is the fabrication of PANI functionalized binary and ternary nanocomposites of graphene oxide, reduced graphene oxide, and MnO2 as nanofillers to make PANI-GO, PANI-RGO, PANI-GO-MnO_2, and PANI-RGO-MnO_2. The PANI-RGO-MnO_2 ternary nanocomposite exhibits an excellent dielectric property owing to its hexagonal nanorods structure. The frequency-dependent study shows that the nanocomposites are quite stable over a long range of frequency, suitable for frequency-dependent energy storage devices. The combination of high energy density with high breakdown strength of the electric field indicates the potential applications of the nanocomposites in electrostatic capacitors and fabrication of high frequency-dependent solid-state devices.

The third major contribution has reported the development of polyaniline (PANI) composites using Nylon-6 (PA6) and reduced graphene oxide (rGO), viz. PA6/PANI, rGO/PANI, and PA6/rGO/PANI, synthesized by *in-situ* chemical oxidative polymerization method. The ternary composites PA6/rGO/PANI were prepared with varied weight percent of PA6 and PANI, maintaining a fixed amount of rGO. It is believed that ternary composites exhibit an inter-crosslinked matrix of PA6 and rGO, encapsulated by the PANI nanorods. As a result,

PA6/rGO/PANI 1:2 follows an excellent supercapacitance performance and improved cyclic stability favorable for energy storage applications. Consequently, using PANI-RGO-ZnO 2:1 nanocomposite for the fabrication of symmetric supercapacitors (SSCs) stack assembly in series shows a steady voltage and yields a stored significant energy density and power density. The fabricated SSC device exhibits an excellent electrochemical performance with higher retention capacitance. Following nanocomposite have glowed of a bunch of white LEDs and operated a ~ 5 V DC motor. Such exclusive properties of the PANI-RGO-ZnO 2:1 electrode material firmly incorporate the advantages of expressive high cycle stability of ZnO and excellent electrical conductivity of PANI, respectively provides synergistic effects. Energy harvesting could play a promising role in the miniaturized electronic technology using thin films of the electrode materials. PANI thin films with different oxidation states, viz. PANI-ES and PANI-EB, and a bilayer composite are consisting of both PANI-ES and PANI-EB, using vacuum thermal evaporation. Detailed morphological analysis based on spectroscopic ellipsometry and AFM shows the formation of well-defined thin films of the materials with a film thickness ranging from 50 to 100 nm. Electrical and dielectric measurements show that PANI-ES, being acid doped, shows the higher electrical conductivity, followed by the composite film. The capacitors fabricated using these thin films show good capacitance and charge density, suitable for energy storage devices.

The fourth major contribution of the thesis is the preparation of hierarchically ordered polyaniline (PANI) nanorods in the presence of anionic (sodium dodecyl sulfate, SDS) and nonionic surfactant (pluronic F127) as the SDAs. The amphiphilic character of F127 facilitates the formation of a core-shell micellar structure, which in turn facilitates the polymerization of PANI in the core region. The polycrystalline nature of the nanorods provides the highest thermal stability, contributes significantly towards the enhanced electrochemical activity, and thus, can successfully be used in sensing applications. The PANI-SDS-F127 at 1:1 ratio exhibits remarkably high glucose sensitivity over the other ternary composites.

Acknowledgement

I express my deepest and most sincere gratitude to my thesis supervisors Prof. Ashok Kumar Dasmahapatra and Prof. Harshal B. Nemade for giving me this wonderful opportunity to be a part of their group. I am highly obliged for their encouragement, support, constructive criticism, knowledgeable discussion, and indispensable advices. I thank them for the unlimited support, invaluable guidance and utmost patience they have shown to me.

I am thankful to my doctorial committee members Prof. Parameswar Krishnan Iyer, Prof. Tapas K. Mandal, and Dr. Partho Sarathi Gooh Pattader for their precious suggestions and time to improve the quality of my research work. I would also like to thank Ministry of Human Resource and Development (MHRD) for providing scholarship during my research work of Ph.D. I am special thankful to Prof. Vimal Katiyar, CoE-Sus-Pol IITG, for allowing me to perform experiments, without his support my first publication couldn't be possible. I would like to thank Prof. Dipankar bandyopadhyay, Chemical Engineering for technical discussion during jogging hours and giving me constant encouragement and support. I extended my thanks to Dr. Hanumant Singh Shekhawat, Electronics and Electrical Engineering for their valuable advices and treated as younger brother throughout my IITG stay. On serious note Hanumant Sir, you have taught me how execution and proper planning can help in achieving your targets both professionally and personally. I extended my thanks to Dr. Amit Arora, Materials Science & Engineering, IIT Gandhinagar, for his care and constant motivation specially for contribution of research.

I would like to thank Central Instrument Facility (CIF), Centre for Excellence in Nanoelectronics & Theranostic Devices (CENTD), and Department of Physics, Department of Chemistry, Department of Mechanical Engineering, and Central Workshop for providing me much needed instrumental facilities. My special thanks to the technical and nontechnical staff of the Centre for Nanotechnology for their support in various tasks. Special mention to Mr. Kaustubh Acharyya, Mr. Inderjit Talukdar, Dr. Gyatri Nathu, Ms. Reena day, Mrs. Amlin for their help during characteristics measurements. My special thanks to my seniors Dr. Jitendra Kumar, Dr. Shyam Trivedi, Dr. Nayan mani, Dr. Sunny Kumar, Dr. Chitrita Kundu, Dr. Ashish Singh, Dr. Aanamika, Dr. Ujjwol Barman, Dr. Namami Goswami, Dr. Mitteradip Bhattacharjee, Dr. Amit Singh for their help support and all the useful technical discussions. I would like to thank my colleagues and labmates Rahul Narshiman, Siddhanta Roy, Pritam Roy, Tamanna Bhuyan, Siddarth Thakur, Pawan Kanchi, Papu Kumar, Rahul Singh, Sofia Devi, Shivani Gupta, Suvendhu Mandal, Thomas T. Daniel, Paromita Bhattacharjee, and Rajesh

Mahato for unconditional care, love, and support. In addition, I would like to thanks Mr. Vimal Yadav, PhD Scholar EEE, Dr. Saniv Niak, and Aakansha Singh, PhD Scholar Department of Physics giving me time for electrical, and dielectric measurements of fabricated devices.

It gives me an inspiration to discuss with Dr. Sonal Yadav, Postdoc CSE, regarding research work. She advised me several times as elder sister and extended my knowledge toward future nanotechnology in quantum computing, nano chips in hardware tools, and artificial intelligence. During five years at IITG, I have several friends that have helped me in several ways. I would like to say a big thank you to all of them for their friendship and support. I will cherish the dinner parties, and spent crucial moments with Mr. Narendra Singh Shekhawat, Sr. Project Scientist SAMEER India, Dharmendra Singh Dhaka (M.Tech.), Swati Deora (M.Tech), Kailash Gurjar (B.Tech.), and Nikhil Joshi (JRF). You guys gave me such a nice company during your stay at IITG.

Next I would like to thank Prof. Dr. Bhairun lal Jat, Pediatrics and Orthopedic specialist, SMS Hospital Jaipur, Ramchandra Palsaniya, Applied Materials USA, Prakash Palsaniya, Indain Navy Ministry of Defence, Ajeet Singh Palsaniya, Sr. Software Developer, for their constant encouragement, love, care and support. During IITG journey I had several loving younger brothers, specially thank to Harbans Singh, Parveen Dangi, Lalit Machanva, Abhay Pal Singh, Deepak Dalal, Vinay Jyani, Sunil Kumar Sihag and many more.

I extremely thankful to Prof. Ashok Kumar Dasmahapatra and Prof. H.B. Nemade for the care and support given to me during my stay at IITG and I always enjoyed dinner parties with special sweets and dishes at their home. Finally, my deepest gratitude goes to my parents, brothers, sisters, relatives for their unconditional love, support, and encouragement throughout my studies and helped me go through the rigors of Ph.D.

Shatrudhan Palsaniya

Contents

List of Figures

List of Tables

List of Acronyms

PANI	:	Polyaniline
G	:	Graphene
EDLCs	:	Electric Double-Layer Capacitors
GO	:	Graphene Oxide
RGO	:	Reduced Graphene Oxide
PANI-ES	:	Polyaniline Emeraldine Salt
PANI-EB	:	Polyaniline Emeraldine Base
SDS	:	Sodium Dodecyl Sulfate
APS	:	Ammonium Persulfate
SDA	:	Structure Directing Agent
CV	:	Cyclic Voltammetry
EIS	:	Electrochemical Impedance Spectroscopy
GCD	:	Galvanostatic Charge-Discharge
CCD	:	Cyclic Charge-Discharge
EDS	:	Energy Dispersive X-ray Spectroscopy
SAED	:	Selected Area Electron Diffraction
ESR	:	Equivalent Series Resistance
ESR	:	Electron Spin Resonance
CPE	:	Constant Phase Element
TMD	:	Transition Metal Dichalcogenides
PA6	:	Polyamide 6 /or Nylon-6
ED	:	Energy Density
PD	:	Power Density
SE	:	Spectroscopic Ellipsometry
RMSE	:	Root Mean Square Error
1D	:	One Dimensional
GCE	:	Glassy Carbon Electrode
GOx	:	Glucose Oxidase
LOD	:	Limit of Detection
STSC	:	Symmetric Tandem Supercapacitor

List of Symbols

C_s	:	Specific capacitance
E	:	Energy density
P	:	Power density
ΔV	:	Potential Window
I	:	Current
V	:	Applied Potential/Voltage
Δt	:	Discharge Time
h	:	Planck Constant
ν	:	Frequency of Photon Energy
K	:	Materials Constant
E_g	:	Optical Band gap
α	:	Absorption Coefficient
n	:	Index for Direct and Indirect Band Transitions
eV	:	Electron Volt
R_{ct}	:	Charge Transfer resistance
Q	:	Constant Phase Element
R_s	:	Series Resistance
Z'	:	Real Impedance
Z''	:	Imaginary Impedance
U_e	:	Energy Density of Capacitor
ε_0	:	Free Space Dielectric Constant
ε_r	:	Relative Dielectric Constant
E_b	:	Breakdown Electric Field
Cu-Kα-Kβ	:	X-ray Radiation Constants
λ	:	Wavelength
σ_{dc}	:	Electrical DC Conductivity
J	:	Current Density
e	:	Electronic Charge
n	:	Electron Density
E	:	Electric Field

ε'	:	Real Dielectric Constant
ε''	:	Imaginary Dielectric Constant
C	:	Capacitance
$\tan(\delta)$	:	Tangent Losses
f	:	Frequency
σ_{ac}	:	AC Conductivity
σ_s	:	Surface Charge Density
D	:	Electric Flux Density
δ	:	Skin Depth
μ	:	Permeability
μ_0	:	Free Space Permeability
τ_0	:	Time Constant
Ψ	:	Amplitude Ratio of Plane Polarizations
Δ	:	Phase Difference
n, k	:	Refractive Index, and Extinction Coefficient
S	:	Glucose Sensitivity

Chapter-1

Introduction

1.1. Introduction

The word "polymer" is derived from the classical Greek word *poly* means "many" and *meres* means "parts". Thus, a polymer is a long-chain molecule that is composed of a large number of repeating units of one or more than one type chemical structures. There are a class of polymers naturally available, such as, proteins, cellulose, and silk; whereas, several polymers such as, polyethylene, polypropylene, polystyrene, polyaniline, and many more are prepared by synthetic methods. Polymeric materials are extensively utilized in almost all areas of day-to-day life [1]. Polymer nanocomposite (viz., polymer mixed with suitable nanofillers) exhibits superior property for the application compared to the parent polymers. The presence of nanofillers enhances various properties, such as mechanical, electrical, and thermal stability, etc.

The enhanced electrical property in the class of polymers indicate about conducting polymers (CPs), offer the potential for manufacturing of semiconducting electronic devices, such as, lightweight electrodes for energy storage devices specifically for automotive and aerospace applications. Example of CPs are polypyrrole, polythiophene, polyacetylene, poly (para-phenylene), poly (phenylene-vinylene), poly (thienylene), poly (furylene-vinylene), polypyridine, poly (fluorene), poly (indole), poly (diphenylamine), and polyaniline etc. The invention of CPs (in the mid of 1970s) has supported the development of industrial products and facilitated the fundamental understanding of the chemistry, physics, and materials science of CPs. In general, the impact of CPs is accredited in 2000 by awarding of Nobel Prize to Alan MacDiarmid, Alan Heeger, and Hideki Shirakawa. It is possible to create CPs with a diverse range of properties. For instance, chemical properties can be changed to produce resultant material's ability to grasp simple anions or to render them bioactive. The electrical properties of CPs can be tuned to facilitate different conductivities and redox properties. The properties of the CPs can be tuned during the synthesis by controlling the doping level (viz., acid or base) for suitable applications. For example, acid doped PANI (viz., PANI-ES) possess better electrical conductivity than the base-doped PANI (PANI-EB), which may be suitable for dielectric applications. Therefore, CPs have been emerged as one of the crucial materials in the area of advanced materials, with the following features - ability to engineer at the molecular level to knew particular stimuli, significant conductive, and are capable of localized processing as well as the actuation of response mechanisms. Conducting Polymers, due to their excellent electrical conductivity, low density, and easy processability, find their applications in semiconductors [2], electrochemical energy storage, photovoltaics, display technologies,

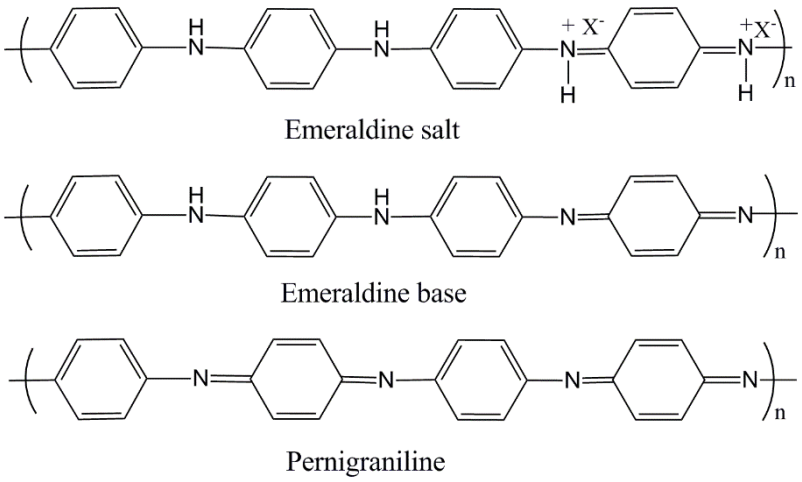

Figure 1.1. Schematic illustration of oxidation states of PANI, protonated form of emeraldine salt, neutral form of emeraldine base and fully oxidized state of pernigraniline.

separation technology, cellular communication, corrosion protection, physical sensors, and micro-electronics fabrications. The development of CPs with sufficient mechanical properties and stability still a challenging issue. However, materials with lower conductivities (100 – 200 S cm^{-1}) can be employed for electromagnetic shielding, and antistatic coating to protect by high voltage surge. Philips Electronics has developed a "plastic chip," where a typical processor chip has been fabricated using PANI and polythienylenevinylene layers [3].

Polyaniline (PANI), one of CPs has been identified as a promising compound and has attracted the attention of researches due to the facile synthesis and its environmental stability. PANI exhibits three main states: emeraldine salt, emeraldine base, and pernigraniline. PANI has a particular structure including of an alternating arrangement of benzene rings and nitrogen groups. Nitrogen atoms exist in either imine (sp^2 hybridization) or an amine (sp^3 hybridization) states. Based on the relative composition of these two states of nitrogen, these states have resulted in various forms of PANI (Figure 1.1) [4]. The acid doped emeraldine salt form of PANI is only electrically conductive among the three types due to the presence of organic counterions (X^-), which retain both oxidized and reduced form of iminium and amine nitrogen groups, respectively [5].

1.2. Preparation of PANI nanomaterials

PANI can be quickly transformed into salt and base states after treating with acid and base, respectively. These states show reversible redox behavior, and pH changing properties. The synthesis route is relatively cost-effective. PANI is commonly synthesized from aniline monomers via chemical, electrochemical, photochemical or enzymatic catalytic oxidative polymerization. These method of preparation usually produce intrinsic PANI, which exhibits

reversible doping-dedoping behavior, with a tunable electrical conductivity. PANI shows molecular self-assembly by forming higher order structures, such as, supramolecular nanofibers, and facilitates itself as multifunctional materials with high surface to volume ratio [6]. Numerous nanostructures have been reported in the form of nanotubes, nanofibers, nanoflowers, and nanospheres [7–9].

The addition of a secondary component into PANI nanomaterials certainly would accelerate its functionality, performance and desired shape [10]. Experimentally, a synergistic effect has been observed between the added components (viz., nanofillers) and PANI, thereby enhancing the characteristic properties of the resultant nanocomposites. This flagship character of nanocomposites has continued to enlarge the scope of new applications [11,12]. Mostly, two types of processes are in use to prepare nanocomposites. First, the single-step redox mechanism of nanoparticles, second, in-situ polymerization in which already developed nanoparticles are blended into the monomer solution using by electrochemical or chemical polymerization. PANI-nanocomposites based on intercalated or layered structures are considered as the most favorable class of hybrid materials. These hybrid materials include plethora of uses such as, in catalysis, wear-resistance or solid lubrication, and in energy storage applications. One of the vital use of CPs in sensing and energy storage devices (batteries and supercapacitors), even though they offer a poor cyclic stability. The intercalated structures extensively enhance their characteristics performance, demonstrating as promising nanomaterials.

1.3. Application of PANI nanomaterials

These outstanding physical properties of PANI based nanomaterials make it applicable in the fabrication of sensors such as biosensors, chemical sensors, piezoelectric sensors, and optical sensors, etc. [13]. These nanomaterials have also been used for various purposes, such as conducting electrodes in solar cells, light-emitting diodes, memory devices, display devices, anti-corrosion layers and merged electromagnetic shielding, etc. [14–16]. In addition, graphene doped PANI nanomaterials also have shown outstanding charge transport properties in electronic devices [17]. The two-dimensional carbon network of graphene nanocomposites have contributed significantly in the area of nanoelectronics [18], biosensors [19], drug delivery, supercapacitors [20], fuel cells, hydrogen storage [21] and hybrid batteries [22–24].

1.4. Supercapacitors

The supercapacitor invention was accredited by the “General Electric” in 1957 when a patent filed for an “electric double layer capacitors (EDLCs).” At that time, the charge storing

mechanism was still unclear when porous carbon was employed as electrode materials, and observed a remarkable capacitance. Afterward, researchers of Standard Oil of Ohio in 1964 have developed an updated versions of the energy storage device [25]. The extended surface area of carbon materials in combination with tetraalkylammonium salt as electrolyte has produced energy storage devices that were commercialized by Standard Oil of Ohio (SOHIO) in 1969 [26]. SOHIO broke down their innovations, and finally, NEC Technology has marketed all energy storage devices as "Supercapacitor" in 1978, by providing backup power to the computing device. The Brian Evans Conway declared a novel idea of charge storage based on redox reactions at the electrode region, and termed as "pseudocapacitor." The first pseudocapacitor was developed using the RuO_2 film as electrode material with outstanding performance in terms of long cyclic stability and reversibility [27]. A new concept of hybrid electric vehicles in 1990s has made supercapacitors popular. Until date, supercapacitors are being researched along with EDLCs and pseudocapacitors using various promising electrode materials.

Supercapacitors also known as ultracapacitors or electrochemical capacitors, have drawn much attention over the past decades due to their distinct properties, such as large power density (> 10 kW kg^{-1}), long cyclic stability (> 100000 cycles) and rapid charge transfer rate [28,29]. Recently, the growth of supercapacitors provides a favorable approach to meet the demands of energy storage applications. Supercapacitors are appeared as a bridge between batteries and typical capacitors, due to high power density as compared to batteries, and high energy density than the conventional capacitors. According to charge storage techniques, supercapacitors mainly classified into two categories: (1) electric double-layer capacitors (EDLC), where the capacitance based on non-faradaic process has developed from the electrostatic charge separation at the interfacial region of electrode and electrolytes. Ion accessible surface region, the pore size of electrode materials, and electrical conductivity are crucial to control the capacitance. Generally, carbon materials employed in the fabrication of EDLCs, exhibit low energy density, high power density, and excellent cyclic stability. (2) Pseudocapacitors follow the faradaic behavior - a rapid and reversible faradaic reactions on the surface of electrode materials [30]. Pesudocapacitors offer high specific capacitance and energy density, where a couple of redox reactions provides significant contribution. As a results, low ionic diffusional rate capability and cyclic stability have been recorded by low faradaic responses [32,33].

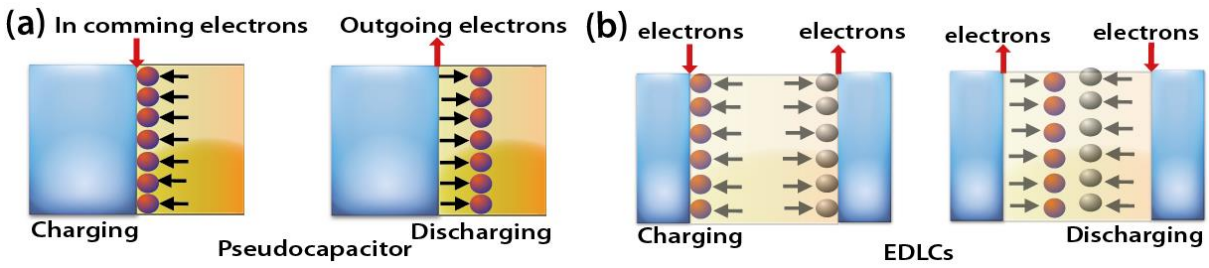

Figure 1.2 Charging-discharging mechanism of (a) Pseudocapacitor and (b) EDLCs supercapacitors. Following diagram redrawn from reference [31].

All kinds of supercapacitors and batteries are constructed using positive and negative electrode materials, and a separator (paper, glass fiber or polymer) is inserted in between the electrode materials. The separator of storage device must be in a conductive environment to allow the ionic charge diffusion, and provide an isolation to restrict the self-discharge. Typically, electrode materials are capable of electrochemical reactions, including ionic and electronic conductivity. The electrode materials are ionically bonded with separator and electronically connected to the metallic surface of current collectors. Therefore, electrode materials and separators are merged into a liquid or semiliquid gel-type solid electrolyte. The above system is typically housed in a well-fitted close box to facilitate energy exchange.

Table 1.1: Different potential conducting polymer candidates for supercapacitors

Materials	**Preparation Method**	**Specific Capacitance (C_s)**	**Energy density (Wh kg^{-1}), and Power density (W kg^{-1})**
PANI	Interfacial polymerization	554 F/g at 1 A/g	
PPy	In-situ polymerization	325 F/g at 5 mV/s	26.7 W h/kg at 140.5 W/kg
PTh	Electro-polymerization	1357.31 mF/g	23.11 mW h/cm^2 at 90.44 mW/cm^2
PANI-CNT	In-situ polymerization	236 F/g at 10 A/g	131 W h/kg at 62.5 kW/kg
PANI-Carbon Nanofiber	Electrochemical polymerization	366 F/g at 100 mV/s	
PANI-hollow carbon sphere	In-situ polymerization	435 F/g at 0.5 A/g	
PANI-Carbon particle	In-situ polymerization	272.6 F/g at 0.63 A/g	
PANI/MnO_2	Oxidative polymerization	383 F/g at 0.5 A/g	53.2 W h/kg at 250 W/kg
Cloth-SWCNT-PANI	Dilute polymerization	410 F/g at 0.5 A/g	26.6 W h /kg at 7000 W/kg
G/PPy	In-situ polymerization	237 F/g at 0.01 V/s	33 Wh/kg and 1184 W/kg
PEDOT-NWs/CC	Electrochemical Polymerization	256 F/g at 0.8 A/g	182.1 Wh/kg at 13.1 kW/kg
CNT/PPy/MnO_2	Electro-polymerization	305.9 F/g at 2 mV/s	8.6 Wh/kg and 16.5 kW/kg
(PPy/LGS)-coated cotton	In-situ chemical oxidative polymerization	304 F/g at 0.1 A/g	20.6 W h/kg

The charging-discharging mechanism is shown in Figure 1.2. This charge storage mechanism is equally applicable for both pseudocapacitors and EDLCs. PANI nanocomposites exhibit high cyclic stability and specific capacitance; hence, they are extensively used in developing supercapacitors. The presence of carbon nanotubes or graphene would increase the storage performance of the electrode materials. We note that PANI functionalized electrode materials can readily be deposited by employing electrochemical deposition method on the desired substrates. Furthermore, MnO_2 based hybrid materials have possessed large capacitance that bears a significant number of charging-discharging cycles [2]. Table 1.1 shows a comparison of various conducting polymers for the application in supercapacitors [34,35].

1.5. Biosensors

In 1906, M. Cremer showed the amount of an acid in a liquid solution, which is equivalent to the electric potential between electrolytes and glasses [36]. In 1909, the concept of pH was presented by Soren Peter Lauritz Sorensen, and the pH measurement electrodes was developed by W.S. Hughes in 1922 [37]. Griffin and Nelson have shown the immobilization of the enzyme, invertase, on charcoal and aluminum hydroxide. The first authentic biosensor developed by Leland C. Clark, Jr in 1956 for the detection of oxygen. He is also known as the father of biosensor as his breakthrough research, consists of his name as "Clark electrode" [38]. In 1962, Leland and Clark reported an amperometric enzymatic glucose biosensor [39]. This method has been followed by Guilbault and Montalvo, Jr in 1969, inventing a first potentiometric biosensor to detect urea [40]. The Yellow Spring Instruments commercialized the first biosensor in 1975 [41]. Afterwards, a remarkable progress was achieved in the field of biosensor. Currently, the field is an interdisciplinary area of interest, which bridges the principles of basic sciences such as physics, chemistry, and biology, including fundamental micro-nanotechnology, electronics, and medicine. A biosensor is a device that analyzes the biological or chemical reactions by producing analog signals to the concentration of an analyte in the reaction medium [41]. Over the last decades, biosensors have been emerged as exciting materials due to their ability to resolve a potentially large number of analytical issues, and challenges in several fields. They are highly capable of delivering quantitative analysis of particular biomolecules and reactions, both *in vivo* and *in vitro* [42], which are promising in the field of medicine. Enormous increasing demand of biosensors has ensured significant development for sensing of an analyte of interest at a sophisticated level. Biosensors possess distinct attributes such as, significant sensitive, specific in nature, fast detection, low-cost, and easy to maintain detection system. The flow diagram of biosensor (Figure 1.3), shows various biosensing techniques. Typically, biosensor

has following sections: (1) a target analyte, which would interact via recognition element, (2) an analyte-bimolecular layer measurement by signal transducer, and (3) an output monitoring system. Primarily, receptor molecules are analyzed at the recognition element, which govern the sensitivity and selectivity of the sensors. Synthetic molecular recognition elements, molecularly imprinted polymers, aptamers, peptides, and metal oxides are used as the sensing elements. The transducer converts biological events into an electrical signal. The transducer of the biosensor is usually distinguished based on the measuring processes. For example, Amperometric, potentiometric, conductometric, and impedance are the electrochemical transducer; fluorescence, colorimetric, luminescence, and interferometry are the optical transducer; Piezoelectric and acoustic wave is the mass-sensitive transducer. The electrochemical transducers are widely used in biosensors. Biosensors address a broad range of applications that are supposed to enhance the living standards. The primary use of biosensors is the detection of biomolecules that can be either a disease symptom or target of the drug. Pollution monitoring required a biosensor that operates for few hours to many days, termed as long term monitoring devices [41].

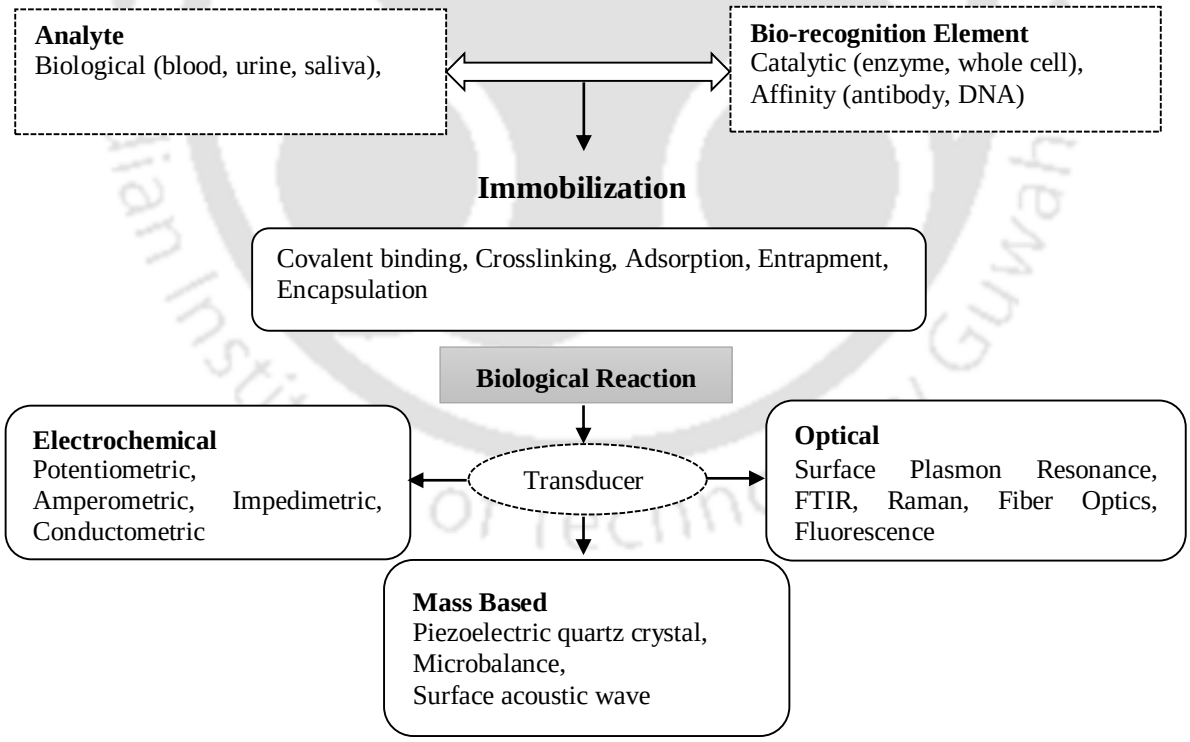

Figure 1.3 Flow diagram shows the biosensor with several biosensing applications.

1.6. Motivations and objectives

1.6.1. Motivations

PANI nanocomposites may exhibit advanced applications in the field of energy storage systems, detection of biological activities, removal and detection of heavy metal ions, gases, viruses and heavy organic toxic constituents. Graphene, a two-dimensional single atomic layer of carbon and thinnest materials in the universe, has exhilarated enormous attention in materials science, chemistry, biology and physics. Graphene-based nanocomposites are promising materials in the application of energy and environment by inserting controlled functional fragments of PANI nanomaterials. Graphene-PANI nanocomposites based dielectric capacitors, electrochemical supercapacitors, and batteries regarded with enhanced energy density. In addition, high dielectric capacitors with high density energy would be promising by the fabrication of PANI thin films using vacuum evaporation to promote miniaturized electronic components due to its property of being lightweight and easy to integrate. The enormous demand for high power pulse capacitors would be fulfilled by the advancement of high-density energy bearer PANI nanomaterials. It has outstanding energy storage efficiency, as has been demonstrated by previously reported research work [33,43–45]. PANI nanomaterials can successfully be utilized in sensing application by controlling its size and shape.

1.6.2. Objectives

The objectives of the thesis are outlined as follows:

1. Graphene functionalized with Polyaniline and MoS_2 to fabricate a nanocomposite for the energy storage applications.
2. Synthesis of Graphene doped Polyaniline and MnO_2 nanocomposites for the application of high density energy storage materials.
3. Preparation of Graphene and PA6 doped hierarchical ordered Polyaniline nanocomposites and fabrication of the symmetric supercapacitor device.
4. Development of Polyaniline-Graphene-ZnO ternary nanocomposites and fabrication of high performance tandem symmetric supercapacitor device.
5. Hybrid thin films depositions of Polyaniline using vacuum evaporation method for the fabrication of thin film capacitors.
6. Preparation of Polyaniline based hierarchical ordered mesoporous structures using anionic and non-ionic surfactants for the application of glucose sensing.

1.7. Organization of thesis

PANI nanomaterials strongly depend on the distribution of nanofillers for property enhancement. Based upon these nanomaterials, a brief introduction of energy storage and sensing devices have been included in **Chapter-1**. **Chapter-2** describes binary and ternary nanocomposites of PANI, G and MoS_2. Among them, PANI-G-MoS_2 ternary nanocomposite exhibits excellent electrochemical activity and enhanced cyclic stability. **Chapter-3** describes GO, RGO, and α–MnO_2 based PANI functionalized binary and ternary nanocomposites. Herein, PANI-RGO-MnO_2 has appeared an excellent candidate for high–density energy storage material with superior dielectric strength. **Chapter-4** presents a comparative study of binary and ternary nanocomposites of PA6, rGO, and PANI components. We have observed that PA6-rGO-PANI 1:2 shows an excellent electrochemical performance with improved cyclic stability, as compared to other composites. Further, fabricated symmetric supercapacitor devices also have demonstrated outstanding performance. C**hapter 5** unveils ZnO (transition metal oxide), and RGO based PANI functionalized nanocomposites. In particular, PANI-RGO-ZnO 2:1 composite reveals a superior performance as an electrode material. **Chapter-6** describes preparation of PANI-ES and PANI-EB thin film, deposited on glass and n-type Si wafer substrates using a vacuum evaporation technique. We have observed that deposition of PANI-EB is relatively easier than PANI-ES. Contrary to PANI-EB, PANI-ES thin-film shows better electrical conductivity. Hence, fabricated thin-film capacitors also have shown remarkable current density and energy density with the high percolation threshold. C**hapter-7** presents a hierarchical mesostructure of PANI nanorods by incorporating SDS and F127 as structure-directing agents (SDAs). The PANI-SDS-F127 1:1 composition has shown higher glucose sensitivity with a lower detection limit, attributed to the synergistic effect of available organic components. C**hapter 8** summarizes the thesis work, with an outlook for future study.

References

[1] P. J. Ludovice, *J. Am. Chem. Soc.* **1996**, *118*, 6098.

[2] Zh. A. Boeva, V. G. Sergeyev, *Polym. Sci. Ser. C* **2014**, *56*, 144.

[3] G. G. Wallace, P. R. Teasdale, G. M. Spinks, L. A. P. Kane-Maguire, P. R. Teasdale, G. M. Spinks, L. A. P. Kane-Maguire, *Conductive Electroactive Polymers : Intelligent Polymer Systems, Third Edition*; CRC Press, 2008.

[4] A. G. MacDiarmid, J. C. Chiang, A. F. Richter, N. L. D. Somasiri, A. J. Epstein, In *Conducting Polymers*; Alcácer, L., Ed.; Springer Netherlands: Dordrecht, 1987; pp. 105–120.

[5] K. M. Molapo, P. M. Ndangili, R. F. Ajayi, G. Mbambisa, S. M. Mailu, N. Njomo, M. Masikini, P. Baker, E. I. Iwuoha, *Int. J. Electrochem. Sci.* **2012**, *7*, 11859.

[6] T. Sen, S. Mishra, N. G. Shimpi, *RSC Adv.* **2016**, *6*, 42196.

[7] Z. J. Gu, J. R. Ye, W. Song, Q. Shen, *Mater. Lett.* **2014**, *121*, 12.

[8] J. Zhang, A. Xing, B. Jia, X. Liu, *High Perform. Polym.* **2019**, *31*, 893.

[9] Y.-Z. Long, M.-M. Li, C. Gu, M. Wan, J.-L. Duvail, Z. Liu, Z. Fan, *Prog. Polym. Sci.* **2011**, *36*, 1415.

[10] L. A. Gallarato, L. E. Mulko, M. S. Dardanelli, C. A. Barbero, D. F. Acevedo, E. I. Yslas, *Colloids Surf. B Biointerfaces* **2017**, *150*, 1.

[11] S. Thomas, G. E. Zaikov, *Polymer Nanocomposite Research Advances*; Nova Publishers, 2008.

[12] X. Lu, W. Zhang, C. Wang, T.-C. Wen, Y. Wei, *Prog. Polym. Sci.* **2011**, *36*, 671.

[13] E. Song, J.-W. Choi, *Nanomaterials* **2013**, *3*, 498.

[14] S. K. Dhawan, D. Kumar, M. K. Ram, S. Chandra, D. C. Trivedi, *Sens. Actuators B Chem.* **1997**, *40*, 99.

[15] Salaneck, *Science and Applications of Conducting Polymers, Papers from the Sixth European Industrial Workshop*; CRC Press, 1991.

[16] A. H. Abdel Aziz, T. S. Jamil, M. S. Shalaby, A. M. Shaban, E. R. Souaya, N. A. Abdel Ghany, *Int. J. Ind. Chem.* **2019**, *10*, 175.

[17] D. Mombrú, M. Romero, R. Faccio, Á. W. Mombrú, *J. Phys. Chem. C* **2016**, *120*, 25117.

[18] J. Wu, W. Pisula, K. Müllen, *Chem. Rev.* **2007**, *107*, 718.

[19] C. Shan, H. Yang, D. Han, Q. Zhang, A. Ivaska, L. Niu, *Langmuir* **2009**, *25*, 12030.

[20] M. D. Stoller, S. Park, Y. Zhu, J. An, R. S. Ruoff, *Nano Lett.* **2008**, *8*, 3498.

[21] G. K. Dimitrakakis, E. Tylianakis, G. E. Froudakis, *Nano Lett.* **2008**, *8*, 3166.

[22] M. Mohiuddin, S. Van Hoa, *Nanoscale Res. Lett.* **2011**, *6*, 419.

[23] Md. E. Uddin, R. K. Layek, N. H. Kim, D. Hui, J. H. Lee, *Compos. Part B Eng.* **2015**, *80*, 238.

[24] K. S. Kim, Y. Zhao, H. Jang, S. Y. Lee, J. M. Kim, K. S. Kim, J.-H. Ahn, P. Kim, J.-Y. Choi, B. H. Hong, *Nature* **2009**, *457*, 706.

[25] H. I. Becker, Low voltage electrolytic capacitor **1957**.

[26] D. L. Boos, Electrolytic capacitor having carbon paste electrodes **1970**.

[27] L. D. Burke, D. P. Whelan, *J. Electroanal. Chem. Interfacial Electrochem.* **1979**, *103*, 179.

[28] L. Li Zhang, X. S. Zhao, *Chem. Soc. Rev.* **2009**, *38*, 2520.

[29] P. Simon, Y. Gogotsi, In *Nanoscience and Technology*; Co-Published with Macmillan Publishers Ltd, UK, 2009; pp. 320–329.

[30] P. Liu, J. Yan, Z. Guang, Y. Huang, X. Li, W. Huang, *J. Power Sources* **2019**, *424*, 108.

[31] M. Zhang, L. He, T. Shi, R. Zha, *Chem. Mater.* **2018**, *30*, 7391.

[32] H. Wang, J. Lin, Z. X. Shen, *J. Sci. Adv. Mater. Devices* **2016**, *1*, 225.

[33] Y. Zhu, Y. Huang, M. Wang, K. Wang, M. Yu, X. Chen, Z. Zhang, *Ceram. Int.* **2018**, *44*, 21690.

[34] I. Shown, A. Ganguly, L.-C. Chen, K.-H. Chen, *Energy Sci. Eng.* **2015**, *3*, 2.

[35] Q. Meng, K. Cai, Y. Chen, L. Chen, *Nano Energy* **2017**, *36*, 268.

[36] M. Cremer, Über die Ursache der elektromotorischen Eigenschaften der Gewebe, zugleich ein Beitrag zur Lehre von den polyphasischen Elektrolytketten; Oldenbourg, 1906.

[37] W. S. Hughes, *J. Am. Chem. Soc.* **1922**, *44*, 2860.

[38] W. R. Heineman, W. B. Jensen, *Biosens. Bioelectron.* **2006**, *8*, 1403.

[39] J. Park, H. H. Nguyen, A. Woubit, M. Kim, *Appl. Sci. Converg. Technol.* **2014**, *23*, 61.

[40] G. G. Guilbault, J. G. Montalvo, *J. Am. Chem. Soc.* **1969**, *91*, 2164.

[41] N. Bhalla, P. Jolly, N. Formisano, P. Estrela, *Essays Biochem.* **2016**, *60*, 1.

[42] Y.-L. Yang, J.-F. Huang, T.-F. Tseng, C.-C. Lin, S.-L. Lou, *Conf. Proc. Annu. Int. Conf. IEEE Eng. Med. Biol. Soc. IEEE Eng. Med. Biol. Soc. Annu. Conf.* **2008**, *2008*, 3162.

[43] M. Zhang, L. He, T. Shi, R. Zha, *Chem. Mater.* **2018**, *30*, 7391.

[44] H. Wang, J. Lin, Z. X. Shen, *J. Sci. Adv. Mater. Devices* **2016**, *1*, 225.

[45] P. Simon, Y. Gogotsi, *Nat. Mater.* **2008**, *7*, 845.

Chapter-2

Synthesis of Polyaniline/Graphene/MoS_2 Nanocomposite for High Performance Supercapacitor Electrode

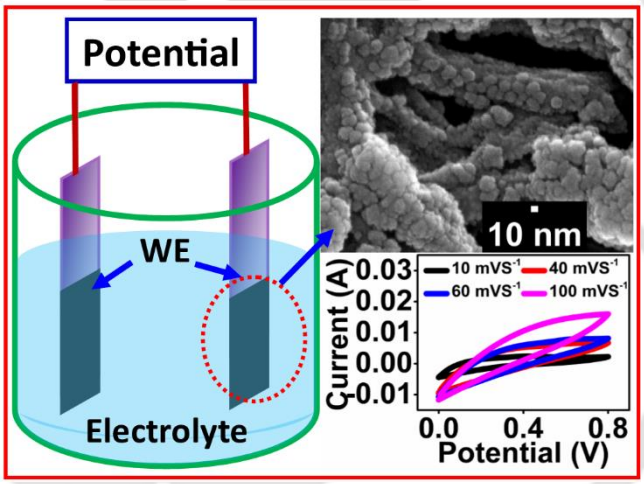

S. Palsaniya, H.B. Nemade, A.K. Dasmahapatra, Synthesis of polyaniline/graphene/MoS_2 nanocomposite for high performance supercapacitor electrode, *Polymer*. 150 (2018) 150–158.

2.1. Introduction

Supercapacitors are ubiquitous in almost every energy storage devices due to their higher power and energy density, and greater cyclic stability compared to the conventional batteries [1,2]. The high specific capacitance in supercapacitor is primarily achieved by the presence of electrical double-layer and Faradaic pseudocapacitance [2]. An increase in surface area usually enhances the double layer capacitance, and the presence of a redox reaction enhances the Faradaic pseudocapacitance. A combination of these two needs a mixture of the materials from both the categories to enhance the supercapacitance behavior. Various materials such as metals [3], metal oxides [2,4], activated carbons and conducting polymers [5–7] have been used in preparing supercapacitors. Out of these, conducting polymers are gaining much attention in preparing supercapacitors due to their high charge density, flexibility and low cost. Polyaniline (PANI) is one of the most promising candidate for the electrode materials of supercapacitor. PANI has extensively been used in energy storage devices due to its significantly high specific capacitance, which can be tuned by doping with suitable dopants. However, the limited cyclic stability restricts its wider applications. To overcome this limitation, nanocomposites of PANI with inorganic materials have been attempted to bring together high mechanical stability of inorganic nano fillers and good pseudocapacitance of PANI [8–10].

In recent years, graphene has been emerged with an excellent charge transport capability, high thermal conductivities, high surface area [11] and good mechanical properties [11–14]. Therefore, the nanocomposites of polyaniline and graphene [13,15,16] would possess excellent electrochemical properties compared to that of pure PANI and graphene [17], for the application of supercapacitors. The nanocomposites of PANI and graphene were successfully prepared by *in-situ* chemical polymerization, and the resulting materials have been found to be suitable for the application in energy storage devices, chemical sensors, memory devices and supercapacitors [18–21]. Similar to graphene, Molybdenum disulfide (MoS_2), a transition metal dichalcogenide material, having a two-dimensional layered structure, possesses an excellent semiconducting behavior that can be applied as a supercapacitor electrode material to achieve higher efficiency. MoS_2 exists primarily in two different phases: a trigonal prismatic 2H phase with smaller capacitive behavior, and an octahedral 1T phase with higher electrochemical behavior, suitable for supercapacitors [22–26]. Therefore, the combination of graphene and MoS_2 nanosheets (NSs) with PANI (conducting polymer) would definitely be a promising candidate for the next-generation supercapacitors [26].

It is reported that the composite of PANI and MoS_2 exhibits a better supercapacitance behavior with high cyclic stability (~ 82%) in comparison with pure PANI, which shows a cyclic stability of ~ 68% [25,27]. Li et al. [28], has shown that the ternary composite of PANI with MoS_2 and reduced graphene oxide (RGO) exhibits an excellent electrochemical properties, suitable for energy storage applications. Wu et al. [13] have reported a composite of chemically converted graphene and PANI film for the supercapacitor application. The composite film exhibits high conductivity (5.5×10^2 S/m), ~ 10 times higher than the intrinsic PANI nanofiber film. Krishnamoorthy et al. [3] have developed MoS_2 sheets over Mo foil using hydrothermal process and investigated their supercapacitor behaviors (192.7 F g^{-1} at 1 mA cm^{-2}). In addition, Pazhamalai et al. [29], have reported a self-charging supercapacitor power cell (SCSPC) containing an ion gel electrolyte and a piezopolymer separator. The composite exhibits high specific capacitance, energy density and power density. Ren et al. [30] have successfully grown PANI nano wires of size 10 – 20 nm on three-dimensional tubular MoS_2 by in situ polymerization of PANI. The resultant nanocomposite showed an excellent electrocatalytic behavior with increased capacitance retention, which is attributed to the specific structure of the composite along with a cooperative effect of MoS_2 and PANI. Interestingly, Wang et al. [31] have synthesized a two-dimensional MoS_2/PANI nanocomposite via a confined synthesis method, which yields an enhanced interlayer distance between MoS_2 layers, close to 1.08 nm from 0.62 nm. The enhanced interlayer distance facilitates higher Na+ and Li+ ion storage, which is attributed to the increased mobility of the ions through the expanded interlayer spacing, supported by an *ab initio* Molecular Dynamic simulation study.

In this work, we demonstrate that nanocomposites of PANI with two-dimensional nanosheets (viz., MoS_2 and graphene) would be an excellent candidate for the use as a supercapacitor with a cyclic stability of ~ 98%. We have employed a solvent exfoliation method for the preparation of MoS_2 and graphene nanosheets. Following this, we have followed an *in-situ* chemical oxidative polymerization process of aniline monomers with the graphene/MoS_2 dispersions for the synthesis of PANI to prepare the nanocomposites. We present results on a series of binary nanocomposites (PANI-G) with varying concentration of graphene, to elucidate the effect of the composition of the fillers on the electrochemical properties of the composites. Finally, we present the results on a ternary nanocomposite of PANI, G and MoS_2, which shows a superior result compared to the binary composites.

2.2. Experimental section

2.2.1. Materials

Graphite powder (99.9999%, metals basis), carbon black (50% compressed), acetylene (99.9%) and poly (vinylidene fluoride) powder were purchased from Alfa Aesar. N-Methyl-2-pyrrolidone (~99.5%), Molybdenum (IV) Sulphide (~98%) and Ammonium Persulphate (99%) were purchased from Sisco Research Laboratories. Aniline (Emparta grade, ≥99.0%) and Acetone (Emplura grade, ≥99.0%) were purchased from Merck Millipore and Hydrochloric acid (assay ~35-37%) was purchased from Fisher Scientific. All the chemicals were of analytical reagent (AR) grade with % of purity as indicated, and used as received.

2.2.2. Synthesis of chemically exfoliated graphene and MoS_2 nanosheets

The synthesis of graphene was carried out through the solvent exfoliation technique [32], with N-methyl-2-pyrrolidone (NMP) as the solvent. An amount of 50 mg of graphite powder was added to 10 ml of NMP. The mixture was sonicated in an Ultrasonic bath at 33 kHz for 8 hours. A dark grey dispersion was obtained. The dispersion was allowed to settle overnight, and then centrifuged at 1500 rpm for 30 minutes. The supernatant liquid was collected and used for further experiments. A similar solvent exfoliation method was adopted for the preparation of MoS_2 nanosheets [33]. An amount of 50 mg of MoS_2 powder (properly grounded) was added to 10 ml of NMP. The mixture was sonicated for 4 hours in an Ultrasonic bath at 33 kHz. The resultant mixture (a light grey dispersion) was left overnight to settle. The dispersion was then centrifuged for 30 minutes at 1500 RPM. The supernatant liquid was used for further experiments. An approximate concentration was determined by measuring the amount of graphite and MoS_2 left unexfoliated. The dispersion was allowed to settle over several hours, and the supernatant was further centrifuged. The collective sediment from these processes was then washed with DI water and finally with acetone to remove NMP. The sediment was dried at 40°C to remove acetone. The unexfoliated particles were weighed; the difference between the final and the initial amount was taken as the approximate amount of particles exfoliated in the dispersion. Based on this, the concentrations of graphene and MoS_2 in the dispersions were determined.

2.2.3. Synthesis of PANI, PANI-G and PANI-G-MoS_2 nanocomposites

The procedure for Polyaniline synthesis as described in the IUPAC technical report was followed with a few modifications [34]. An amount of 3.72 g of aniline monomer was added to a 50 ml of 1M HCl, and stirred for 40 minutes. Another solution was prepared with 9.1 g of ammonium persulfate (APS) in 50 ml of 1M HCl. The APS solution was then added to the aniline solution drop by drop at 0 °C with constant stirring. The solution was a colorless

mixture. Gradually, the color was changed from blue to dark blackish green, indicating the formation of PANI-ES (Polyaniline Emeraldine Salt). The mixture was allowed to polymerize for 24 hours, then filtered and washed with 0.2 M HCl, followed by acetone, and finally with 0.2M HCl. The precipitate of PANI was vacuum dried at 60 °C for 24 hours. The dried sample was collected in a glass petri dish or further studies. PANI nanocomposites were prepared with graphene by *in-situ* chemical oxidative polymerization in the presence of solvent-exfoliated graphene (Figure 2.1a). A solution was prepared with 0.5 gm of aniline monomers in 50 ml of 1M aqueous HCl and stirred for 15 minutes. To the above solution, x amount of graphene was added from the graphene in NMP dispersion, where x is the weight % of graphene. The concentration of graphene was varied as 0.4, 1 and 2 weight %. A solution of 1.5 gm APS in 40 ml of 1 M HCl was prepared and added dropwise to the above aniline solution. The reaction mixture was stirred at 400 RPM at 0 °C for an hour. Then, the mixture was kept at 0 - 4 °C for 24 hours, to complete the polymerization. The precipitate was filtered and washed with 0.2 M HCl solution, and vacuum dried at 60 °C for 24 hours. For each sample (viz., PANI-G 0.4%, PANI-G 1% and PANI-G 2%) all weight and molar ratios were calculated with respect to the initial amount of the aniline monomer taken.

The ternary nanocomposite of PANI, graphene and MoS_2 was prepared in a similar manner as described above (Figure 2.1b). In a solution of 0.5 gm aniline and 50 ml of 1M aqueous HCl, equal amount of graphene (2 weight %) and MoS_2 (2 weight %) were added from their respective dispersion in NMP. This mixture was stirred for 15 minutes at room temperature. It was then sonicated at 33 kHz for 45 minutes. The mixture was then cooled down to 0 °C. A solution of 1.5 gm of APS in 40 ml of 1M HCl has prepared. The APS solution was then added drop by drop to the above mixture at constant stirring. The reaction mixture was stirred at 400 RPM at 0°C for an hour, and then kept for 24 hours to complete the polymerization. Following this, the mixture was filtered and the precipitate was washed with 0.2M HCl solution, acetone and again with 0.2M HCl solution. The washed sample was vacuum dried at 60 °C for 24 hours. The dried dark green powder was collected in a plain petri dish for the further study.

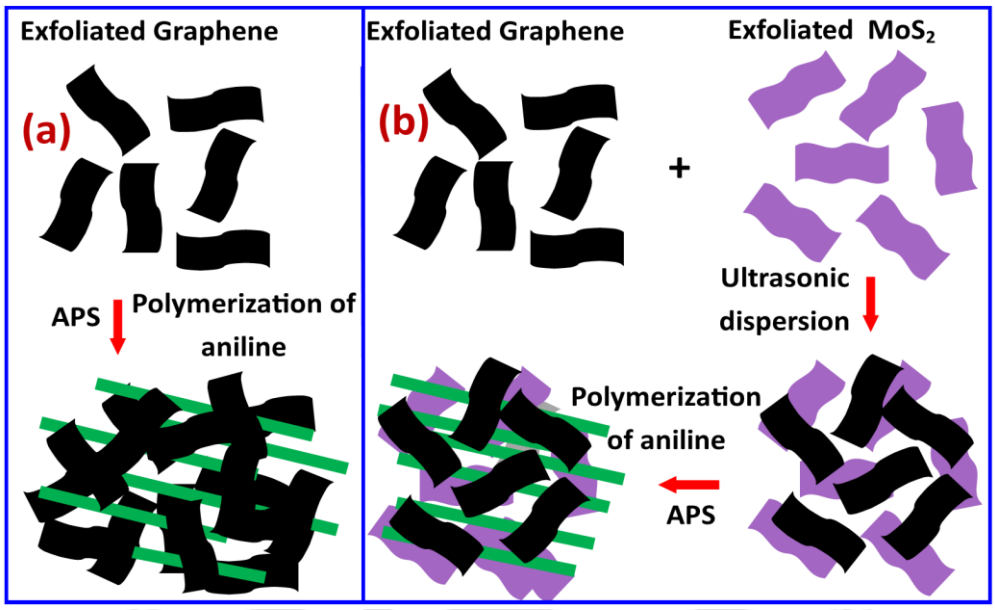

Figure. 2.1. Schematic diagram of the experimental method: (a) binary nanocomposites of PANI and graphene, (b) ternary nanocomposite of PANI, graphene and MoS_2. Dispersion of MoS_2 and graphene nanosheets followed by an in situ polymerization of PANI.

2.2.4. Materials characterization and measurements

The Micro Raman spectra of the nanocomposites were recorded using Horiba Jobin Vyon, Model LabRam HR with an excitation wavelength of 514 nm. The FTIR spectra were recorded using Shimadzu model no IR Affinity-1, with the dried KBr in the range of 400-4000 cm^{-1}, after palletization of the solid powder samples. The UV-Visible absorption spectra were collected via Shimadzu, UV-2600 230V EN, in the wavelength range, 200 - 800 nm. The crystalline structures of the nanocomposites were evaluated using X-ray diffraction (XRD) analysis. The structural patterns were carried out in a rotating anode high power XRD (Rigaku, model TX-III), operated at 50 kV, 180 mA, with radiation of Cu kα, with an angle ranging from 10° to 70°. Following this, the crystallographic planes were analyzed via xpert high score plus software. The morphological features of the polymer nanocomposites were studied by a field emission scanning electron microscope (JEOL, JSM-7610F FESEM), at an accelerating voltage of 15 kV and the dimensions of the nanocomposites were analyzed with the help of ImageJ software. The transmission electron microscopy (TEM) performance was carried out on a JEOL, JEM 2100 at the acceleration voltage of 200 kV. The thermogravimetric analysis (TGA) of the nanocomposites was carried out by using TGA/DTG (Netzsch, Model STA449F3A00), at a heating rate of 10 °C min^{-1} under an inert atmosphere by purging argon gas at 20 mL min^{-1}. The electrochemical measurements were carried out in three electrode and

two electrode setup using the Autolab electrochemical work station of Metrohm (PGSTAT204), with 1M H_2SO_4 at room temperature. The working electrodes (WE) were fabricated by mixing of active materials in the 80:15:5 ratios. Typically, 5.1 mg of the nanocomposite material, 0.9 mg of acetylene black (as a negative electrode material) and 0.3 mg of PVDF (as a binding agent), were put into a mortar, and a 'paste' was prepared by mixing with adequate amount of NMP. The paste was coated on a stainless steel woven mesh and pressed under 20 MPa pressure to ensure an evenly dispersed system to have adequate electrical properties. The detailed description of the electrochemical measurements has been given as follows:

Cyclic Voltammetry (CV) results were analyzed at various scan rates from 5 to 100 mV sec^{-1}. The electrochemical impedance spectroscopy (EIS) measurements were analyzed by applying an AC voltage at 10 mV in the frequency range of 0.1Hz to 100 kHz. The galvanostatic charge/discharge (GCD) measurements were also recorded at various current densities. The value of the specific capacitance (C_s) was calculated from cyclic voltammetry and GCD curves as given by following equations [35]:

C_s from CV curves

$$C_s = \frac{\int i\, dv}{m*v*\Delta V} \tag{2.1}$$

C_s from GCD curves

$$C_s = \frac{I*\Delta t}{m*\Delta V} \tag{2.2}$$

According to the calculated value of C_s, energy density (E) and power density (P) have been analyzed according to the following equations[36].

$$E = \frac{1}{2*3.6} * C_s * \Delta V^2 \ (Wh\ kg^{-1}) \tag{2.3}$$

$$P = \frac{E}{t} * 3600 \ (W\ kg^{-1}) \tag{2.4}$$

where, total integrated absolute value of CV curve is $\int i\, dv$, v is the scan rate (mV s^{-1}), I is the discharge current (A), the discharge time is Δt (s), ΔV is the potential window (volt, V), m is the mass of the active electrode materials (g), C_s is the specific capacitance (F g^{-1}) and t is the discharging time (s).

2.3. Results and discussions

We begin with describing the detailed microstructures of PANI, PANI-G binary nanocomposites with varying quantity of graphene and PANI-G-MoS_2 ternary nanocomposite.

Subsequently, we discuss the electrochemical behavior of all the materials, including three- and two-electrode measurement methods.

2.3.1. Materials structure and morphology

The Raman spectra of the composites (Figure 2.2a) explores the strong interaction of π-π* symmetric bonding between PANI, graphene and MoS_2. The formation of PANI-G and PANI-G-MoS_2 hybrids has been identified by the presence of the peaks of C-N bond stretching, ranging from 1327 cm^{-1} to 1295 cm^{-1}. The peak at 1158 cm^{-1} corresponds to the C-H quinoid bending. The peaks at 1458 cm^{-1} and 1582 cm^{-1} are attributed to the bond vibrations of C=N and C=C, respectively, associated with quinoid stretching, revealing the formation of well-dispersed PANI nanocomposites [37,38]. The Raman spectra of exfoliated MoS_2 have consecutive E'_{2g} and A'_{2g} modes, based on which a frequency difference can be calculated for the determination of the numbers of layers of MoS_2 [39] present in the composites. Accordingly, the analysis of the peaks displayed in the frequency range from 582 cm^{-1} to 628 cm^{-1} correspond to the Raman shift of PANI-G-MoS_2 shows 6-7 layers of MoS_2. Figure 2.2b represents the X-ray diffraction (XRD) patterns of PANI, PANI-G and PANI-G-MoS_2 nanocomposites. The characteristic peaks at 20° and 25° reveal the isomorphous nature of the nanocomposites. The variations in the intensity of the corresponding peaks suggest the continuous parallel and perpendicular arrangement of PANI chains. The peaks of PANI at the diffraction angles of 14.8°, 20.16°, 25.3° and 27.03° correspond to the crystallographic planes of (1 1 2), (0 2 0), (1 2 2) and (2 1 0), respectively [40]. Interestingly, the diffraction peak of PANI at 25.3° appears to be more intense compared to the PANI-G nanocomposites, suggesting the presence of a maximum amount of crystalline PANI in the composite.

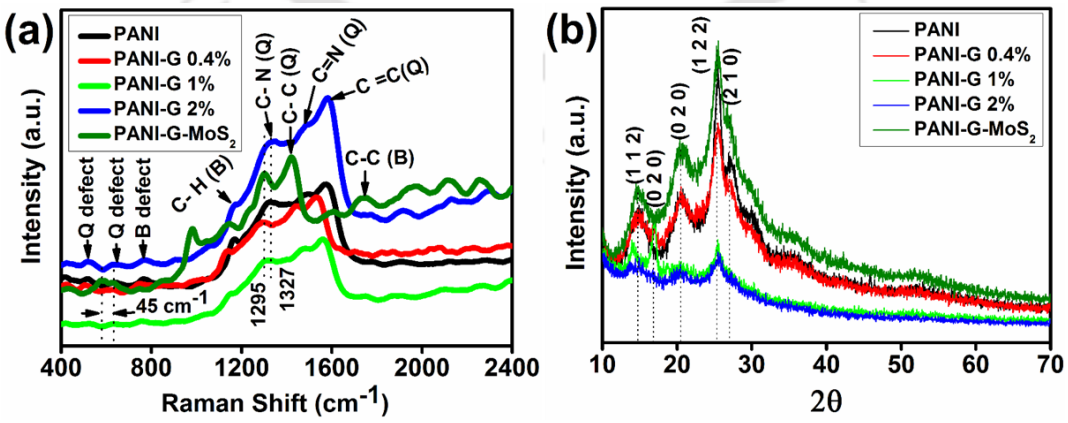

Figure 2.2. (a) Raman spectra, (b) XRD patterns with plane configurations, of pure PANI, PANI-G 0.4%, PANI-G 1%, PANI-G 2% and PANI-G-MoS_2 nanocomposites.

From the XRD patterns, it is evident that the crystallinity of PANI decreases with increasing graphene loading, which is attributed to the loss of chain mobility of PANI in the presence of graphene sheets. However, for the ternary nanocomposite (viz., PANI-G-MoS_2), we observe an increase in crystallinity due to the presence of MoS_2**.** The higher crystallinity in the ternary nanocomposite compared to the binary nanocomposites, would be beneficial for an easy charge transport for the application in supercapacitors. The XRD pattern of ternary nanocomposite of PANI-G-MoS_2 exhibit a strong and intense peak at 25.3° corresponding to (1 2 2) plane with an interplanar spacing of 3.51 Å, higher than that of pure PANI (3.48 Å), PANI-G 0.4% (3.48 Å), and PANI-G 2.0 % (3.44 Å). The higher interplanar spacing of PANI-G-MoS_2 ternary nanocomposite over the binary nanocomposites signifies an exfoliated structure of MoS_2 layers. Further, the characteristic diffraction peak at 14.9° corresponds to the (1 1 2) plane, resulted from the restacking of MoS_2 even before the polymerization of PANI [41,42].

The asymmetric structure and compositions of the prepared nanocomposite materials have been confirmed by FTIR spectra, as shown in Figure 2.3. The FTIR spectra were recorded to identify the stretching and bending vibrations of the functional groups present in the prepared NCs. The characteristic peaks at 1420 cm^{-1} and 1632 cm^{-1} are for the C=C stretching vibration corresponding to benzene and quinoid rings, respectively. The characteristic peak at 1213 cm^{-1} is due to C-N stretching of the benzene amine group, and a peak at 1098 cm^{-1} is due to the in-plane bending vibration of C-H bonds. The peak at 550 cm^{-1} in PANI-G-MoS_2 is attributed to the Mo-S bond vibrations. The peaks at 2050 cm^{-1} to 2060 cm^{-1} confirms the presence of the N-H bond of aromatic amine. Furthermore, the characteristic peaks at 3400 cm^{-1} is visible to all the FTIR spectra of nanocomposites, which corresponds to the stretching vibration of the O-H bond. The finite interval of transmittance of all the spectra is attributed to the decreasing order of hydroxyl groups, as PANI nanorods being coated upon graphene and MoS_2 nanosheets. The FTIR spectra clearly reveals the formation of PANI-G and PANI-G-MoS_2 nanocomposites [43,44] and corroborate the observation in UV-VIS spectra, as discussed below. The optical properties of π–π^* bonding and polaron transitions via surface interaction were analyzed by the UV absorbance. The excellent charge transport properties is due to the incorporation of graphene nanofillers in PANI-G nanocomposites. Figure 2.4 shows the UV-visible spectra of pure PANI, binary nanocomposite of PANI-G at various concentrations of graphene nanosheets and the ternary composite, PANI-G-MoS_2.

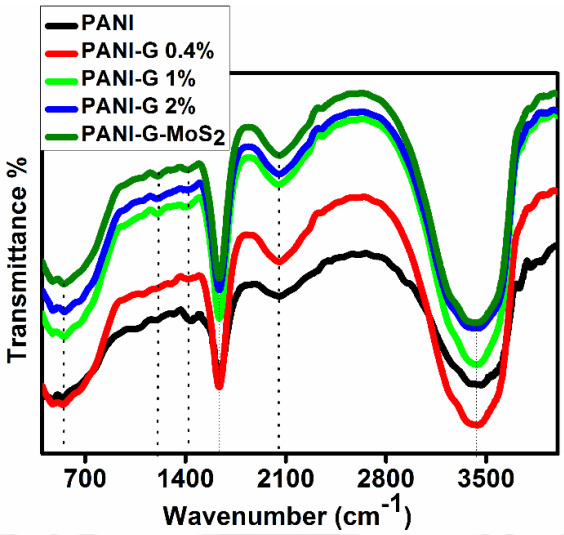

Figure 2.3. FTIR spectra of pure PANI, PANI-G 0.4%, PANI-G 1%, PANI-G 2% and PANI-G-MoS_2 nanocomposites.

The first characteristic absorption band at 300-350 nm corresponds to the π-π* transition of C-C bond and the second absorption band at 470 nm is due to the polaron transition. These characteristics absorbance are correlated to the protonated form of PANI dispersion in acidic medium. It has been noticed that PANI-G nanocomposites have a higher intensity of absorbance as compared to the intrinsic PANI. The absorption behaviour of the ternary nanocomposite indicates a red shift, which is attributed to the extensive electronic conjugation between PANI, G and MoS_2 [45]. The direct and indirect band gap of all the nanocomposite materials have been presented in Figure 2.5 and Figure 2.6. The change in absorption spectra as mentioned above, confirms an interfacial functionalization of PANI with the graphene nanosheets. The absorption band occurs at the PANI-MoS_2 interface, which results a surface plasmon due to metal-polymer interface. Consequently, the plasmonic nanostructure changes the energy levels and corresponding resonant wavelengths with an appearance of the red shift. Furthermore, MoS_2 and graphene nanosheets exhibit an interfacial adhesion upon PANI, facilitated by the electronic conjugation via benzene rings of PANI. The discrete variations in energy bands have been observed at the maximum absorption of π-π* transition. The maximum absorption spectra of PANI, PANI-G 0.4%, PANI-G 1% and PANI-G 2% were obtained at 260 nm, which corresponds to the maximum polaron bond localization, compared to the absorption at 455–480 nm wavelength for strong π-π* transition.

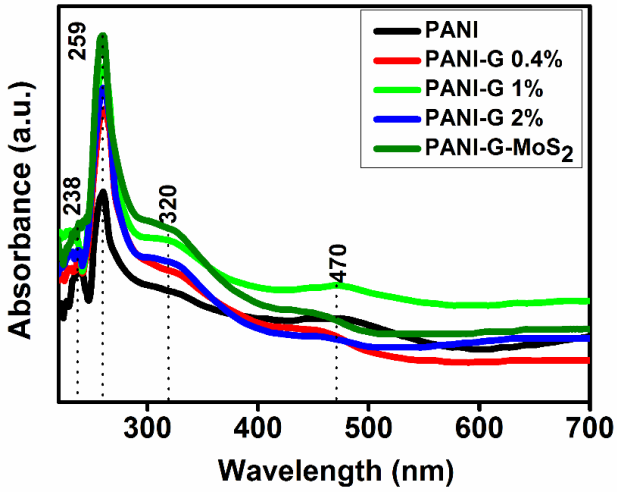

Figure 2.4. UV visible absorbance spectroscopy of the nanocomposite samples.

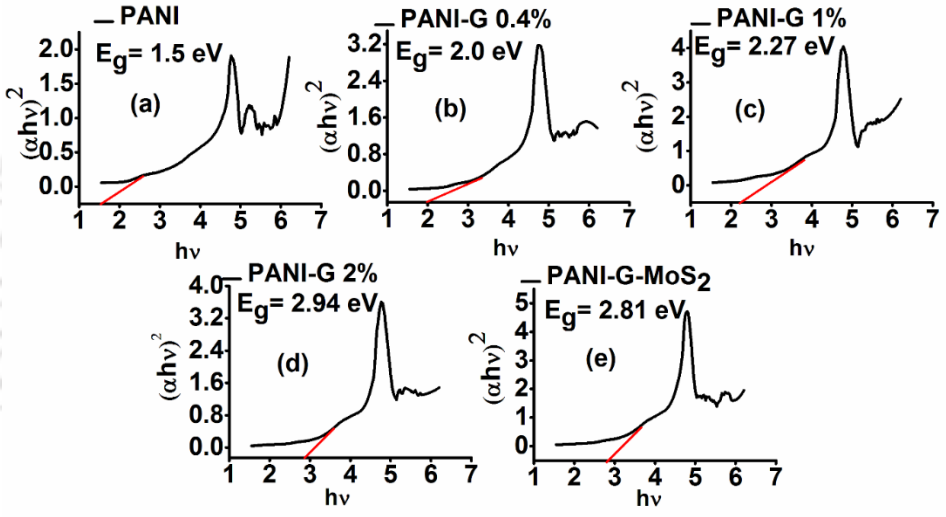

Figure 2.5. Direct band gap energy calculation using tauc plot of (a) pure PANI, (b) PANI-G 0.4%, (c) PANI-G 1%, (d) PANI-G 2% and (e) PANI-G-MoS_2.

The extended optical band gap of the binary nanocomposites (Fig. 2.5a-d) reveals that PANI has grown over graphene nanolayers. A direct band transition of MoS_2 takes place as we move from a bulk to a few-layered structure [46]. The increment of the direct energy band with the loading of weight % of the graphene in the composites indicates a blue shift. The nanocomposite of PANI-G-MoS_2 (Figure 2.5e), exhibits a higher absorbance intensity at 259 nm accompanying with a slightly lowered energy band gap as compared to PANI-G 2%. The indirect band gap calculation of the nanocomposites has been shown in Figure 2.6a-e, clearly reveals that the deviation of band gap from pure PANI is very less.

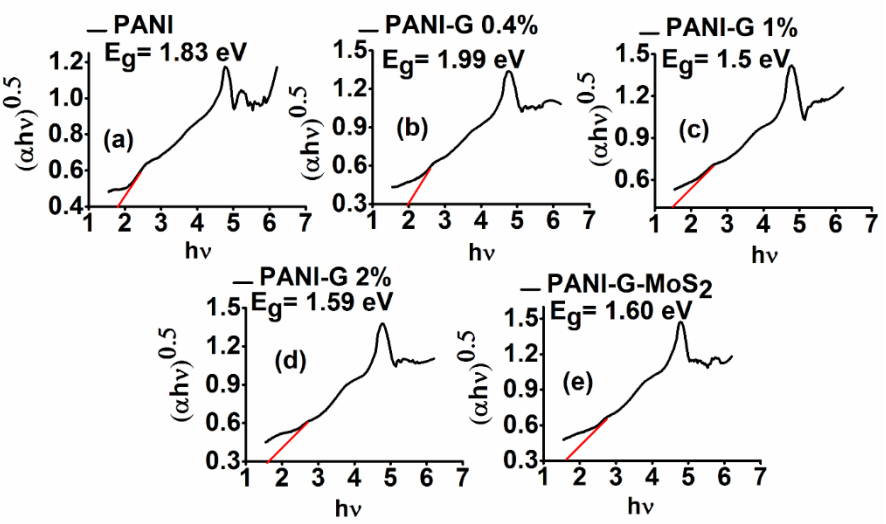

Figure 2.6. Indirect band gap energy calculation using tauc plot of (a) pure PANI, (b) PANI-G 0.4%, (c) PANI-G 1%, (d) PANI-G 2% and (e) PANI-G-MoS_2.

Hence, there is no significant role of the doped graphene and MoS_2 over the band gap, resulting a direct band gap transition only. Typically, UV-Visible spectra were used to identify the optical properties. The optical band gap of the nanocomposite materials has been calculated using the tauc plots with the help of the following equation [44], by plotting $(\alpha h\nu)^2$ vs. hν.

$$k(h\nu - E_g) = (\alpha h\nu)^{\frac{1}{n}} \quad (2.5)$$

where, E_g is the band gap of the nanocomposite materials, k is the materials constant, ν is the frequency of photon energy (hν), h is the Plank's constant, α is the linear absorption coefficient and n is the index representing the nature of the band gap. The value of n = 0.5 and 2.0 for direct and indirect band transitions, respectively. A tangent to the curve gives the value of the band gap of nanocomposites. The calculated optical band energies for the direct and indirect transitions of PANI, PANI-G 0.4%, PANI-G 1%, PANI-G 2% and PANI-G-MoS_2 are exhibit below in Table 2.1.

Table 2.1. Comparative study of band energies of the nanocomposites

Nanocomposites	Direct Band Gap (eV)	In-Direct Band Gap (eV)
PANI	1.5	1.83
PANI-G 0.4%	2.0	1.99
PANI-G 1%	2.27	1.50
PANI-G 2%	2.94	1.59
PANI-G-MoS_2	2.81	1.60

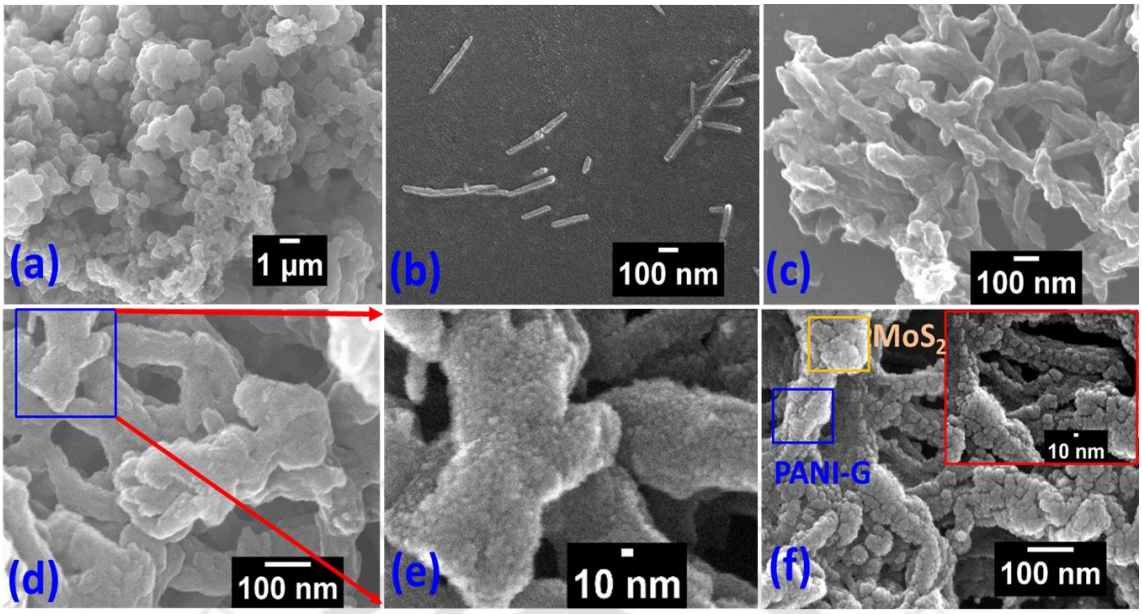

Figure 2.7. (a) FESEM image of synthesized polyaniline and graphene doped samples of PANI micro beads, (b) nanorods of PANI-G 0.4%, (c) PANI-G 1%, (d) PANI-G 2% at lower magnification (e) at higher magnifications, (f) ternary nanocomposite of PANI-G-MoS_2, inset image is of high magnification as indicated.

The FESEM image of pure PANI (Figure 2.7a) exhibits a randomly distributed morphology of spherical micro-beads with an average diameter of 222.17 nm. In an acidic medium, PANI micro-beads form a dark green colored (emeraldine salt) agglomerated structure. Since PANI was synthesized in the presence of graphene and MoS_2 nanosheets, the morphology of the resultant composites would also be influenced by these nano fillers. Figure 2.7b exhibits a nanorod shape morphology of PANI-G 0.4% with an average length and diameter of 176.65 nm and 18.16 nm, respectively. Figure 2.7c shows the image of PANI-G 1% with an average length and diameter of 309.26 nm and 51.22 nm diameter, respectively. It has been observed that the average diameter of PANI-G 1% is larger than that of PANI-G 0.4%, (Figure 2.7b), which is attributed to the swelling property of PANI nanorods in the presence of higher graphene content. However, for PANI-G 2%, the average size of the layered structure decreases to 94.62 nm, as shown in Figure 2.7d and Figure 2.7e (at a higher magnification). The decrease in size may be attributed to the favorable electrostatic interaction between PANI and graphene, leading to the formation of an intercalated and uniformly cross-linked layered structure. The presence of a significant amount of graphene content is responsible for the enhancement of electronegativity of the PANI-graphene nanocomposites (cf., PANI functionalized graphene) [37].

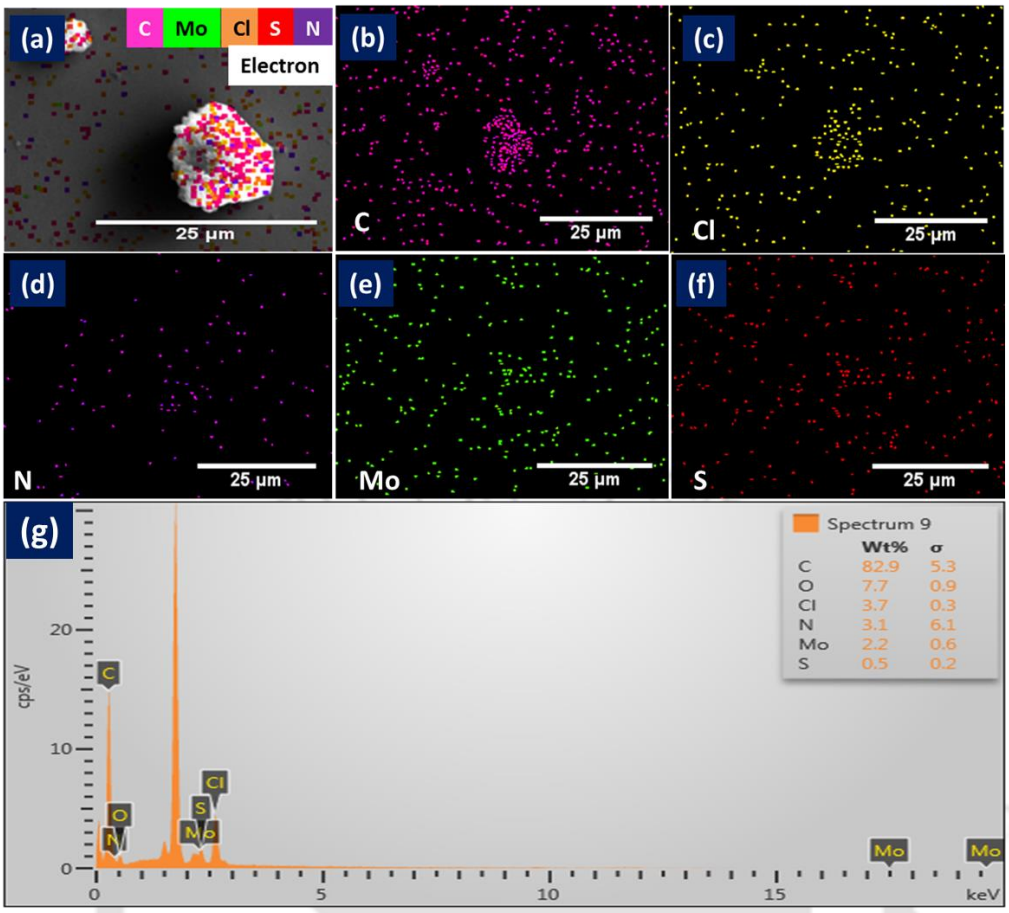

Figure 2.8. EDS analysis with elemental mapping of the ternary nanocomposite of PANI-G-MoS_2 surface, which was characterized over the silicon wafer substrate, as shown in (a) to (f) and map sum spectrum, as shown in (g) of the PANI-G-MoS_2 nanocomposite.

The FESEM image of the PANI-G-MoS_2 ternary nanocomposite (Figure 2.7f) reveals that the MoS_2 nanoflakes and graphene layers are evenly intercalated with PANI nanorods. The average size of the layered structure of the ternary composite is ~ 267 nm with ~ 18 nm diameter of PANI nanorods. Therefore, the resultant ternary composite appears to be an interlayered structure of graphene and MoS_2, encapsulating the PANI nanorods. The highly porous structure as shown in FESEM images (Figure 2.7) coupled with the presence of +ve (PANI) and –ve moiety (graphene and MoS_2) makes the binary PANI-G and ternary PANI-G-MoS_2 nanocomposites excellent materials for the use as supercapacitors [38,47]. Further analysis based on FESEM-EDS shows that the elements (viz., C, Cl, N, Mo and S) are uniformly distributed over the entire surface of the nanocomposites, as shown in Figure 2.8.

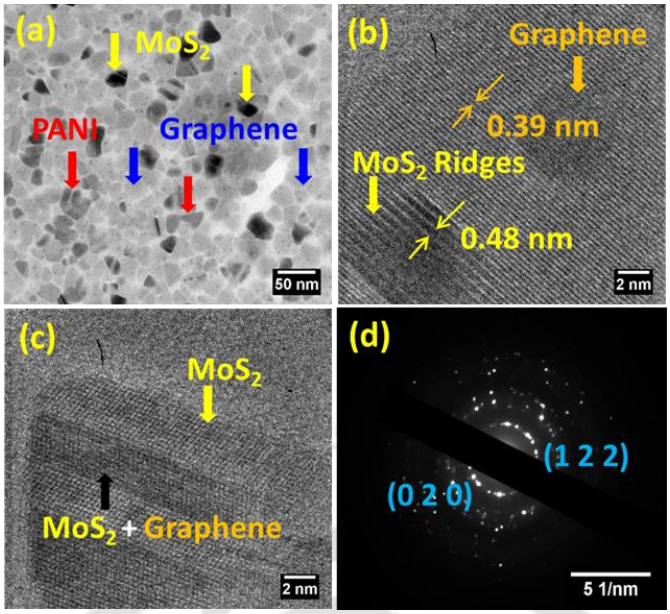

Figure 2.9. (a) TEM image of the PANI-G-MoS_2 nanocomposite, (b) HRTEM image of graphene and MoS_2 lattice regions, (c) HRTEM image of MoS_2 and mixed region of graphene with MoS_2 ridges, (d) SAED pattern of PANI-G-MoS_2.

To understand the detailed microstructure and the growth pattern of PANI nanorods, the morphological studies have been carried out with the help of TEM images for all the prepared nanocomposites. As shown in Figure 2.9a (for PANI-G-MoS_2), a darker region of the image reveals the presence of a few layers of MoS_2; whereas, a relatively opaque region confirms a stable graphene layer. The semi-transparent surface regions indicate the presence of PANI chains that have grown over the graphene and MoS_2 nano flakes. In particular, the average size of the PANI-G-MoS_2 nanocomposite was estimated to be 15±4.38 nm with 29.23% polydispersity. Additionally, the high resolution TEM (viz., HRTEM) images exhibit two different types of lattice spacing of graphene and MoS_2 nanosheets (Figure 2.9b). The interplanar spacing of 0.48 nm and 0.39 nm corresponds to the (1 2 2) and (0 2 0) planes, respectively. The MoS_2 and graphene are uniformly cross-linked on the surface of PANI nanorods, as shown in Figure 2.9c. A typical selected area electron diffraction (SAED) pattern in Figure 2.9d justifies a polycrystalline character of the resultant nanocomposite material. An individual layer of planes in a single grain level clearly reveals a layered structure of S-Mo-S atoms. As a result, the interlayered structure of graphene and MoS_2 appears to be a collection of evenly spaced strip of ridges [37,41].

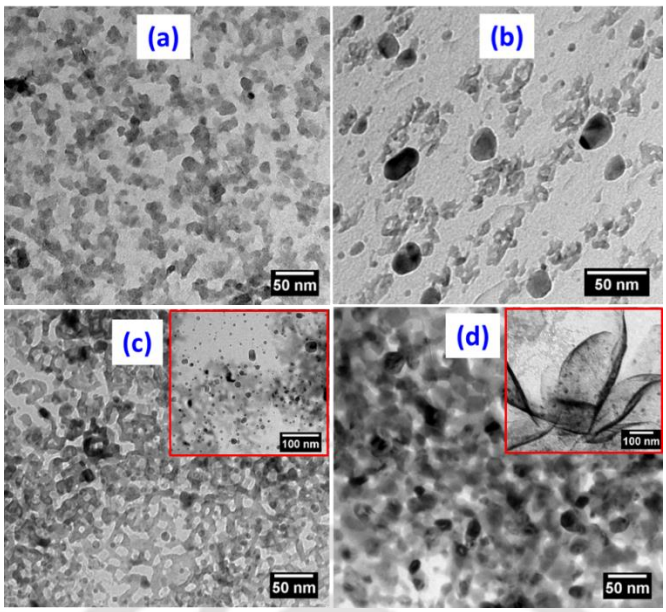

Figure 2.10. TEM analysis of the (a) pure PANI, (b) PANI-G 0.4%, (c) PANI-G 1% and (d) PANI-G 2%, nanocomposites.

The TEM images of PANI, PANI-G 0.4%, PANI-G 1% and PANI-G 2% samples have been presented in Figure 2.10. The nanocomposite, PANI-G 2%, exhibits a relatively higher average size (27±4.23 nm with 15.4% polydispersity) of the PANI nanorods as compared to the other compositions, which is attributed to the restacking of graphene, and swelling of PANI nanorods. The average size of the nanorods for pure PANI, PANI-G 0.4%, PANI-G 1% and PANI-G-MoS_2 were estimated as 21±8.28 nm, 15±5.31 nm, 17.5±0.61 and 15±4.38 with polydispersity as 39.4%, 35.4%, 3.4% and 29.23%, respectively.

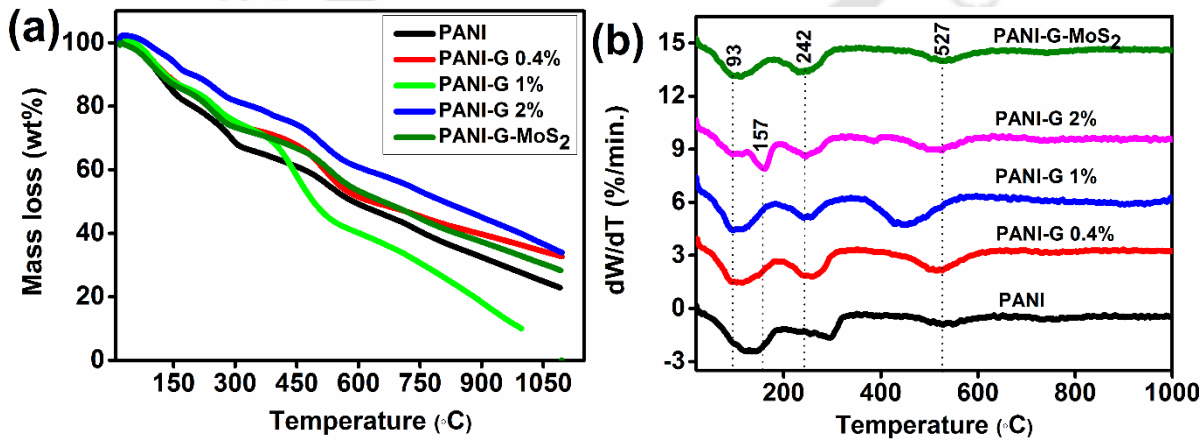

Figure 2.11. (a) Thermogravimetric analysis, and (b) time dependent differential thermogravimetric analysis.

To get a comprehensive idea of the thermal stability of the nanocomposites, we have carried out the thermogravimetric (TGA) analysis of all the prepared composites, as shown in Figure 2.11a. The first loss of mass at around 70-150 °C signifies the dehydration of water contents from the nanocomposites. Secondly, between 150 to 300 °C each curve shows a mass loss in a small amount as the decomposition of PANI takes place. The maximum weight residue of pure PANI was 60.55% at a temperature of 460 °C. In comparison, the maximum mass residue of PANI-G-MoS_2, PANI-G 2%, PANI-G 1% and PANI-G 0.4% were 66.06%, 73.47%, 70.20% and 67.17%, respectively at 460 °C, exhibit an excellent thermal stability of the nanocomposites. In summary, the addition of graphene and MoS_2 increases the thermal stability up to a large extent with respect to the pure PANI [38]. For the exact degradation behaviour with time, we have carried out a differential thermogravimetric analysis (DTG), presented in Figure 2.11b. The DTG measurement of the prepared nanocomposite materials at their temperature window, shows the time-dependent decomposition of nanocomposite materials. The first transition takes place in temperature range of 70-150 °C, which is related to the loss of water in the PANI, PANI-G 0.4%, PANI-G 1% and PANI-G-MoS_2 graphs with 5% weight loss at the maximum transition temperature of 93°C. Whereas, PANI-G 2% sample graph has shown a 7% weight loss at the maximum temperature of 157 °C. In the second transition, the temperature range is 180-300 °C and a maximum decomposition of mass was at the temperature of 242 ˚C. At this step 20% mass losses being occurred that can be ascribed to degradation of low molecular weight PANI. The third transition is in the temperature range of 450-1000 °C, at the 527 ˚C a maximum decomposition of mass have been recorded , that can be related to the decomposition of PANI with 63% weight loss [48,49].

2.3.2. Electrochemical analysis

The electrochemical measurements of PANI, PANI-G 0.4%, PANI-G 1%, PANI-G 2% and PANI-G-MoS_2 nanocomposites have been performed using 1M H_2SO_4 electrolyte solution, based on three electrode method. The cyclic voltammetry (CV) curves measured at a scan rate of 50 mV s^{-1} with a potential window of -0.4 to 1.0 V, of all the samples, presented in the Figure 2.12a. The rectangular shape of the CV curves confirms the suitability of the prepared nanocomposites as electrode materials for supercapacitors [50]. In particular, PANI-G-MoS_2 exhibits the highest current density as shown by the large size of the cyclic loop, which represents an enhanced maximum specific capacitance (C_s), arises from the synergistic effect between PANI, graphene

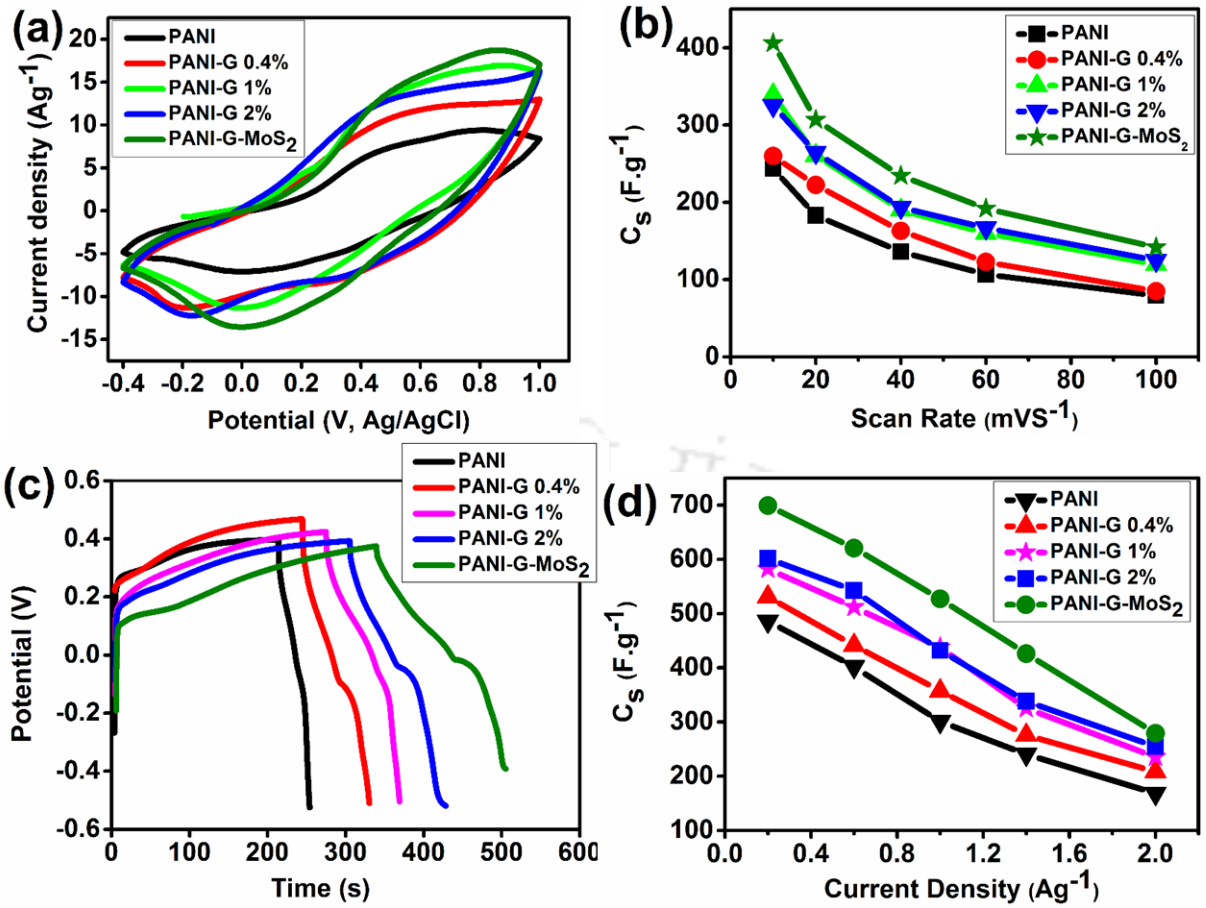

Figure 2.12. Three electrode measurements of all the samples. (a) The Cyclic voltammograms (CV) at a scan rate of 50 mV s^{-1}, (b) specific capacitance (C_s) as a function of scan rate, (c) galvanostatic charge/discharge (GCD) plots at a current density of 1.4 A g^{-1}, and (d) specific capacitance at various current densities from 0.2 to 2.0 A g^{-1}.

and MoS_2 layers. In the ternary composite, MoS_2 nanoflakes and graphene nanosheets (negative electrodes) embedded into PANI nanorods (positive electrode), exhibiting high specific capacitance, in comparison with the PANI-G binary nanocomposites. It is to be noted that MoS_2 nanosheets is structurally analogous to graphene, and hence, it facilitates the formation of an intercalated layered structure of the resultant nanocomposites. However, in all the CV results, an 'S' shape (deviation from the usual rectangular shape) curve clearly demonstrates the presence of the Faradaic charge storage phenomenon[41]. The charge storage capacity have been calculated from the variation of specific capacitance with scan rate (Figure 2.12b). We observed that the specific capacitance decreases as the scan rate increases. The decreasing value of specific capacitance is ascribed to the internal effect of material resistance as the scan rate is increased. It is also to be noted that as the scan rate increases the electrolyte ions migrate into the electrode up to the saturation level of ion diffusion, making the ion diffusion more facile due to the porous structure of the nanocomposites (see Figure

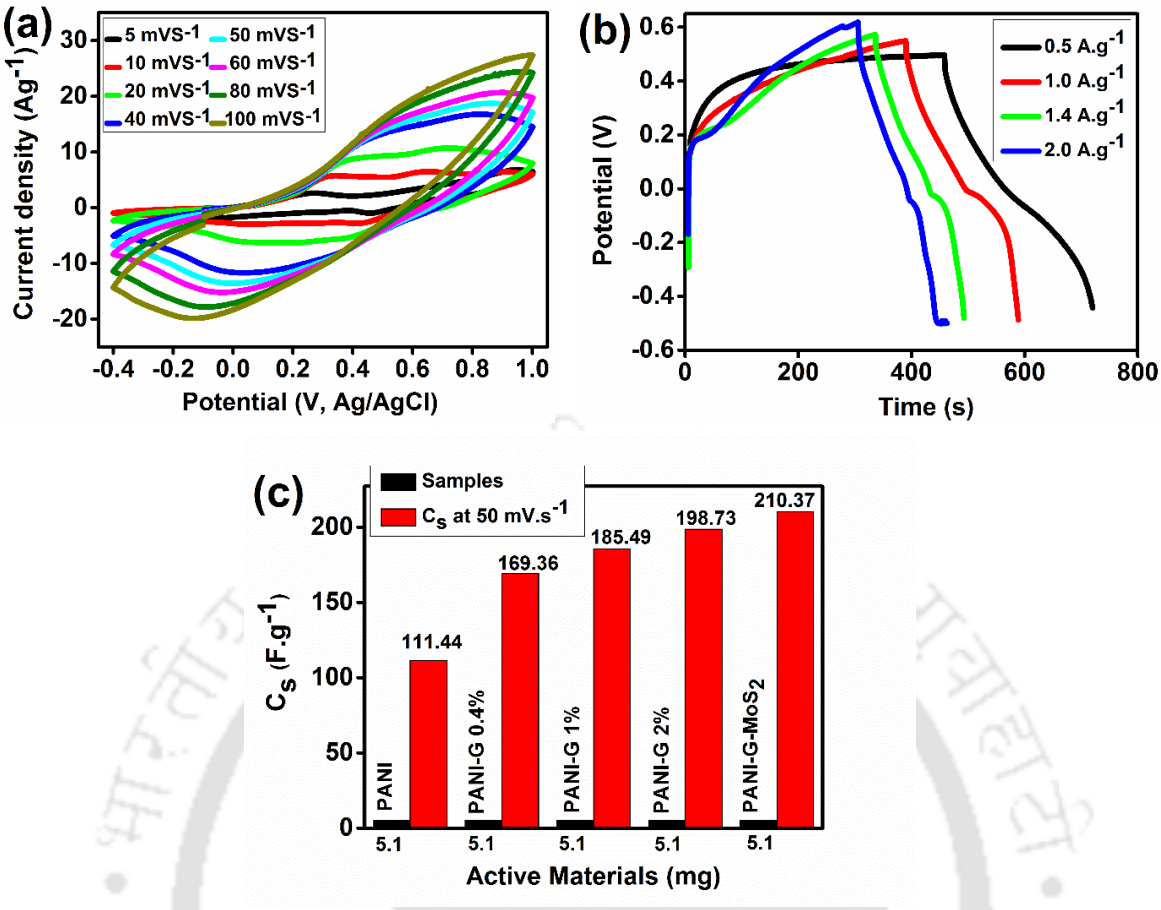

Figure 2.13. (a) CV profile of PANI-G-MoS_2 at various scan rates, (b) GCD measurements at various current densities of PANI-G-MoS_2 (c) C_s at 50 mV S^{-1} for all the samples.

2.7). Consequently, the probability of ion diffusion will be the maximum at a lower scan rate as they have enough time to execute the electrochemical reaction with the generation of higher electrostatic charge. Therefore, the specific capacitance obtained at the lower scan rate would be considered for the application as an electrode material [49,50]. The highest specific capacitance shown by PANI, PANI-G 0.4%, PANI-G 1%, PANI-G 2% and PANI-G-MoS_2 composite are 244, 260, 339, 325 and 406 Fg^{-1}, respectively at a scan rate of 10 mV S^{-1}.

The GCD curves (Figure 2.12c) representing the galvanostatic charging/discharging behavior of PANI, PANI-G 0.4%, PANI-G 1%, PANI-G 2% and PANI-G-MoS_2 based fabricated electrodes with a voltage window of -0.5 to 0.5 V, at current density of 1.4 Ag^{-1}. The non-linearity in the time trajectory of the potential is attributed to the Faradic redox reaction [51]. The onset of charging at above 0.1 V is due to the oxidation of PANI based composites in the electrolyte solution. However, a small voltage drop indicates a good interfacial contact between the active working electrode and the substrate (SS mesh) during GCD measurements. It has been observed that the widths of the GCD curves were expanded at lower current density, while

in contrast, the curves were shrinking at higher current densities. Therefore, the specific capacitance follows an inverse relationship with the current density (Figure 2.12d). The inverse relationship between current density and specific capacitance is due to the redox reaction that takes place at the interface between electrode and electrolyte [51,52]. In addition, at the lower current density, the electrolyte ions get enough time (cf., residence time) to react with the active electrode materials, and hence, the specific capacitance increases. Among all the nanocomposites, the ternary composite of PANI-G-MoS_2 exhibits highest specific capacitance, 699 Fg^{-1} at the current density of 0.2 Ag^{-1}. The magnitudes of the specific capacitance of PANI, PANI-G 0.4%, PANI-G 1% and PANI-G 2% are 485, 530, 582 and 602 Fg^{-1}, respectively.

Following this, the cyclic voltammograms were performed on PANI-G-MoS_2 at varied scan rates (Figure 2.13a,). It has been noticed that shapes of all the CV curves are rectangular, indicating an excellent characteristic of the electrode materials. The increase in current density with increasing the scan rate shows the electrochemical stability of the electrode materials as a pseudocapacitor. At varied scanning rate, increase in current density with the scan rate reveals the large anodic current due to sufficient +ve charge carriers. During the CV study, recombination of +ve and –ve charge carriers of PANI and PANI-G nanocomposites show a relatively lower reduction, compared to PANI-G-MoS_2, which is attributed to the presence of MoS_2 layer, which balances the charge carriers with enhanced current. As a result, almost equal numbers of positive and negative charge carriers are present during charge recombination, giving an enhanced specific capacitance. The galvanostatic charge/discharge (GCD) measurements (Figure 2.13b) clearly demonstrates the applicability of the ternary composite as supercapacitor material. The specific capacitance of all the composites have been calculated at a scan rate of 50 mV S^{-1} (Figure 2.13c). Further, a comprehensive study of specific capacitance (C_s) under a scanning rate of 50 mV S^{-1} of the prepared nanocomposites. The specific capacitance of PANI-G-MoS_2, PANI-G 2%, PANI-G 1%, PANI-G 0.4% and PANI samples were 201.37, 198.73, 185.49, 169.36 and 111.44 F g^{-1}, respectively at the scan rate of 50 mV S^{-1}.

Further, for the practical application of the ternary nanocomposite (viz., PANI-G-MoS_2), a symmetrical working electrode have been fabricated to investigate the two electrode based electrochemical measurements, in an aqueous solution of 1 M H_2SO_4[53]. Figure 2.14a, shows the CV performance of the PANI-G-MoS_2 based symmetric electrodes at varying scan rates ranging from 10 to 100 mV s^{-1} at the potential range of 0 to 0.8 V. The rectangular shape of CV graphs indicates the absence of redox phenomenon, and is attributed to the pseudocapacitance behavior [54]. The symmetric configuration of the CV graphs over the entire

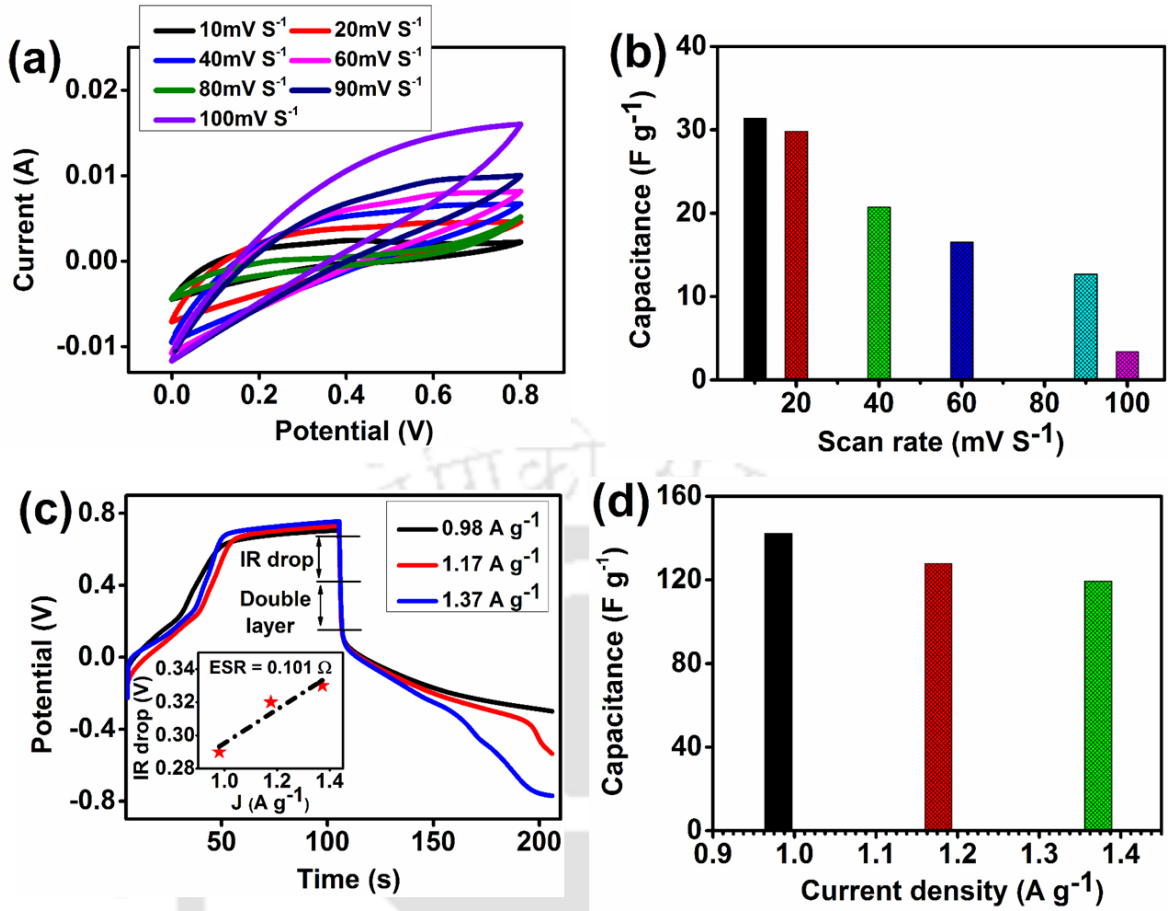

Figure 2.14. Two electrode measurements of PANI-G-MoS_2. (a) The CV profile at various scan rates, (b) C_s as a function of scan rate, (c) galvanostatic charge/discharge (GCD) behaviour at various current densities, the inset shows an (ESR) equivalent series resistance and (d) C_s at various current densities from 0.98 to 1.37 A g^{-1}.

scan rates, suggests a high reversibility of the fabricated electrodes. The specific capacitance shows a decreasing trend with the scan rate (Figure 2.14b). The maximum specific capacitance obtained by the PANI-G-MoS_2 symmetric electrodes appears to be 31.35 F g^{-1} at a scan rate of 10 mV s^{-1}. Figure 2.14c shows the GCD profile of the PANI-G-MoS_2 symmetric electrodes at various current densities, from 0.98 to 1.37 A g^{-1}, in the same potential range of 0 to 0.8 V. The observed GCD graphs correspond to a nonlinear behavior of capacitance. During the discharging cycle, in the initial portion, the appearance of an ohmic or IR drops and double layer effects is attributed to the contribution from double layer capacitance. The gradual decrease of potential in the later portion is attributed to the contribution form the Faradaic pseudocapacitance. In CV profile, the absence of redox peaks is also an indication of the pseudocapacitance behavior. The equivalent series resistance (ESR) at 0.101 Ω (inset of Figure 2.14c), shows a linear relationship between current density and IR drops. It has been observed that the ohmic drops slightly increases with increasing current density, suggesting that the

device would offer an enhanced supercapacitance behavior at low current density. The recorded highest capacitance was 142.3 F g^{-1}, at a current density of 0.98 A g^{-1}, as shown in Figure 2.14d. The observed specific capacitance based on GCD measurements of PANI-G-MoS_2 symmetric electrodes is significantly higher than the previously reported results on $ZnCo_2O_4$ nanorods deposited over Ni wire via hydrothermal process (10.9 F g^{-1}) [55], MoS_2 based (3.40 F g^{-1}) and WS_2 based electrode (3.50 F g^{-1}) [56], and Ti_2CT_xMXene based electrodes (51 F g^{-1}) [57]. We have conducted the electrochemical impedance spectroscopy (EIS) measurements based on three electrode system for all the nanocomposites to investigate the charge transfer mechanism in the interfacial region of working electrode and electrolyte. The Nyquist plot of the PANI and its nanocomposites have been recorded in the frequency range of 1 Hz to 1 MHz, with an open circuit potential, as shown in Figure 2.15a. All the spectra show a semicircle followed by a linear regime in the frequency range.

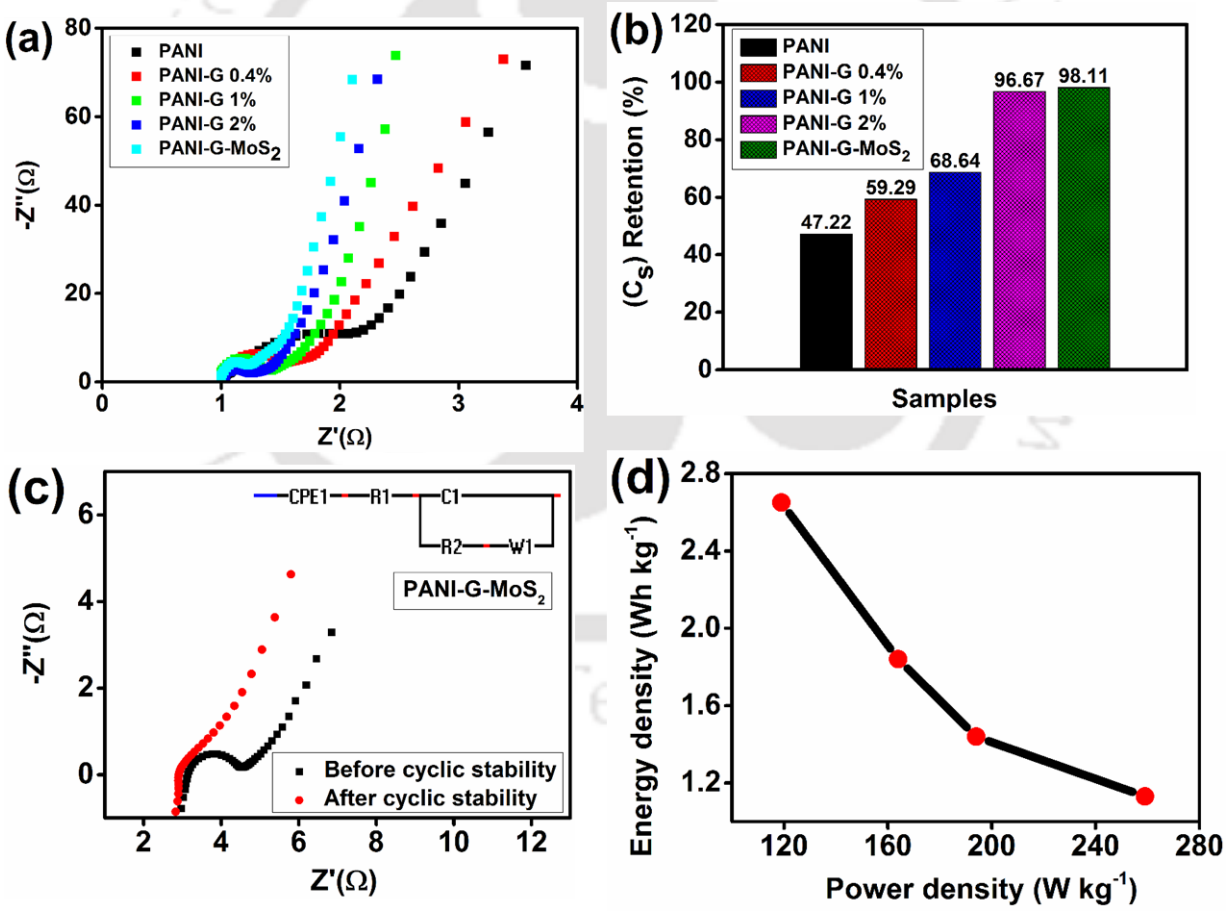

Figure 2.15. (a) Nyquist plots, (b) cyclic stability, of PANI, PANI-G 0.4%, PANI-G 1%, PANI-G 2% and PANI-G-MoS_2 samples. (c) Nyquist plot before and after the cyclic stability, and (d) ragone plot based on two electrode measurement of the ternary nanocomposite of PANI-G-MoS_2.

The related interfacial charge transfer resistance (R_{ct}) corresponds to the diameter of the semicircle in the high frequency region. The phase constant element (Q) with an equivalent series resistance (ESR, R_s) is helpful to provide a linear fit to the Nyquist plot. The values of R_s have been estimated at high frequency via an intersection on the real axis. Typically, the impedance is a combined resistance of electrode and electrolyte. The rate of charge transfer inversely varies with the charge transfer resistance. With an increased wt% of graphene in PANI, diameter of semicircles is reduced. As a result, the R_{ct} (1.01 Ω) of PANI-G-MoS_2 appears to be smaller than the R_{ct} (1.3 Ω) of PANI, indicating a rapid rate of charge transfer. The binary nanocomposites (viz., PANI-G 0.4%, PANI-G 1% and PANI-G 2%) show a slope close to 45° revealing that the nanocomposite materials are quite responsive for the protonation that yields readily charge polarization. The spectral slope of the EIS curve in the lower frequency range represents the Warburg impedance (W), indicating a diffusive ion transfer, and the dominance of capacitance behavior.

We estimate the electrochemical stability of the electrode materials in terms of the percentage of capacitance retention based on CV scanning at a scan rate of 100 mV S^{-1} for 500 cycles, as shown in Figure 2.15b. The specific capacitance retention (%) for all the samples, calculated from the 500^{th} cycle to the first cycle. The ternary nanocomposite of PANI-G-MoS_2 exhibits a capacitance retention of 98.11% of its initial capacitance, revealing that it is suitable material for supercapacitor with significant electrochemical stability. The PANI-G 2% also shows a good cyclic stability with 96.67% retention. However, PANI-G 1%, PANI-G 0.4% and PANI show a relatively less capacitance retention (68.64%, 59.29% and 42.22%, respectively). Figure 2.15c represents the EIS plots before and after the cyclic stability, based on symmetric two electrode measurements. We observe that the Warburg line of after cyclic stability has been slightly shifted towards lower Z' and higher Z'', from that of before cyclic stability, indicating that the prepared nanocomposite material has an excellent supercapacitive property. The performance of the electrode material after cyclic stability appears to be better than that of before the cyclic stability. Therefore, the PANI-G-MoS_2 symmetric electrode device would possess a long life cycle with an excellent supercapacitive behavior. The Ragone plot for symmetric two electrode measurements (Figure 2.15d) shows a decreasing trend of energy density with increasing power density, with a highest energy density of 2.650 Wh kg^{-1} at a power density of 119.212 W kg^{-1}.

2.4. Conclusions

The property enhancement in polymer nanocomposite strongly depends on the distribution of nanofillers within the polymer matrix. An evenly dispersed polymer nanocomposite would definitely yield a superior property over the one with uneven distribution. In this paper, we report the successful preparation of binary (PANI-G with varying weight% of graphene) and ternary nanocomposite (PANI-G-MoS_2) via solvent exfoliation followed by *in-situ* oxidative polymerization method. This method of preparation ensures the formation of a homogeneous dispersion of PANI nanorods over graphene and MoS_2 nanoflakes, as reveled by the structural analysis. The morphological and structural analysis of the nanocomposites confirms that the higher crystalline materials are excellent candidates for the facile movement of electrons, resulting higher conductivity. In the ternary nanocomposite (PANI-G-MoS_2), PANI nanorods are inter-crosslinked, and intercalated within nanoflakes of negative electrode materials (Graphene and MoS_2), maintaining an equilibrium between charge carriers during the redox reaction. As a result, the ternary nanocomposite exhibits an excellent electrochemical activity and enhanced cyclic stability with improved performance as a supercapacitor compared to the pure PANI and PANI-G binary composites.

References

[1] A. Burke, *J. Power Sources* **2000**, *91*, 37.

[2] K. Krishnamoorthy, G. K. Veerasubramani, P. Pazhamalai, S. J. Kim, *Electrochimica Acta* **2016**, *190*, 305.

[3] S. Sahoo, P. Pazhamalai, K. Krishnamoorthy, S.-J. Kim, *Electrochimica Acta* **2018**, *268*, 403.

[4] Z. Deng, Y. Hu, D. Ren, S. Lin, H. Jiang, C. Li, *Chem. Commun.* **2015**, *51*, 13838.

[5] S. L. Candelaria, Y. Shao, W. Zhou, X. Li, J. Xiao, J.-G. Zhang, Y. Wang, J. Liu, J. Li, G. Cao, *Nano Energy* **2012**, *1*, 195.

[6] S. Chen, J. Zhu, X. Wu, Q. Han, X. Wang, *ACS Nano* **2010**, *4*, 2822.

[7] S. S. Shinde, G. S. Gund, V. S. Kumbhar, B. H. Patil, C. D. Lokhande, *Eur. Polym. J.* **2013**, *49*, 3734.

[8] K. Xie, J. Li, Y. Lai, Z. Zhang, Y. Liu, G. Zhang, H. Huang, *Nanoscale* **2011**, *3*, 2202.

[9] Z. Luo, Y. Zhu, E. Liu, T. Hu, Z. Li, T. Liu, L. Song, *Mater. Res. Bull.* **2014**, *60*, 105.

[10] G. Xu, D. Xu, J. Zhang, K. Wang, Z. Chen, J. Chen, Q. Xu, *J. Colloid Interface Sci.* **2013**, *411*, 204.

[11] J. R. Potts, D. R. Dreyer, C. W. Bielawski, R. S. Ruoff, *Polymer* **2011**, *52*, 5.

[12] K. S. Novoselov, A. K. Geim, S. V. Morozov, D. Jiang, Y. Zhang, S. V. Dubonos, I. V. Grigorieva, A. A. Firsov, *Science* **2004**, *306*, 666.

[13] Q. Wu, Y. Xu, Z. Yao, A. Liu, G. Shi, *ACS Nano* **2010**, *4*, 1963.

[14] J. Wu, G. Huang, H. Li, S. Wu, Y. Liu, J. Zheng, *Polymer* **2013**, *54*, 1930.

[15] Y. Xu, H. Bai, G. Lu, C. Li, G. Shi, *J. Am. Chem. Soc.* **2008**, *130*, 5856.

[16] S. Stankovich, D. A. Dikin, G. H. B. Dommett, K. M. Kohlhaas, E. J. Zimney, E. A. Stach, R. D. Piner, S. T. Nguyen, R. S. Ruoff, *Nature* **2006**, *442*, 282.

[17] Y. F. Huang, C. W. Lin, *Polymer* **2012**, *53*, 2574.

[18] C. N. R. Rao, A. K. Sood, K. S. Subrahmanyam, A. Govindaraj, *Angew. Chem. Int. Ed.* **2009**, *48*, 7752.

[19] M. Fang, K. Wang, H. Lu, Y. Yang, S. Nutt, *J. Mater. Chem.* **2009**, *19*, 7098.

[20] J. Huang, S. Virji, B. H. Weiller, R. B. Kaner, *J. Am. Chem. Soc.* **2003**, *125*, 314.

[21] J. Huang, R. B. Kaner, *Angew. Chem. Int. Ed Engl.* **2004**, *43*, 5817.

[22] M. Chhowalla, H. S. Shin, G. Eda, L.-J. Li, K. P. Loh, H. Zhang, *Nat. Chem.* **2013**, *5*, 263.

[23] M. R. Lukatskaya, O. Mashtalir, C. E. Ren, Y. Dall'Agnese, P. Rozier, P. L. Taberna, M. Naguib, P. Simon, M. W. Barsoum, Y. Gogotsi, *Science* **2013**, *341*, 1502.

[24] C. Hao, F. Wen, J. Xiang, L. Wang, H. Hou, Z. Su, W. Hu, Z. Liu, *Adv. Funct. Mater.* **2014**, *24*, 6700.

[25] C. Yang, Z. Chen, I. Shakir, Y. Xu, H. Lu, *Nano Res.* **2016**, *9*, 951.

[26] H. Tang, J. Wang, H. Yin, H. Zhao, D. Wang, Z. Tang, *Adv. Mater.* **2015**, *27*, 1117.

[27] K.-J. Huang, L. Wang, Y.-J. Liu, H.-B. Wang, Y.-M. Liu, L.-L. Wang, *Electrochimica Acta* **2013**, *109*, 587.

[28] X. Li, C. Zhang, S. Xin, Z. Yang, Y. Li, D. Zhang, P. Yao, *ACS Appl. Mater. Interfaces* **2016**, *8*, 21373.

[29] P. Pazhamalai, K. Krishnamoorthy, V. K. Mariappan, S. Sahoo, S. Manoharan, S.-J. Kim, *Adv. Mater. Interfaces* **2018**.

[30] L. Ren, G. Zhang, Z. Yan, L. Kang, H. Xu, F. Shi, Z. Lei, Z.-H. Liu, *ACS Appl. Mater. Interfaces* **2015**, *7*, 28294.

[31] H. Wang, H. Jiang, Y. Hu, N. Li, X. Zhao, C. Li, *J. Mater. Chem. A* **2017**, *5*, 5383.

[32] U. Khan, A. O'Neill, H. Porwal, P. May, K. Nawaz, J. N. Coleman, *Carbon* **2012**, *50*, 470.

[33] A. Jawaid, D. Nepal, K. Park, M. Jespersen, A. Qualley, P. Mirau, L. F. Drummy, R. A. Vaia, *Chem. Mater.* **2016**, *28*, 337.

[34] J. Stejskal, R. G. Gilbert, *Pure Appl. Chem.* **2002**, *74*.

[35] Y. Jin, H. Chen, M. Chen, N. Liu, Q. Li, *ACS Appl. Mater. Interfaces* **2013**, *5*, 3408.

[36] R. R. Salunkhe, J. Lin, V. Malgras, S. X. Dou, J. H. Kim, Y. Yamauchi, *Nano Energy* **2015**, *11*, 211.

[37] L. Al-Mashat, K. Shin, K. Kalantar-zadeh, J. D. Plessis, S. H. Han, R. W. Kojima, R. B. Kaner, D. Li, X. Gou, S. J. Ippolito, W. Wlodarski, *J. Phys. Chem. C* **2010**, *114*, 16168.

[38] X. Liu, Y. Zheng, X. Wang, *Chem. – Eur. J.* **2015**, *21*, 10408.

[39] C. Lee, H. Yan, L. E. Brus, T. F. Heinz, J. Hone, S. Ryu, *ACS Nano* **2010**, *4*, 2695.

[40] L. Qiu, H. Zhang, W. Wang, Y. Chen, R. Wang, *Appl. Surf. Sci.* **2014**, *319*, 339.

[41] J. Wang, Z. Wu, K. Hu, X. Chen, H. Yin, *J. Alloys Compd.* **2015**, *619*, 38.

[42] H. Baniasadi, A. Ramazani S.A., S. Mashayekhan, F. Ghaderinezhad, *Synth. Met.* **2014**, *196*, 199.

[43] D. Saini, T. Basu, *Appl. Nanosci.* **2012**, *2*, 467.

[44] Q. Zhang, K. Zhang, D. Xu, G. Yang, H. Huang, F. Nie, C. Liu, S. Yang, *Prog. Mater. Sci.* **2014**, *60*, 208.

[45] J. Stejskal, P. Kratochvíl, N. Radhakrishnan, *Synth. Met.* **1993**, *61*, 225.

[46] S. Ahmad, S. Mukherjee, *Graphene* **2014**, *03*, 52.

[47] M. S. Nam, U. Patil, B. Park, H. B. Sim, S. C. Jun, *RSC Adv.* **2016**, *6*, 101592.

[48] K. Khezri, *RSC Adv.* **2016**, *6*, 109286.

[49] F. A. Rafiqi, K. Majid, *RSC Adv.* **2016**, *6*, 22016.

[50] Z. Yin, H. Zhou, C. Fu, N. Zhang, D. Liu, Y. Kuang, *RSC Adv.* **2016**, *6*, 41142.

[51] B. Vidhyadharan, I. I. Misnon, R. A. Aziz, K. P. Padmasree, M. M. Yusoff, R. Jose, *J. Mater. Chem. A* **2014**, *2*, 6578.

[52] S. M. Pawar, A. I. Inamdar, K. V. Gurav, Y. Jo, H. Kim, J. H. Kim, H. Im, *Mater. Lett.* **2015**, *141*, 336.

[53] K. Krishnamoorthy, P. Pazhamalai, S. J. Kim, *Electrochimica Acta* **2017**, *227*, 85.

[54] G. A. Muller, J. B. Cook, H.-S. Kim, S. H. Tolbert, B. Dunn, *Nano Lett.* **2015**, *15*, 1911.

[55] H. Wu, Z. Lou, H. Yang, G. Shen, *Nanoscale* **2015**, *7*, 1921.

[56] M. A. Bissett, S. D. Worrall, I. A. Kinloch, R. A. W. Dryfe, *Electrochimica Acta* **2016**, *201*, 30.

[57] R. B. Rakhi, B. Ahmed, M. N. Hedhili, D. H. Anjum, H. N. Alshareef, *Chem. Mater.* **2015**, *27*, 5314.

Chapter-3

Graphene Based PANI/MnO_2 Nanocomposites with Enhanced Dielectric Properties for High Energy Density Materials

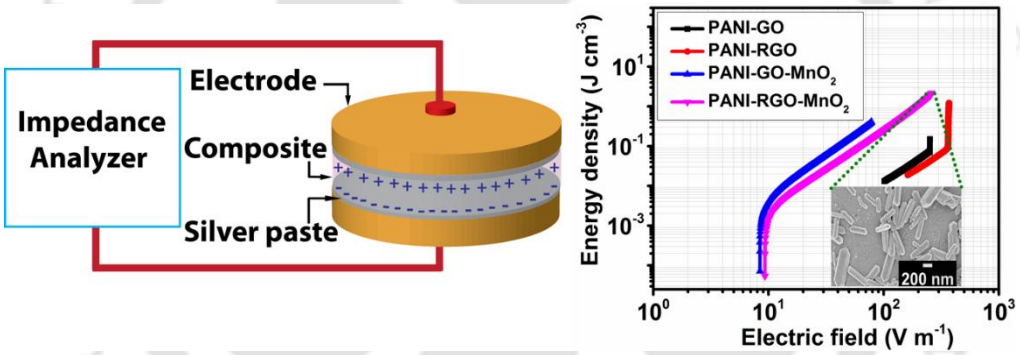

S. Palsaniya, H.B. Nemade, A.K. Dasmahapatra, Graphene based PANI/MnO_2 nanocomposites with enhanced dielectric properties for high energy density materials, *Carbon*. 150 (2019) 179–190.

3.1 Introduction

Electrostatic energy storage devices, e.g. capacitors, are being utilized extensively in the electronic appliances, such as, electric motor vehicle, high power electronics, handheld laser devices, portable electronics and high frequency devices, such as radars [1–4]. However, these conventional capacitors are typically based on low energy density materials that require more area for a given energy requirement, and results a steep escalation in manufacturing cost. The discharge energy density in a capacitor can be estimated for linear dielectric nanocomposite materials using the following relation [5,6]:

$$U_e = \frac{1}{2}\varepsilon_0 \varepsilon_r E_b^2 \quad (3.1)$$

where, ε_r is the relative permittivity of the nanocomposite, ε_0 is the permittivity of vacuum, and E_b is the breakdown electric field. The storage energy density of a capacitor can be determined by the measured value of E_b and ε_r of the nanocomposites [7–9]. It is reported that, the recasting of the surface texture of microstructures can be achieved by incorporating organic fillers [10,11]. These nanocomposites exhibit high storage permittivity [12–15] along with a high breakdown strength, in comparison with the ceramic materials, which are known to have a high permittivity [12,16–18]. The enhancement of the dielectric property strongly depends on the type of nanoparticles. The nanoparticles of materials with intrinsically high dielectric property generally enhance the dielectric property of the resultant composites. However, in some cases, due to the presence of non-uniform electric field, the storage permittivity decreases [19–21]. These properties are apparently dependent on the solid phase of the nanocomposites instead of electrochemical activities, because the orientation of polar solvent under an electric field turns into dipole saturation, which decreases the dielectric permittivity [22].

Typically, inorganic and organic nanofillers are equally used to enhance the dielectric properties of the nanocomposites. Among the inorganic nanofillers, mostly the metal oxides, $CoFe_2O_4$ [23] and MnO_2 [24,25], and sulphides such as, MoS_2 [26] have been used extensively. It is evident that use of MnO_2 is largely due to its high specific capacitance (two dimensional MnO_2), fast charge-discharge potential, and environmental stability [27–29]. MnO_2 can easily be tailored to adopt various shapes with high surface area such as, nanoflakes [30], nanoparticles [31], unidirectional nanorods [32], nanofibers[33], and outspread nanostructures [34]. Therefore, nanocomposites with MnO_2 have been realized to be a significant improvement in the energy storage applications. Moreover, MnO_2 shows a strong oxidizing behaviour, as reported by Han et al.[35], for the supercapacitor application using graphene oxide (GO)/polyaniline (PANI)/MnO_2 ternary nanocomposites.

Similar to MnO_2, organic nanofillers, such as, graphene and its derivatives equally facilitate achieving an excellent charge conduction, superior mechanical resilience, and high chemical and thermal stability [35]. Compared to pure graphene, GO has been regarded as a better dispersion candidate in liquid solutions by virtue of its enhanced functionality, which results a remarkably high dielectric stability. Similarly, reduced graphene oxide (RGO) also has been exploited as a key nanofiller to provide smooth charge transport, which is associated to high strength of electric breakdown in the dielectric medium [36]. To produce a high power device, often both the inorganic and organic nano-fillers are combined as electrode materials that yield high energy density with a long lifespan. Yan et al. [37] reported a binary nanocomposite of MnO_2 and graphene, showed a high electrical conductivity and energy storage. Jafta et al. [38] have investigated a supercapacitor with high energy storage using GO/α–MnO_2 composite. In this case, GO shows a significantly higher electro-catalytic activity than pristine graphene, which is attributed to the additional electronic charge interaction by the oxygen content. Further, Li et al. [25] has been shown an improved energy storage using a paper-embedded flexible RGO/MnO_2/PANI (ternary nanocomposite) electrode materials.

In addition to the quality of nanoparticles, the nature of the polymer also plays a crucial role in achieving the desired dielectric property of the nanocomposites. PANI [39] and Polyvinylidene fluoride (PVDF) [2], poly (pentafluorophenyl acrylate) (PPFPA) [40], polyurethane [41], vinyl acetate and maleic anhydride (VAMA) copolymers, composite with lead zirconate titanate (PZT) [42] are extensively used in preparing such nanocomposites. In particular, PANI based nanocomposites being widely used due to its excellent electrical conductivity, large dielectric constant and environmental stability along with an ability to exhibit the reverse redox phenomenon [40]. Therefore, PANI-based nanocomposites find suitable applications in the area of electrostatic charge storage [39]. For example, Khan et al. have shown that the presence of $CoFe_2O_4$ in PANI/$CoFe_2O_4$ nanocomposites has improved optical, electrical and dielectric properties along with a higher photocatalytic activity [23] compared to pure PANI. Mombru et al. have reported that GO can be blended between PANI fibre in PANI/GO nanocomposite with an enhanced charge transport ability under a low electric field [43]. Mariano et al. have also reported an enhancement of five orders of magnitude of electrical conductivity in PANI/CNT (carbon nanotubes) nanocomposite on addition of only 4 wt% of CNT [44]. Higher amount of CNT has enabled the nanocomposite in crossing the barrier height of an insulating region of PANI with a percolation threshold of the conductivity at ~ 1%. The nanocomposite made up of carbon fibres coated with PANI exhibited significantly higher magnetoresistance and dielectric properties [45].

The degree of enhancement in various properties of the nanocomposites strongly depends on the interaction of PANI with the nanofillers. Sometimes, surface functionalization of either the polymer or the nanofillers is done to form a well-mixed composite. For example, PVDF was surface functionalized by polydopamine for PVDF/$BaTiO_3$ nanocomposite [46]; whereas, silane coupling agent was used to functionalize $BaTiO_3$ in epoxy/$BaTiO_3$ composite [47]. The presence of more than one type of nanofillers have been shown to be more effective in achieving the desired property. Typically, in a ternary nanocomposite, one component, viz. nanofillers, acts as a functionalization group, and facilitates the mixing to get a well-mixed composite. Luo et al. have shown a mixed effect of the ternary nanocomposite of PANI with RGO and ferrite materials, $Ba_{0.9}La_{0.1}Fe_{11.9}Ni_{0.1}O_{19}$, (BF), for the microwave absorption applications [48]. In this nanocomposite, BF nanoparticles are essentially functionalized with RGO, which in turn facilitates the formation of the nanocomposites.

In this work, we report the preparation of ternary nanocomposite of PANI with two nanofillers – inorganic (MnO_2) and organic (functionalized graphene, RGO), via in-situ polymerization of PANI. We have also studied other ternary composite, PANI-GO-MnO_2 and binary nanocomposites, PANI-GO and PANI-RGO. The in-situ polymerization method ensures the formation of a well-mixed composite with the formation of hexagonal-shaped nanorods of MnO_2. The presence of RGO can be realized as a mediator to enhance the charge transport properties. Hence, PANI-RGO-MnO_2 exhibits highest electrical conductivity, notable permittivity, and high breakdown strength of electric field, and would substantially influence to the energy storage applications.

3.2 Materials and methods

3.2.1 Materials

Graphite (99.99%, 200 mesh) was obtained from Alfa Aesar. Sodium nitrate (assay > 99%), Potassium permanganate (assay > 98.5%), 50 % Hydrogen peroxide, Hydrazine hydrate (assay 99%), Ammonium persulfate (assay > 99%), Methanol (assay > 99%), Aniline (assay > 99%) were obtained from Merck Co. Barium chloride (assay > 99%) was purchased from Sigma Aldrich. Sulphuric acid (assay > 97%) and Hydrochloric acid (assay 35-37%) were obtained from Fischer Scientific. All the chemicals were of analytical grade and were used without further purification. The Milli-Q grade water was used for preparing the samples.

3.2.2 Synthesis of GO and RGO

The GO was prepared following the synthesis method reported by Marcano et al. [49]. Initially, 0.6 g of graphite flakes were mixed with 70 mL solution of H_2SO_4/ H_3PO_4 (maintaining 9:1 ratio). Further, 3.6 g $KMnO_4$ (1:6 ratio with graphite) was added in portions to the solution

slowly maintaining the temperature below 20 ˚C with the help of an ice bath. The ice bath was removed and the temperature was increased to about 50 ˚C, and stirred for about 24 hours at 450 rpm. The reaction mixture was allowed to cool at room temperature. The mixture was incubated in an ice bath to lower the temperature to ~ 0 ˚C, and then 3.0 mL of 30% H_2O_2 and about 50 mL of DI water solution was added above to the mixture under stirring for two hours at 450 rpm. An additional amount of 50 mL of DI water was further added and the mixture stirred for another three hours at 450 rpm. The resultant yellow mixture kept aside for a few hours to settle down the solid particles. A clear transparent liquid above is separated and the remaining solid particles are centrifuged at 4000 rpm for 15 minutes. The supernatant is removed and the remaining particles have been washed with 10% HCl and DI water successively until sulphate is not detected by barium chloride, and a neutral pH is attained. After these multiple washing process, remaining material is vacuum dried for overnight at room temperature.

The addition of hydrazine hydrate in the ratio of 10:7 is used for GO reduction [50]. We prepared a dispersion (1 mg/mL) of GO flakes in DI water via ultra-sonication for an hour to obtain a homogeneous yellow-brown solution. The pH of the dispersion is adjusted to ~11 by adding desired amount of ammonia solution. Hydrazine hydrate was then added to the solution and heated at 80 ºC for 24 hours. A black coloured flocculent substance precipitated out, which was filtered and washed with methanol and DI water in turns. Finally, RGO was obtained and dried at 80 ºC for 24 hours.

3.2.3 Synthesis of PANI-GO and PANI-RGO binary nanocomposites

Freshly synthesized 50 mg RGO dispersion in NMP (1 mg/mL) was ultrasonicated for 2 h by obtaining an exfoliated light brown heterogeneous mixture. A solution of aniline monomers (6.0 g) in 40 mL of 1 M HCl was slowly added into the above RGO dispersion with vigorously stirring to obtain a RGO/aniline suspension. We prepared a solution of ammonium persulfate (Aniline: APS at 1:3) in 40 mL of 1.0 M HCl, and added dropwise into the above mixture at ~ 0 °C under continuous stirring for 30 min. The resultant solution mixture was incubated at 0 – 4 °C for 24 h. The dark green precipitate was filtered, washed by 1.0 M HCl repeatedly until the filtrate became transparent. The sample was vacuum dried at 60 ˚C for 24 h to get a PANI-RGO nanocomposite. Following the same method, we have prepared PANI-GO nanocomposite.

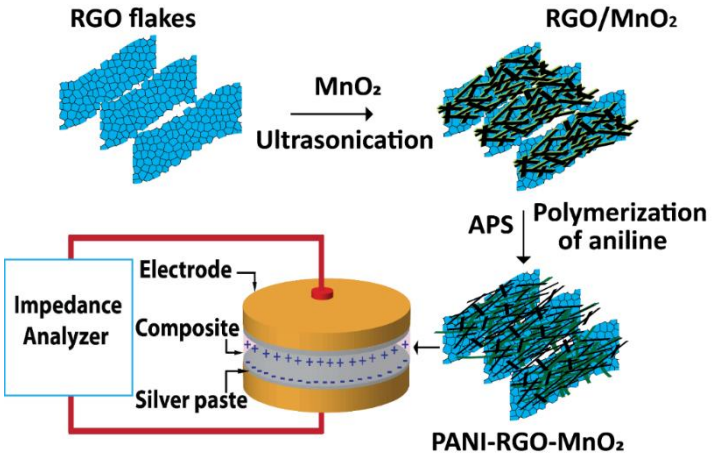

Figure 3.1 Schematic representation of the synthesis process of the PANI-RGO-MnO_2 ternary nanocomposite and measurement setup for electrostatic properties.

3.2.4 Synthesis of PANI-GO-MnO_2 and PANI-RGO-MnO_2 ternary nanocomposites

To prepare ternary composites, we first prepared MnO_2 by following the reduction method [51,52]. $KMnO_4$ (1.32 g) was mixed in 200 mL of DI water and simultaneously 10 mL of ethanol was added in drops under vigorous stirring condition at room temperature. After 3 h, the purple colour solution was turned into dark brown colour. The mixture was exfoliated by probe sonication (220 V, 400 W) at 30 % amplitude and 0.5 duty cycle for 30 min, forthwith heated at 100 ºC for 20 h. The dark brown precipitate was filtered and washed thoroughly with DI water and ethanol. The filtrate was heated at 100 ºC for 24 h, and finally, MnO_2 collected in the form of a brown coloured powder. To prepare PANI-RGO-MnO_2, an aqueous dispersion of MnO_2 (50 mg MnO_2 in 50 mL DI water) and a dispersion of RGO in ethanol (50 mg RGO in 50 mL ethanol) were prepared by ultra-sonication (220 V, 120 W) for 30 min. Both the dispersions were mixed in 50 mL DI water under vigorous stirring.

The ternary nanocomposite of PANI was synthesized by the following method [51,53], as shown in Figure 3.1. The above RGO-MnO_2 suspension was transferred into an ice bath, and aniline solution (6.0 mL of aniline in 40 mL of 1.0 M HCl) added slowly. The solution immediately turns into light green, indicating the initiation of the polymerization process. After about 30 minutes, a solution of 2.0 g of APS in 40 mL of 1 M HCl was added into the above mixture to ensure complete polymerization. The mixture was kept under stirring on an ice bath for ~ 3 h. The obtained product PANI-RGO-MnO_2 was washed with 1.0 M HCl aqueous solution and DI water, and then vacuum dried at 60 ºC. Following a similar method, we have prepared PANI-GO-MnO_2 nanocomposite by keeping the same amount of materials.

3.2.5 Characterization

The micro Raman spectra **(**Horiba Jobin Vyon, LabRam HR) acquired at an acquisition time of 10 s with an excitation wavelength of 532 nm. The confirmation of functional groups was investigated by Fourier transform infrared spectroscopy (FTIR) (Perkin Elmer Spectrum Two) in the frequency range of 400 to 4000 cm^{-1}. The X-ray diffraction (XRD) (Bruker, D8 Advance using Cu-Kα-Kβ radiations at λ=1.54 A°, 40 kV, 40 mA) patterns were recorded in the range of 5 to 70° at a scan rate of 1° per minute. The UV visible (Shimadzu, UV-2600 230V EN spectrophotometer) absorbance was recorded in the UV visible region. The electron microscopic images were recorded by field emission scanning electron microscope (FESEM at 10 kV) (JEOL, JSM-7610F), and field emission transmission electron microscope (FETEM) (JEOL, JEM 2100 at the acceleration voltage of 200 kV) to study the surface morphology of nanocomposites. Topography scanning were recorded at room temperature with atomic force microscopy (AFM) (Bruker, Innova) using the tapping mode. The thermal stability of the nanocomposites was investigated by the thermogravimetric analyser (PerkinElmer TGA-4000) at a heating rate of 10 K per minute. The electron spin resonance (ESR) (JEOL, JES-FA200) signals were recorded at room temperature to uncover the unpaired electrons. The DC conductivities leading by I-V measurements of the samples were analyzed by the parameter analyzer (Keithley, 4200-SCS) at room temperature. The AC conductivities, dielectric and electrostatic properties were investigated at room temperature using a definitude impedance analyzer (IM7581, HIOKI) in the frequency range of 100 kHz to 300 MHz. as shown in an experimental setup of Figure 3.1.

3.3 Results and discussion

3.3.1 Structures and morphologies

Raman spectra of PANI-GO, PANI-RGO, PANI-GO-MnO_2 and PANI-RGO-MnO_2 powder nanocomposites were recorded using the microscopic glass slide as the substrate (Figure 3.2a). The band vibrations at 1338 cm^{-1} (C–C disordered form of D band) and 1596 cm^{-1} (C=C structure of G band) in all the samples confirm the presence of GO and RGO nanoflakes [54]. The in-plane bending of C–H plane of quinoid ring, in plane bending of C-H plane of benzenoid ring, stretching vibrations of quinoid ring C–C plane, stretching vibration of quinoid ring of C=C plane and C=C plane vibrations of benzenoid ring are observed at 1176, 1251, 1392, 1480 and 1592 cm^{-1}, respectively [55]. The wavenumber at 1340 cm^{-1} denotes the stretching of C–N.$^{+}$ due to the electrostatic interaction of C–N^{+} stretching of PANI chain with carboxyl group of GO and RGO [56]. The band from 500 to 680 cm^{-1} is related to Mn–O stretching vibrations, and indicates presence of MnO_2 in the nanocomposites [24]. The low intensity of MnO_2

stretching vibrations is due to the growth of PANI nanorods over the GO, RGO, and MnO_2 surfaces. The appearance of a 2D band in the region ~ 2657 cm^{-1} is associated with the two-phonon vibrations that can be attributed to an increased proportion of sp^2 carbons in RGO [57]. The characteristic band of infrared absorption (Figure 3.2b) exhibits almost at the same positions of all graphs, suggesting the formation of well-mixed nanocomposites. The band transitions at 1492 and 1634 cm^{-1} are attributed to benzene ring and C=N bond stretching, respectively. The weak and strong absorptions at 1310 cm^{-1} and 1390 cm^{-1} are associated to the stretching vibrations of N–B–N and C=C bonds, respectively [58,59]. The weak band absorption peaks in the range of 1090 to 1240 cm^{-1} correspond to C–O stretching vibrations of alkyl and epoxy groups, and framework vibrations of graphene layers. In addition, the peaks at 613 and 1237 cm^{-1} are related to the outer plane bending of C–H and stretching mode of C=N bonds, respectively. These characteristic bands confirm the formation of PANI in the prepared binary and ternary nanocomposites. The weak absorption peaks at 2853 and 2931 cm^{-1} are attributed to the symmetric and asymmetric vibrations of CH_2, typically appear due to the presence of GO and RGO. In the nanocomposites, the broad peak at 3443 cm^{-1} is related to the H–O–H bending of absorbed water molecules. The characteristic band in the range of 465 to 797 cm^{-1} is due to the Mn–O stretching vibrations, and confirms the presence of MnO_2 in the prepared nanocomposites [24,58]. Further, the characteristic strong absorption peaks of the ternary nanocomposites reveal about PANI growth over the GO/MnO_2 and RGO/MnO_2 surfaces, and it brings a complex structure due to intermolecular bond formation during polymerization. Figure 3.2c shows XRD patterns of binary and ternary nanocomposites. PANI-GO and PANI-RGO exhibit weak diffraction peaks at $2\theta = 8.7^{\circ}$ (1 1 0), 14.42° (2 0 0), 20.18° (0 1 2) and broad diffraction peak at 25.13° (0 0 6), suggesting the formation of PANI emeraldine salt [60]. These diffraction peaks for ternary nanocomposites are relatively stronger as compared to binary nanocomposites, indicating the enhanced surface area due to the incorporation of GO and RGO with MnO_2. The MnO_2 peaks at ~ 44.42° and ~ 69.7° correspond to (4 0 0) and (5 4 1) planes, respectively [61]. PANI-GO-MnO_2 exhibits significant crystallinity compared to PANI-RGO-MnO_2, and shows a weak broad peak (viz., less crystallinity). The less crystallinity of PANI-RGO-MnO_2 is attributed to the presence of RGO, which induces partial strain due to random orientation of PANI chains between intra-molecular segments of the PANI-RGO-MnO_2 composite.

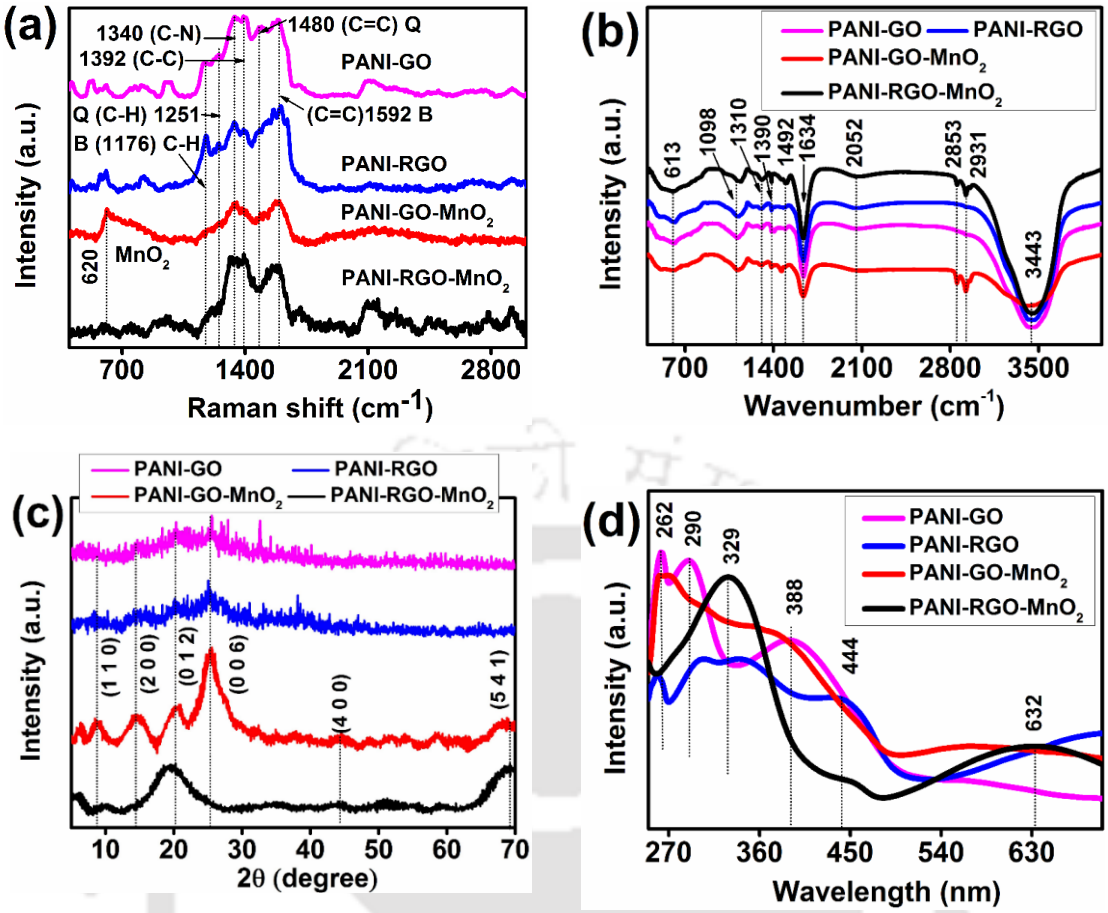

Figure 3.2 Structural properties by (a) Raman spectra, (b) FTIR spectra, (c) XRD patterns, and (d) UV absorbance spectroscopy of all the nanocomposites.

The UV visible absorbance of the composites are presented in Figure 3.2d. PANI-GO exhibits three characteristic absorption bands at 262, 290 and 388 nm, correlated to the π–π* interactions, π*–polaron and π–polaron electronic transitions, respectively [55]. PANI-RGO exhibits a slightly red shift from PANI-GO with three characteristic band absorptions at 300, 341 and 444 nm, associated to the strong interactions of π–π* electronic, polaron and bipolaron transitions, respectively. The red shift is attributed to the strong interactions between PANI and RGO, facilitating electron delocalization; and hence an enhanced electrical conductivity would be expected. PANI-RGO-MnO_2 exhibits the absence of multiple absorbance peaks, indicating a heavily doped material with an ordered phase [62,63]. The band absorptions of PANI-GO-MnO_2 at 262, 388 and 632 nm, and PANI-RGO-MnO_2 at 329, 444 and 632 nm are attributed to π–π* electronic interactions, π*–polaron, and π–polaron band interactions, respectively. The multiple layers of RGO and MnO_2 nanofillers have introduced the π–π* phase defect into PANI that can be eliminated from an ordered molecular arrangement. Consequently, an improved

charge transport capability would be achieved to make the composite a suitable candidate for solid charge storage device. In addition, structural analysis of pure GO, RGO, MnO_2 and PANI have been carried out and presented in Figure 3.3. The structural corroboration of the GO, RGO, PANI, and MnO_2 materials has been evaluated by the Raman spectra as shown in Figure 3.3a, using n-type silicon wafer as the substrate. The peak intensities at 1345 cm^{-1} and 1592 cm^{-1} indicate to the D and G bands with I_D/I_G ratio of 1.10, 1.16, corresponding to GO, and RGO flakes, respectively. The enhanced value of I_D/I_G ratio confirms the reduction of GO to RGO with an enhanced structural defect [64]. The peak intensities of pure PANI at 1091, 1387, and 1606 cm^{-1} represent the C–N bond stretching, quinoid and benzenoid stretching, respectively. The plane vibration at ~ 640 cm^{-1} correspond to α-MnO_2 phase [65]. As shown in Figure 3.3b, the peak intensity of XRD spectra at ~ 10˚ attributed to GO, and at ~ 25° (2 2 0) for RGO nanoflakes [66,67].

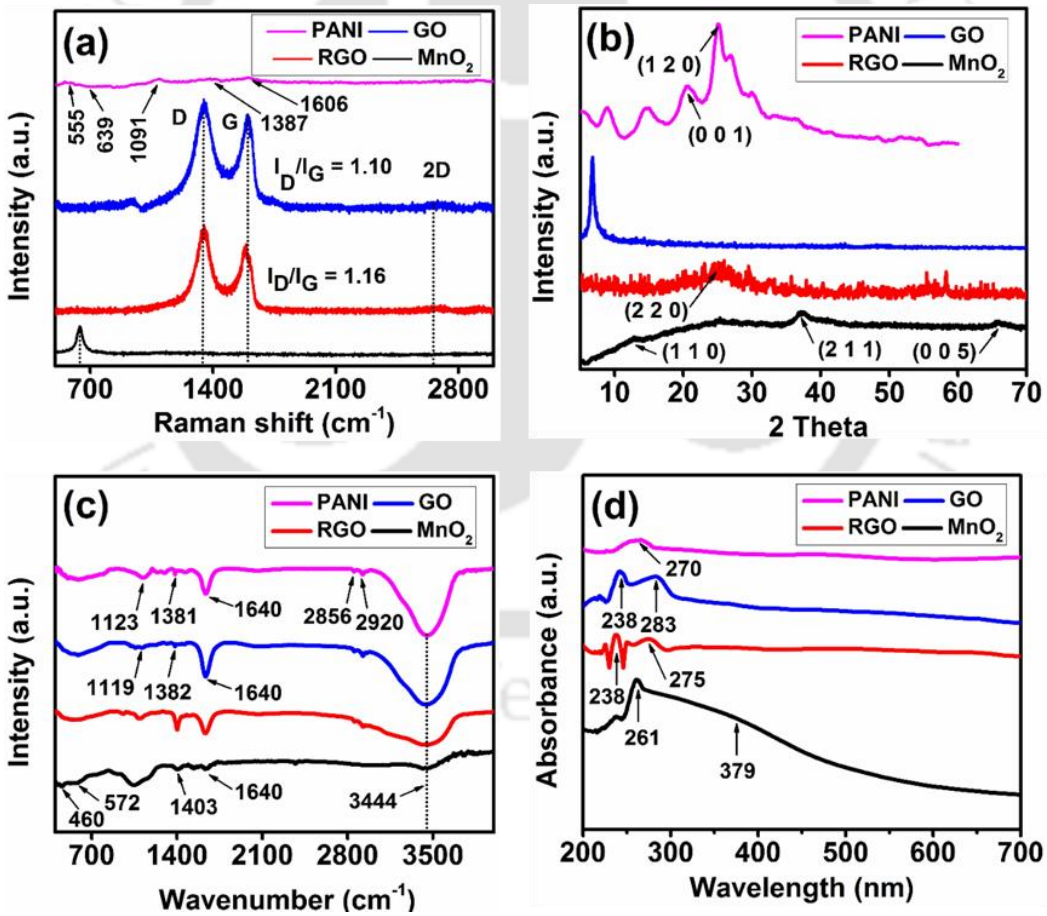

Figure 3.3 Structural analysis (a) Raman spectra, (b) XRD patterns, (c) FTIR, and (d) UV visible absorbance spectroscopy of PANI, GO, RGO, and MnO_2 intrinsic materials.

The characteristic planes (1 1 0), (2 1 1), and (0 0 5) corresponding to 12.78º, 37.52º and 65.44º, indicates manganese oxide (MnO_2) in the tetragonal structure. The XRD patterns for pure PANI ~ 20.3° and 25.1° belongs to (0 0 1) and (1 2 0) crystallographic planes, associated to the perpendicular alignment of PANI fragments, reveals an amorphous structure. The interplanar spacing of each plane were 0.45 and 0.35 nm, respectively.

As shown in Figure 3.3c, the FTIR spectra ~ 3444 and 1640 cm^{-1} exhibit stretching and bending vibrations of the hydroxyl group of Mn–OH and absorbed moisture, respectively. The band vibrations ~572 cm^{-1} represents Mn–O vibrations. The peak at ~ 1403 cm^{-1} represents to the O–Mn–O bond vibrations. In addition, for pristine α–MnO_2, the vibrations at ~ 460 cm^{-1} is attributed to Mn–O bond [68,69]. A broad spectrum of GO at ~3444 cm^{-1}, is attributed to hydroxyl groups [70]. The characteristic absorption peak at ~ 1640 and at ~ 1382 cm^{-1} belong to C=C stretching, and O–H bending, respectively. The band absorption at ~ 1119 cm^{-1} is related to C=O stretching vibrations. In the case of RGO, the peak intensity of the corresponding hydroxyl group and substantial oxygen groups are less than GO [71]. Further, band vibrations at 1123 and 1381 cm^{-1} exhibit quinoid-benzenoid-quinoid and benzenoid units, respectively. The oxidation state of PANI corresponds to 1640 cm^{-1}, reveals C=C stretching of quinoid rings. Moreover, a weak absorption in the range of 2800–3000 cm^{-1}, is attributed to C–H and N–H stretching of PANI. In Fig. 3d, GO shows two bands at 238 and 283 nm by virtue of π–π* aromatic transitions of C–C bonds and n–π* transition by C=O bonds, respectively. The peak absorbance at ~ 275 nm is blue shifted, the stipulated maximum absorbance that GO is completely reduced [72]. The optical properties of α–MnO_2 show a broad absorbance at ~ 379 nm, associated with d–d transition of Mn^{4+} ions, and at ~ 261 nm is contributed by Mn^{3+} ions [73,74]. Further, UV absorbance for PANI at ~ 270 nm corresponds to π-π* electronic transition of benzenoid units.

As shown in FESEM micrographs (Figure 3.4), filler materials (viz., GO, RGO and MnO_2) are uniformly distributed into the PANI matrix, during *in-situ* polymerization. In PANI-GO nanocomposite (Figure 3.4a) due to the significant amount of oxide elements, an intramolecular crosslinking with anilinium ions facilitates forming a uniform dispersion. The average length and diameter of the nanorods are found to be 200 nm and 65 nm, respectively. RGO facilitates producing an exfoliated network structure (Figure 3.4b) with an increased size of the nanorods (length ~322 nm, diameter ~108 nm). Incorporation of MnO_2 further modifies the morphology of ternary nanocomposites. PANI chains are self-assembled over the GO and MnO_2, establishing intercalated multi-layered structures.

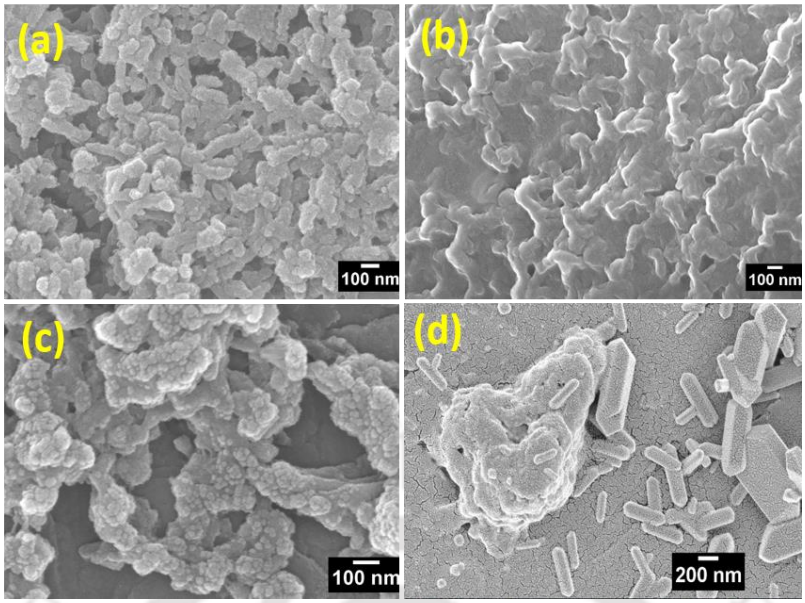

Figure 3.4 FESEM micrographs of the (a) PANI-GO, (b) PANI-RGO, (c) PANI-GO-MnO_2 and (d) PANI-RGO-MnO_2 nanocomposites.

An ionic interaction between PANI, GO, and MnO_2 nanoparticles (Figure 3.4c) leads to the formation of cross-linked agglomerated structures with an average size of ~278 nm. This is in contrast with the recent work reported by Han et al. [35], on the formation of MnO_2 nanorods in PANI/GO/MnO_2 nanocomposite, facilitated by the absorbent cotton precursor. In the present work, MnO_2 nanoparticles are dispersed with GO and RGO layers, prior to *in-situ* polymerization, and hence, PANI has successfully been grown over the surface. However, the ternary nanocomposite of PANI, RGO and MnO_2 (Figure 3.4d) exhibits a distinctly different surface texture, as compared to the PANI-GO-MnO_2. It is observed that MnO_2 has been shaped into hexagonal nanorods and exerts a relatively high interfacial area. The RGO nanoflakes, due to its restacking property, are folded at room temperature. As a result, MnO_2 being encapsulated by RGO sheets, has agglomerated to form nanorod-shaped structures. Hence, MnO_2 structured with uniform distribution (average length 412 nm and width 114 nm) equivalent to hexagonal cylindrical shape (Figure 3.5).

PANI chains have grown at the RGO/MnO_2 surface, resulting in a favourable electrostatic interaction between the polar charge carriers of PANI and oxygenated groups of RGO, suggesting charge delocalization. It can be appraised that the illustrated unidirectional shapes are typically advantageous for easy charge flow, and can provide an excellent charge storage proficiency. In addition, FESEM images for pure PANI, GO, RGO and MnO_2 shown in Figure 3.6, can be correlated with PANI nanocomposites. Agglomeration of PANI nanofibers yields a porous morphology (Figure 3.6a).

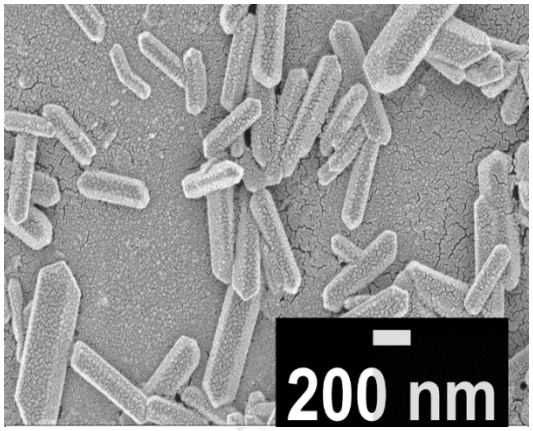

Figure 3.5. FESEM micrograph of symmetrical nanorods of PANI-RGO-MnO_2.

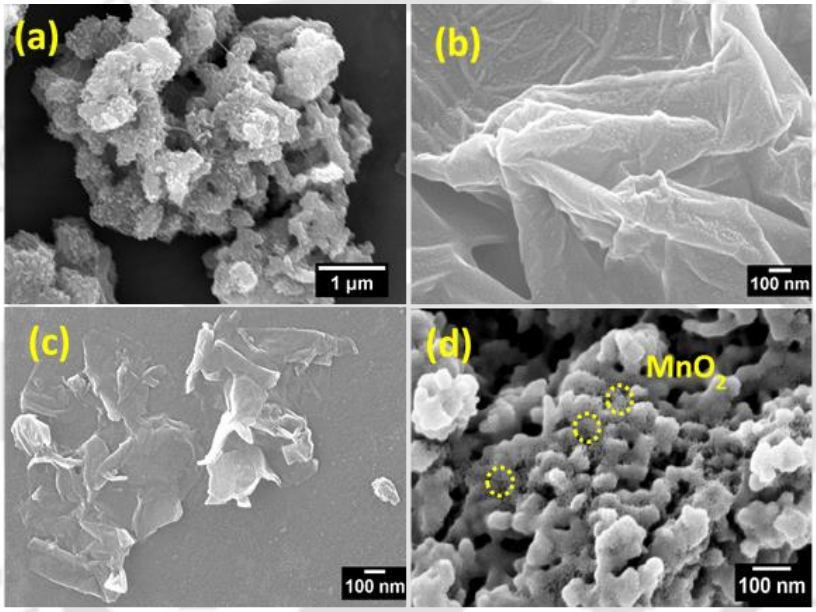

Figure 3.6. FESEM micrographs of pure materials of (a) PANI, (b) GO, (c) RGO, and (d) MnO_2.

The layered texture of GO and RGO (Figure 3.6b – c) is intercalated within the porous region of PANI fragments, and constitute a homogeneous distribution of PANI-GO and PANI-RGO binary composites. The α–MnO_2 nanoparticles are distributed over the entire surface of ternary composites (Figure 3.6d). The detailed morphology of the nanocomposites has also been studied by FETEM. A dark region in the FETEM image of PANI-GO composite in Figure 3.7a indicates the growth of PANI chains over GO flakes, speculated from Figure 3.a. The HRTEM image (Figure 3.7b) clearly shows the development of a crystalline phase with a lattice spacing of 0.255 nm. The SAED pattern corresponds to the polycrystalline nature in the plane (0 0 2), as shown in the inset of Figure 3.7b. The PANI-RGO nanocomposite in Figure 3.7c shows a uniform distribution, as RGO nanoflakes prevent restacking, and results into an

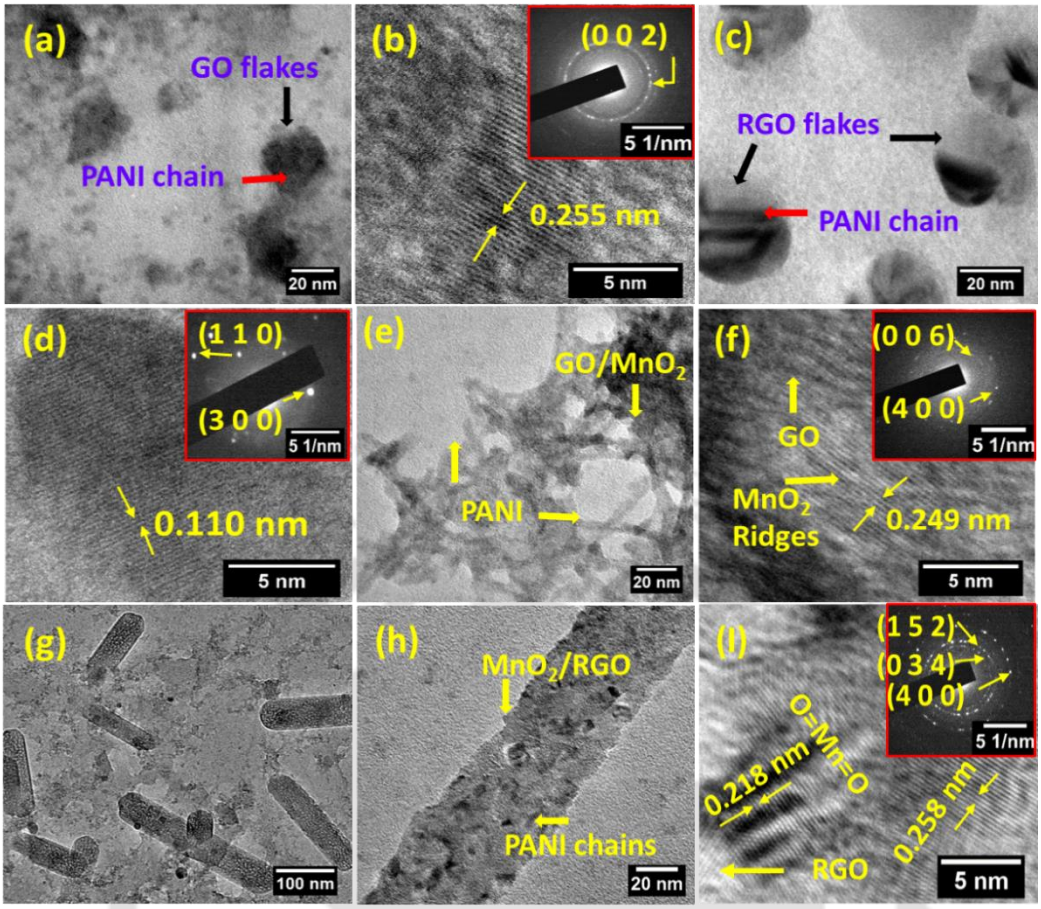

Figure 3.7. (a) FETEM image, (b) HRTEM image, and SAED pattern (inset) of the PANI-GO. (c) FETEM image, (d) HRTEM image, and SAED pattern (inset) of the PANI-RGO. (e) FETEM image, (f) HRTEM image, and SAED pattern (inset) of PANI-GO-MnO_2. (g) FETEM image of PANI-RGO-MnO_2, (h) FETEM image at high resolution, (i) HRTEM image and SAED pattern (inset) of the PANI-RGO-MnO_2 nanocomposite.

exfoliated state, and assumed an enhanced surface area towards the growth of the PANI chains during polymerization. The HRTEM image shows an appreciable crystalline structure, with a smaller lattice spacing of 0.110 nm as compared to PANI-GO (0.255 nm). The inset of Figure 3.7d exhibits SAED pattern along with the plane configurations of (1 1 0) and (3 0 0), attributed to a polycrystalline morphology. In the presence of MnO_2, PANI forms an intercalated structure with GO and RGO in PANI-GO-MnO_2 and PANI-RGO-MnO_2 nanocomposites, respectively. The presence of GO and MnO_2 makes the nanocomposite a multi-layered structure, evidenced by Figure 3.4c that has functionalized with PANI chains (Figure 3.7e) and shows certain electrostatic charge storage property. This structure consists of sufficient voids due to intercalated structure in the polymer matrix. Therefore, greater ionic diffusion leads to the diffusional capacitance with an enhanced electrostatic charge storage. The HRTEM analysis of PANI-GO-MnO_2 exhibits two separate lattice regions of GO and MnO_2 (Figure 3.7f). The

crystal phase of MnO_2 appears to be larger compared to the GO, with an overall lattice spacing of 0.249 nm. The SAED pattern (inset of Figure 3.7f) shows a polycrystalline behaviour with an orientation along (0 0 6) and (4 0 0) planes. An impressive rod-shaped morphology is observed in the presence of RGO in PANI-RGO-MnO_2 nanocomposite. Figure 3.7g shows a collection of nanorods scattered throughout the sample, viewed at a low magnification (100 nm). At high magnification (20 nm), the internal structure of nanorods is clearly visible (Figure 3.7h). The average length and diameter of the nanorods are measured as ~ 151 nm and ~ 48 nm, respectively. We have noted that the average size of the PANI-RGO-MnO_2 nanorod is slightly deviated from FESEM image (Figure 3.4d). This difference in sizes is attributed to the difference in sample preparation for FESEM and FETEM measurements. During the *in-situ* polymerization process, PANI chains grow over the RGO surface followed by a synergistic effect of mutual interaction of PANI, RGO and MnO_2, the entire nanocomposite turns into a unique shape (hexagonal nanorods). Following this, PANI-RGO-MnO_2 nanorods would enhance charge transport compared to microrods due to the high surface to volume ratio. A rod shape structure readily transports the lossless charge species end to end. This structure can attribute to high depth of penetration to constitute a unidirectional confinement of the charge carriers. The HRTEM image (Figure 3.7i) of the nanocomposite shows a crystalline phase with the lattice spacing of 0.218 and 0.258 nm, representing MnO_2 and RGO, respectively. Further, the SAED pattern (inset of Figure 3.7i) clearly shows a polycrystalline behaviour. The orientations of three different planes, (1 5 2), (0 3 4) and (4 0 0) are attributed to the individual components, PANI, RGO and MnO_2, respectively. The closely packed structure of the nanocomposite would definitely be suitable for rapid charge accumulation with an improved electrical conductivity. To get a detailed understanding on the surface topography, we have carried out AFM scanning of the nanocomposites, using a scan area of $5 \times 5\ \mu m^2$, as shown in Figure 3.8a – d. PANI-GO binary composite shows a uniform surface with an average peak height of 5.1 nm (Figure 3.8a). The smaller height of PANI-GO film compared to pure GO (~ 6.0 nm, Figure 3.9d) is an indication of the formation of a smooth dispersion of PANI matrix, which results a uniform film with reduced thickness. However, PANI-RGO nanocomposite shows a relatively rough surface with an average peak height of 10.4 nm (Figure 3.8b). The increased roughness of PANI-RGO over PANI-GO may be attributed to more exfoliated structure. The thick intense peaks are attributed to the presence of PANI nanorods over GO and RGO surfaces. The PANI-GO-MnO_2 composite shows even a higher surface roughness with an average peak height of 37.9 nm (Figure 3.8c).

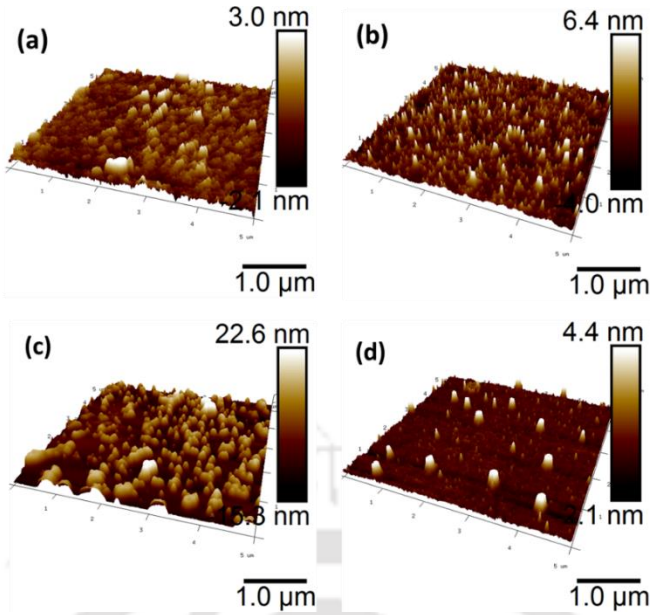

Figure 3.8. AFM micrographs of (a) PANI-GO, (b) PANI-RGO, (c) PANI-GO-MnO_2, and (d) PANI-RGO-MnO_2 nanocomposites at scan area of 5 × 5 µm^2.

In contrary, PANI-RGO-MnO_2 nanocomposite exhibits a relatively uniform surface topography with average peak height of 6.5 nm (Figure 3.8d) with the lowest surface roughness (Table 3.1). The enhanced smoothness of the surface of PANI-RGO-MnO_2 may be associated with the continuous dispersion and formation of well-defined hexagonal nanorods, as has been observed by FESEM (Figure 3.4d) and FETEM (Figure 3.7g) analysis. It may be expected that the uniform surface of PANI-RGO-MnO_2 would provide an efficient charge transfer, suitable for energy storage applications. In addition, the AFM analysis of pure GO, RGO, and MnO_2 shows peak height of 6.5, 16.45 and 29.12 nm, respectively (Figure 3.9).

Table 3.1: Surface roughness values based on AFM measurement.

Materials	Average roughness (R_a, nm)	RMS roughness (R_q, nm)
GO	3.02	4.68
RGO	4.11	5.81
PANI-GO	0.471	0.657
PANI-RGO	1.12	2.24
PANI-GO-MnO_2	5.20	6.35
PANI-RGO-MnO_2	0.367	0.708

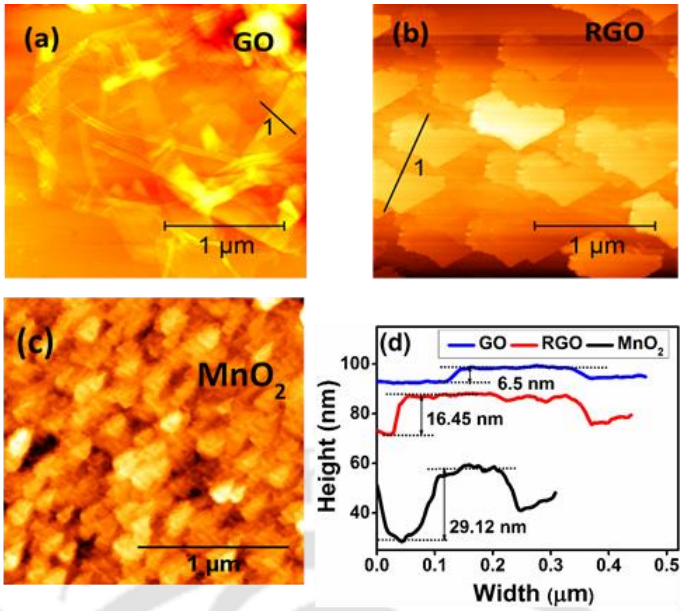

Figure 3.9. Tapping mode AFM micrographs of (a) GO, (b) RGO, (c) MnO_2, and corresponding (d) flakes size measurements.

3.3.2 Thermal stability

To understand the thermal stability of the nanocomposites, we have carried out their thermo gravimetric analysis (TGA) (Figure 3.10a). It has been observed that PANI-RGO-MnO_2 ternary nanocomposite exhibits the highest thermal stability (with ~65% residue), among the nanocomposites. The highest thermal stability may be attributed to the intrinsic interaction among the constituent components (viz., PANI, RGO and MnO_2) of the composite, forming well-defined hexagonal-shaped nanorods. PANI-GO-MnO_2, PANI-RGO and PANI-GO nanocomposites show relatively less thermal stability with 27%, 50% and 6% residues, respectively. Therefore, PANI-RGO-MnO_2 nanocomposite would be a better choice for the application in energy storage even at high temperature.

3.3.3 Electron spin resonance analysis

Usually, conducting polymers have mobile radicals, whose mobility may be tuned by the presence of nanofillers, such as GO, RGO and MnO_2. Figure 3.10b represents the electron spin resonance (ESR) analysis of all the nanocomposites studied, at a frequency of ~ 9.5 GHz. The typical parameters are described as follows: The lower value of ΔH_{pp} (peak-to-peak line width) corresponds to an improved charge mobility, which is found to be slightly higher in RGO doped composites. In the ESR measurements, spin quantum number (S =1/2) of an electron has two magnetic components, $m_s = \pm 1/2$. Accordingly, under an applied magnetic field, the unpaired electrons would adjust toward spin parallel and perpendicular, attributed to the lower and

Table 3.2. The calculated parameters of ESR signal.

Nanocomposites	g-factor	Asymmetric factor (A/B)	ΔH_{pp} (mT)	ΔE (J)
PANI-GO	2.01034	3.42	4.0	6.2572×10^{-21}
PANI-RGO	2.01402	1.13	3.5	6.2572×10^{-21}
PANI-GO-MnO_2	2.01244	1.55	4.5	4.2261×10^{-19}
PANI-RGO-MnO_2	2.01273	1.67	4.0	6.2592×10^{-21}

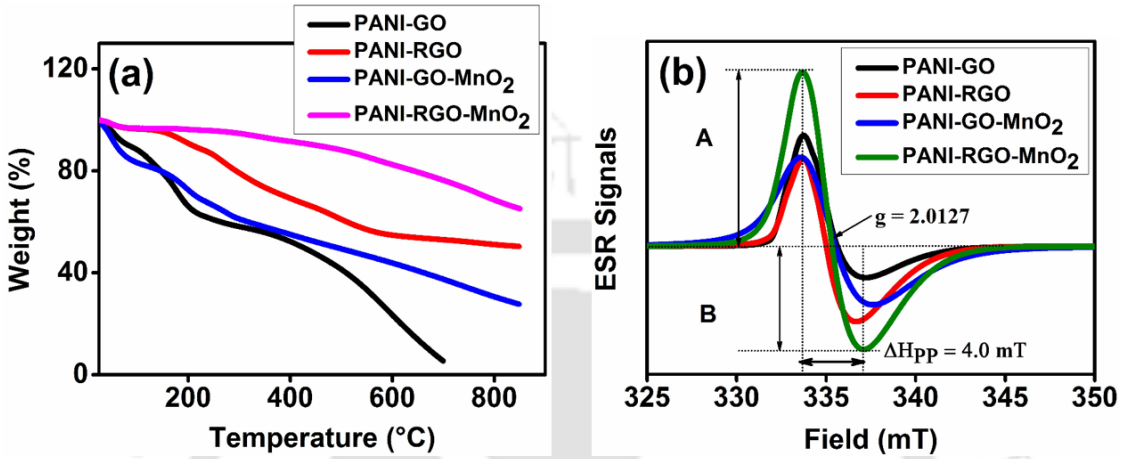

Figure 3.10. (a) Thermogravimetric analysis (TGA) of the nanocomposite materials, (b) ESR spectrum of nanocomposite materials in solid state at microwave frequency of ~ 9.5 GHz.

higher split energy absorption, respectively. The absorbed energy splits into high and low energy states, which lies in the electromagnetic spectrum. For this transition, the requisite energy (hν) may be defined by the following equation [75].

$$\Delta E = h\nu = g_e \mu_B B \qquad (3.2)$$

where g_e is Lande's g-factor, μ_B is Bohr magneton and B is magnetic field strength. The magnitudes of ΔE for all the nanocomposites have been shown in Table 3.2. It can be estimated that the occupancy of free radicals is proportional to the intensity of ESR signal.

Nanocomposites show the g-factor close to 2.0, signifying the existence of unpaired electrons [75]. The ESR signal does not show a hyperfine splitting, indicating a close binding of π–electrons mediated by PANI-grafted nanofillers (viz., GO, RGO and MnO_2), and exhibits a sharp resonance of the hyperfine signals. This sharp ESR spectrum could be ascribed to highly ordered texture of the nanocomposites. Consequently, the positive charges on PANI backbone are able to interact with the negatively charged RGO layers [76]. Therefore, the ratio of the maximum and minimum intensities of the ESR signals (viz., asymmetry factor) is an indication of heavily doped PANI matrix with stimulated charge carriers. Among the nanocomposites, PANI-RGO-MnO_2 nanocomposite exhibits the presence of significant unpaired electrons due

to additional interactions between π–cloud of RGO carbon atoms with the unpaired electron of Mn^{2+}, which would give a higher electrical conductivity.

3.3.4 Electrical conductivity

The dc electrical conductivity of nanocomposites was calculated using two-probe setup, in the applied voltage range of ±1 V. After multiple measurements of resistance, an average value was chosen to calculate the dc conductivity [77] using the following relation;

$$\sigma_{dc} = \frac{t}{A}\frac{I_m}{V_m} \tag{3.3}$$

where, t is thickness of the specimen (PANI-GO, PANI-RGO, PANI-GO-MnO_2, PANI-RGO-MnO_2 are 1.18, 1.67, 1.52, and 2.03 mm, respectively), A is cross-sectional area ($\pi\frac{d^2}{4}$), d is diameter, I_m is current, and V_m is the applied voltage [78,79]. The resistivity ($\frac{1}{\sigma_{dc}} = \rho_{dc}$) of nanocomposites were 990, 0.098, 7.194, 0.066 Ω cm, corresponds to PANI-GO, PANI-RGO, PANI-GO-MnO_2 and PANI-RGO-MnO_2, respectively. The calculated dc electrical conductivities for PANI-GO, PANI-RGO, PANI-GO-MnO_2 and PANI-RGO-MnO_2 were 101 × 10^{-5}, 10.158, 0.139 and 15.037 S cm^{-1}, respectively. Further, the current density (J A m^{-2}) also can be evaluated using the following relation as given below.

Assuming that the current flow (I) is uniform cross cross-sectional area, then:

$$I = \int J.ds \tag{3.4}$$

$$I = \int J\, ds \cos 0° \tag{3.5}$$

$$I = J \int ds \tag{3.6}$$

I=JA, where J is current density and A is cross-sectional area.

Alternatively, it is well known that $I=neAV_d$, where $V_d = \frac{eE}{m}$, therefore $I = \frac{nAEe^2}{m}$

$$I = \frac{nAe^2E}{m} \tag{3.7}$$

where, n is electron density, e is electronic charge and E is applied electric filed.

We have:

$$J = \frac{I}{A} = \frac{ne^2E}{m} \tag{3.8}$$

J=σE, where, σ is dc electrical conductivity [78]. From the I–V characteristics (Figure 3.11a), it is observed that the PANI-RGO-MnO_2 and PANI-GO nanocomposites exhibit maximum and minimum dc conductivities, respectively, with a non-ohmic behaviour. Typically, GO exhibits very low conductivity, therefore, the overall conductivity of the GO-doped composites is reduced as compared to the RGO-doped composites. Relatively, GO has significant impurities,

hence charge transport ability being reduced and become unstable. Thus shifted the threshold voltage. Among all the composites, PANI-RGO-MnO_2 shows higher conductivity, which is attributed to the formation of a well-dispersed composite with hexagonal-shaped nanorods.

3.3.5 Dielectric and electrostatic properties

The dielectric permittivity (ε′) and dielectric losses (ε") have been plotted as a function of the applied frequency for all the nanocomposites in Figure 3.11b and Figure 3.11c, respectively. The mathematical expressions for ε' and ε" have been presented as follows;

$$\varepsilon' = \frac{C \times t}{A \times \varepsilon_0} = \frac{C \times t}{\frac{\pi d^2}{4} \times \varepsilon_0} \tag{3.9}$$

where, ε′ is dielectric permittivity, C is capacitance, t is thickness of the pellet, A is cross-sectional area, and ε_0 $\left(8.85 \times 10^{-12} \frac{F}{m}\right)$ free space permittivity [80]. The dielectric losses can be defined as follows;

$$\varepsilon'' = \varepsilon' \times \tan(\delta) \tag{3.10}$$

where, tan(δ) is tangent losses, considered as loss factor (D), and ε′ is dielectric permittivity. Furthermore, the frequency dependent ac conductivity can be estimated as follows [81,82]:

$$\sigma_{ac} = \omega \times \varepsilon_0 \times \varepsilon'' \tag{3.11}$$

$\sigma_{ac} = 2\pi f \times \varepsilon_0 \times \varepsilon' \times \tan(\delta)$, the f is applied frequency range in Hz.

All the nanocomposites show a reasonable dielectric property with frequency. All the materials are stable at high frequency. Beyond a certain frequency, the materials become unstable, which is shown by a sudden drop in the magnitude of ε′. Across all the composites, the RGO-based composites exhibit higher ε′ value compared to the GO-based composites, and it is attributed to the enhanced surface area that arises from the interfacial adhesion between RGO and PANI matrix. The magnitude of ε′ of nanocomposites essentially emulate the capability to polarize the charge carriers under an applied electric field. The decreasing ε′ with the increasing frequency (viz., at high enough frequency) is attributed to the dielectric relaxation [83], leading to a disruption of charge localization. Along with rising frequency dipolar polarization is reduced, thus ε′ follows typical non-linear decreasing order. The dielectric loss (ε") exhibits a non-monotonic trend with frequency, significantly decreases in the frequency range, ~ 10^5 to 10^7 Hz and then increases at higher frequency region (~10^8 Hz). The gradual decay in dielectric loss is attributed to the phase separation at grain boundaries, leading to the formation of a regular surface structure. Therefore, the intramolecular interactions are decrease with an enhanced materials resistivity [23,84]. At high enough frequency, due to charge polarization, charge agglomeration takes place, which leads to an increase in dielectric loss.

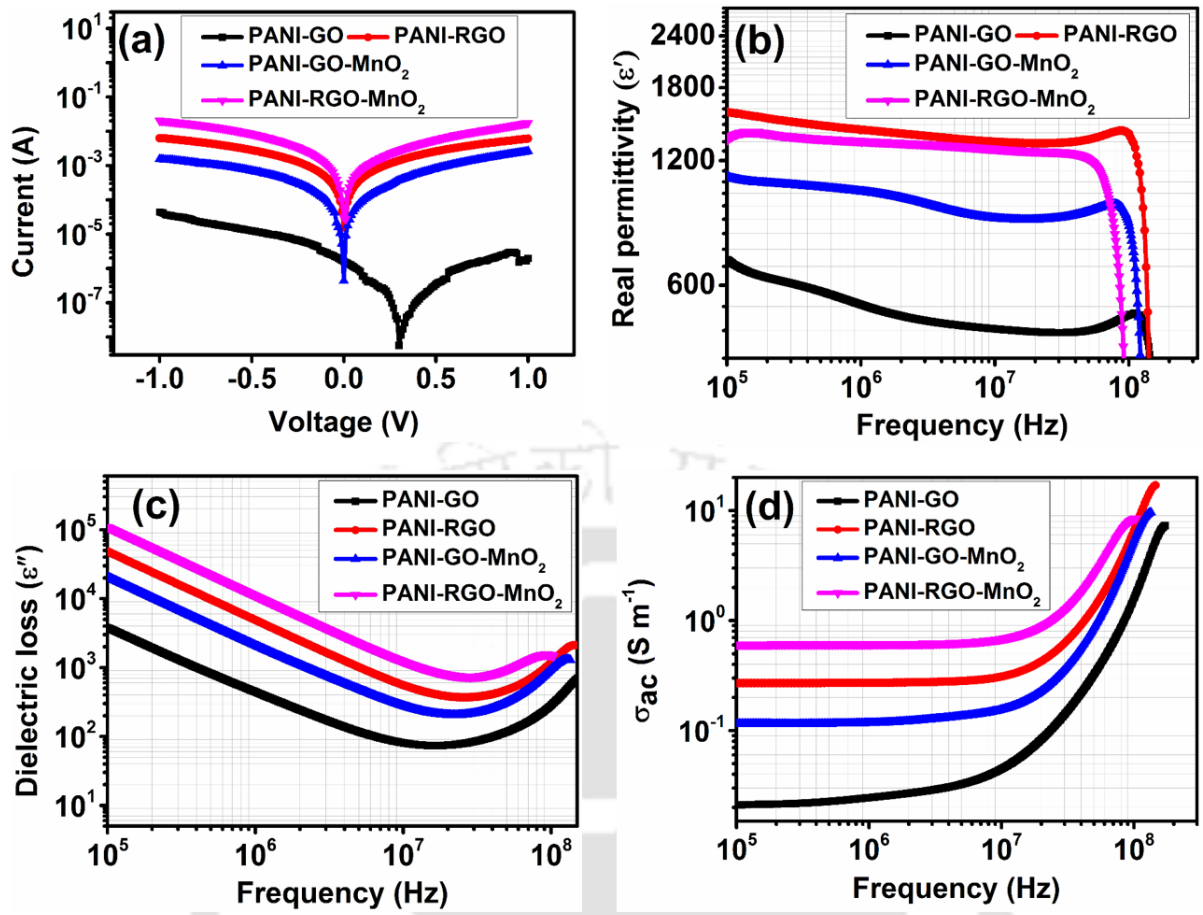

Figure 3.11. Electrical and dielectric properties against the frequency of the nanocomposites, (a) I-V characteristics, (b) dielectric permittivity, (c) dielectric losses, and (d) AC conductivity.

The nanocomposites of PANI-RGO-MnO_2 and PANI-RGO exhibit relatively higher dielectric losses than PANI-GO and PANI-GO-MnO_2. The higher value of ε" is an indication of higher electrical conductivity [44], due to the presence of an increased numbers of free charge carriers. Thus, the nanocomposites would not only be suitable for additional charge carriers, but would also provide a convenient conduction path due to highly ordered surface texture, as shown in Figure 3.4. Measurement of the ac conductivity (Figure 3.11d) closely corroborate with the trend of dielectric loss. PANI-RGO-MnO_2 and PANI-RGO nanocomposites exhibit higher ac conductivity compared to the PANI-GO and PANI-GO-MnO_2. The magnitude of the ac conductivity (σ_{ac}) increases very slowly with increasing frequency, and shows a sudden jump after ~ 10^7 Hz, which is attributed to the accumulation of charge carriers led by electron hopping mechanism [85]. To get an estimate on the electrostatic property, we have calculated capacitance (C_p, Farad), impedance (Z, k ohm), leakage current density (J, A m^{-2}) and electric displacement (D, kC m^{-2}), for all the nanocomposites (Figure 3.12).

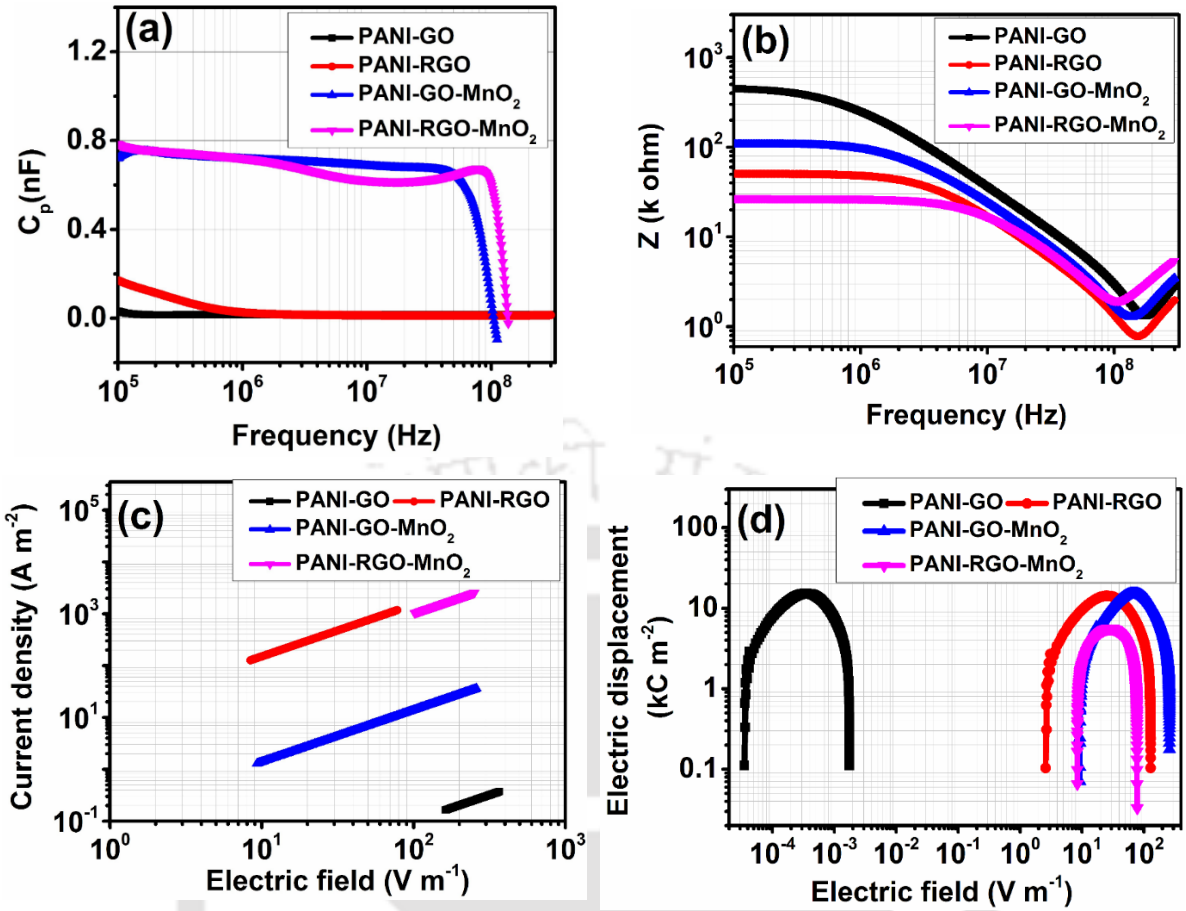

Figure 3.12. Electrostatic properties of all the nanocomposites: change in (a) capacitance with frequency, (b) impedance with frequency, (c) current density with the applied electric field and (d) electric displacement with the applied electric field.

We have observed a marginal decrease in the C_p value of PANI-RGO-MnO_2 and PANI-GO-MnO_2 by 11 and 6%, respectively, with increasing frequency in the range of 10^5 to 10^8 Hz (Figure 3.12a). However, for RGO-based nanocomposites, C_p shows a sudden decrease beyond a frequency of ~10^7 Hz, due to the considerable loss of charge carriers. RGO-based nanocomposites show relatively higher values of C_p compared to GO-based composites. Therefore, RGO-based nanocomposite, especially, PANI-RGO-MnO_2 would be a good candidate for high energy storage material. The high value of C_p for PANI-RGO-MnO_2 can easily be corroborated with the enhanced ac conductivity, as shown in Figure 3.7d.

Complex impedance analysis is the most reliable, promising and non-destructive technique to realize systematic electrical properties of nanocomposites over a wide range of frequency. Figure 3.12b represents the real (Z) component of the complex impedance for all the nanocomposites, as a function of frequency. As expected, Z sharply decreases with increasing frequency. PANI-RGO-MnO_2 exhibits the lowest Z, while PANI-GO shows the highest Z,

which is in corroboration with the trend in ac conductivity (Figure 3.11d). The increase in electrical conductivity of PANI-RGO-MnO_2 is attributed to the uniform shape of nanorods (see Figure 3.4d) that facilitates an easy charge transport. In the higher frequency range (~10^8 Hz), a gradual increment of Z, represented by resonant notch (a small v shape of curves) is due to the resonance phenomenon that arises from the high polarization of the π–conjugate radicals. The high charge localization has also been presented by ESR measurements (Figure 3.10b).

The leakage current density (J) has been estimated against the applied electric field (E, Vm^{-1}) for all the nanocomposites, and plotted in Figure 3.12c. The J of PANI-RGO-MnO_2 (2.588×10^3 A m^{-2}) and PANI-RGO (1.180×10^3 A m^{-2}) appears to be higher than, PANI-GO (0.3946 A m^{-2}) and PANI-GO-MnO_2 (37.684 A m^{-2}). The higher J of RGO-based nanocomposites is attributed to a rapid free electron migration as compared to GO-based nanocomposites. The GO-based nanocomposites are more functional compared to RGO-based nanocomposites, and provides an isolation to reduce the electron flow, reducing current density, J [4]. The current densities of all the nanocomposites exhibit an increasing trend with the applied electric field (Figure 3.12c). The electric displacement (D) of the nanocomposites was analysed against the applied electric field (Figure 3.12d), and the detailed calculations are shown as follows;

The measurement of electric flux density is needed to calculate electric charge per unit volume of the nanocomposites. Following this, the total electric charge per unit surface area or volume can be calculated. Hence, the surface charge density (σ_s) can be expressed as [86]:

$$\sigma_s = \frac{Q}{A} = \frac{Q}{2\pi r(h+r)} \text{ (Coulomb*m}^{-2}\text{)} \qquad (3.12)$$

where, A is the area of the pellets: $A = 2\pi r\,(h + r)$. The Q is the total surface charge, r is the radii, and h is the height (thickness) of the pellets.

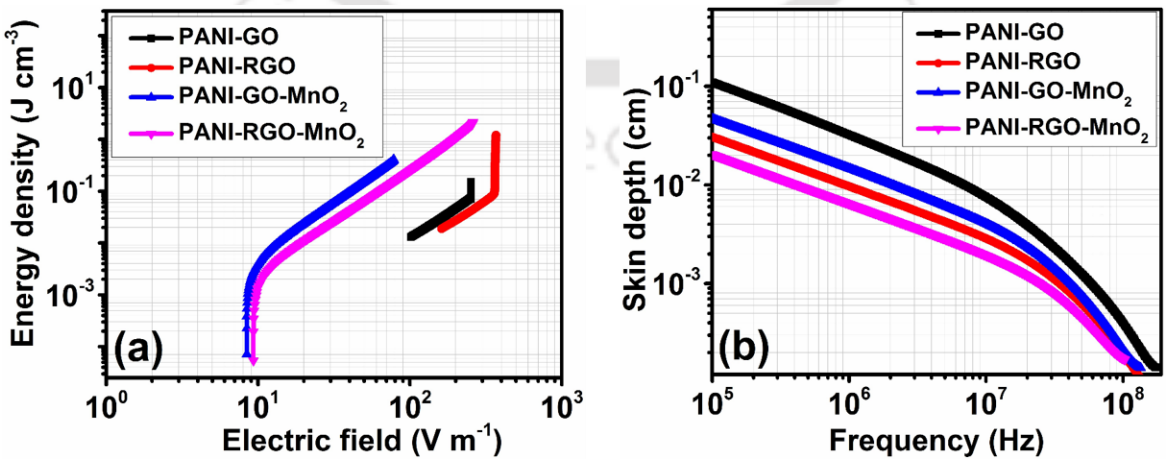

Figure 3.13. (a) Variation in energy density with the applied electric field, and (b) variation of skin depth with the frequency, for all the nanocomposites.

Further, the surface charge density (σ_s) and electric flux density (D) are considered to be the same ($D = \sigma_s$). The generated electric field is due to the surface charge density. Apparently, $D = \varepsilon_0 E$, where, E is electric field (V m^{-1}). Thus, the electric field has been calculated based on the following relation [87]:

$$E = \frac{V}{d}\ V\ m^{-1} \qquad (3.13)$$

Finally, the energy density has been estimated by $U_e = \frac{1}{2}\varepsilon_0\varepsilon_r E^2\ \frac{J}{cm^3}$ [88].

The unipolar shape of the curves corresponds to a forward scanning with the electric field (E > 0). The polarization effect in the nanocomposites strongly depends on the incorporation of nanofillers [40,89]. As shown in Figure 3.12d, the PANI-GO composite has polarization effect in the lower region of the electric field (10^{-3} V m^{-1}), whereas, the remaining nanocomposites show the polarization in the higher electric field (10^2 V m^{-1}).

The PANI-GO nanocomposite is unstable at high electric field due to the significant reduction of oxygen vacancies, allowing a decreasing relaxation time that cannot sustain a long polarization. However, the presence of MnO_2 has significantly improved the stability in PANI-GO-MnO_2 ternary nanocomposite. The RGO and MnO_2 doped nanocomposites exhibit an easy charge displacement by means of equal mobile charge carriers, resulting in increased charge polarization effect. The energy densities of the binary and ternary nanocomposites are remarkably high under unipolar electric field. The energy density (U_e) is directly proportional to the electric field: $U_e = \frac{1}{2}\varepsilon_0\varepsilon_r E^2$, where ε_0 (F m^{-1}) is the permittivity of free space, ε_r is the relative permittivity, and E is applied electric field [2]. The calculated values of U_e for PANI-GO, PANI-RGO, PANI-GO-MnO_2 and PANI-RGO-MnO_2 are 0.179, 1.382, 0.449 and 2.422 J cm^{-3} respectively, in a field of ~ 1 kV m^{-1} (Figure 3.13a). The PANI-RGO-MnO_2 shows the highest U_e, establishing as a promising candidate for high charge storage applications. The increasing U_e is due to the presence of an intrinsic interaction of nanofillers (RGO and MnO_2) with the PANI matrix. PANI-RGO-MnO_2 exhibits a higher value of U_e (superior energy storage material) compared to the reported materials, such as, based on polypropylene (U_e ~ 1.2 J cm^{-3}) [3], c-BCB/BT (U_e, = 0.81 J cm^{-3}), c-BCB/BNNS/BT (U_e = 0.99 J cm^{-3}) polymer nanocomposites [90], BST/P (VDF–HFP) and PPFPA@BST/P(VDF–HFP) nanocomposites (U_e ~ 2 J cm^{-3} [40], and antiferroelectric ceramic (PLZST) based nanocomposite (U_e, = 0.41–0.31 J cm^{-3}) [91].

Typically, skin effect is based on ac current, distributed over the charge conducting surface. As a result, a uniform current density exists throughout the conducting surface. Usually, the skin

effect is characterized by the skin depth, (δ, cm), which is inversely proportional to the electrical conductivity: $\delta = \sqrt{\frac{2}{\omega\mu\sigma_{ac}}}$, where ω =2πf as f is applied frequency, μ is permeability, and σ_{ac} is ac conductivity [92]. Figure 3.13b shows that the skin depth decreases with increasing frequency, which is attributed to maximum absorption of radiated surface charge density. The calculated skin depth decreases from 2.0 to 1.5 cm, from 3.0 to 0.9 cm, from 4.9 to 1.3 cm and from 10.8 to 1.3 cm for PANI-RGO-MnO_2, PANI-RGO, PANI-GO-MnO_2 and PANI-GO, respectively. A brief discussion on skin phenomenon of the nanocomposites, has been given as follows;

The skin effect is dominated by the doped Mn^{4+} ions in the nanocomposites. In the binary nanocomposites (PANI-GO and PANI-RGO), the skin effect is considerably less with a low impedance due to the significant charge localization. The RGO nanolayers have an important role for excellent electron conduction; hence, maximum electronic charge would be reflected through the surface of the materials. The PANI-RGO-MnO_2 unveils minimum skin effect, suggesting a maximum absorbance by the composite. Consequently, the PANI-RGO-MnO_2 shows the lower skin depth as compared to the GO doped composites, which is attributed to the geometrically ordered structures. In contrast, GO doped materials have an uneven surface, therefore, at high-frequency, penetration depth is increased [93]. After a certain distance, the applied field is reduced by a factor of 1/e, which is termed as skin depth (δ). Following relation has been used to estimate the skin depth [94]:

$$\delta = \sqrt{\frac{2}{\mu_0\mu_r\sigma f}} \qquad (3.14)$$

where, f is frequency, free space permeability ($\mu_0 = 4\pi \times 10^{-7}$) H/m and, relative permeability (μ_r) = 1 for nonmagnetic materials, and σ is ac conductivity of the nanocomposites. The PANI-RGO-MnO_2 possesses the lowest skin depth across the frequency range, indicating the formation of an excellent nanocomposite with a low loss and increased surface charge activity. The surface lattice beyond a certain depth (viz, skin depth) will not be effected. In the high frequency region (viz., > 10^8 Hz), the lattice vibrations and corresponding defects will be minimum for low skin depth materials. Therefore, PANI-RGO-MnO_2 would be suitable in the applications for high frequency absorption as stealth materials.

3.4 Conclusion

The enhancement of dielectric and energy storage properties of polymer-based nanocomposites driven by uniform nanofillers into the polymer matrix. The evenly distributed nanofillers would have adequate interaction with the polymer matrix leading to the enhancement of the property.

In this paper, we present the preparation of binary (PANI-GO and PANI-RGO) and ternary nanocomposites (PANI-GO-MnO_2 and PANI-RGO-MnO_2) of PANI. We have observed a remarkable storage permittivity with the attenuated dielectric losses. The presence of GO, RGO and PANI as nanofillers has greatly improved the dielectric and energy storage property of the nanocomposites. The RGO-based nanocomposites appear to be more effective compared to GO-based nanocomposites. The high charge conduction of PANI-RGO-MnO_2 (15.037 S m^{-1}) and PANI-RGO (10.158 S m^{-1}) exhibits an increased current density of 2.588×10^3 and 1.180×10^3 A m^{-2}, respectively. This increase in charge conduction is an evidence of high charge polarization at an applied electric field of ~ 1 kV m^{-1}. Comparatively, the PANI-GO and PANI-GO-MnO_2 exhibit considerably lower electron conduction, storage permittivity, current density along with a suppressed dielectric loss. The enhancement of properties is attributed to the homogeneous mixture of PANI and nanofillers, achieved via *in-situ* polymerization of PANI. Among all the nanocomposites, PANI-RGO-MnO_2 presents an excellent candidate for an energy storage material with high energy density and high dielectric strength. The remarkable properties of PANI-RGO-MnO_2 are attributed to the well dispersed hexagonally-shaped nanorods, facilitating easy charge transfer and enhancing the dielectric property. The high energy density nanocomposites investigated in this paper can be utilized to improve the performance of energy storage devices used in consumer electronics and high frequency high power applications.

References

[1] J. Y. Li, L. Zhang, S. Ducharme, *Appl. Phys. Lett.* **2007**, *90*, 132901.

[2] B. Chu, X. Zhou, K. Ren, B. Neese, M. Lin, Q. Wang, F. Bauer, Q. M. Zhang, *Science* **2006**, *313*, 334.

[3] M. Rabuffi, G. Picci, *IEEE Trans. Plasma Sci.* **2002**, *30*, 1939.

[4] H. Luo, J. Roscow, X. Zhou, S. Chen, X. Han, K. Zhou, D. Zhang, C. R. Bowen, *J. Mater. Chem. A* **2017**, *5*, 7091.

[5] H. Luo, D. Zhang, C. Jiang, X. Yuan, C. Chen, K. Zhou, *ACS Appl. Mater. Interfaces* **2015**, *7*, 8061.

[6] H. Tang, Z. Zhou, C. C. Bowland, H. A. Sodano, *Nano Energy* **2015**, *17*, 302.

[7] L. Xie, X. Huang, K. Yang, S. Li, P. Jiang, *J. Mater. Chem. A* **2014**, *2*, 5244.

[8] H. Tang, Y. Lin, H. A. Sodano, *Adv. Energy Mater.* **2012**, *2*, 469.

[9] P. Hu, Y. Song, H. Liu, Y. Shen, Y. Lin, C.-W. Nan, *J. Mater. Chem. A* **2013**, *1*, 1688.

[10] M. K. Vyas, A. Chandra, *J. Mater. Sci.* **2018**, *53*, 4987.

[11] K. I. Winey, R. A. Vaia, *MRS Bull.* **2007**, *32*, 314.

[12] C. Huang, Q. M. Zhang, J. Y. Li, M. Rabeony, *Appl. Phys. Lett.* **2005**, *87*, 182901.

[13] N. Maity, A. Mandal, A. K. Nandi, *Polymer* **2016**, *103*, 83.

[14] L. A. Fredin, Z. Li, M. T. Lanagan, M. A. Ratner, T. J. Marks, *ACS Nano* **2013**, *7*, 396.

[15] D. Wang, T. Zhou, J.-W. Zha, J. Zhao, C.-Y. Shi, Z.-M. Dang, *J. Mater. Chem. A* **2013**, *1*, 6162.

[16] D. K. Das-Gupta, K. Doughty, *Thin Solid Films* **1988**, *158*, 93.

[17] Q. M. Zhang, H. Li, M. Poh, F. Xia, Z.-Y. Cheng, H. Xu, C. Huang, *Nature* **2002**, *419*, 284.

[18] Y. Rao, S. Ogitani, P. Kohl, C. P. Wong, *J. Appl. Polym. Sci.* **2002**, *83*, 1084.

[19] H. Luo, C. Chen, K. Zhou, X. Zhou, Z. Wu, D. Zhang, *RSC Adv.* **2015**, *5*, 68515.

[20] F. Peruani, G. Solovey, I. M. Irurzun, E. E. Mola, A. Marzocca, J. L. Vicente, *Phys. Rev. E Stat. Nonlin. Soft Matter Phys.* **2003**, *67*, 066121.

[21] H. Luo, D. Zhang, C. Jiang, X. Yuan, C. Chen, K. Zhou, *ACS Appl. Mater. Interfaces* **2015**, *7*, 8061.

[22] H. Chen, I. Nakamura, *J. Phys. Chem. C* **2015**, *119*, 24714.

[23] J. A. Khan, M. Qasim, B. R. Singh, S. Singh, M. Shoeb, W. Khan, D. Das, A. H. Naqvi, *Spectrochim. Acta. A. Mol. Biomol. Spectrosc.* **2013**, *109*, 313.

[24] G. Wang, Q. Tang, H. Bao, X. Li, G. Wang, *J. Power Sources* **2013**, *241*, 231.

[25] H. Li, Y. He, V. Pavlinek, Q. Cheng, P. Saha, C. Li, *J. Mater. Chem. A* **2015**, *3*, 17165.

[26] S. Palsaniya, H. B. Nemade, A. K. Dasmahapatra, *Polymer* **2018**, *150*, 150.

[27] F. Meng, X. Yan, Y. Zhu, P. Si, *Nanoscale Res. Lett.* **2013**, *8*, 179.

[28] G.-R. Li, Z.-P. Feng, Y.-N. Ou, D. Wu, R. Fu, Y.-X. Tong, *Langmuir* **2010**, *26*, 2209.

[29] S. Deng, L. Wang, T. Hou, Y. Li, *J. Phys. Chem. C* **2015**, *119*, 28783.

[30] Y. Omomo, T. Sasaki, Wang, M. Watanabe, *J. Am. Chem. Soc.* **2003**, *125*, 3568.

[31] D. Ghosh, S. Bhandari, D. Khastgir, *Phys. Chem. Chem. Phys.* **2016**, *18*, 32876.

[32] M. Aghazadeh, M. Asadi, M. G. Maragheh, M. R. Ganjali, P. Norouzi, F. Faridbod, *Appl. Surf. Sci.* **2016**, *364*, 726.

[33] P. R. Jadhav, M. P. Suryawanshi, D. S. Dalavi, D. S. Patil, E. A. Jo, S. S. Kolekar, A. A. Wali, M. M. Karanjkar, J.-Hyeok. Kim, P. S. Patil, *Electrochimica Acta* **2015**, *176*, 523.

[34] J. B. Fei, Y. Cui, X. H. Yan, W. Qi, Y. Yang, K. W. Wang, Q. He, J. B. Li, *Adv. Mater.* **2008**, *20*, 452.

[35] G. Han, Y. Liu, L. Zhang, E. Kan, S. Zhang, J. Tang, W. Tang, *Sci. Rep.* **2014**, *4*, 4824.

[36] S. Cho, M. Kim, J. S. Lee, J. Jang, *ACS Appl. Mater. Interfaces* **2015**, *7*, 22301.

[37] J. Yan, Z. Fan, T. Wei, W. Qian, M. Zhang, F. Wei, *Carbon* **2010**, *48*, 3825.

[38] C. J. Jafta, F. Nkosi, L. le Roux, M. K. Mathe, M. Kebede, K. Makgopa, Y. Song, D. Tong, M. Oyama, N. Manyala, S. Chen, K. I. Ozoemena, *Electrochimica Acta* **2013**, *110*, 228.

[39] M. Li, X. Huang, C. Wu, H. Xu, P. Jiang, T. Tanaka, *J. Mater. Chem.* **2012**, *22*, 23477.

[40] S. Wang, X. Huang, G. Wang, Y. Wang, J. He, P. Jiang, *J. Phys. Chem. C* **2015**, *119*, 25307.

[41] N. Frickel, A. G. Greenbaum, M. Gottlieb, A. M. Schmidt, *J. Phys. Chem. C* **2011**, *115*, 10946.

[42] J. Yao, C. Xiong, L. Dong, C. Chen, Y. Lei, L. Chen, R. Li, Q. Zhu, X. Liu, *J. Mater. Chem.* **2009**, *19*, 2817.

[43] D. Mombrú, M. Romero, R. Faccio, Á. W. Mombrú, *J. Appl. Phys.* **2017**, *121*, 045109.

[44] L. C. Mariano, R. V. Salvatierra, C. E. Cava, M. Koehler, A. J. G. Zarbin, L. S. Roman, *J. Phys. Chem. C* **2014**, *118*, 24811.

[45] B. Qiu, J. Guo, Y. Wang, X. Wei, Q. Wang, D. Sun, M. A. Khan, D. P. Young, R. O'Connor, X. Huang, X. Zhang, B. L. Weeks, S. Wei, Z. Guo, *J. Mater. Chem. C* **2015**, *3*, 3989.

[46] Y. Song, Y. Shen, H. Liu, Y. Lin, M. Li, C.-W. Nan, *J. Mater. Chem.* **2012**, *22*, 16491.

[47] X. Huang, L. Xie, K. Yang, C. Wu, P. Jiang, S. Li, S. Wu, K. Tatsumi, T. Tanaka, *IEEE Trans. Dielectr. Electr. Insul.* **2014**, *21*, 480.

[48] J. Luo, Y. Zuo, P. Shen, Z. Yan, K. Zhang, *RSC Adv.* **2017**, *7*, 36433.

[49] D. C. Marcano, D. V. Kosynkin, J. M. Berlin, A. Sinitskii, Z. Sun, A. Slesarev, L. B. Alemany, W. Lu, J. M. Tour, *ACS Nano* **2010**, *4*, 4806.

[50] N. Cao, Y. Zhang, Study of Reduced Graphene Oxide Preparation by Hummers' Method and Related Characterization. *J. Nanomater.* **2015**.

[51] G. Han, Y. Liu, L. Zhang, E. Kan, S. Zhang, J. Tang, W. Tang, *Sci. Rep.* **2014**, *4*, srep04824.

[52] X. Chen, S. Yan, N. Wang, S. Peng, C. Wang, Q. Hong, X. Zhang, S. Dai, *RSC Adv.* **2017**, *7*, 55734.

[53] S. Palsaniya, H. B. Nemade, A. K. Dasmahapatra, *ACS Appl. Polym. Mater.* **2019**, *1*, 647.

[54] R. Kumar, R. M. Kumar, D. Lahiri, I. Lahiri, *Surf. Coat. Technol.* **2017**, *309*, 931.

[55] G. Xu, N. Wang, J. Wei, L. Lv, J. Zhang, Z. Chen, Q. Xu, *Ind. Eng. Chem. Res.* **2012**, *51*, 14390.

[56] X. Yan, Z. Han, Y. Yang, B. Tay, *J. Phys. Chem. C* **2007**, *111*, 4125.

[57] A. C. Ferrari, D. M. Basko, *Nat. Nanotechnol.* **2013**, *8*, 235.

[58] H. Li, Y. He, V. Pavlinek, Q. Cheng, P. Saha, C. Li, *J. Mater. Chem. A* **2015**, *3*, 17165.

[59] N. Hu, Z. Yang, Y. Wang, L. Zhang, Y. Wang, X. Huang, H. Wei, L. Wei, Y. Zhang, *Nanotechnology* **2014**, *25*, 025502.

[60] Z. Yin, H. Zhou, C. Fu, N. Zhang, D. Liu, Y. Kuang, *RSC Adv.* **2016**, *6*, 41142.

[61] A. Phakkhawan, P. Klangtakai, A. Chompoosor, S. Pimanpang, V. Amornkitbamrung, *J. Mater. Sci. Mater. Electron.* **2018**, *29*, 9406.

[62] I. Baltog, M. Baibarac, L. Mihut, N. Preda, T. Velula, C. Bucur, M.-A. Husanu, *Vibrational properties of polyaniline functionalized PbI2*; 2009; Vol. 54.

[63] M. Mitra, C. Kulsi, K. Chatterjee, K. Kargupta, S. Ganguly, D. Banerjee, S. Goswami, *RSC Adv.* **2015**, *5*, 31039.

[64] M. P. Lavin-Lopez, J. L. Valverde, M. C. Cuevas, A. Garrido, L. Sanchez-Silva, P. Martinez, A. Romero-Izquierdo, *Phys. Chem. Chem. Phys.* **2014**, *16*, 2962.

[65] G. S. Gund, D. P. Dubal, N. R. Chodankar, J. Y. Cho, P. Gomez-Romero, C. Park, C. D. Lokhande, *Sci. Rep.* **2015**, *5*, 12454.

[66] D. C. Marcano, D. V. Kosynkin, J. M. Berlin, A. Sinitskii, Z. Sun, A. Slesarev, L. B. Alemany, W. Lu, J. M. Tour, *ACS Nano* **2010**, *4*, 4806.

[67] M. Fathy, A. Gomaa, F. A. Taher, M. M. El-Fass, A. E.-H. B. Kashyout, *J. Mater. Sci.* **2016**, *51*, 5664.

[68] D. Ghosh, S. Bhandari, D. Khastgir, *Phys. Chem. Chem. Phys.* **2016**, *18*, 32876.

[69] H. Wang, Y. Wang, Y. Sun, X. Pan, D. Zhang, Y. F. Tsang, *Process Saf. Environ. Prot.* **2018**, *113*, 40.

[70] N. Wu, X. She, D. Yang, X. Wu, F. Su, Y. Chen, *J. Mater. Chem.* **2012**, *22*, 17254.

[71] R. Vinoth, S. G. Babu, V. Bharti, V. Gupta, M. Navaneethan, S. V. Bhat, C. Muthamizhchelvan, P. C. Ramamurthy, C. Sharma, D. K. Aswal, Y. Hayakawa, B. Neppolian, *Sci. Rep.* **2017**, *7*, 43133.

[72] A. K. Das, M. Srivastav, R. K. Layek, M. E. Uddin, D. Jung, N. H. Kim, J. H. Lee, *J. Mater. Chem. A* **2013**, *2*, 1332.

[73] Y. He, Y. Cai, W. Huang, *ChemistrySelect* **2017**, *2*, 8478.

[74] A. V. Soldatova, C. Butterfield, O. F. Oyerinde, B. M. Tebo, T. G. Spiro, *JBIC J. Biol. Inorg. Chem.* **2012**, *17*, 1151.

[75] W. He, Y. Liu, W. G. Wamer, J.-J. Yin, *J. Food Drug Anal.* **2014**, *22*, 49.

[76] B. H. Kim, S. H. Hong, J. Joo, I.-W. Park, A. J. Epstein, J. W. Kim, H. J. Choi, *J. Appl. Phys.* **2004**, *95*, 2697.

[77] A. Ladhar, M. Arous, H. Kaddami, M. Raihane, A. Kallel, M. P. F. Graça, L. C. Costa, *J. Mol. Liq.* **2015**, *209*, 272.

[78] M. D. Janezic, R. K. Kaiser, J. R. Baker-Jarvis, G. Free, *Tech. Note NIST TN - 1531* **2004**.

[79] L. Sun, S. S. Park, D. Sheberla, M. Dincă, *J. Am. Chem. Soc.* **2016**, *138*, 14772.

[80] N. Guo, S. A. DiBenedetto, P. Tewari, M. T. Lanagan, M. A. Ratner, T. J. Marks, *Chem. Mater.* **2010**, *22*, 1567.

[81] J. Yuan, A. Luna, W. Neri, C. Zakri, T. Schilling, A. Colin, P. Poulin, *Nat. Commun.* **2015**, *6*, 8700.

[82] G. Sarasqueta, K. Roy Choudhury, D. Y. Kim, F. So, *Appl. Phys. Lett.* **2008**, *93*, 123305.

[83] J. Zhu, S. Wei, L. Zhang, Y. Mao, J. Ryu, N. Haldolaarachchige, D. P. Young, Z. Guo, *J. Mater. Chem.* **2011**, *21*, 3952.

[84] W. Fan, B. Kabius, J. M. Hiller, S. Saha, J. A. Carlisle, O. Auciello, R. P. H. Chang, R. Ramesh, *J. Appl. Phys.* **2003**, *94*, 6192.

[85] F. Alam, S. A. Ansari, W. Khan, M. Ehtisham Khan, A. H. Naqvi, *Funct. Mater. Lett.* **2012**, *05*, 1250026.

[86] B. D. Paulsen, C. D. Frisbie, *J. Phys. Chem. C* **2012**, *116*, 3132.

[87] C. Wu, Y. Wang, C. Zhu, *J. Shanghai Univ. Engl. Ed.* **2008**, *12*, 43.

[88] Q. Li, L. Chen, M. R. Gadinski, S. Zhang, G. Zhang, H. U. Li, E. Iagodkine, A. Haque, L.-Q. Chen, T. N. Jackson, Q. Wang, *Nature* **2015**, *523*, 576.

[89] Q. Li, F. Liu, T. Yang, M. R. Gadinski, G. Zhang, L.-Q. Chen, Q. Wang, *Proc. Natl. Acad. Sci.* **2016**, *113*, 9995.

[90] Q. Li, F. Liu, T. Yang, M. R. Gadinski, G. Zhang, L.-Q. Chen, Q. Wang, *Proc. Natl. Acad. Sci.* **2016**, *113*, 9995.

[91] R. Xu, Z. Xu, Y. Feng, X. Wei, J. Tian, D. Huang, *J. Appl. Phys.* **2016**, *119*, 224103.

[92] M. Jouni, A. Buzlukov, M. Bardet, F. Da Cruz-Boisson, A. Eddarir, V. Massardier, G. Boiteux, *Compos. Sci. Technol.* **2014**, *104*, 104.

[93] *Compos. Sci. Technol.* **2014**, *104*, 104.

[94] P. R. Agarwal, R. Kumar, S. Kumari, S. R. Dhakate, *RSC Adv.* **2016**, *6*, 100713.

Chapter-4

Hierarchical Nylon-6/Reduced Graphene Oxide/Polyaniline Nanocomposites with Enhanced Dielectric Properties for Energy Storage Applications

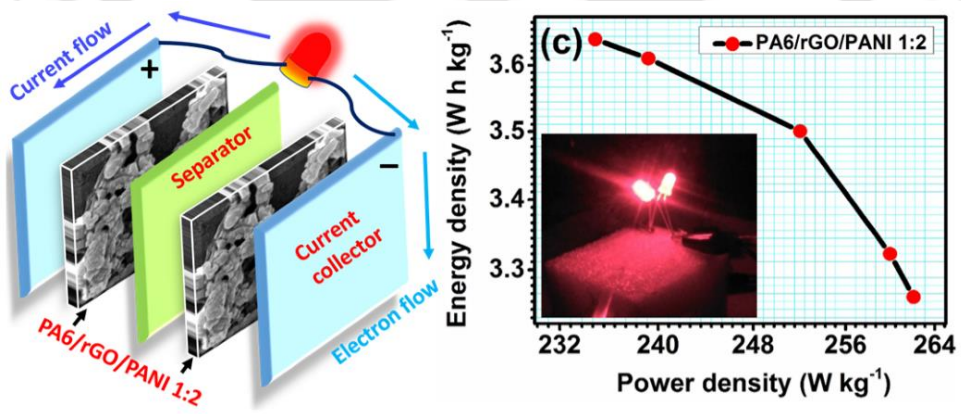

Communicated

4.1. Introduction

A supercapacitor is a high power storage device, which is superior to the conventional energy storage devices, such as batteries due to its outstanding performance with rapid charge-discharge capability, excellent cyclic stability, and remarkable rate capability. Usually, supercapacitors possess low specific energy as compared to conventional batteries, resulting in restricted commercial applications [1–3]. Typically, supercapacitors are classified into two categories – electric double-layer capacitor (EDLC) and pseudocapacitor. EDLC signifies the non-faradaic surface charge interaction over the electrode and electrolyte, whereas, in the pseudocapacitor, the charge allocation is accomplished by following the redox reaction at the electrode surface [3,4]. In recent years, numerous developments have been carried out by introducing advanced technologies employing novel nanostructured materials. Among them, graphene, carbon nanotubes (CNT), carbon nanofibers, 2D transition metal dichalcogenides (TMD) are proven to be promising candidates for energy storage [5–8] applications. Besides, conducting polymers such as polyaniline (PANI) [9,10], polythiophene (PT) [11], and poly (3, 4-ethylene dioxythiophene) (PEDOT) [12] are being employed as electrode materials for energy storage by virtue of their lightweight, high corrosion resistance, and outstanding dielectric strength. Metal-organic frameworks have also been used as energy storage materials due to attractive specific capacitance performance. Some of the recently used materials are MWCNT-functionalized PANI-Au [13], TiO_2/polymer nanohybrids [14], poly (o-toluidine) silver (POT-Ag) [15], SiO_2/poly (3-aminophenyl boronic acid) (PAPBA) [16], CNT/Ag nanoparticle ink [17], and graphene functionalized MnO_2 and MoO_3 nanocomposites [18].

Polyaniline is known to be a p-type semiconductor, with characteristics properties such as tunable electrical conductivity and high thermal stability [19]. PANI was shown to be an excellent candidate for various applications, such as in sensing [20–22], electrochromic devices [23], corrosion resistance [24], fabrication of artificial tissues [25], and electromagnetic interference shielding [26]. To improve the electrochemical property of PANI, GO or RGO can be used as nanofillers. The miscibility of these nanofillers is limited; hence another polymer matrix can be employed to overcome this limitation. Apart from this, PANI is also brittle in nature, difficult to process to make flexible materials.

Recently, numerous nanocomposites based on Nylon-6 (PA6) and PANI have been prepared. PA6 is relatively flexible in nature and contributes to a large surface area. PA6 is extensively used in textile industries by virtue of its easy processing and excellent durability. The combination of PANI and PA6 would facilitate the formation of fibers by electrospinning leading to the fabrication of flexible and wearable electronics. Valiavalappil and Harinipriya

et al. [27] have prepared PANI-Nylon 6,6 nanocomposite with tunable electrical conductivity by controlling PANI composition. Even at a low concentration of PANI, the composite showed a significant electrical conductivity. Bagheri and Aghakhani et al. [28] have prepared a PANI-Nylon 6,6 nanocomposite for the adsorptive microextraction. In this work, the electrospinning technique has been adapted to prepare nano-shaped sorbents with controllable dimensions. Further, Xia and his co-workers [29] have developed a nanocomposite fiber of PANI/PA6 having a specific core-skin type structure to apply in separating dye from wastewater. Lee et al. [30] have reported a nanocomposite of PA6,6/PANI nanofibers as electrode materials for the supercapacitor application. The flexible PA6,6 nanofibers membrane incorporated with PANI has enabled a core-stealth structure, resulting in an improved specific capacitance.

GO and rGO functionalized PA6 and PANI could develop nanocomposites with outstanding properties such as uniform texture [31–33], high thermal conductivity, mechanically robust, and rapid charge transport [34–37]. Graphene incorporated PANI nanocomposites are treated as grafted fillers to construct a uniform PANI matrix, which strongly improves the reinforcement, yielding a high-density energy material. Moreover, graphene-functionalized PA6 nanocomposites also have shown noticeable energy storage. For example, Pan et al. [38] have reported that the nanocomposite of PA6/Graphene showed good electrical conductivity with a superior areal capacitance. PA6/GO nanocomposite showed a tunable morphology with varying concentrations of GO [39]. An optimum amount of GO (125 mg) into 25 g of 22 wt% PA6 solution has produced the highest electrical conductivity and viscosity, which is suitable for a bimodal fibrous mat.

Nanocomposites based on PA6 and PANI have been reported to possess a remarkable conductivity that can be applied in energy storage devices, as PA6 has contributed to improving specific permittivity. Graphene-based fillers (viz., graphene, GO, or rGO) would work as a conductive medium to enhance charge storage efficiency. Herein, we present the successful preparation of ternary nanocomposites of PA6, PANI, and rGO with varying ratios of PA6 and PANI, keeping rGO fixed. The in-situ polymerization of PANI ensures the formation of a well-mixed ternary nanocomposite with adequate porosity to produce high charge accumulation. The fabricated symmetric supercapacitors based on the nanocomposites exhibit high specific power and energy. The excellent energy storage behaviour is attributed to the synergistic effect of all the three components present in the nanocomposite. PA6 behaves as a dielectric material, which can store electrostatic energy efficiently while rGO facilitates easy charge transport. The combination of these three materials provides an efficient material with high energy storage capability.

4.2. Experimental section

4.2.1. Materials

Nylon-6 pellets were purchased from Sigma-Aldrich. Aniline (Emparta, ≥99.0%), formic acid (Emplura, ≥85%), potassium permanganate (Emplura, ≥98.5%), Ortho-phosphoric acid 88% GR, and hydrogen peroxide (Emplura, 48-52%) were purchased from Merck Ltd. Hydrochloric acid (~35-37%) and sulphuric acid (~97%) were purchased from Fisher Scientific. Graphite powder (99.9999%), poly (vinylidene fluoride), carbon black (50% compressed), and acetylene (99.9%) were purchased from Alfa-Aesar. N-Methyl-2-pyrrolidone (~99.5%) and Ammonium peroxydisulphate (99%) were purchased from Sisco Research Laboratories. The DI water for all synthesis processes has been obtained from the Millipore-Q Plus water purifier. All chemicals were of analytical grade and used without further purification.

4.2.2. Synthesis of rGO

Graphene oxide (GO) was prepared by improved Hummer's method [40]. Initially, 200 mg graphite powder and 1200 mg of potassium permanganate (at ~1:6 ratio) were added to a solution of 24 ml of sulphuric acid and 2.67 ml phosphoric acid (at ~9:1 ratio). The resultant solution was stirred (at 500 rpm) for 20 h at 50 ºC, and allowed to cool at room temperature, and 200 mg ice and 5 ml water were added. Further, hydrogen peroxide (30%) was added under stirring to the above mixture until yellow color appeared. The solution was centrifuged at 1300 rpm for 10 minutes, using 10 ml of each HCl (30%), DI water, and ethanol, successively, to remove impurities. The sample (viz., GO) was dried at 95 ºC for 24 h. The reduced graphene oxide (rGO) was prepared using reduction method [41]. The GO dispersion in DI water (1 mg/ml) has been prepared, followed by ultrasonication (0.5 h, 33 kHz). The pH of yellow-brown GO dispersion was adjusted at ~11 by adding ammonia solution under stirring followed by the addition of hydrazine hydrate (1:5 volume ratio of hydrazine hydrate and DI water) at 80 ºC for 24 h. The black precipitate of rGO was successively washed with methanol and DI water and collected after centrifuging at 1500 rpm.

4.2.3. Synthesis of rGO/PANI nanocomposite

The binary nanocomposite of rGO/PANI was synthesized by *in-situ* chemical oxidative polymerization method [42]. First, rGO dispersion was prepared in formic acid (1 mg/ml) under stirring at 500 rpm, 40 ^{o}C for 2 h. Aniline hydrochloride solution (1 g aniline in 10 ml 1M HCl) was poured into 20 ml of rGO dispersion under stirring, keeping the temperature at 0 ºC. A solution of 3 g of ammonium persulfate (APS) in 20 ml of 1 M HCl was added dropwise into

the above mixture. The resultant solution turned into a dark green color from light bluish, indicating the formation of PANI emeraldine salt. The solution was kept at 0 – 4 °C for 48 h to complete the polymerization, and then the precipitate was filtered and washed with DI water and 1 M HCl, successively. Finally, the precipitate was dried in vacuum at 60 °C for 24 h for further use.

4.2.4. Synthesis of PA6/PANI and PA6/rGO/PANI nanocomposites

PA6/PANI binary nanocomposite was synthesized by *in-situ* chemical oxidative polymerization method [43]. First, we prepared two individual dispersions of 1 g PA6 in 20 ml of formic acid under stirring for 2 h at 40 °C, 500 rpm, and 1 g aniline in 10 ml of 1 M HCl. The aniline hydrochloride solution was poured into the above PA6 dispersion at 0 ºC temperature. Further, APS solution (3 g APS in 20 ml of 1 M HCl) was added dropwise into the PA6/Aniline hydrochloride solution to initiate the polymerization of aniline. The resultant solution was kept at 0 – 4 °C for 48 h to complete polymerization. The precipitate was filtered and washed using DI water and 1 M HCl, successively, vacuum dried at 60 °C overnight.

The ternary nanocomposites were synthesized, as shown in Figure 4.1a. We have prepared a solution of 1 g PA6 in 20 ml of formic acid by stirring at 500 rpm on 40 °C for 2 h. The rGO dispersion (1 mg/ml) in formic acid being prepared via sonication, and mixed to the PA6 solution to make a homogeneous mixture. Then, a solution of 2 g aniline in 15 ml of 1 M HCl was prepared and added into the above PA6/rGO dispersion. Further, 6 g of APS was dissolved in 40 ml of 1 M HCl and added dropwise to the above mixture under stirring at 600 rpm by keeping the temperature 0 ºC. The resultant solution was kept at 0 – 4 °C for 48 h to complete the polymerization. The precipitate was filtered and washed with 1 M HCl and DI water, successively. The resultant nanocomposite material of PA6/rGO/PANI at 1:2 ratio was dried in vacuum at 60 °C for 24 h. A similar method was followed to prepare other ternary nanocomposites of PA6/rGO/PANI with 2:1 and 1:1 ratio of PA6:PANI keeping the amount of rGO constant.

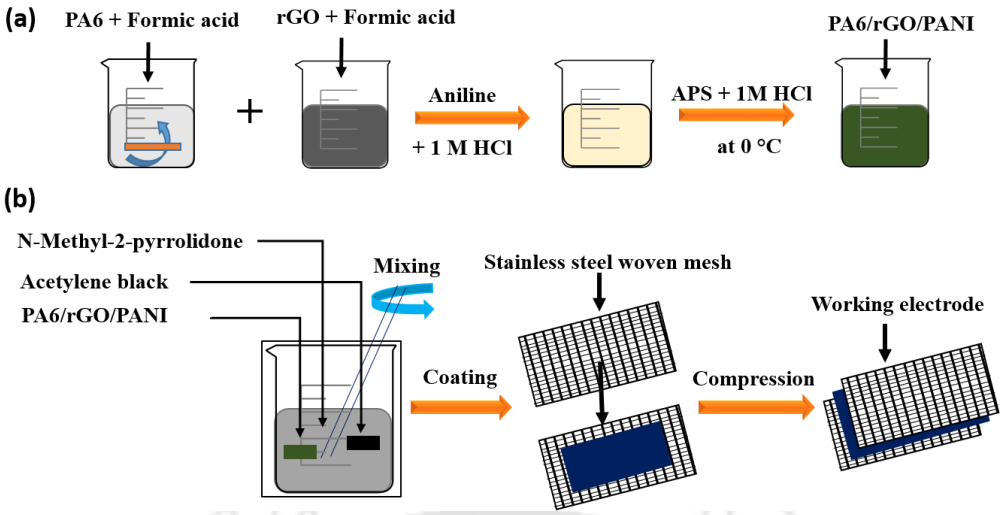

Figure 4.1. (a) Schematic diagram of the synthesis process of PA6/rGO/PANI ternary nanocomposite, and (b) fabrication process of supercapacitors of PA6/rGO/PANI for electrochemical measurements.

4.2.5. Characterization

Micro Raman spectra were recorded using Horiba Jobin Vyon, Model LabRam HR, with an excitation wavelength of 514 nm. The structural patterns were carried out in a rotating anode high power XRD (Rigaku, model TX-III), operated at 50 kV, 180 mA, with radiation of Cu kα, with an angle ranging from 10° to 70°. The crystallographic plane orientations were analyzed using Xpert high score plus software. UV-Visible absorption spectra (Shimadzu, UV-2600 230V EN) were recorded in the range of 200 – 800 nm. Thermal stabilities of the nanocomposites were determined using Netzsch STA449F3A00 at a heating rate of 10 °C min^{-1} in an inert atmosphere by purging argon gas at a rate of 20 ml min^{-1}. The morphology features of the nanocomposites were examined by the field emission scanning electron microscope at 3 kV accelerating voltage (ZEISS, Gemini), and corresponding dimensions of the nanocomposites were evaluated by the ImageJ software. The crystallographic plane and lattice parameters were evaluated by the field emission transmission electron microscope (FETEM) (JEOL, JEM 2100 F at 200 kV acceleration voltage). Surface topography has been analyzed by using AFM (Innova SPM) in the tapping mode at room temperature. BET analyzer (micromeritics TriStar II) was used for the surface area measurement. The electron paramagnetic resonance (JEOL, JES-FA200) analysis was done to investigate the presence of unpaired electrons in the nanocomposites. I–V characteristics were measured using the Keithley semiconductor parameter analyzer (4200 SCS) in a potential range of ±5V at room temperature. Dielectric and A.C. conductivity measurements were carried out

by using Agilent E4991A, Novocontrol BDS2300. The Electrochemical analysis was recorded by using Gamry Reference 600^{+} electrochemical workstation.

4.2.6. Electrochemical measurements of symmetric supercapacitor

The electrochemical measurements of the nanocomposites were analyzed in a three-electrode cell using platinum wire as counter electrode and Ag/AgCl as a reference electrode in an electrolytic solution of 1 M H_2SO_4. The working electrodes (WE) were prepared by mixing the electrode materials in the proportion of 80:15:5, wherein 30 mg of electrode materials was added to 5.8 mg acetylene black, and 2.0 mg polyvinylidene fluoride (PVDF as a binding agent) in a mortar with an adequate amount of N-methyl-2-pyrrolidone (NMP) as the solvent. The mixture was coated over the stainless steel woven mesh (1×1 cm^2), and 20 MPa pressure was applied to obtain a uniform distribution of the electrode materials (Figure 4.1b). The entire electrode assembly was dried in air at 60 °C overnight.

To test the device performance, a symmetric supercapacitor (viz., two-electrode system) has been fabricated using PA6/rGO/PANI 1:2 nanocomposite as the electrode material. The prepared slurry was pasted over aluminium sheets (area: 4×2 cm^2, thickness: 0.5 mm) keeping ~2 mm space between the sheets for the output contacts, and vacuum dried at ~ 60 °C for 2 h. Further, both the electrodes were assembled face to face using Whatman filter paper (soaked in 1 M H_2SO_4 electrolyte for 5 s) as a separator. The device was covered by Kepton tape to provide isolation from the ambient while retaining the desired electrochemical performance. The calculation of specific capacitance (C_s) from the electrochemical measurements has been done using both cyclic voltammetry (CV) and galvanostatic charge-discharge (GCD) methods as given in equation 4.1 and 4.2, respectively.

C_s from CV profile

$$C_s = \frac{\int i\, dv}{m * v * \Delta V} \tag{4.1}$$

C_s from GCD process

$$C_s = \frac{I * \Delta t}{m * \Delta V} \tag{4.2}$$

where, $\int i\, dv$ is the total mathematical area of CV curve, ν is the scan rate (mV s^{-1}), I is the discharging current (A), Δt (s) is the discharging time, ΔV is the potential difference (V), m is mass of the electrode materials (g), and C_s is the specific capacitance (F g^{-1}). The above C_s is further used to estimate the specific energy (ED) and specific power (PD) based on the following equations [44].

$$ED=\frac{1}{2*3.6}*C_s*\Delta V^2 \ (Wh\ kg^{-1}) \quad (4.3)$$

$$PD=\frac{E}{t}*3600\ (W\ kg^{-1}) \quad (4.4)$$

4.3. Results and discussions

4.3.1. Structure and morphology

Raman scattering was used to investigate the structural properties and corresponding band vibrations of all the nanocomposites, as shown in Figure 4.2a. The spectrum displays two prominent peaks: D band (I_D) at 1350 cm^{-1} corresponds to the sp^3 defects in the graphitic layers, and the G band (I_G) at 1580 cm^{-1} corresponds to the vibrations of sp^2 hybridized carbon atoms. The intensity ratio, I_D/I_G, suggests a change in the average size of the sp^2 domains.

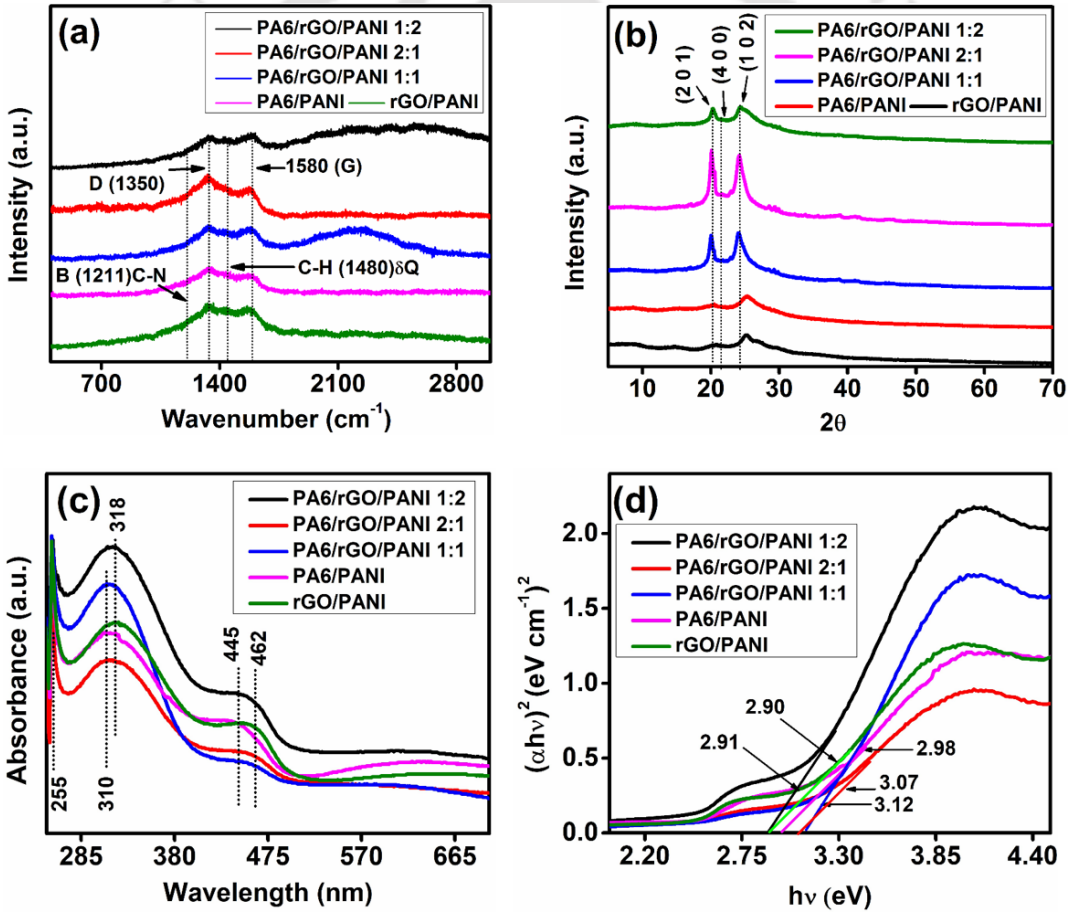

Figure 4.2. Structural analysis by (a) Raman spectra, (b) XRD patterns, (c) UV visible absorbance spectra, and (d) optical band gap energies.

The enhanced value of I_D/I_G ratio of RGO ascertains the presence of a significant amount of structural defects. This ratio also indicates the functionalization of RGO with PA6 and anilinium ions of PANI, resulting in an increased π–π conjugation. This enhanced π–π interaction is believed to facilitate charge transfer between RGO and PANI, and thus influence the charge transport properties of the composites. The peaks at 1161, 1211, and 1480 cm^{-1} are due to C-H stretching vibration of the quinonoid units, C-N stretching vibration of the benzenoid ring, and the semi-quinonoid cationic structure of PANI, respectively [45,46].

Figure 4.2b shows the XRD spectra of all the nanocomposites. The characteristic peak at 20º (2 0 1) corresponds to PANI chains oriented to the characteristic plane. The variations in the intensity of the corresponding peaks suggest the continuous parallel and perpendicular arrangement of the PANI chains. The peak at ~25º (1 0 2) suggests the presence of a significant amount of RGO in the nanocomposites. The XRD peaks for PA6 appear at around 20º and 23º [47], which slightly overlap with the peaks of PANI and RGO. The absence of a distinct peak of PA6 signifies the formation of a well-mixed nanocomposite. We have observed a significant decrease in the crystalline structure of the ternary nanocomposites with a decreasing amount of PA6 (viz., PA6:PANI). This reduction in crystalline structures may be attributed to a randomly oriented planar structure with reduced particle size and high surface area. Moreover, a broad XRD pattern of 1:2 nanocomposite represents a highly porous structure (viz., less crystalline), which would facilitate excellent ionic diffusion leading to significant potential of energy storage (viz., supercapacitors) [10,48].

Figure 4.2c shows strong absorption spectra in the wavelength range of 285 –350 nm. The absorption of PA6/rGO/PANI 1:2 nanocomposite is stronger than the other nanocomposites. The higher absorption signifies a greater electronic activity that would enhance electrochemical performance. The absorbance range ~ 255 nm revealed the presence of cationic anilinium ions. The ternary nanocomposite with a higher amount of PANI (viz., PA6:PANI = 1:2) exhibits a redshift of ~ 8 nm (absorption at ~ 310 to 318 nm), which may be due to the presence of hydrogen bonding between PA6 and PANI matrix [49]. The absorption range ~285–350 nm is attributed to π–π* electron transition of PANI backbone and a weak absorption range ~ 445–462 nm corresponds to polaron–π* transition driven by protonation [50]. The optical bandgap energy calculated from the Tauc plot (Figure 4.2d) shows bandgap ~ 3 eV. The wide bandgap of nanocomposites allows high threshold voltage with efficient charge transport in developing smaller, faster, and efficient electronic devices [51].

Surface morphologies of all the nanocomposites were quantified via FESEM, FETEM, and AFM images. The FESEM micrograph of PA6/rGO/PANI 1:2 (Figure 4.3a) reveals a homogeneous distribution of all the components throughout the matrix. The growth of PANI chains (average length ~ 237 nm and average diameter ~ 67 nm) is clearly visible over the PA6 and rGO surfaces. It can be estimated that PANI and PA6 chain segments successfully functionalize rGO; thus, facilitating in producing an amorphous structure. The FETEM micrograph (Figure 4.3b) exhibits a symmetric distribution of the "flower shape" morphology of PA6/rGO/PANI 1:2 nanocomposite. This structure depicts the PANI nanorods evenly distributed over the rGO and PA6 surfaces, resembling a core-sheath structure [30], and constitute a complex porous morphology, which would be suitable for supercapacitor applications. The extensive functionalization between PANI and PA6 during polymerization of PANI is manifested by the presence of H-bonding and π–π* stacking interactions. The HRTEM image (Figure 4.3c) of PA6/rGO/PANI 1:2 exhibits a polycrystalline structure with a lattice constant of 0.208 nm, as supported by SAED pattern (inset of Figure 4.3c). An elemental mapping based on the FETEM image (Figure 4.3d – i) reveals a uniform distribution of the relevant elements (viz., C, Cl, O, N, and S) throughout the polymer matrix.

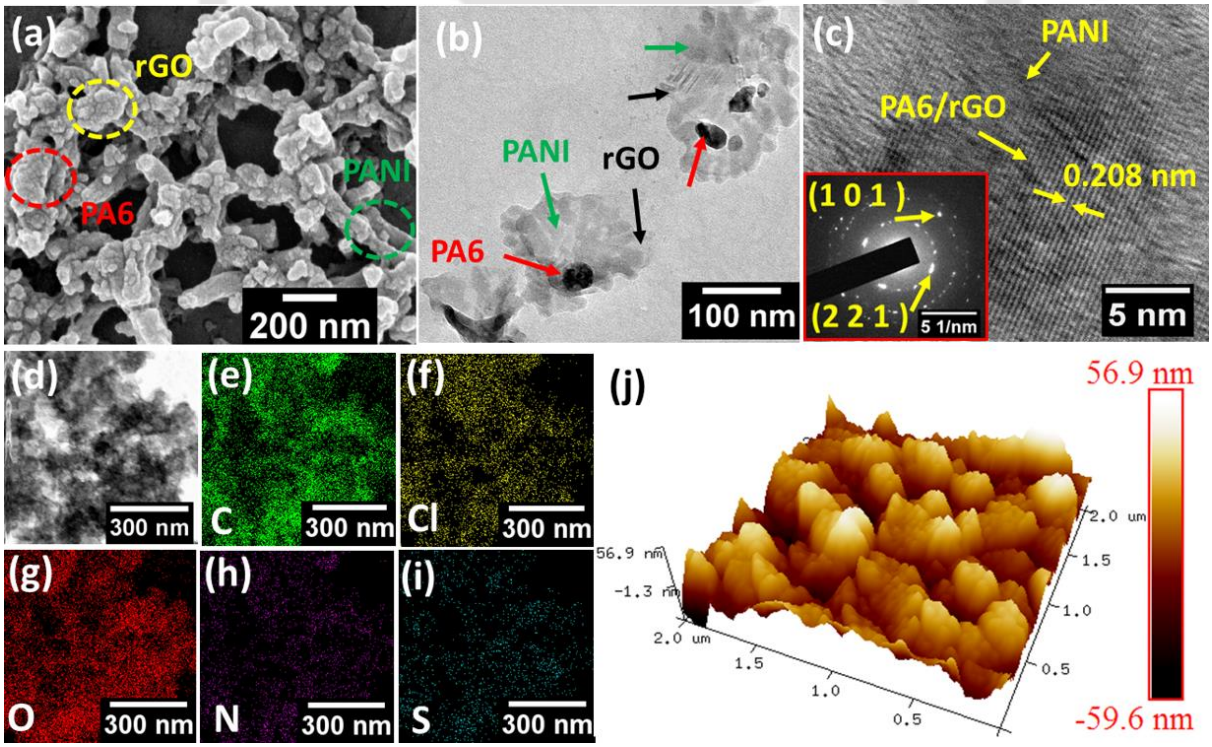

Figure 4.3. Electron microscopic images of PA6/rGO/PANI 1:2 nanocomposite: (a) FESEM image (b) FETEM image, (c) HRTEM image and inset of SAED patterns, (d-i) elemental mapping, and (j) AFM image.

The surface topography analysis by AFM scanning (Figure 4.3j) shows that the surface is reasonably rough. The roughness of the surface can well be corroborated with the porous structure, as revealed by FESEM results (Figure 4.3a).

The morphological analysis of all the other composites (viz., PA6/rGO/PANI 2:1, PA6/rGO/PANI 1:1, PA6/PANI, and rGO/PANI) are presented in Figure 4.4 – 4.7. The average dimension shows a decreasing trend with increasing the proportion of PA6 in the ternary nanocomposite (Figure 4.4 – 4.6). Increased PA6 restricts the agglomeration and growth of PANI chains. The roughness and surface area measurement of all the nanocomposites from AFM analysis is presented in Table 4.1.

Table 4.1. Topographic analysis of AFM images in terms of root mean square average roughness and relative surface area of the nanocomposites.

Sample Name	Roughness (R_q) nm)	Relative surface area (μm^2)
PA6/rGO/PANI 1:2	16.2	4.30
PA6/rGO/PANI 2:1	26.1	4.03
PA6/rGO/PANI 1:1	5.48	3.97
PA6/rGO	27	4.33
rGO/PANI	15.8	4.42

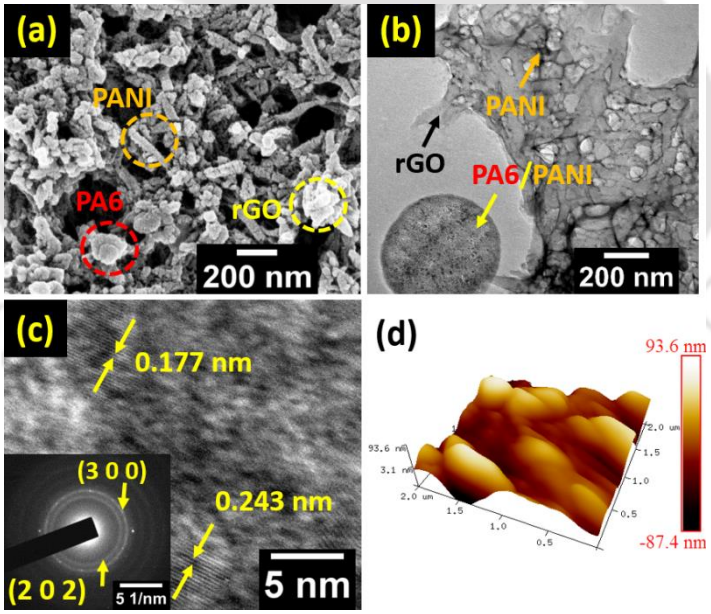

Figure 4.4. Micrographs of PA6/rGO/PANI 2:1 nanocomposite: (a) FESEM image shows an even distribution of the components (viz., rGO, PA6, and PANI) present in the nanocomposite. The average dimension of the rod shape geometry appears to be ~ 181 nm in length and ~ 65 nm in diameter. (b) FETEM image: the dark region indicates the presence of PA6/PANI combination, and the semi-dark region indicates rGO sheets. (c) HRTEM, and inset is SAED pattern that shows a polycrystalline phase. (d) AFM image shows a rational rough surface.

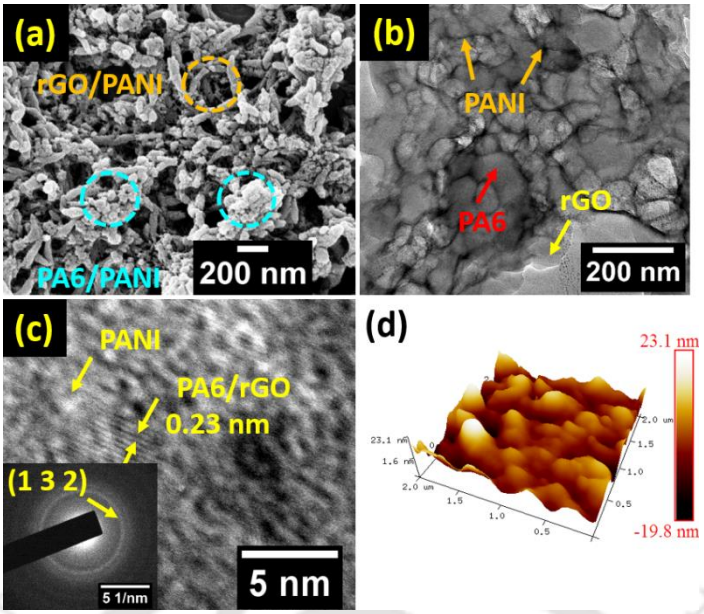

Figure 4.5. Micrographs of PA6/rGO/PANI 1:1 nanocomposite: (a) FESEM shows an agglomerated surface associated to PA6 segments with a rod shape geometry of PANI. The average dimension is: ~ 203 nm (length) and ~ 47 nm (diameter). (b) FETEM image shows the homogeneous distribution of curly fiber shape of the components, (c) HRTEM with a lattice spacing of 0.23 nm, and inset SAED patterns show polycrystalline domains. (d) The AFM image corresponds to the lowest roughness and relative surface area.

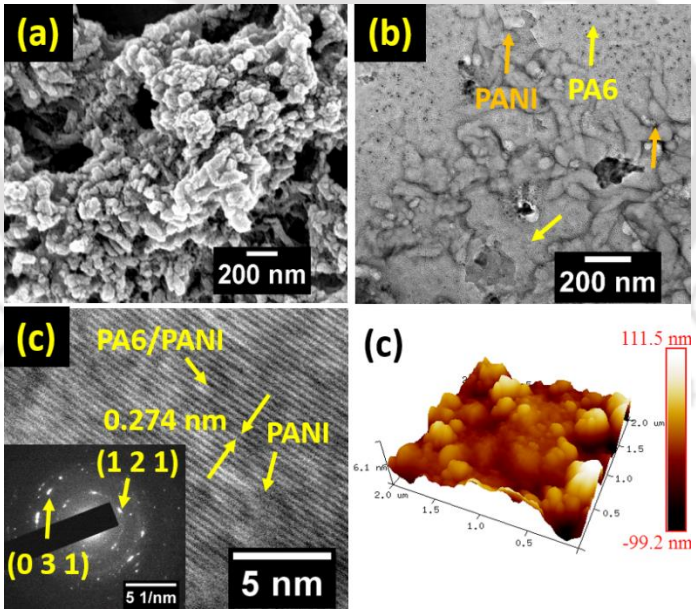

Figure 4.6. Electron microscopic images of PA6/PANI nanocomposite: (a) FESEM shows an agglomerated structure of the PANI matrix. The average diameter is ~ 138.8 nm of the nanoparticles, (b) FETEM shows the presence of individual components, (c) HRTEM image shows a lattice spacing of 0.274 nm, and inset SAED patterns convey a polycrystalline structure of the composite. (d) AFM image associated with the highest roughness and relative surface area, which clarify the incorporation of PA6.

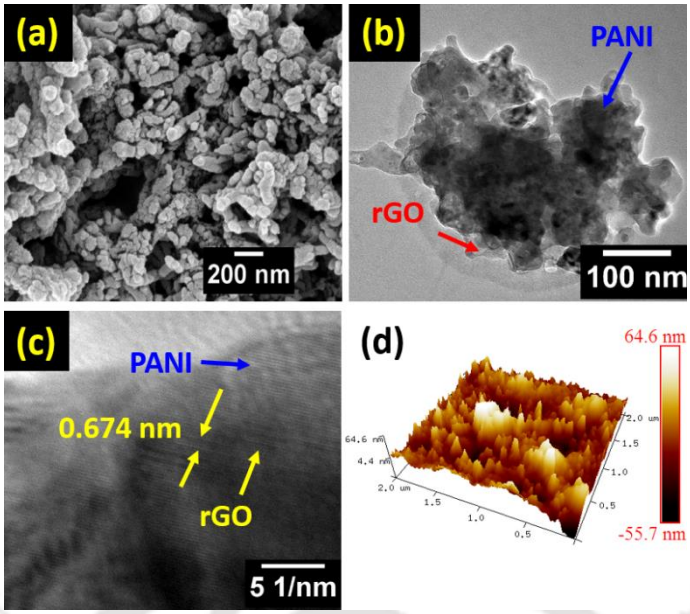

Figure 4.7. Electron microscopic images of rGO/PANI nanocomposite: (a) FESEM image shows a well-dispersed morphology of the PANI matrix with average length ~ 203 nm, and diameter ~ 67.5 nm. (b) FETEM image constitutes a close pack structure of each component. (c) HRTEM with a lattice spacing of 0.674 nm linked to the polycrystalline phase. (d) The AFM image reveals a slightly rough surface.

The average dimensions of PA6/rGO/PANI 2:1 are - length ~ 181 nm and diameter~ 65 nm, while PA6/rGO/PANI 1:1 nanocomposite shows an average length and diameter of ~ 203 and ~ 47 nm, respectively. The high dielectric property of PA6 would enhance the charge storage proficiency, and the presence of PANI/RGO would facilitate an easy charge transport; thus, the ternary nanocomposite would be an excellent material for energy storage applications.

To get an estimate on the surface area and pore size distribution, we have carried out Brunauer–Emmett–Teller (BET) measurements of all the nanocomposites. The trend of the isotherms shown in Figure 4.8a indicates a type IV adsorption. Among all the nanocomposites, the 1:2 exhibits the maximum surface area and pores volume (Table 4.2). The increasing amount of PA6 (viz., a higher ratio of PA6:PANI) produces low surface area due to an increasing order of crystalline behaviors, as has been confirmed by XRD patterns (Figure 4.2b). Thus, the surface area of PA6/rGO/PANI 2:1 is relatively lower compared to 1:1 nanocomposite. Therefore, it can be inferred that PA6 and PANI form an intercalated structure mediated by rGO nanoflakes, resulting in the formation of a compact surface structure. In comparison to the ternary nanocomposites, PA6/PANI and rGO/PANI binary nanocomposites show a relatively lower surface area.

Table 4.2. The BET surface area, average particle size, BJH pore size, and pore volume distributions of the nanocomposites.

Nanocomposites	BET surface area ($m^2 g^{-1}$)	Average particle size (nm)	BJH adsorption avg. pore diameter (nm)	BJH adsorption pores volume ($cm^3 g^{-1}$)
PA6/rGO/PANI 1:2	25.958	231.136	4.536	0.02280
PA6/rGO/PANI 2:1	13.965	429.645	6.138	0.01627
PA6/rGO/PANI 1:1	15.771	380.428	6.036	0.01946
PA6/PANI	10.490	571.973	5.092	0.00603
rGO/PANI	5.825	1029.901	5.274	0.01556

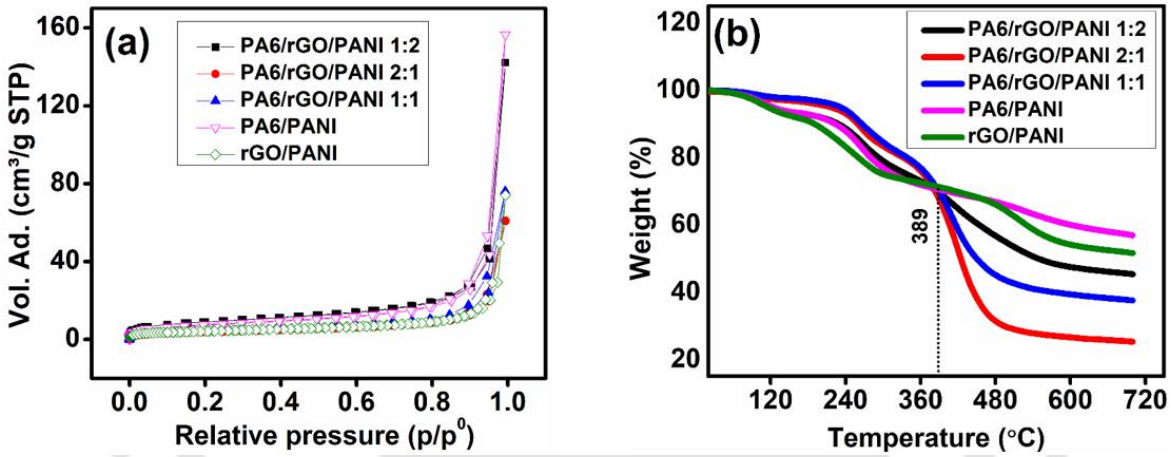

Figure 4.8. (a) N_2 adsorption-desorption isotherms, and (b) thermal stability of all the nanocomposites.

However, PA6/PANI shows marginally higher surface area than rGO/PANI, which can be correlated to the excellent surface adhesion between PA6 and PANI fragments.

4.3.2. Thermal stability

Thermal behavior of the nanocomposites being investigated using thermogravimetric analysis (TGA) as shown in Figure 4.8b. We observe that 1:2 nanocomposite is thermally more stable with ~ 45% residue compared to 2:1 and 1:1 with ~ ~25% and ~38% residues, respectively, at ~ 389 ºC temperature. The binary composites PA6/PANI and rGO/PANI show slightly higher thermal stability even after ~389 ºC with ~56% and ~51% residues, respectively, that may be associated with the good functionality between the components. Differential thermogravimetric analysis (DTA) suggests that among all the ternary nanocomposites, 1:2 exhibits the lowest degradation rate even at high temperatures (Figure 4.9). The significantly high thermal stability of PA6/rGO/PANI 1:2 may be attributed to the synergistic effect between the components at the given composition.

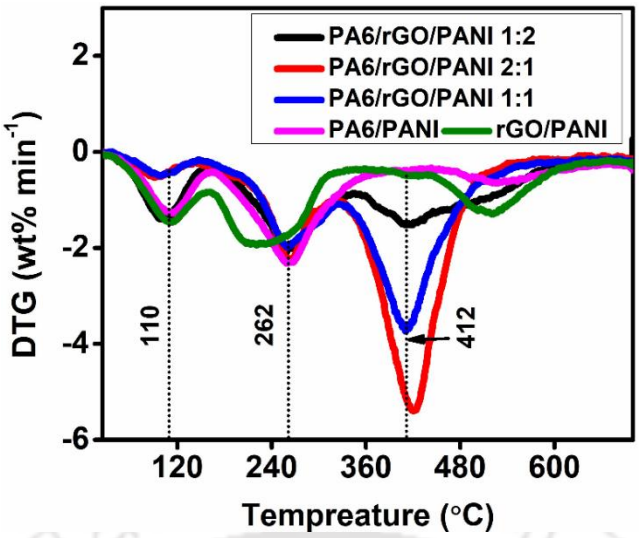

Figure 4.9. Differential thermogravimetric analysis of the nanocomposites.

4.3.3. Electron paramagnetic resonance (EPR) analysis

Typically, conducting polymers possess significant numbers of mobile radicals, and their mobility can be tuned by incorporating suitable nanofillers, such as graphene, GO, rGO, and conjugated polymers with compatible functional groups. Herein, rGO and PA6 functionalize with PANI to enhance the mobility of the available free charge carriers being determined using EPR spectroscopy at a frequency of ~ 9.4 GHz (Figure 4.10a).

The peak-to-peak line width (ΔH_{pp}) is inversely related to the charge mobility – lower the value, higher is the charge mobility. We have observed that the ternary nanocomposite, PA6/rGO/PANI 1:2 exhibits the lowest value of ΔH_{pp}, signifying enhanced charge mobility. The spin quantum numbers ($S=\frac{1}{2}$) of an electron is related with two magnetic components $\left(m_s=\pm\frac{1}{2}\right)$. When a magnetic field is applied, the unpaired electrons orient towards parallel and perpendicular directions, representing low and high energy states, respectively. Accordingly, the absorbed energy is also split into lower and higher The transition energy (hν) required can be formulated by the following equation [52].

$$\Delta E = h\nu = g_e \mu_B B \qquad (4.5)$$

Here, g_e is the Lande's factor, μ_B is the Bohr magnetron, and B is the magnetic field strength. The ΔE magnitudes of the nanocomposites have been exhibited in the Table 4.3. We predicted that the existence of free radicals is directly proportional to the EPR signals. The g-factor of all the nanocomposites is close to 2.0, suggesting the presence of unpaired electrons [53].

Table 4.3. The analyzed parameters of EPR signals.

Nanocomposites	g_e-factor	Asymmetric factor (A/B)	ΔH_{pp} (mT)	ΔE (J)
PA6/rGO/PANI 1:2	2.0122	1.8201	1.82	8.4744×10^{-4}
PA6/rGO/PANI 2:1	2.0132	1.1709	2.86	8.4745×10^{-4}
PA6/rGO/PANI 1:1	2.0054	5.3513	3.02	8.4747×10^{-4}
PA6/PANI	2.0047	8.5386	3.66	8.4742×10^{-4}
rGO/PANI	2.0122	1.5259	3.13	8.4741×10^{-4}

The EPR signals do not exhibit a hyperfine splitting, indicating the existence of close binding of π–electrons facilitated by PANI grafted nanofillers (viz., rGO and PA6), and show a sharp resonance of the hyperfine signals. The sharpness of EPR spectrum is an indication of the presence of an ordered texture of the nanocomposites. As a result, positive charge carriers on PANI fragments are readily paired with negative charges over rGO surface [54]. The asymmetric factor, the ratio of maximum and minimum intensities of EPR signals, indicates heavily doped PANI nanocomposites with improved charge carriers. Among all the nanocomposites, PA6/rGO/PANI 1:2 exhibits a greater amount of unpaired electrons by supplementary interaction between π–electron cloud of rGO and polyamide groups of PANI, which would support to enhance electrical conductivity.

4.3.4. I-V characteristics

The current-voltage (I-V) characteristics of all the nanocomposites are shown in Figure 4.10b with an inset for a schematic representation of the measurement system. We observe that the PA6/rGO/PANI 1:2 displays nonlinear behaviour with a maximum response beyond ± 2 V.

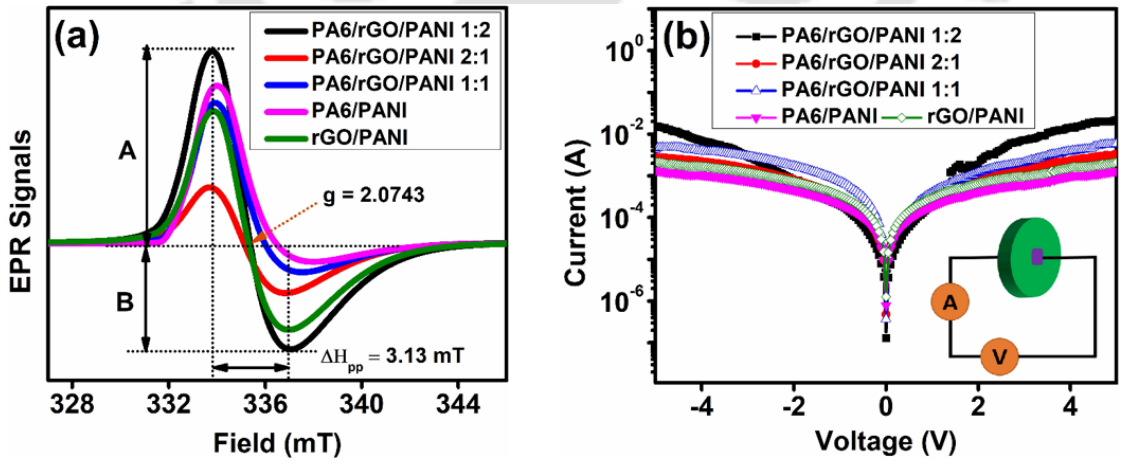

Figure 4.10. (a) Electron paramagnetic resonance spectra, and (b) I-V characteristics of all the nanocomposites.

This curve shows an exponential trend in the lower voltage region (< 2 V) that can be associated with the Schottky barrier. The increased current in the higher voltage range can be attributed to the semiconducting nature of delocalized electrons. The I-V characteristics approaches origin indicating semiconducting trend of the nanocomposites. The PA6/rGO/PANI 2:1 (higher proportion of PA6) has resulted in an additional decrease in electrical conductivity. Beyond a certain amount, PA6 acts as a charge barrier in the nanocomposites. However, PA6/PANI shows less current response than rGO/PANI, while PA6/rGO/PANI 1:2 exhibit higher current activity. PANI chains are conjugated with PA6 segments and construct a homogeneous polymer matrix. PANI has contributed sufficient electronic charges due to π–conjugate ions, which are transported through rGO functionalized polymer matrix, improving the overall charge transport properties of the nanocomposites [29]. The calculated DC electrical conductivities (σ_{dc} in S/cm) of PA6/rGO/PANI 1:2, PA6/rGO/PANI 1:1, PA6/rGO/PANI 2:1, rGO/PANI and PA6/PANI are 5.57×10^{-4}, 4.474×10^{-4}, 3.718×10^{-4}, 9.621×10^{-5} and 1.333×10^{-9}, respectively.

4.3.5. Dielectric and electrostatic properties

The dielectric permittivity (ε′) and dielectric loss (ε″) as a function of the applied frequency for all the nanocomposites are plotted in Figure 4.11a and b, respectively. All the nanocomposites exhibit a reasonable dielectric property against frequency. At low frequency, the PA6/rGO/PANI 1:2 nanocomposite shows the maximum permittivity (ε′) (Figure 4.11a) compared to others, which may be attributed to the presence of larger surface area (Table 4.2). A gradual decrease of ε′ of 1:2 nanocomposite reflects the dielectric relaxation, ascribed to high π–π* electronic transition leading to an enhanced electrical conductivity. Higher the ε′ would exhibit significantly high charge polarization against electric field [55]. This distinct polarization behaviour of 1:2 nanocomposite would facilitate in exhibiting rapid charge-discharge behaviour; thus, it would be suitable in energy storage devices. Except for the 1:2 nanocomposite, all other materials have shown almost a static response of ε′, which is typically a relaxation step related to a slower reduction in polarization due to low dipolar polarization, as have been reported by Prateek et al. [56]. The dielectric losses (ε″) follows almost a similar trend (Figure 4.11b) to that of ε′. The gradual decrease of ε″ with frequency in 1:2 nanocomposite is an indication of higher electrical conductivity (Figure 4.10b) [57] owing to the disruption of charge localization, and phase separation of rGO/PA6-mediated grain boundaries into the PANI matrix [53].

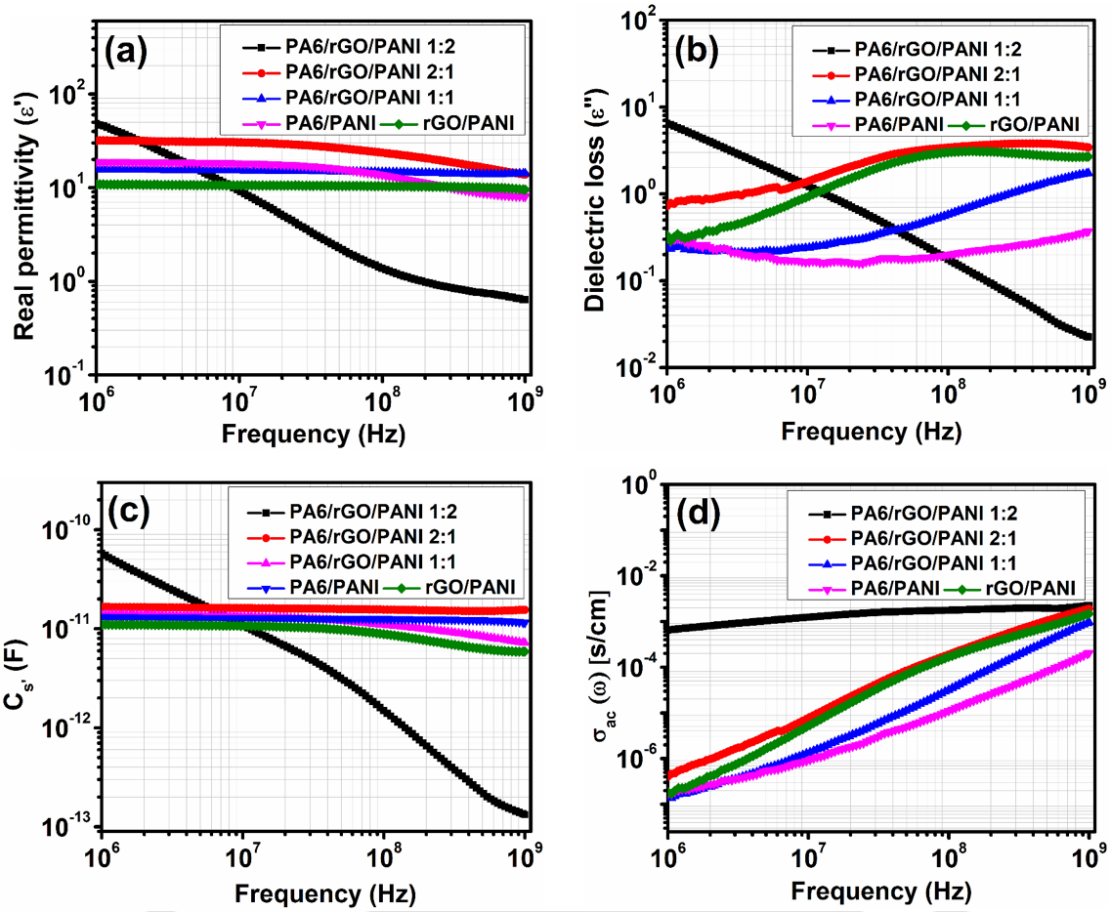

Figure 4.11. Dielectric and electrical properties against frequency of the nanocomposites (a) dielectric permittivity, (b) dielectric loss, (c) capacitance, and (d) A.C. conductivity.

In the 1:2 sample, sufficient surface area facilitates charge agglomeration (Figure 4.3a), resulting in a higher capacitance (Figure 4.11c). The A.C. conductivity ($\sigma_{ac}(\omega)$, Figure 4.11d) shows a monotonically increasing trend with frequency for all the nanocomposites except 1:2, which shows almost a steady value over the entire frequency range, and the value is the highest among all the nanocomposites. The significantly high value of $\sigma_{ac}(\omega)$ indicates that the material would be extremely useful in the energy storage device with acceptable charge-discharge behaviour.

4.3.6. Electrochemical analysis

Cyclic Voltammogram (CV) performances of all the nanocomposites have been recorded at varying scan rates of 10 to 100 mV s^{-1} in the 0−1 V potential range in a three-electrode cell using 1 M H_2SO_4 as the electrolytic medium (Figure 4.12a). The CV responses are in a symmetrical shape, which can be attributed to the pseudocapacitance leading by the availability of significant charge carriers.

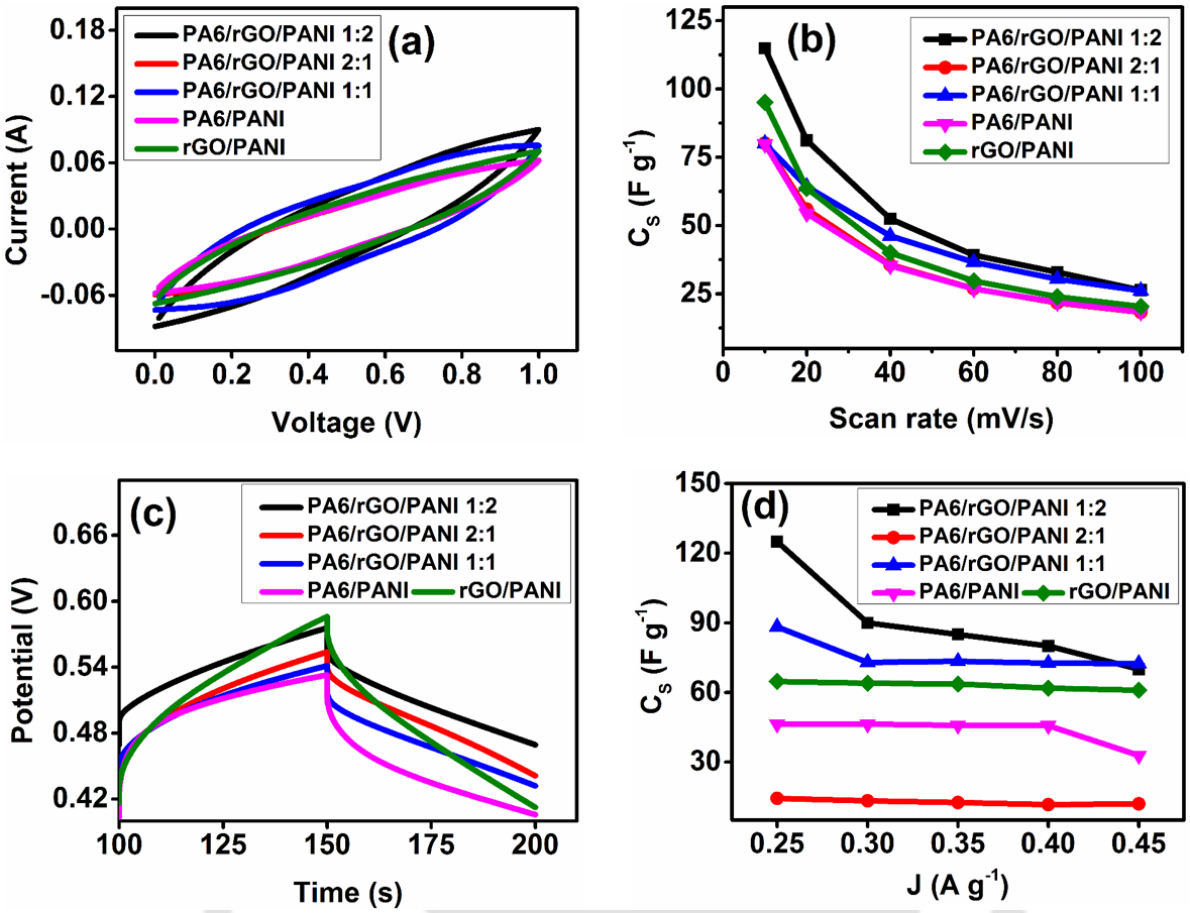

Figure 4.12. Three electrode system of (a) CV profiles at the scan rate of 40 mV s^{-1}, (b) specific capacitance at various scan rates, (c) galvanostatic charge-discharge curves at the current density of 0.25 A g^{-1}, and (d) specific capacitance at the various current densities of the nanocomposites.

A steady increase in current against potential shows diffusion of ionic charge carriers. The width of CV profiles being increased along with scan rates, which is a good indication of the supercapacitive response. The specific capacitances (C_s) have been evaluated from the CV responses using equation 1 (section 2.6) [58]. The PA6/rGO/PANI 1:2 shows the maximum width of the CV graph, results in a higher C_s (~ 115 F g^{-1}) as compared to other nanocomposites. The overall response in terms of C_s with scan rates is shown in Figure 4.12b. Increasing the scan rate giving rise to lower C_s due to reduced ionic diffusion. The galvanostatic charge-discharge (GCD) performance of all the nanocomposites is analyzed at a current density of 0.25 A g^{-1}, as shown in Figure 4.12c. The charge-discharge curves are almost symmetrical and non-linear, revealing the presence of electrical double-layer capacitance and quasi pseudocapacitance behaviours [59]. Among all the nanocomposites, 1:2 shows the slowest discharging rate, suggesting a better candidate for energy storage application. We have calculated C_s from the GCD curves for all the nanocomposites, by applying equation 4.2

(section 2.6). The trend of C_s with current density (Figure 4.12d) shows that the nanocomposites possess a good rate capability. The 1:2 nanocomposite shows the highest C_s almost over the entire range of current density. At 0.25 A g^{-1}, the related C_s of PA6/rGO/PANI 1:2, PA6/rGO/PANI 1:1, rGO/PANI, PA6/PANI, and PA6/rGO/PANI 2:1 is ~ 125, ~ 85, ~ 65, ~ 47, and ~ 15 F g^{-1}, respectively. The CV profiles of the nanocomposites at different scan rates (10-100 mV s^{-1}) in the potential window of 0 − 1 V are shown in Figure 4.13a – e. It is noteworthy that PA6/rGO/PANI 1:2 shows the maximum current in the given potential range, revealing higher electrochemical activity. We have estimated C_s of all the nanocomposites at a fixed scan rate of 40 mV s^{-1} (Figure 4.13f), which shows that PA6/rGO/PANI 1:2 possesses maximum C_s of 52.44 F g^{-1}. In general, a higher proportion of PA6 retards ionic mobility due to the increase in diffusion length. Therefore, the proportion of PA6 in the PA6:PANI higher than 1:1 shows a reduction in overall C_s of the electrode materials. In contrast, a smaller amount of PA6 would improve the C_s; hence PA6/rGO/PANI 1:2 exhibits the higher value of the C_s. Figure 4.14 presents GCD measurements of all the nanocomposites at various current densities (0.25 to 0.45 A g^{-1}), and the inset shows their equivalent series resistance (ESR). The ESR of PA6/rGO/PANI 1:2, PA6/rGO/PANI 2:1, PA6/rGO/PANI 1:1, PA6/PANI, and rGO/PANI is found to be 0.11, 0.12, 0.05, 0.078, and 0.07 Ω, respectively. Conclusively, the electrode materials exhibit a long lifespan with rapid charge transport via redox reactions over the electrode and electrolyte interface.

Electrochemical impedance spectroscopy (EIS) measurements have been performed to investigate the kinetic response of the ionic diffusion for charge storage features of all the nanocomposites. The Nyquist plots (Figure 4.15a) show a semicircle region, attributed to high faradaic resistance of nanocomposites in the electrolytic solution [60]. These plots in the high and low-frequency regions show solution resistance (R_s) and ESR, respectively. Herein, ESR is supported by the ionic and electronic resistances. The slope of the straight line of EIS spectra determines the diffusion rate of ionic molecules up to a finite level, termed as Warburg impedance (W). The charge transfer resistance (R_{ct}) corresponds to the diameter of a semicircle and reveals ionic contribution. The distribution of C_s with respect to frequency can be understood in the form of the constant phase element (CPE), which is defined as: $Z_{CPE}=\frac{1}{(Q(j\omega))^n}$, where, Q (μF/$cm^2$) is ascribed surface activity at the electrode-electrolyte interface, j is an imaginary operator, ω is the frequency, and 'n' is a correction factor that can be calculated by linear fitting of impedance–frequency response [58,59].

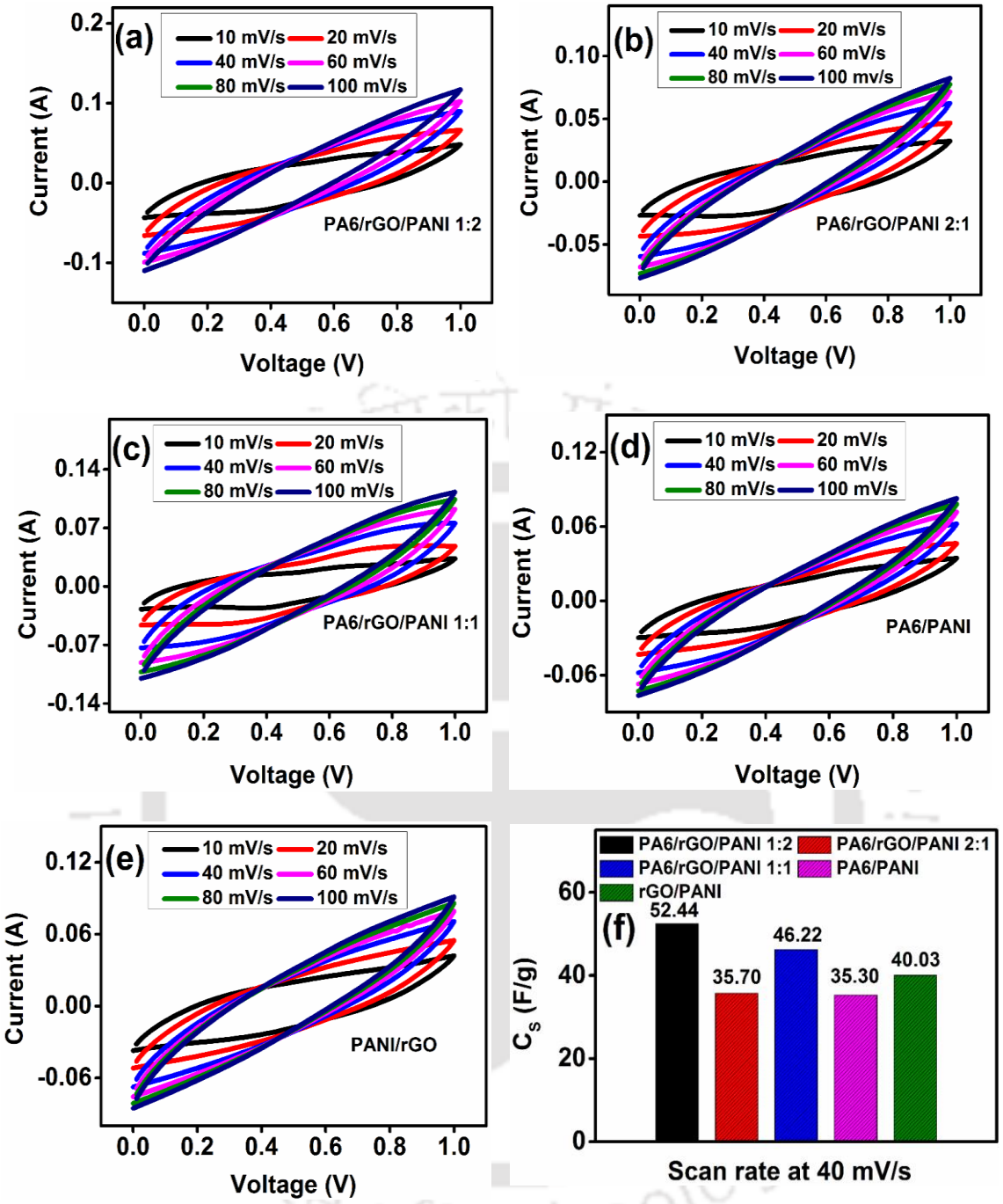

Figure 4.13. CV profiles at various scan rates of (a) PA6/rGO/PANI 1:2, (b) PA6/rGO/PANI 2:1, (c) PA6/rGO/PANI 1:1, (d) PA6/PANI, (e) rGO/PANI, and (f) representing C_s at the fix scan rate of 40 mV s^{-1}.

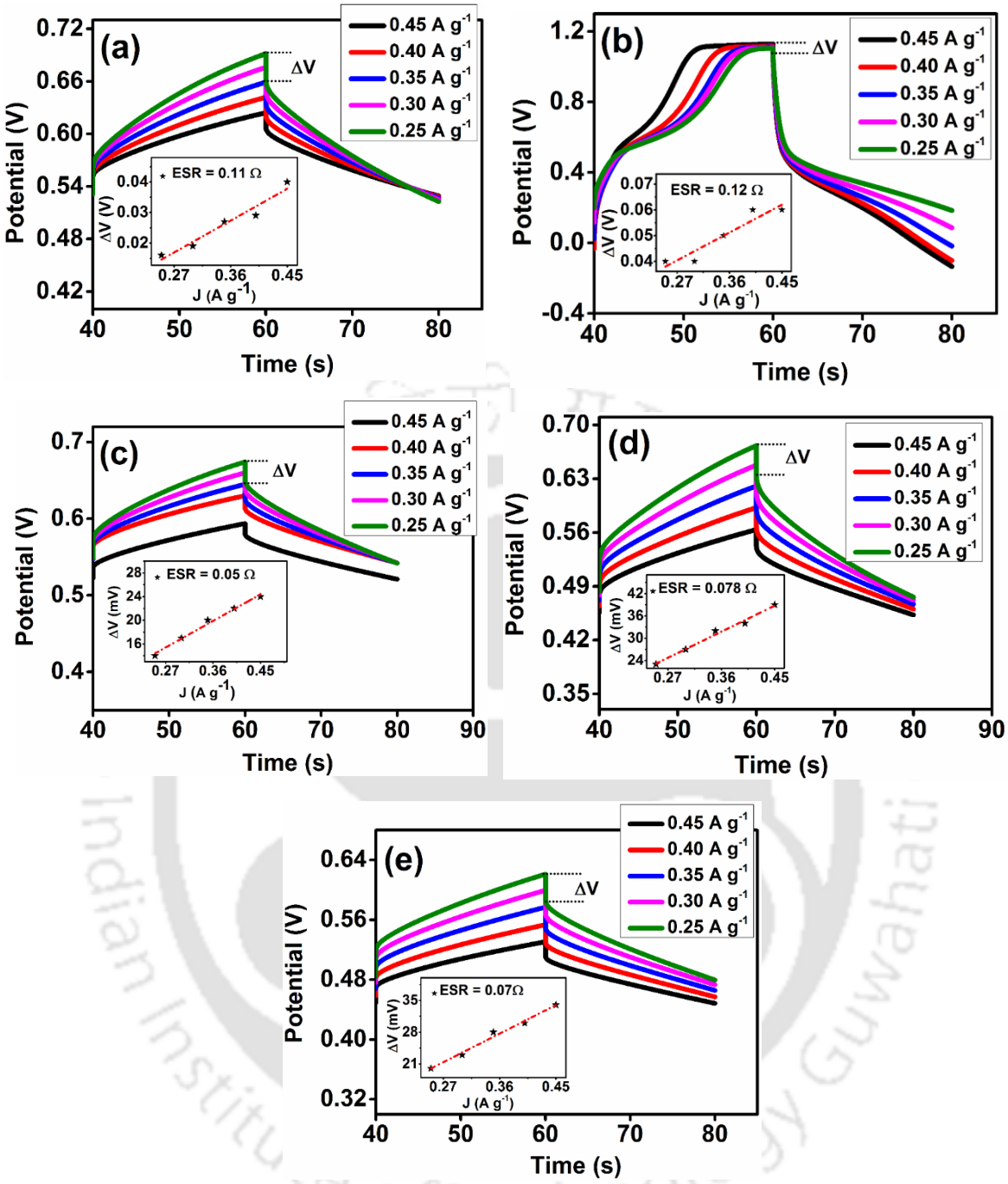

Figure 4.14. Galvanostatic charge-discharge process of (a) PA6/rGO/PANI 1:2, (b) PA6/rGO/PANI 2:1, (c) PA6/rGO/PANI 1:1, (d) PA6/PANI, and (e) rGO/PANI at the various current densities.

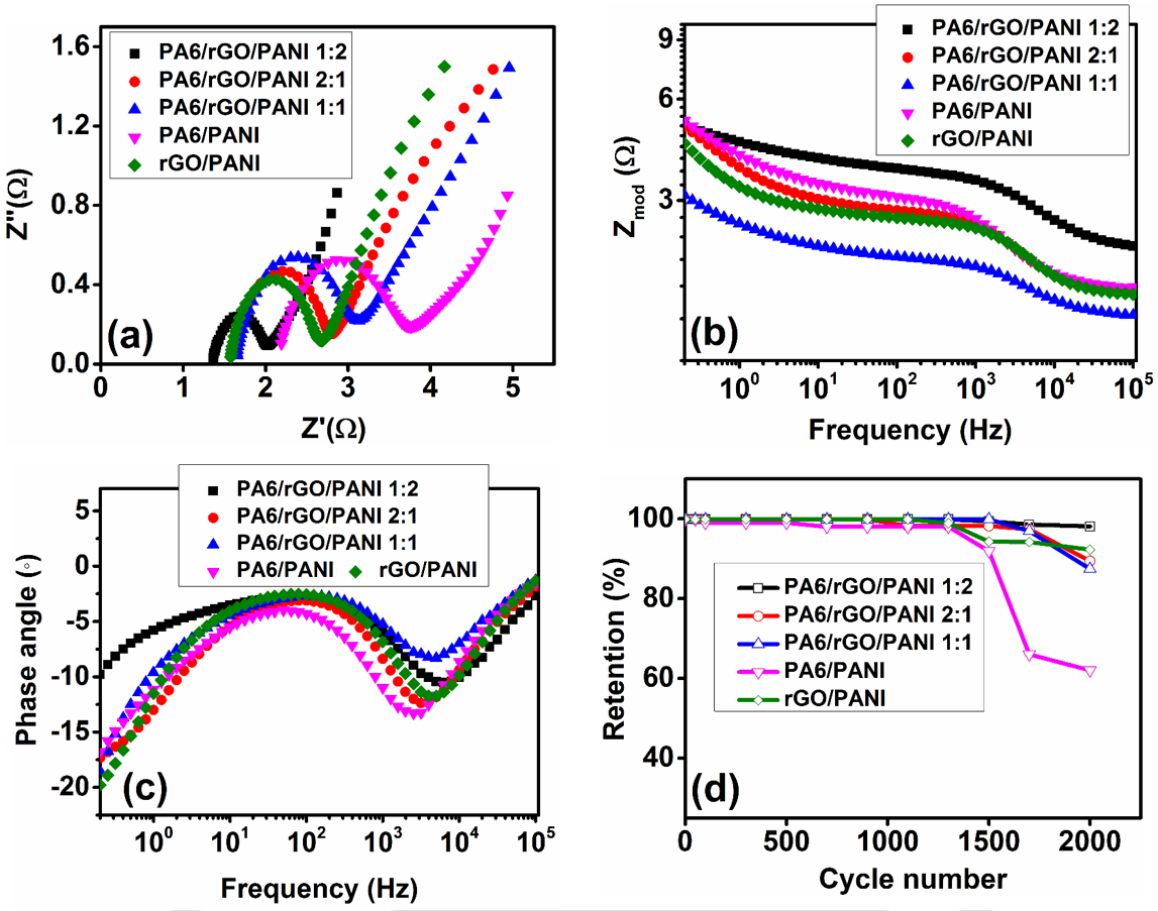

Figure 4.15 (a) EIS measurements, (b − c) bode plots, and (d) cyclic stability of all the nanocomposites.

The EDLC performance is represented by CPE due to ion exchange at the interfacial region of electrode and electrolyte. The PA6/rGO/PANI 1:2 nanocomposite shows a maximum slope denoting the highest C_s, and PA6/PANI shows the lowest. The values of R_s, R_{ct}, and n are shown in Table 4.4. Figure 4.15b and 4.15c present bode plots of the magnitude of impedance and phase angle against frequency, respectively. In the high frequency region (~10^5 Hz), impedance decreases, revealing the faradaic reduction with improved C_s [61]. In low frequency region, impedance follows almost a linear decaying function, indicating high charge accumulation [62].

Table 4.4. The numerical values of solution resistance (R_s), charge transfer resistance (R_{ct}), a correction factor (n), and relaxation time (τ_0) of the nanocomposites.

Sample	R_{ct} (Ω)	R_s (Ω)	n	τ_0 (ms)
PA6/rGO/PANI 1:2	0.67	1.37	0.66	0.12
PA6/rGO/PANI 2:1	1.20	1.59	0.58	0.28
PA6/rGO/PANI 1:1	1.45	1.66	0.41	0.28
PA6/PANI	1.55	2.19	0.63	0.15
rGO/PANI	1.10	1.58	0.54	0.10

The composites 1:1 and 1:2 show an improved C_s at a lower impedance. Figure 4.15c shows the -20° phase shift in the low-frequency region (~ 0.20 Hz), indicating the double-layer charge transport phenomenon of nanocomposites [62]. The phase angle at ~ -12°, the characteristics point, is known as the knee frequency (f_0 ~ 317 Hz). At this point, capacitance and resistance show equal values, and beyond this point, the supercapacitive behaviour may retain high resistance [63]. We have calculated the dielectric relaxation time constant ($\tau_0 = \frac{1}{2\pi f}$) from the imaginary capacitance (C", F g^{-1}) in the complex bode plot to estimate the response time of the supercapacitor [64] (Table 4.4). Among all the ternary nanocomposites, PA6/rGO/PANI 1:2 exhibits the lowest values of both R_{ct} and τ_0, which is attributed to the rapid charge-discharge cycle of the supercapacitor. The capacitance retention (%) of each of the nanocomposites has been evaluated for over 2000 cycles (Figure 4.15d). The capacitance retention (%) of PA6/rGO/PANI 1:2, PA6/rGO/PANI 2:1, PA6/rGO/PANI 1:1, PA6/PANI, and rGO/PANI are ~ 98, ~ 89, ~ 87, ~ 31, and 92%, respectively. Among the composites PA6/rGO/PANI 1:2 displays the highest stability with ~ 98% retention, indicating an excellent material for the supercapacitor application.

The electrochemical measurements are investigated using PA6/rGO/PANI 1:2 nanocomposite material for the symmetric supercapacitor device (Figure 4.16). The CV profiles at different scan rates (viz., 10 to 100 mV s^{-1}) show almost rectangular shape accredit to excellent electrochemical behaviour with improved C_s, as shown in Figure 4.16a. The CV profiles do not show redox peaks that signifies a rapid charging-discharging process of pseudocapacitance response [65]. The gradually decreasing C_s with increasing scan rates (Figure 4.16b) shows an excellent rate capability. At increased scan rates, the shape of CV profiles does not alter by virtue of good ion adsorption, claiming high reversibility of the electrode material. It can be correlated to the presence of a significant microporous surface (BET area, Figure 4.8a) that holds the electronic charge, which may reduce the transition time of ionic diffusion. The CCD profile for PA6/rGO/PANI 1:2 nanocomposite at various current densities (0.25 to 0.45 A g^{-1}) revealed almost symmetric charge-discharge performance (Figure 4.16c). The maximum C_s is ~ 38 F g^{-1} at a current density of 0.25 A g^{-1}. The variation of C_s with the function of current density in Figure 4.16d shows excellent rate capability up to a current density of 0.45 A g^{-1}. The CCD profile represents quasi rectangular shapes at each current density with a marginal deviation, indicating an excellent pseudocapacitive behaviour of the material.

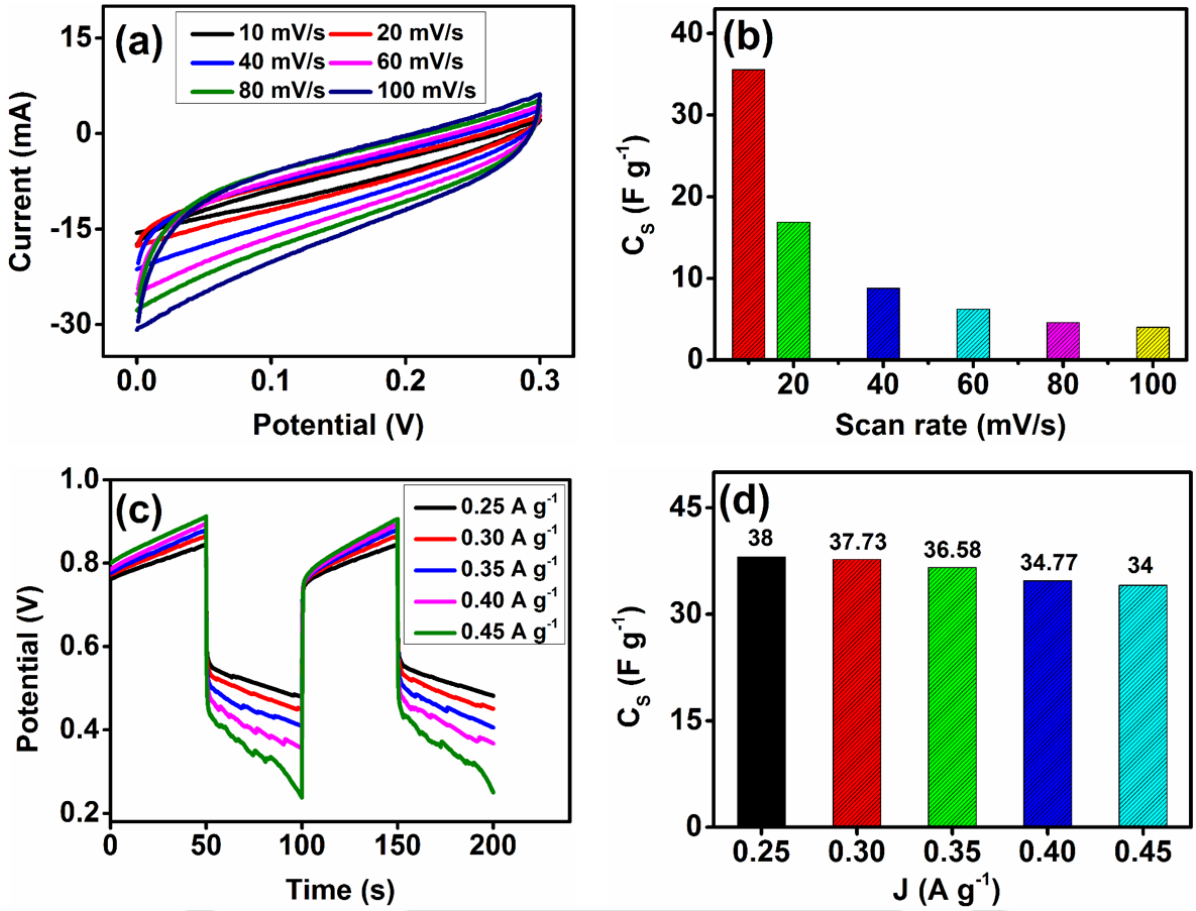

Figure 4.16. Two electrode system of (a) CV profile and (b) specific capacitance, at the various scan rates, (c) galvanostatic charge-discharge, and (d) specific capacitance, at the different current densities of the PA6/rGO/PANI 1:2.

Further, a low value of equivalent series resistance (0.30 Ω), calculated from the slope of the plot of IR drop versus discharge current density (Figure 4.17) for symmetric supercapacitor device of PA6/rGO/PANI 1:2, unveils superior electrochemical activity.

Figure 4.18a shows the EIS plot of PA6/rGO/PANI 1:2 symmetric electrodes before and after the cyclic stability. At the 1st cycle, R_{ct} and ESR are ~ 0.68 Ω and ~ 2.61 Ω, and at the end of the 2000th cycle, R_{ct} and ESR are 1.79 Ω and 3.41 Ω, respectively. We have fitted the EIS data using the ZSimpWin software (version 3.2.1) and have drawn the relevant equivalent circuit diagrams in Figure 4.18b. We observed a small deviation of ESR and R_{ct} values at the last cycle compared to that of the first cycle.

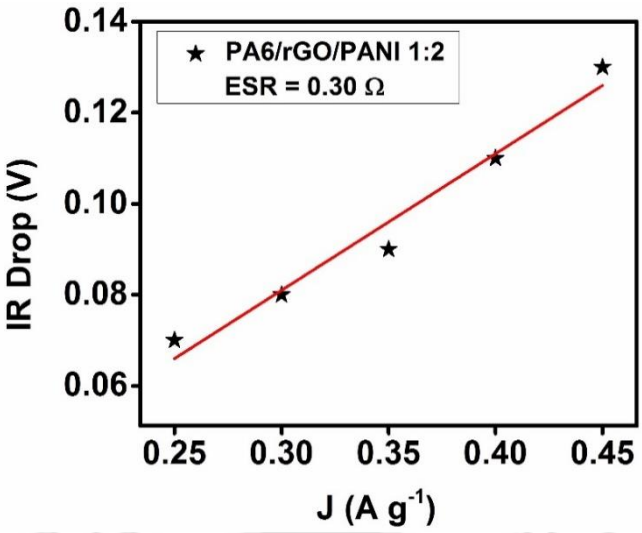

Figure 4.17. Analysis of equivalent series resistance of PA6/rGO/PANI 1:2 based symmetric supercapacitor.

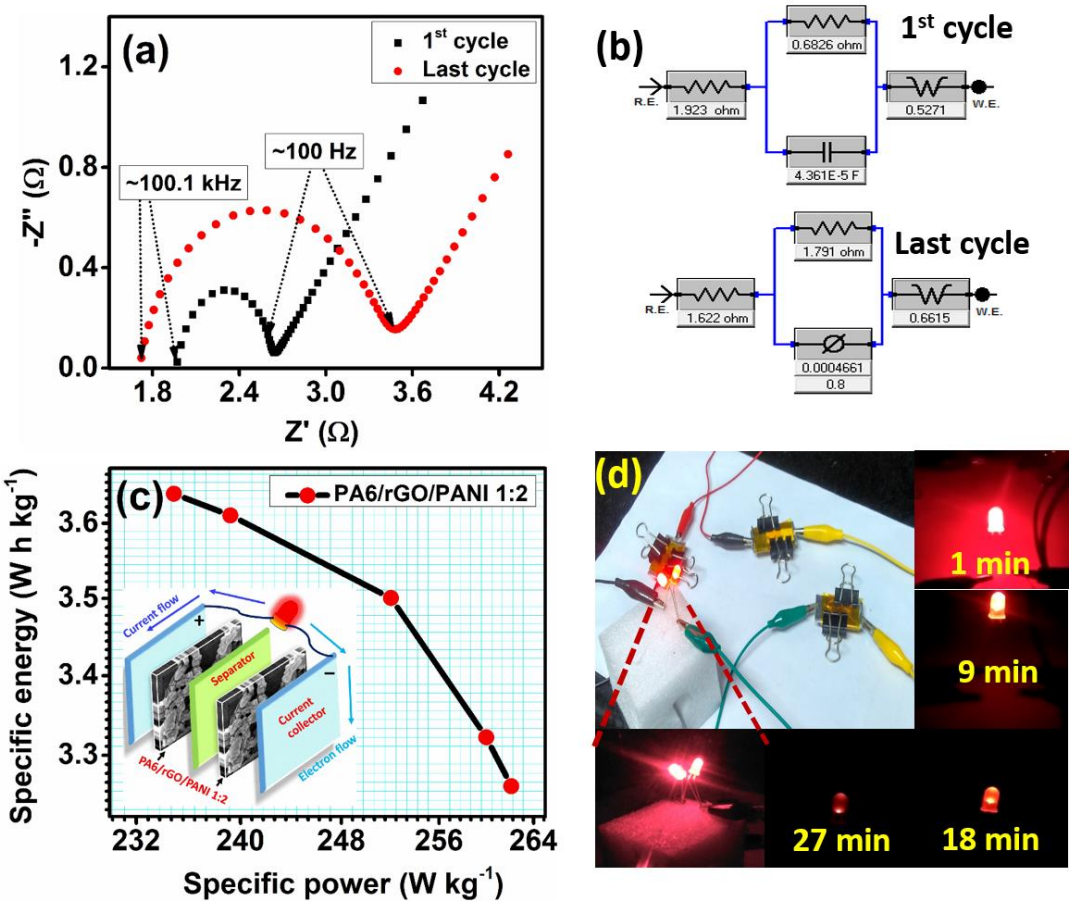

Figure 4.18. (a) EIS spectra at the first and last cycle, (b) equivalent circuit diagrams, (c) Ragone plot and the inset shows a schematic arrangement of electrodes, (d) inset exhibits supercapacitor devices powering to LEDs, and glowing a LED for about 27 minutes powered by electrode materials of PA6/rGO/PANI 1:2.

The modest value of R_{ct} of PA6/rGO/PANI 1:2 is attributed to an excellent electrical conductivity. The initial cycle of PA6/rGO/PANI 1:2 symmetric supercapacitor offers diffusion capability of the charge carries via the separation layer at the electrode and electrolyte interface with a diffusion capacitance, C_d ~ 0.436 µF. Further, in the 2000th cycle, the presence of a double layer capacitance leads to a CPE ~ 0.00046 with an increasing number of cycles. The CPE increases (see the equivalent circuits) due to double-layer capacitance, which arises at the interfacial region of a solid electrode and electrolytic solution owing to ionic and electronic charge separation [66]. The obtained results are in good agreement with the improved capacitance retention (Figure 4.15d). After cycle stability measurements, C_s increases steadily, as EIS spectra show a right-shift (Figure 4.18a), suggesting excellent electrochemical stability of the electrode material. Further, ED and PD of the symmetric supercapacitor are estimated using the relations given in Equations 3 and 4. The Ragone plot (viz., ED vs. PD) is attributed to CCD performance of symmetric supercapacitor based on PA6/rGO/PANI 1:2 (Figure 4.18c). We have recorded a maximum ED of ~3.66 W h Kg^{-1} with PD of ~234.84 W kg^{-1}, and a minimum ED of ~3.26 W h Kg^{-1} with PD of 262.13 W kg^{-1}. Moreover, The ED values are high and more desirable than various reported works based on equivalent organic composite materials for supercapacitors, such as polypyrrole and cladophora nanocellulose (1.75 W h kg^{-1}) [67], inkjet printing technology-based graphene/PANI nanocomposites (2.4 W h kg^{-1}) [68], carbon nanotubes coated cellulose papers (0.12 W h kg^{-1}) [69], graphene-coated carbon cloth (1.64 W h kg^{-1}) [70], and three-dimensional graphene hydrogel films (0.61 W h kg^{-1}) [71]. To test the performance, three symmetric supercapacitors are assembled in a series configuration and glow a red LED (~ 2.0 V) for ~ 30 minutes (Figure 4.18d), ensuring excellent stability with significant storage capability. When we put two red LEDs together, the same assembly is capable of power for about five minutes, which ensures that the combination of three supercapacitors is capable of delivering more than 4 V (viz., single supercapacitor produces ~ 1.5 V). Thus, it is estimated that PA6/rGO/PANI 1:2 nanocomposite appears to be a potential electrode material for the electrochemical energy storage applications.

4.4. Conclusions

The enhancement of the functional properties of a polymer nanocomposite is governed by the uniform dispersion of nanofillers within the polymer matrix. A judicial choice of nanofillers, along with the suitable polymer matrix, would lead to the development of tailor-made material with desirable properties. In this work, we report the ternary nanocomposites of PA6, rGO, and PANI for the application of supercapacitor with enhanced specific power and energy. The *in-*

situ polymerization of PANI ensures the formation of nanocomposites with evenly distributed nanofillers within the polymer matrix. The presence of PA6 in the nanocomposite would bring flexibility into the materials and would compensate for the brittleness of PANI. The electrical charge storage property is enhanced in the presence of rGO. Therefore, the ternary nanocomposite would be a suitable candidate as a flexible supercapacitor for energy storage applications. The detailed morphological and structural analysis reveals the polycrystalline behaviour of the nanocomposites, which would exhibit an excellent charge transport property. Among all the ternary nanocomposites, the one with a 1:2 ratio of PA6 and PANI exhibits superior properties over others, which is attributed to the synergistic effect of all the components present in the nanocomposite. PANI nanorods are intercrosslinked with PA6 and intercalated with rGO layers, in the ternary nanocomposite (PA6/rGO/PANI 1:2) that preserves a balance charge distribution during the redox reaction. PA6/rGO/PANI 1:2 has shown excellent electrochemical performance with improved cyclic stability and capacity retention (~ 98% at a scan rate of 100 mV s^{-1}), as compared to the other binary (viz., PA6/PANI and rGO/PANI) and ternary composites (viz., PA6/rGO/PANI 1:1 and PA6/rGO/PANI 2:1). The applicability of the fabricated supercapacitor has been demonstrated by a glowing red LED for ~ 30 minutes.

References

[1] J.-M. Tarascon, M. Armand, In *Materials for Sustainable Energy*; Co-Published with Macmillan Publishers Ltd, UK, 2010; pp. 171–179.

[2] M. Winter, R. J. Brodd, *Chem. Rev.* **2004**, *104*, 4245.

[3] R. Sahoo, A. Pal, T. Pal, *J. Mater. Chem. A* **2016**, *4*, 17440.

[4] L. Hao, X. Li, L. Zhi, *Adv. Mater.* **2013**, *25*, 3899.

[5] X. Xiang, W. Zhang, Z. Yang, Y. Zhang, H. Zhang, H. Zhang, H. Guo, X. Zhang, Q. Li, *RSC Adv.* **2016**, *6*, 24946.

[6] N. C. Abeykoon, J. S. Bonso, J. P. Ferraris, *RSC Adv.* **2015**, *5*, 19865.

[7] B. Z. Jang, C. Liu, D. Neff, Z. Yu, M. C. Wang, W. Xiong, A. Zhamu, *Nano Lett.* **2011**, *11*, 3785.

[8] Q. Zheng, A. Kvit, Z. Cai, Z. Ma, S. Gong, *J. Mater. Chem. A* **2017**, *5*, 12528.

[9] E. Frackowiak, V. Khomenko, K. Jurewicz, K. Lota, F. Béguin, *J. Power Sources* **2006**, *153*, 413.

[10] S. Palsaniya, H. B. Nemade, A. K. Dasmahapatra, *Polymer* **2018**, *150*, 150.

[11] M. Mastragostino, C. Arbizzani, F. Soavi, *J. Power Sources* **2001**, *97–98*, 812.

[12] K. R. Reddy, W. Park, B. C. Sin, J. Noh, Y. Lee, *J. Colloid Interface Sci.* **2009**, *335*, 34.

[13] K. R. Reddy, B. C. Sin, K. S. Ryu, J.-C. Kim, H. Chung, Y. Lee, *Synth. Met.* **2009**, *159*, 595.

[14] K. R. Reddy, M. Hassan, V. G. Gomes, *Appl. Catal. Gen.* **2015**, *489*, 1.

[15] K. R. Reddy, K.-P. Lee, Y. Lee, A. I. Gopalan, *Mater. Lett.* **2008**, *62*, 1815.

[16] Y.-P. Zhang, S.-H. Lee, K. R. Reddy, A. I. Gopalan, K.-P. Lee, *J. Appl. Polym. Sci.* **2007**, *104*, 2743.

[17] S. Wang, N. Liu, J. Tao, C. Yang, W. Liu, Y. Shi, Y. Wang, J. Su, L. Li, Y. Gao, *J. Mater. Chem. A* **2015**, *3*, 2407.

[18] C. Yang, Y. Shi, N. Liu, J. Tao, S. Wang, W. Liu, Y. Wang, J. Su, L. Li, C. Yang, Y. Gao, *RSC Adv.* **2015**, *5*, 45129.

[19] Z. Pang, J. Fu, L. Luo, F. Huang, Q. Wei, *Colloids Surf. Physicochem. Eng. Asp.* **2014**, *461*, 113.

[20] M. Singh, N. Nesakumar, S. Sethuraman, U. M. Krishnan, J. B. B. Rayappan, *J. Colloid Interface Sci.* **2014**, *425*, 52.

[21] W. Leng, S. Zhou, G. Gu, L. Wu, *J. Colloid Interface Sci.* **2012**, *369*, 411.

[22] S. Palsaniya, H. B. Nemade, A. K. Dasmahapatra, *ACS Appl. Polym. Mater.* **2019**, *1*, 647.

[23] G. Cai, J. Tu, D. Zhou, J. Zhang, Q. Xiong, X. Zhao, X. Wang, C. Gu, *J. Phys. Chem. C* **2013**, *117*, 15967.

[24] N. Wang, Y. H. Wu, K. Q. Cheng, J. Zhang, *Mater. Corros.* **2014**, *65*, 968.

[25] B. Guo, P. X. Ma, *Biomacromolecules* **2018**, *19*, 1764.

[26] J. Lyu, X. Zhao, X. Hou, Y. Zhang, T. Li, Y. Yan, *Compos. Sci. Technol.* **2017**, *149*, 159.

[27] S. Valiavalappil, S. Harinipriya, *Synth. Met.* **2012**, *162*, 2027.

[28] H. Bagheri, A. Aghakhani, *Anal. Chim. Acta* **2012**, *713*, 63.

[29] Y. Xia, T. Li, J. Chen, C. Cai, *Synth. Met.* **2013**, *175*, 163.

[30] K. M. Lee, M. Kim, E. Lee, S. H. Baeck, S. E. Shim, *Electrochimica Acta* **2016**, *213*, 124.

[31] X. Fu, C. Yao, G. Yang, *RSC Adv.* **2015**, *5*, 61688.

[32] D. Zheng, G. Tang, H.-B. Zhang, Z.-Z. Yu, F. Yavari, N. Koratkar, S.-H. Lim, M.-W. Lee, *Compos. Sci. Technol.* **2012**, *72*, 284.

[33] Z. Xu, C. Gao, *Macromolecules* **2010**, *43*, 6716.

[34] J. S. Bunch, S. S. Verbridge, J. S. Alden, A. M. van der Zande, J. M. Parpia, H. G. Craighead, P. L. McEuen, *Nano Lett.* **2008**, *8*, 2458.

[35] C. Lee, X. Wei, J. W. Kysar, J. Hone, *Science* **2008**, *321*, 385.

[36] X. Du, I. Skachko, A. Barker, E. Y. Andrei, *Nat. Nanotechnol.* **2008**, *3*, 491.

[37] J. P. Rourke, P. A. Pandey, J. J. Moore, M. Bates, I. A. Kinloch, R. J. Young, N. R. Wilson, *Angew. Chem.* **2011**, *123*, 3231.

[38] Q. Pan, E. Shim, B. Pourdeyhimi, W. Gao, *ACS Appl. Mater. Interfaces* **2017**, *9*, 8308.

[39] H. R. Pant, C. H. Park, L. D. Tijing, A. Amarjargal, D.-H. Lee, C. S. Kim, *Colloids Surf. Physicochem. Eng. Asp.* **2012**, *407*, 121.

[40] D. C. Marcano, D. V. Kosynkin, J. M. Berlin, A. Sinitskii, Z. Sun, A. Slesarev, L. B. Alemany, W. Lu, J. M. Tour, *ACS Nano* **2010**, *4*, 4806.

[41] L. Qiu, H. Zhang, W. Wang, Y. Chen, R. Wang, *Appl. Surf. Sci.* **2014**, *319*, 339.

[42] S. Palsaniya, H. B. Nemade, A. K. Dasmahapatra, *Carbon* **2019**, *150*, 179.

[43] S. Palsaniya, H. B. Nemade, A. K. Dasmahapatra, *Polymer* **2018**, *150*, 150.

[44] R. R. Salunkhe, J. Lin, V. Malgras, S. X. Dou, J. H. Kim, Y. Yamauchi, *Nano Energy* **2015**, *11*, 211.

[45] L. Dennany, P. C. Innis, S. T. McGovern, G. G. Wallace, R. J. Forster, *Phys. Chem. Chem. Phys.* **2011**, *13*, 3303.

[46] S. Perumbilavil, P. Sankar, T. Priya Rose, R. Philip, *Appl. Phys. Lett.* **2015**, *107*, 051104.

[47] T. M. Majka, M. Cokot, K. Pielichowski, *J. Therm. Anal. Calorim.* **2018**, *131*, 405.

[48] H. Baniasadi, A. Ramazani S.A., S. Mashayekhan, F. Ghaderinezhad, *Synth. Met.* **2014**, *196*, 199.

[49] E. Nasybulin, I. Menshikova, V. Sergeyev, K. Levon, *J. Appl. Polym. Sci.* **2009**, *114*, 1643.

[50] A. A. Athawale, M. V. Kulkarni, V. V. Chabukswar, *Mater. Chem. Phys.* **2002**, *73*, 106.

[51] J. Y. Tsao, S. Chowdhury, M. A. Hollis, D. Jena, N. M. Johnson, K. A. Jones, R. J. Kaplar, S. Rajan, C. G. V. de Walle, E. Bellotti, C. L. Chua, R. Collazo, M. E. Coltrin, J. A. Cooper, K. R. Evans, S. Graham, T. A. Grotjohn, E. R. Heller, M. Higashiwaki, M. S. Islam, P. W. Juodawlkis, M. A. Khan, A. D. Koehler, J. H. Leach, U. K. Mishra, R. J. Nemanich, R. C. N. Pilawa-Podgurski, J. B. Shealy, Z. Sitar, M. J. Tadjer, A. F. Witulski, M. Wraback, J. A. Simmons, *Adv. Electron. Mater.* **2018**, *4*, 1600501.

[52] W. He, Y. Liu, W. G. Wamer, J.-J. Yin, *J. Food Drug Anal.* **2014**, *22*, 49.

[53] S. Palsaniya, H. B. Nemade, A. K. Dasmahapatra, *Carbon* **2019**, *150*, 179.

[54] B. H. Kim, S. H. Hong, J. Joo, I.-W. Park, A. J. Epstein, J. W. Kim, H. J. Choi, *J. Appl. Phys.* **2004**, *95*, 2697.

[55] S. Palsaniya, H. B. Nemade, A. K. Dasmahapatra, *J. Phys. Chem. C* **2019**, *123*, 27959.

[56] Prateek, D. Singh, N. Singh, A. Garg, R. K. Gupta, *Compos. Sci. Technol.* **2019**, *174*, 158.

[57] L. C. Mariano, R. V. Salvatierra, C. E. Cava, M. Koehler, A. J. G. Zarbin, L. S. Roman, *J. Phys. Chem. C* **2014**, *118*, 24811.

[58] P. Tamilarasan, S. Ramaprabhu, *J. Mater. Chem. A* **2014**, *2*, 14054.

[59] Y. Cao, B. Lin, Y. Sun, H. Yang, X. Zhang, *Electrochimica Acta* **2015**, *178*, 398.

[60] J. Qiu, P. Zhang, M. Ling, S. Li, P. Liu, H. Zhao, S. Zhang, *ACS Appl. Mater. Interfaces* **2012**, *4*, 3636.

[61] R. Zhang, L. Wang, W. Shi, *RSC Adv.* **2015**, *5*, 95750.

[62] M. Biswal, A. Banerjee, M. Deo, S. Ogale, *Energy Environ. Sci.* **2013**, *6*, 1249.

[63] T. Purkait, G. Singh, D. Kumar, M. Singh, R. S. Dey, *Sci. Rep.* **2018**, *8*, 640.

[64] P. Ramakrishnan, S. Shanmugam, *ACS Sustain. Chem. Eng.* **2016**, *4*, 2439.

[65] S. D. Perera, B. Patel, N. Nijem, K. Roodenko, O. Seitz, J. P. Ferraris, Y. J. Chabal, K. J. Balkus, *Adv. Energy Mater.* **2011**, *1*, 936.

[66] W. Wang, S. Guo, I. Lee, K. Ahmed, J. Zhong, Z. Favors, F. Zaera, M. Ozkan, C. S. Ozkan, *Sci. Rep.* **2014**, *4*, 4452.

[67] A. Razaq, L. Nyholm, M. Sjödin, M. Strømme, A. Mihranyan, *Adv. Energy Mater.* **2012**, *2*, 445.

[68] Y. Xu, I. Hennig, D. Freyberg, A. James Strudwick, M. Georg Schwab, T. Weitz, K. Chih-Pei Cha, *J. Power Sources* **2014**, *248*, 483.

[69] Y. J. Kang, H. Chung, C.-H. Han, W. Kim, *Nanotechnology* **2012**, *23*, 065401.

[70] S. Wang, B. Pei, X. Zhao, R. A. W. Dryfe, *Nano Energy* **2013**, *2*, 530.

[71] Y. Xu, Z. Lin, X. Huang, Y. Liu, Y. Huang, X. Duan, *ACS Nano* **2013**, *7*, 4042.

Chapter-5

PANI/RGO/ZnO Ternary Nanocomposites for High Performance Symmetric Tandem Supercapacitor

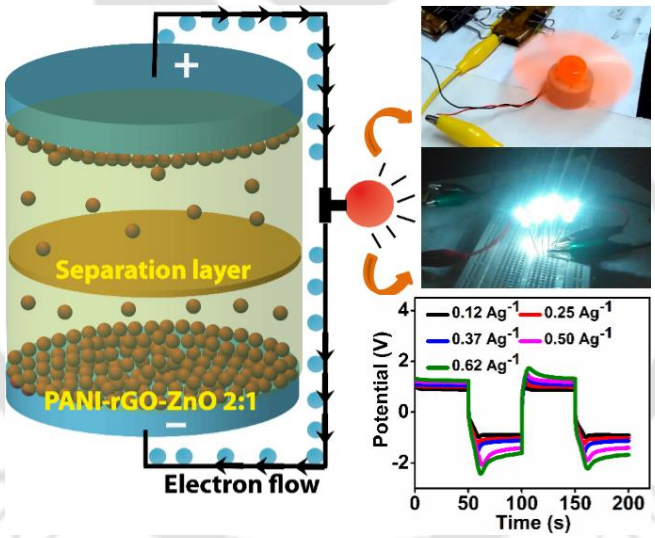

Communicated

5.1. Introduction

Solid-state supercapacitor devices have attracted much attention in the development of smart electronic devices, for the applications in medical devices, micro-robotics, smartphones, smart bracelets, and hybrid electric vehicles [1–3]. Supercapacitors, owing to excellent reversible faradaic redox reactions at the electrode surface, offer high specific capacitance with high energy density. Energy harnessing based on aqueous electrolytes [4], metal oxide nanocomposites [5], organic-inorganic framework [6], transition metal oxides (TMO) and hydroxides [7], and mesoporous composites [8] is largely classified as pseudocapacitors due to excellent electron conduction. The organic compound-based electrochemical double-layer capacitors (EDLCs) [9] are equally promising towards energy storage applications due to their long life cycle, fast charging-discharging process, high environmental stability, easy to fabricate, and capable of building a hybrid system [10,11]. The efficiency of supercapacitors is primarily governed by the structure and morphology of electrode materials, electrolytes, charge transport mechanisms, and electrocatalytic activities [12,13]. Therefore, the selection of electrode materials and electrolytes is essential in device fabrication. For example, carbon-based nanomaterials, such as intrinsic graphene, graphene oxide (GO), and reduced graphene oxide (RGO) have been investigated in numerous symmetric (SSC) and asymmetric (ASC) supercapacitor devices[14–16]. Although ASC is relatively more stable with a higher energy and power density than SSC, the high production cost, long fabrication process, and complex structure limit their applications in comparison with SSC. The performance of SSCs, in terms of energy storage, can also further be enhanced by tailoring the device architecture [14,17].

Nanostructure materials, especially polymer nanocomposites, are emerging as novel materials for the supercapacitor applications. Several polymers have been used in preparing such polymer-based supercapacitors, such as polyvinylidene fluoride (PVDF), polytetrafluoroethylene (PTFE), poly(3,4-ethylenedioxythiophene) (PEDOT), poly(pyrrole) (PPY), polyaniline (PANI), poly(3-hexylthiophene) (P3HT), etc. A wide variety of nanofillers has been used with adequate proportions to enhance electrochemical properties. Among the polymers, conducting polymers, such as PANI, PPY, and P3HT, are used extensively to fabricate supercapacitors for energy storage applications. PANI is used massively in various electrochemical applications due to its excellent properties in electrical conduction, lightweight, and environmental stability. PANI is a p-type semiconducting material when doped with an acid (viz. PANI-ES). In spite of having an excellent electrical property, the use of PANI is restricted due to its low adhesion behavior with electrolytes, which would result in

low specific capacitance [15]. This particular drawback can be improved by incorporating suitable organic (viz., graphene, graphene oxide, reduced graphene oxide) and inorganic nanofillers (e.g., ZnO). The PANI nanocomposites with organic-inorganic nanofillers would enhance the electrochemical properties because of high interfacial adhesion of electrode materials and electrolyte, and an improved surface to volume ratio.

Zinc oxide is a well-recognized n-type semiconductor with a wide bandgap (~ 3.3 eV) that shows remarkable electrical and optical properties. Typically, ZnO is utilized in solar cells, photocatalyst, energy harvesting, and sensing applications [18]. ZnO has been employed as an active electrode material exhibiting good electrical conductivity with a large current density (~ 650 A g^{-1}), suitable for the fabrication of ASC and SSC devices [19]. Graphene is an excellent charge transport agent; however, restacking properties of graphene is the main disadvantage that can be managed by forming a novel nanostructure by incorporating ZnO nanoparticles having Wurtzite hexagonal structure. The ZnO nanostructure would be helpful in wrapping graphene layers during restacking, resulting in the unique core-shell nanostructure. This nanostructure would be extremely useful in delivering an efficient electronic charge storage device. The ZnO based PANI-RGO nanocomposites have been employed for several applications. For example, Cao and Han et al. [20] have developed a uniform PANI-coated hollow spherical shape of ZnO, which was used for the preparation of the ternary nanocomposite, PANI-ZnO@ZIF-8, for flexible supercapacitors. A similar flexible supercapacitor was developed by using PANI-wrapped ZnO core-shell nanostructures on polyethylene terephthalate substrate [21]. Furthermore, Karthik and Thambiduari [22] have synthesized RGO-Cobalt functionalized ZnO-PANI hybrid for supercapacitor electrodes. They have also unveiled that the ternary composite, RGO-ZnO-PANI, shows higher specific capacitance than the binary composite of PANI and RGO.

Bera et al. [23] have prepared a 3D hierarchical flower shape of ZnO-graphene-PANI ternary nanocomposite with increased electrochemical performance. Further, Chee et al. [24] have developed a flexible supercapacitor using PPy-GO-ZnO nanocomposites. Ghanbari et al. [25] have successfully demonstrated direct detection of dopamine (detection limit 0.8 nM) and uric acid (detection limit 0.042 µM) using ZnO-PANI-RGO ternary nanocomposite. Since ZnO is a good photocatalyst, it can also be utilized in preparing photoactive (or photoresponsive) devices, as have been shown by Wu et al. [26] for the removal of organic contaminants from water. Zhang et al. [27] have reported that the presence of ZnO in PANI-ZnO nanocomposite has expanded the visible light spectrum. Hence, a novel nanocomposite of the PANI-Fe_3O_4@ZnO core-shell microstructure delivered increased photocatalytic activities.

Herein, we report the fabrication of SSC-based tandem supercapacitor using PANI-RGO-ZnO ternary nanocomposite for significant energy storage applications. The in-situ chemical oxidative polymerization of PANI ensures the formation of a well-mixed nanocomposite, as shown in Figure 5.1. We observe the formation of the flower shape of PANI nanostructures, which provides a homogeneous morphology with high interfacial interaction. Among all the nanocomposites, PANI-RGO-ZnO 2:1 (PANI:ZnO) appears to be the best suitable electrode material for energy storage devices with characteristic properties such as, high electron conduction, high specific capacitance, and remarkable energy density. We have demonstrated multiple applications (two terminals as well as tandem devices) based on the PANI-RGO-ZnO 2:1 nanocomposites. The fabricated SSC device supports DC motor operation (high current density), powers LED (high energy density), and renders an output voltage of 6.0 V (high power density). The fabricated SSC device successfully delivers an adequate power to glow LED lights for ~ 30 minutes with a charging time of ~ 5 minutes.

5.2. Experimental section

5.2.1. Materials

Zinc acetate hexahydrate, Sodium nitrate (> 99%), Potassium permanganate (> 98.5%), Hydrogen peroxide 50%, Hydrazine hydrate (99%), Ammonia solution (~ 25%) and Aniline (Emparta ≥ 99%) were purchased from Merck Co. Graphite powder (99.9999%, metal basis) was purchased from Alfa-Aesar. Hydrochloride acid (~ 35–37%) was purchased from Fisher Scientific. Ammonium persulfate was purchased from Sisco Research Laboratories. All the chemicals were at analytical grade and were used as received without further purification.

5.2.2. Synthesis of PANI-RGO

Firstly, reduced graphene oxide (RGO) was synthesized by reduction of graphene oxide (GO) following the procedure reported by Marcano et al. [28,29]. Graphite powder (0.7 g) was mixed in 70 mL solution of H_2SO_4/H_3PO_4 (at 9:1 ratio). KMnO4 (at 1:6 with graphite) was slowly added into the above solution keeping the temperature ~ 20 °C. Further, temperature was fixed at ~ 50 °C under stirring at 450 rpm for 24 h. The mixture was allowed to cool at ~ 0 °C, and added 3 mL of 30% H_2O_2 with 50 mL of DI water under stirring at 450 rpm for 4 h. The obtained yellow precipitate was kept aside overnight, and resultant GO mixture was centrifuged at 5000 rpm for 10 minutes followed by washing with 10% HCl and DI water. The pH of the GO dispersion (1 mg per mL in DI water) is maintained ~ 10 using ammonia solution, and further reduced by treating with hydrazine hydrate under stirring at ~ 80 °C for 24 h. The resultant precipitate (RGO) was filtered and successively washed with methanol and DI water, dried in vacuum at 60 °C for 48 h.

The nanocomposite PANI-RGO was prepared using the method reported previously [6]. In brief, 20 mL of DI water was used to disperse 20 mg of RGO using ultrasonication for an hour. Further, 3 mL of aniline was added to the above dispersion and was stirred until dissolution took place. In addition, a solution of 3 g ammonium persulfate in 15 mL of 1 M HCl (at 1:1 ratio of aniline and APS) was prepared, and mixed into the above aniline/RGO dispersion dropwise under stirring at 450 rpm in an ice bath. The appearance of green colour depicts the polymerization of aniline. The mixture was incubated at 0 – 4 ˚C for 24 h to ensure the complete polymerization.

5.2.3. Synthesis of PANI-RGO-ZnO derivatives

Zinc oxide (ZnO) was prepared using the previously reported method [30]. A solution of 6 g of zinc acetate hexahydrate in 300 mL of DI water was prepared. Further, 30 mL of ammonia solution was mixed into the above solution dropwise under stirring (450 rpm) at 70 ºC for 2 h. The mixture (milky white) was filtered and dried in a hot air oven at 80 °C for 24 h.

As shown in Figure 5.1a, first a homogeneous dispersion of 20 mg RGO and 3 mL of aniline was prepared in a 40 mL of DI water. The 1.5 g of ZnO (previously prepared) was added into the aniline/RGO mixture under stirring at 300 rpm for 30 minutes. A separate solution of 3 g of APS in 10 mL of 1 M HCl was prepared and added into the above solution dropwise under stirring at 300 rpm in an ice bath for 6 h. A dark green precipitate was resulted, indicating polymerization of the aniline monomers, was kept at 0 – 4 ˚C for 24 h for the complete polymerization. The resultant solution was filtered and washed thoroughly with DI water and 1 M HCl. The precipitate of PANI-RGO-ZnO at 2:1 was vacuum dried at 60 ˚C for 24 h.

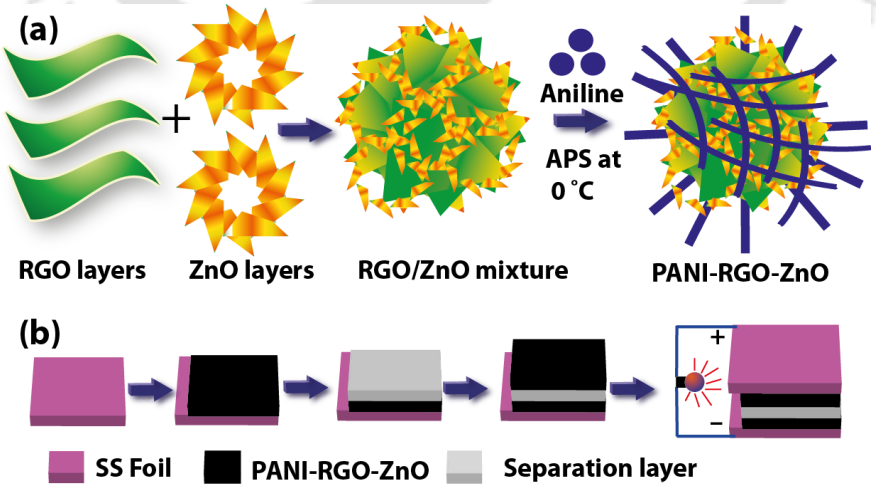

Figure 5.1. Schematic representation of the (a) preparation of PANI-RGO-ZnO nanocomposites, and (b) fabrication of symmetric supercapacitor.

Similarly, nanocomposite of PANI-RGO-ZnO 1:2 was prepared with 1:2 ratio of aniline and ZnO at the fixed amount of RGO.

5.2.4. Characterization

The Raman spectra (Model: LabRAM HR Evolution) were recorded at an excitation wavelength of 532 nm at 10 s acquisition time. The composition analysis were confirmed by Fourier transform infrared spectroscopy (FTIR) (Perkin Elmer Spectrum Two) in the range of 400 to 4000 cm^{-1}. The X-ray diffraction (XRD, Bruker, D8 Advance at Cu-Kα-Kβ radiations, λ=1.54 A°, 40 kV, and 40 mA) patterns were recorded in the range of 10 to 60° at a scan rate of 1° per minute. The UV visible absorbance spectra (Shimadzu, UV-2600 230V EN) were measured in the range of 200 to 800 nm. The field emission scanning electron microscopy at 15 kV (FESEM, JEOL, JSM-7610F), and field emission transmission electron microscopy (FETEM, JEOL, JEM 2100) at an acceleration voltage of 200 kV were used to examine the morphologies. The thermal stability was investigated by the thermogravimetric analyzer (PerkinElmer TGA-4000) at a scan rate of 10 K per minute. The BET analyzer (model no. micromeritics TriStar II) was used to estimate the surface area and pore size.

5.2.5. Fabrication and electrochemical measurements of the symmetric supercapacitor

The working electrodes for three-electrode system were prepared by the active electrode materials in a fixed ratio of 80:15:5. For example, 80 mg of composite material, 15 mg of acetylene black, and 5 mg polyvinylidene fluoride were mixed using N-methyl-2-pyrrolidone as solvent to prepare a homogeneous paste. The mixture was sandwiched between stainless steel woven meshes (1×1 cm^2) under 20 MPa pressure for equal distribution. Further, the samples were dried in hot air oven overnight at 60 °C. The electrochemical observations of the electrode materials were calibrated using platinum wire as the counter electrode, and Ag/AgCl as the reference electrode, using 1 M H_2SO_4 electrolyte to perform the cyclic voltammetry (CV), cyclic charge discharge (CCD), and electrochemical impedance spectroscopy (EIS) adopting electrochemical workstation of Gamry, Reference 600^+.

For the two-electrode measurements, we have developed a symmetric supercapacitor device. The prepared materials paste was coated over the stainless steel (SS) thin sheets (0.25 mm thick, size 20 × 40 mm^2) by keeping uncoated space ~ 3 mm as current collector, and dried ~ 2 h at 60 °C in a vacuum oven. At this stage, a whatman filter paper soaked in 1 M KOH solution for 30 s was intermediated via SS electrodes, as shown in Figure 5.1b. Following this, we have fabricated a tandem structure of the supercapacitors to obtain large voltage. The Kapton tape was used as an isolation layer to prevent the symmetric supercapacitors from environmental effects. We have estimated specific capacitance (C_s), energy and power

densities via the cyclic charging-discharging (CCD) curves based on the following equations [31,32]:

$$C_s = \frac{I*\Delta t}{m*\Delta V} \quad (5.1)$$

$$ED = \frac{1}{2 * 3.6} * C_s * \Delta V^2 \ (\text{Wh kg}^{-1}) \quad (5.2)$$

$$PD = \frac{E}{t} * 3600 \ (\text{W kg}^{-1}) \quad (5.3)$$

where, C_s (F g^{-1}) is the capacitance of the supercapacitor device, I is the current density (mA g^{-1}), ΔV is the potential window (V) of the discharging curves during the CCD measurements, m is the mass (g) of the active electrode materials, Δt is the discharging time (s), E (Wh kg^{-1}) is energy density, and P is the power density (W kg^{-1}).

5.3. Results and discussion

We begin with a detailed description of microstructures of PANI-RGO binary and PANI-RGO-ZnO ternary nanocomposites with varying ratios of PANI and ZnO (viz., PANI:ZnO). Following this, we present the thermal stability and adsorption-desorption analysis of all the nanocomposites. Finally, we discuss the electrochemical behavior of all the nanocomposites, including three- and two-electrode measurements with a couple of applications of the fabricated device based on PANI-RGO-ZnO 2:1 nanocomposite.

5.3.1. Structures and morphologies

Raman spectra of all the nanocomposites (Figure 5.2a) show two strong peaks at ~ 1340 and ~ 1591 cm^{-1}, which are attributed to D (lattice defects of E_{1g} mode) and G (E_{2g} mode of sp^2 regions) bands, respectively [33]. The benzenoid ring deformation by C-H bending, stretching of C–N^+, stretching of C=N, and C=C quinoid stretching corresponds to the band at ~ 1158, ~ 1340, ~ 1486, and ~ 1591 cm^{-1}, respectively, clearly reveals the growth of PANI chains [34,35]. Moreover, the bands ~ 1240 and ~ 1396 cm^{-1} are attributed to C–N benzenoid and C=N quinoid stretching, respectively. The characteristic absorption of PANI-RGO-ZnO 1:2 is slightly red-shifted by ~ 28 cm^{-1} as compared to PANI-RGO, which is attributed to chemically converted RGO with the inorganic moiety ZnO in the nanocomposites [23].

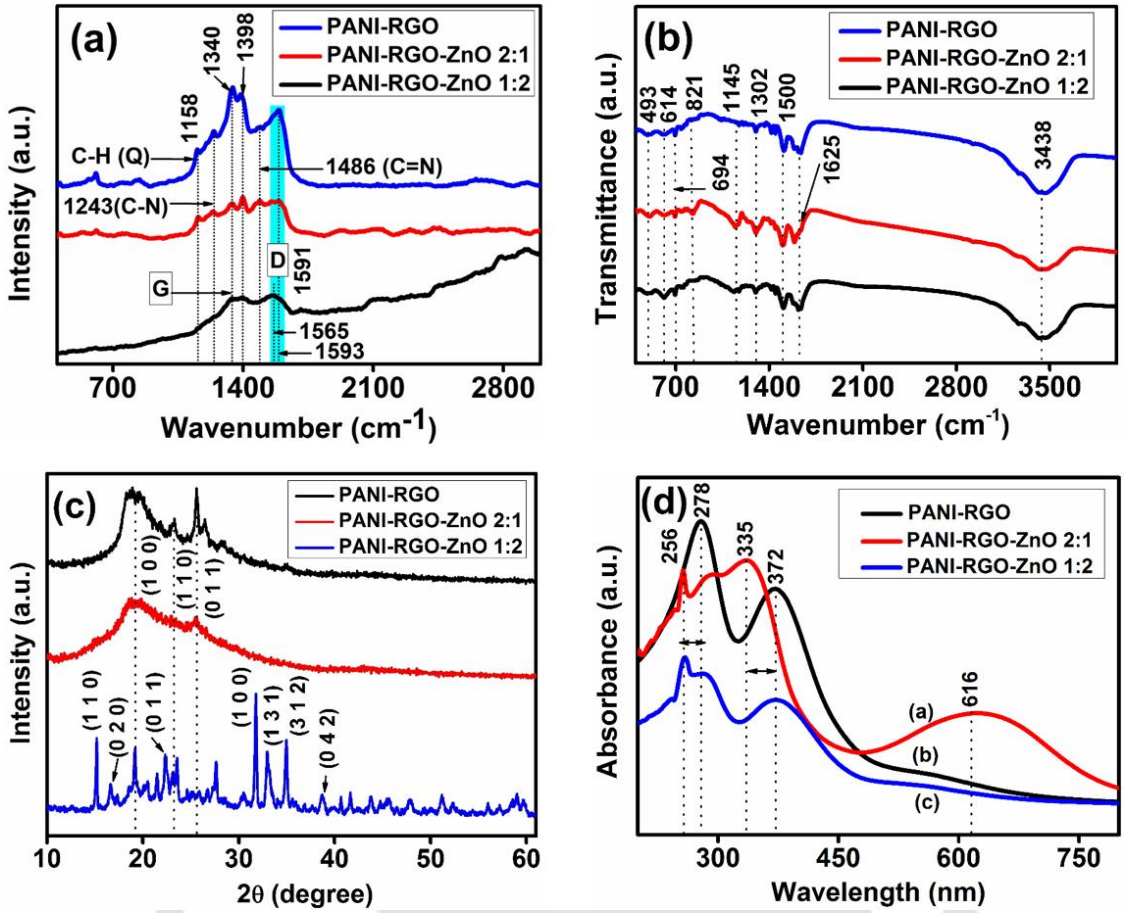

Figure 5.2. Structural analysis by (a) Raman spectra, (b) FTIR spectra, (c) XRD spectra, and (d) UV visible absorbance spectra, of all the nanocomposites.

FTIR spectra provide characteristics information regarding the presence of functional groups, molecular arrangement, and intermolecular bonding. Figure 5.2b shows the FTIR spectra of all the nanocomposites. The band vibrations at ~ 1145, ~ 1302, ~ 1500, and ~ 1625 cm^{-1} correspond to N=Q=N stretching mode of quinoid rings, C–N band stretching, C=C stretching mode of benzenoid rings, and quinoid stretching of C=C bands, respectively [23,36,37]. The characteristic band vibrations in the range of 400 to 694 cm^{-1} indicate the existence of ZnO nanostructure, as reported by Bera et al. [38]. The band at 3438 cm^{-1} corresponds to the intercalated –OH groups. The characteristic absorption spectra confirm the presence of PANI chains in the nanocomposites. The band absorption of PANI-RGO-ZnO composites is close to the PANI-RGO, indicating the growth of PANI in the composites. The ternary nanocomposites exhibit strong interactions as compared to the binary composite, suggesting a synergistic effect involving a strong π–π* interaction of the PANI matrix with RGO, and ZnO mediated by H-bonding and oxygen atoms, respectively.

The XRD spectra of PANI/RGO and PANI-RGO-ZnO 2:1 nanocomposites show broaden patterns in the range of 2θ = 10 to 30° that may be correlated to the presence of non-crystalline domains in the nanocomposite. (Figure 5.2c). The presence of non-crystalline domains contributes towards the enhancement of the surface area in 2:1 compared to 1:2 nanocomposite. It is noted that the diffraction peaks are correlated to the polycrystalline phase of the materials as the exhibited peaks have a combined region of broad and sharp peaks, which may be attributed to the presence of PANI chains. The diffraction peaks at 2θ = ~ 19° (1 0 0), ~ 23° (1 1 0), and ~ 25° (0 1 1) are associated with the semi-crystalline phase of PANI emeraldine salt [39,40]. The diffracted peaks of PANI-RGO-ZnO 2:1 and PANI-RGO are distinctly different from the PANI-RGO-ZnO 1:2, which is attributed to the higher wt% of PANI present in the nanocomposite, contributing towards an excellent growth of the PANI at the RGO surface. A similar observation was reported by Mostafaei and Zolriastaein [41] in terms of the crystalline peaks of PANI at different compositions (wt%) of ZnO. During in-situ polymerization, PANI had grown over the RGO and ZnO surfaces; hence PANI peaks are dominant at the 2θ = ~ 19° and ~ 25°. The increased wt% of ZnO facilitates the appearance of sharp crystalline peaks, and have constructed an ordered texture.

UV visible absorbance spectra (Figure 5.2d) of PANI-RGO has a π–π* transition peak at ~ 278 nm, showing a red shift relative to ZnO-based ternary composites. This red shift is due to the reduction of π–electrons in RGO layers. The peaks at ~ 372 and ~ 616 nm correspond to π–π* and π*–polaron band transitions in the benzenoid rings of PANI, respectively. The PANI-RGO-ZnO composites show a blue shift as compared to the PANI-RGO composite, which is attributed to the delocalization of π–electrons of RGO layers with excellent interactions of ZnO nanostructure [36,42]. In addition, the nanocomposite incorporated with a higher amount of ZnO has a smaller optical bandgap. Thus, PANI-RGO-ZnO 1:2 has a lower optical bandgap in comparison with PANI-RGO-ZnO 2:1. PANI/RGO shows a slightly higher bandgap than the PANI-RGO-ZnO 1:2 composite, signifying that the addition of ZnO decreased the bandgap. Below we have shown Figure 5.3 about the band gap. The structural properties of the constituting components of the nanocomposites (viz., PANI, RGO, and ZnO) have been shown in Figure 5.4a–d.

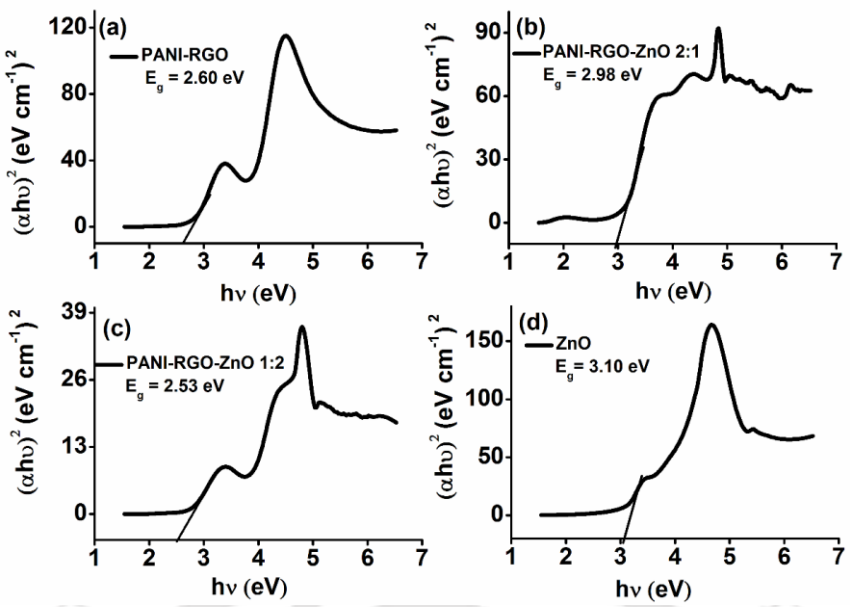

Figure 5.3. Optical bandgap energies of (a) PANI-RGO nanocomposite, (b) PANI-RGO-ZnO 2:1 nanocomposite, (c) PANI-RGO-ZnO 1:2 nanocomposites, and (d) ZnO nanoparticles.

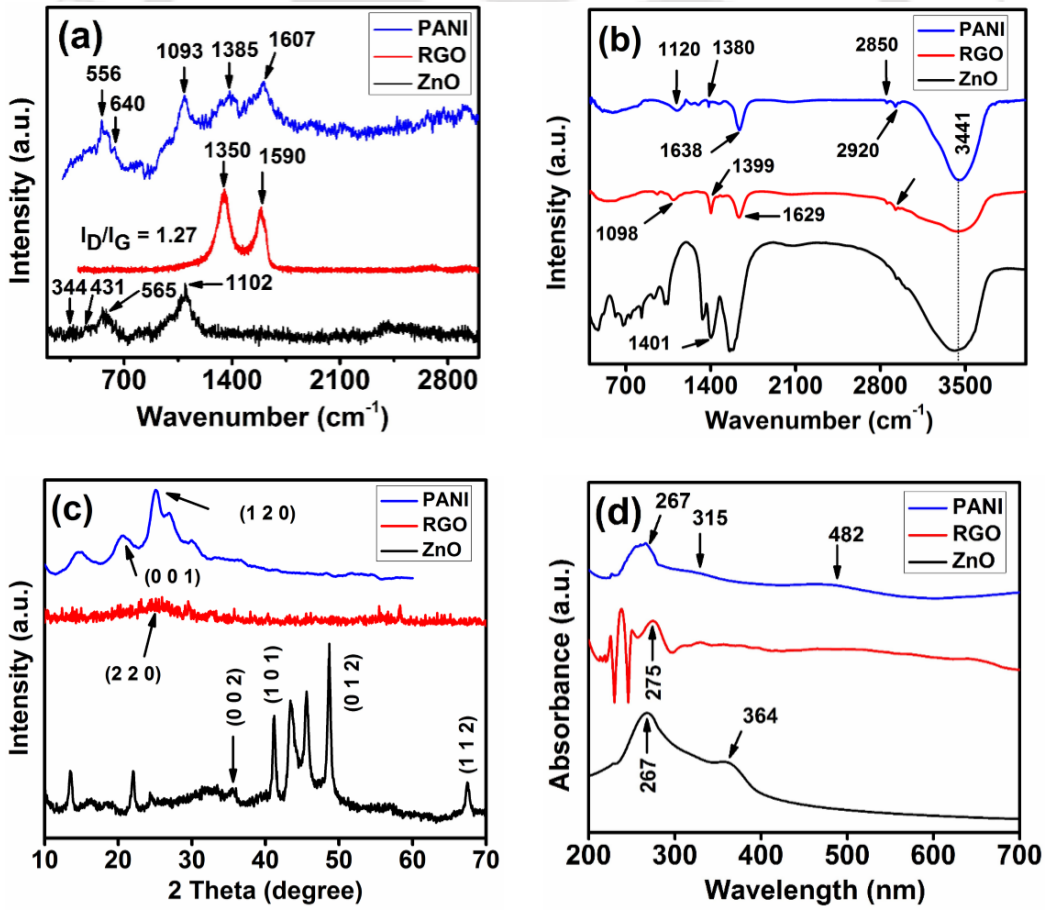

Figure 5.4. Structural characterizations of pure PANI, RGO, and ZnO nanomaterials: (a) Raman spectra, (b) FTIR spectra, (c) XRD patterns, and (d) UV absorbance spectra.

The structural information of pure PANI, RGO, and ZnO has been described by performing Raman spectra, as shown in Figure 5.4a. The samples were characterized in powder form of the PANI and ZnO, and spin-coated RGO thin film over glass substrates. The Peak intensities of pure PANI observed at 1093, 1607, and 1385 cm^{-1} are represented to C–N bond stretching, benzenoid, and quinoid stretching, respectively. The peak intensities at 1350 and 1590 cm^{-1} are associated with D and G bands with I_D/I_G of 1.27, shows defective few layers of RGO [43]. ZnO is n-type semiconductor consist of hexagonal structure with auxiliary optical phonon, represented as follows [44];

$$A_1+2B_1+E_1+2E_2 \quad (5.4)$$

Raman active polar splitting of phonons regarded transverse optical and longitudinal optical, attributed to A_1 and E_1, are found at the designated peaks of ~344 and ~565 cm^{-1}, respectively. The B_1 corresponds to infrared and Raman inactive mode. Further, two nonpolar modes of E_2 (high) and E_2 (low) are Raman active associated with the peak at 431 cm^{-1}, and ~ 1102 cm^{-1} reveals second-order modes of the ZnO compound [45].

FTIR spectra (Figure 5.4b) shows band absorption ~ 1560 – 1638 cm^{-1} and absorption peak ~ 3441 cm^{-1} for each molecular structure related to bending and stretching vibrations of the absorbed moisture and a hydroxyl group, respectively. The characteristic absorption peak ~ 1399 cm^{-1} and ~ 1098 cm^{-1} denoting C=C stretching and stretching vibrations of C=O bonding, respectively. The band vibrations at ~1380 and ~1120 cm^{-1} exhibit benzenoid and quinoid-benzenoid-quinoid units, respectively. The absorption peak of approximately 1640 cm^{-1} correlated to the PANI oxidation state reveals the C=C stretching of quinoid rings. The weak band absorption 2800–3000 cm^{-1} attributed to N–H and C–H stretching of PANI. The band absorption ~ 461 – 611 cm^{-1} representing the Zn–O bond stretching. The absorption peak ~1401 cm^{-1} is contributed by the bending vibrations of H–O–H [31,44].

The XRD patterns (Figure 5.4c) show crystallographic planes (0 0 1) and (1 2 0) at 2θ with the interplanar distance (d, nm) of ~ 20.1° (0.45 nm) and ~25° (0.35 nm), respectively are associated to perpendicular and parallel arrangement of semi-crystalline PANI chains [46]. The characteristic peak appears approximately at 2θ = 25° (2 2 0) shows the presence of RGO [28,47]. The characteristic planes (0 0 2), (0 1 2), (1 0 1) and (1 1 2) are allocated about at 2θ = 34.55º, 36.39°, 47.68º and 67.91º, suggesting hexagonal crystal structure of ZnO [48]. The data were correlated with the Match! Version: 3.7.1.132 software, and obtained the space group of 'p 63 mc' with the wurtzite structure. UV absorbance spectra (Figure 5.4d) of pure PANI at ~ 267, ~ 315, and ~ 482 nm correspond to π-π* electronic transition of benzenoid units, polaron and bipolaron transitions [49], confirmed the formation of PANI emeraldine salt. Further, RGO

shows the band at 251, and 275 nm due to the π–π* and n–π* transitions concur with C–C and C=O bonds, respectively. The absorbance peak around 275 nm is blue shifted, confirmed by the Das et al. [50], and corroborate about complete RGO formation. The band at ~ 364 nm signifies the presence of ZnO nanoparticles [51].

The morphologies of an agglomerated structure of PANI and layered morphology of RGO has have shown in Figure 5.5a – b that can be correlated to nanocomposites. Furthermore, the nanocomposites were found in a hierarchical order due to a 'nanopetal-shaped' structure of ZnO (Figure 5.6a).The morphologies of ZnO and PANI-RGO-ZnO are well agreed with the work reported by Ghanbari and Moloudi [52]. The FESEM image of PANI-RGO (Figure 5.6b) indicates the formation of randomly oriented PANI nanofibers over RGO layers. The morphology appears to be highly agglomerated, with an even distribution of PANI-RGO with an average size of ~ 102 nm that can be attributed to homogeneous polymerization of aniline monomers. Further, the morphology of PANI-RGO-ZnO 2:1 exhibits an excellent interaction between PANI and ZnO nanoparticles mediated by –NH groups. The ZnO petals are well functionalized with the RGO through carboxylic groups [53]. It is worthy to note that the growth of PANI chains is facilitated by the "scaffolds" of ZnO petals [23], and provides a continuous unidirectional growth of the PANI chains, as shown in Figure 5.6c. This specific structure of PANI chains shows an average size of ~ 107 nm, suggesting the development of a high surface area, which could be responsible for easy electron transport with an enhanced specific capacitance. The higher proportion of ZnO in PANI-RGO-ZnO 1:2 nanocomposite leads to the formation of an exfoliated morphology, as shown in Figure 5.6d. It is predicted that during polymerization, PANI chains grow in the exfoliated space between ZnO nanopetals and RGO layers. Moreover, 1:2 nanocomposite has a significant amount of ZnO, which facilitates various 2D active sites during PANI growth, results in an intercalated morphology.

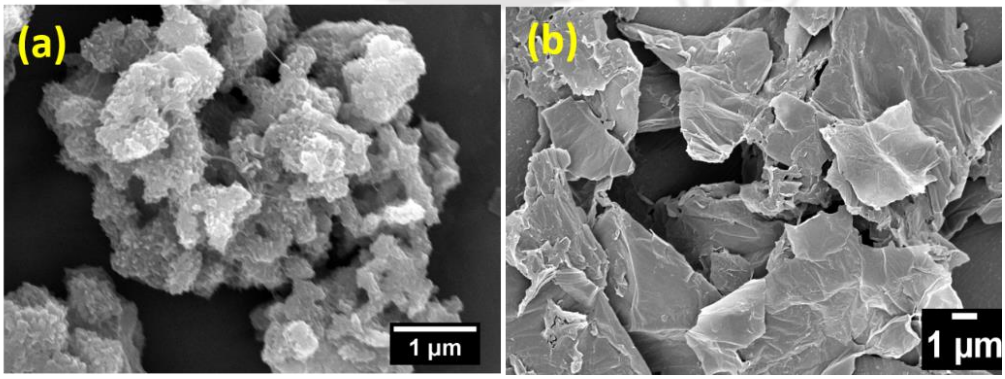

Figure 5.5. FESEM images of pure (a) PANI and (b) RGO.

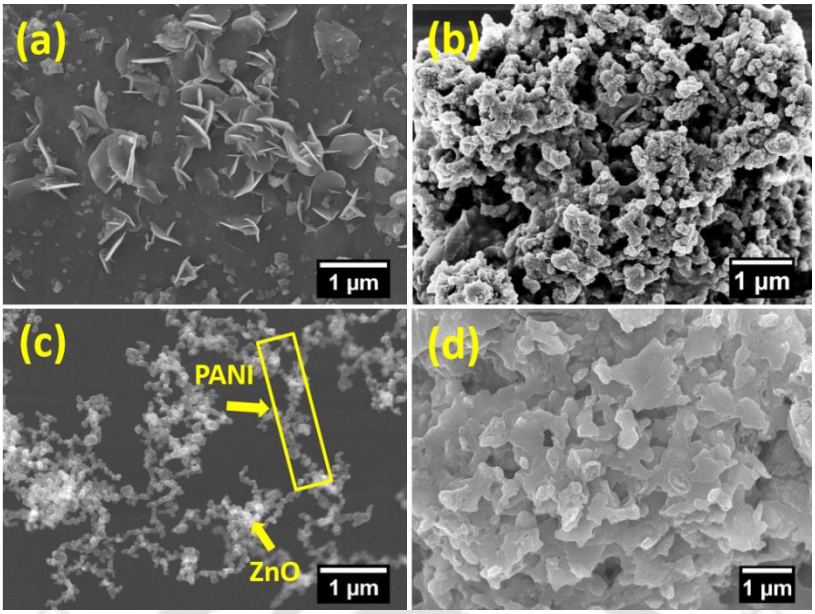

Figure 5.6. FESEM images show the morphology of (a) ZnO, (b) PANI-RGO binary nanocomposite, (c) PANI-RGO-ZnO 2:1 ternary nanocomposite, and (d) PANI-RGO-ZnO 1:2 ternary nanocomposites.

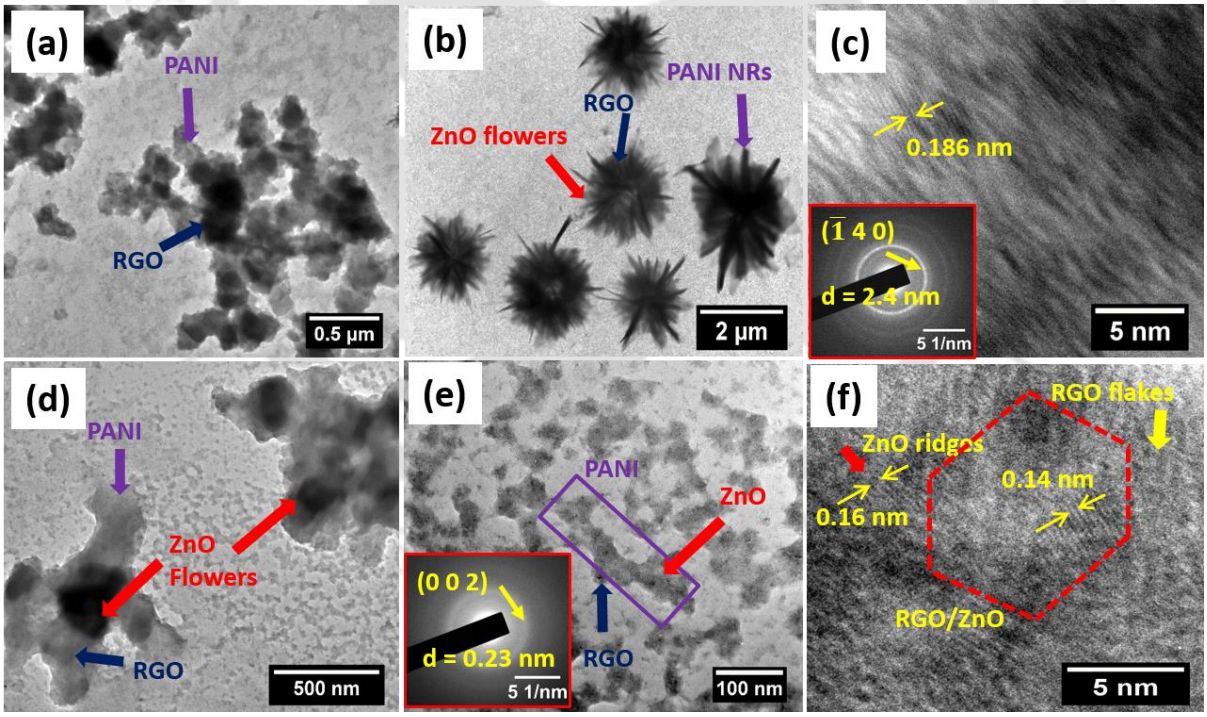

Figure 5.7. (a) FETEM image of PANI-RGO, (b) FETEM image of PANI-RGO-ZnO 2:1, (c) HRTEM image and inset shows a SAED pattern of the PANI-RGO-ZnO 2:1, (d-e) FETEM images at lower and higher resolution and inset of (e) is the SAED pattern of PANI-RGO-ZnO 1:2, and (f) is the HRTEM image.

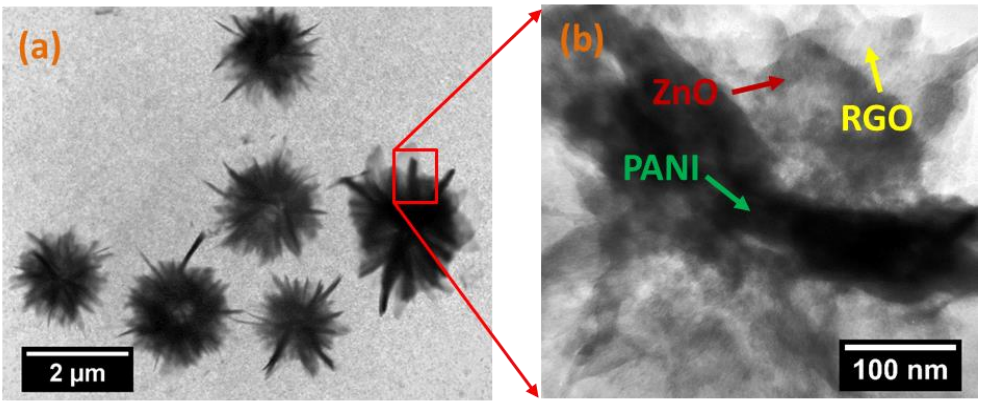

Figure 5.8. (a) FETEM image at low magnification, (b) FETEM image at high magnification of PANI-RGO-ZnO 2:1

Thus, the diffusional length of charge carriers increases that may result in a reduction in specific capacitance. Figure 5.7 exhibit FETEM images of the hierarchically ordered nanocomposites. PANI-RGO exhibits a uniform growth of PANI segments over the RGO surface (Figure 5.7a). Hence, RGO nanosheets are functionalized with anilinium ions during the in-situ polymerization of PANI. Figure 5.7b shows a highly agglomerated fibre structure of PANI-RGO, associated with charging localization that may reduce overall charge storage density. The ternary nanocomposite, PANI-RGO-ZnO 2:1, exhibits a uniformly distributed spherical flower shape morphology at low resolution (2 µm), as shown in Figure 5.7b. It is well displayed that PANI had grown to a significant chain length on ZnO and RGO surfaces, during polymerization (see Figure 5.6c) that would facilitate an excellent electrostatic charge delocalization via π–π* conjugation. The effect of confinement on polymer segments leads to increased ionic mobility, as reported by Elmahdy et al. [54] Therefore, the isotropically confined PANI segments with a higher surface to volume ratio and extended surface area in PANI-RGO-ZnO 2:1 would lead to a significant ion exchange ability with an enhanced specific capacitance. The HRTEM image (Figure 5.7c) explored the interplanar spacing (~ 0.186 nm) of the PANI-RGO-ZnO 2:1 nanocomposite. It is to be noted that the selected area diffraction (SAED) patterns (Figure 5.7c, inset) are indicative of the presence of polycrystalline phase with ($\bar{1}$ 4 0) plane with the planer spacing of ZnO ~ 2.4 nm. Figure 5.7d and 5.7e represent the geometrical arrangement of PANI-RGO-ZnO 1:2 with varying resolution (viz., 500 to 100 nm). The morphology appears to be a crystalline phase due to the presence of a large amount of ZnO (at PANI:ZnO = 1:2), as has been evidenced by the SAED pattern (Figure 5.7e, inset) with (0 0 2) plane at a lattice spacing of 0.23 nm. The HRTEM image (Figure 5.7f) exhibits a well-

organized hexagonal structure corresponding to ZnO and RGO-ZnO dispersion with the lattice spacing of 0.16 and 0.14 nm, respectively. As such results, 2:1 nanocomposite possesses an excellent interfacial interaction between RGO and ZnO that would facilitate direct charge transfer leading to a superior ionic diffusion during the redox mechanism, as compared to the other nanocomposites. Therefore, it may be concluded that the 2:1 nanocomposite would be more favourable in energy storage applications. The high resolution image of Figure 5.7b clearly exhibit the presence of all the components in the nanocomposite, as shown in Figure 5.8.

5.3.2. Thermal stability

The thermal degradation behavior of all the nanocomposites was observed by TGA, as shown in Figure 5.9a. The initial weight loss of ~ 2% at ~ 165 °C corresponds to the vaporization of water molecules. A gradual weight loss is observed in the temperature range of 165–287 °C, which is attributed to the degradation of PANI segments. The ternary nanocomposite PANI-RGO-ZnO 2:1 exhibits higher thermal stability compared to the 1:2 and PANI-RGO nanocomposite, which may be attributed to the high surface area, and partial decomposition of RGO-ZnO compositions. The third stage of degradation is observed in the range of 267 – 480 °C, corresponding to the RGO-ZnO decomposition. We observe a relatively less weight loss of 2:1 nanocomposite (~ 40% residue) compared to the 1:2 nanocomposite. The higher thermal stability of the ternary nanocomposite with the 2:1 ratio is ascribed to the homogeneous dispersion of PANI chains with the intercalated surfaces of RGO and ZnO, providing a better functionalization, as has been confirmed by FESEM analysis (Figure 5.6c).

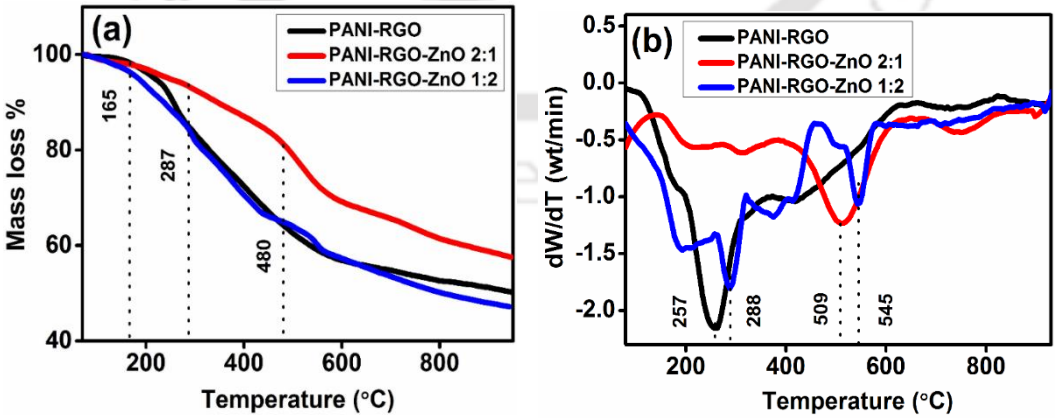

Figure 5.9. (a) Thermal stability analysis, and (b) differential thermogravimetric analysis of all the nanocomposites.

The differential thermogravimetric analysis (Figure 5.9b) also shows that 2:1 nanocomposite retains the lowest decomposition rate and weight loss, among all the nanocomposites.

5.3.3. Brunauer, Emmett, and Teller (BET) measurements

The specific surface area and related physical parameters have been estimated based on BET analyzer, as shown in Figure 5.10a. The N_2 adsorption-desorption isotherms of all the nanocomposites follow the type IV isotherms exhibiting a hysteresis loop, indicating the presence of mesoporous structure [55,56].

Table 5.1. The BET surface area, average particle size, BJH adsorption pore size and pores volume of the nanocomposites.

Nanocomposites	BET surface area ($m^2 g^{-1}$)	Average particle size (nm)	BJH ad. pore diameter (nm)	BJH ad. pores volume ($cm^3 g^{-1}$)
PANI-RGO	5.333	1124.955	14.486	0.03803
PANI-RGO-ZnO 2:1	7.220	831.004	14.764	0.05314
PANI-RGO-ZnO 1:2	0.4404	13613.972	11.307	0.00277

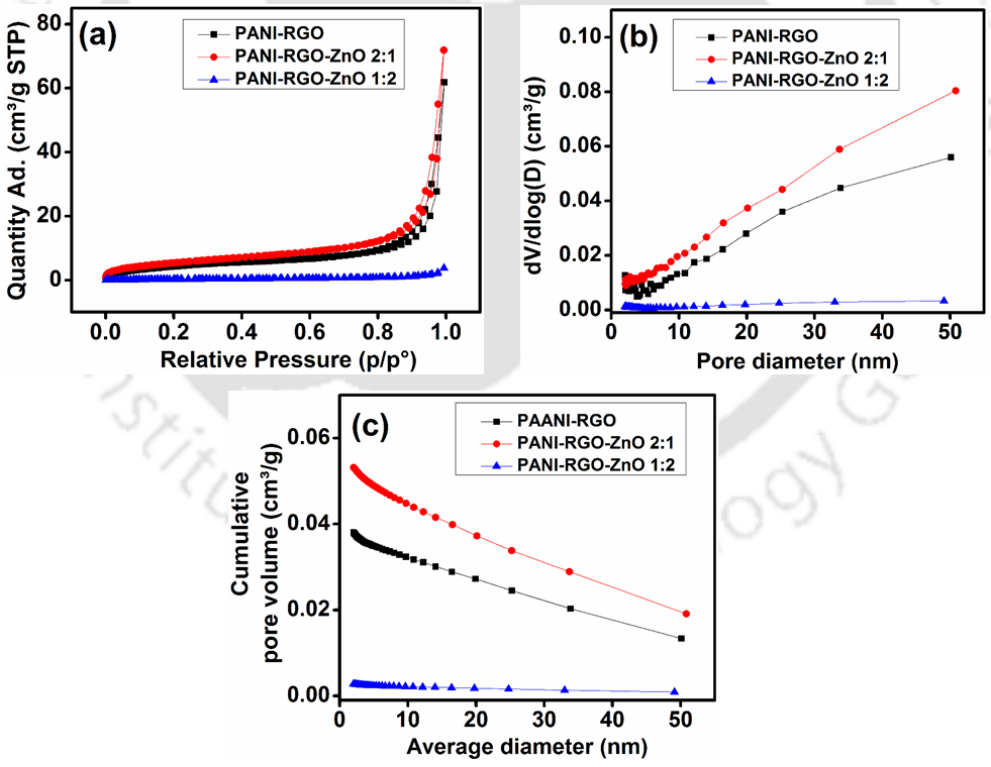

Figure 5.10. (a) N_2 adsorption and desorption isotherms, (b) BJH pore size distribution, and (c) distribution of cumulative pore volume of the nanocomposites.

Following the Barrett-Joyner-Halenda (BJH) method the pore size distributions and cumulative pore volume were analyzed, as shown in Figure 5.10b and 5.10c, respectively. The parameters related to BET measurements of the nanocomposites are listed in the Table 5.1. It is observed that the PANI-RGO-ZnO 2:1 exhibits the highest surface area with pore volume, and lowest particle size, indicting high surface to volume ratio. These structural arrangements are correlated with a smooth and symmetrical flower shape morphology, confirmed by FESEM (Figure 5.6c) and FETEM images (Figure 5.7b). The lower surface area of the 1:2 and PANI-RGO nanocomposites suggests the development of a non-uniform texture, indicating polycrystalline nature, as has been observed by the XRD pattern (see Figure 5.2c). Thus, high surface area corresponds to the high interfacial adhesion that can provide excellent diffusion of the ionic charge carriers during redox reactions in the electrolytic medium. Therefore, the PANI-RGO-ZnO 2:1 nanocomposite would be an excellent material for energy storage systems with an improved efficiency.

5.3.4. Electrochemical measurements

Initially, a three-electrode system was adopted to measure the electrochemical activities of PANI-RGO, PANI-RGO-ZnO 2:1, and PANI-RGO-ZnO 1:2 nanocomposites in 1M H_2SO_4 electrolyte to investigate the appropriate composite for the supercapacitor applications. Figure 5.11a shows the typical CV profile of the nanocomposites as the electrode materials measured at a fixed scan rate of 50 mV s^{-1} in the potential window of 0 – 0.8 V.

The quasi-rectangular shapes of the CV profile because of the redox mechanism manifest their ability of significant electronic charge accumulation and pseudocapacitive performance. However, potential below ~ 0.2 V, the CV curves slightly deviate from the rectangular shape, which may be attributed to the presence of an electrical double layer phenomenon. This electrical behavior may be caused by RGO [57]. The cyclic charge-discharge (CCD) characteristic responses of the fabricated electrode materials obtained at a constant current density of 0.35 mA g^{-1} are shown in Figure 5.11b. The quasi-linear behavior of the CCD curves is attributed to pseudo-capacitance with stable charge producing capability. The linear discharging curves exhibit a rapid voltage drop with the development of electrical double layer phenomena [58].

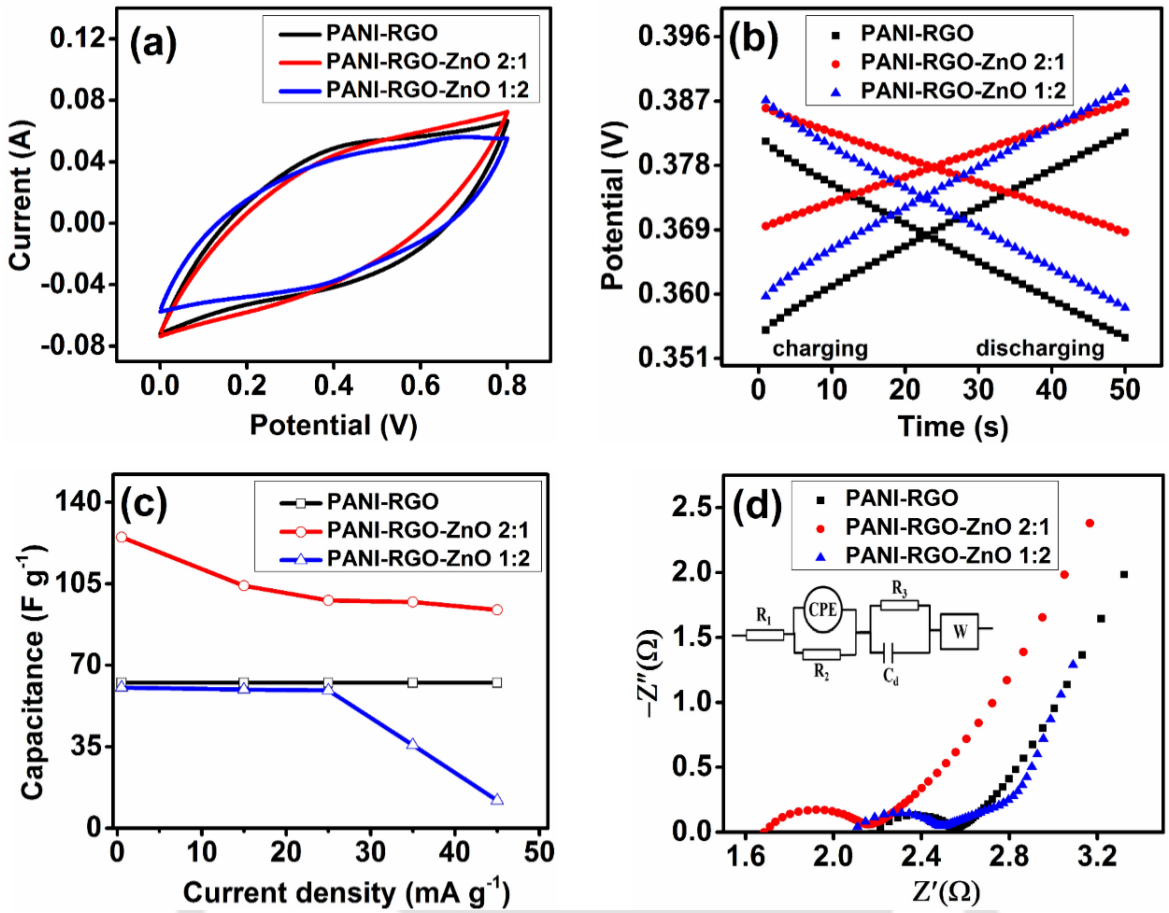

Figure 5.11. Three-electrode measurement of all the nanocomposites: (a) CV profile at a scan rate of 50 mV s^{-1}, (b) cyclic charge-discharge (CCD) measurements at a current density of 35 mA g^{-1}, (c) specific capacitance at various current densities, and (d) EIS measurements and inset shows an equivalent circuit diagram of PANI-RGO-ZnO 2:1 nanocomposite.

Among the three-electrode materials, PANI-RGO-ZnO 2:1 nanocomposite has recorded the lowest potential difference, exhibiting the higher specific capacitance. This behaviour could arise under the exceptional migration of electrocatalytic ions led by the π–conjugation in the PANI backbone of composites during the redox reactions. It can be predicted that a significant amount of PANI backbone in the 2:1 composite facilitates lower pH as compared to the 1:2 composite. A higher amount of ZnO offers a high pH that can transform the PANI emeraldine salt into the emeraldine base, decreasing the overall electrical conductivity. Figure 5.11c represents the capacitance vs. current density plots for all the nanocomposites. All the nanocomposites exhibit high C_s values at low current densities. The specific capacitances of PANI-RGO, PANI-RGO-ZnO 2:1, and PANI-RGO-ZnO 1:2 composites are ~ 63, ~ 125, and ~ 61 F g^{-1}, respectively, at a current density of 0.5 mA g^{-1}.

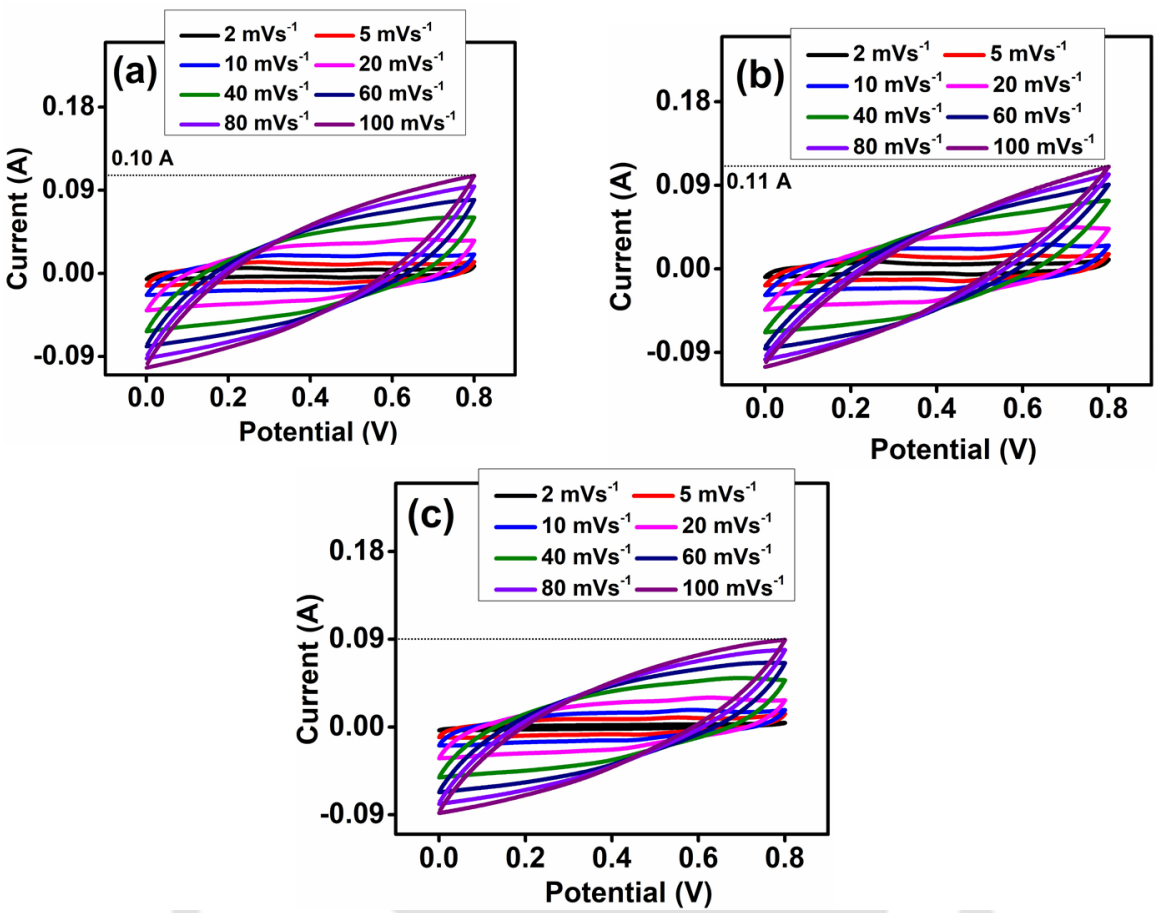

Figure 5.12. CV profile of (a) PANI-RGO, (b) PANI-RGO-ZnO 2:1, and (c) PANI-RGO-ZnO 1:2 nanocomposites at varying scan rates.

Particularly, PANI-RGO-ZnO 2:1 exhibits remarkably high C_s (almost twice that of other nanocomposites), which would be more favorable for energy storage applications.

The EIS measurements were carried out with an open circuit potential of 10 mV in the frequency range of 0.1 Hz to 100 kHz. The Nyquist plots of the nanocomposites were plotted, as shown in Figure 5.11d. In the high-frequency region, the x-axis intercept of the Nyquist plot provides the equivalent series resistance (ESR). We observe that PANI-RGO-ZnO 2:1 shows a lower ESR (~ 1.68 Ω at ~ 63 kHz) than the PANI-RGO (~ 2.21 Ω at ~ 15.8 kHz), and PANI-RGO-ZnO 1:2 (~ 2.10 Ω at ~ 15.8 kHz) nanocomposites. A certain amount of ZnO facilitates an excellent functionality with the carboxylic groups of RGO layers, provides an ordered nanostructure of the PANI matrix, and results in low ESR value. The charge transfer resistance (R_{ct}) of PANI-RGO, 2:1, and 1:2 nanocomposites are ~ 2.55 Ω, ~ 2.15 Ω, and ~ 2.50 Ω, respectively.

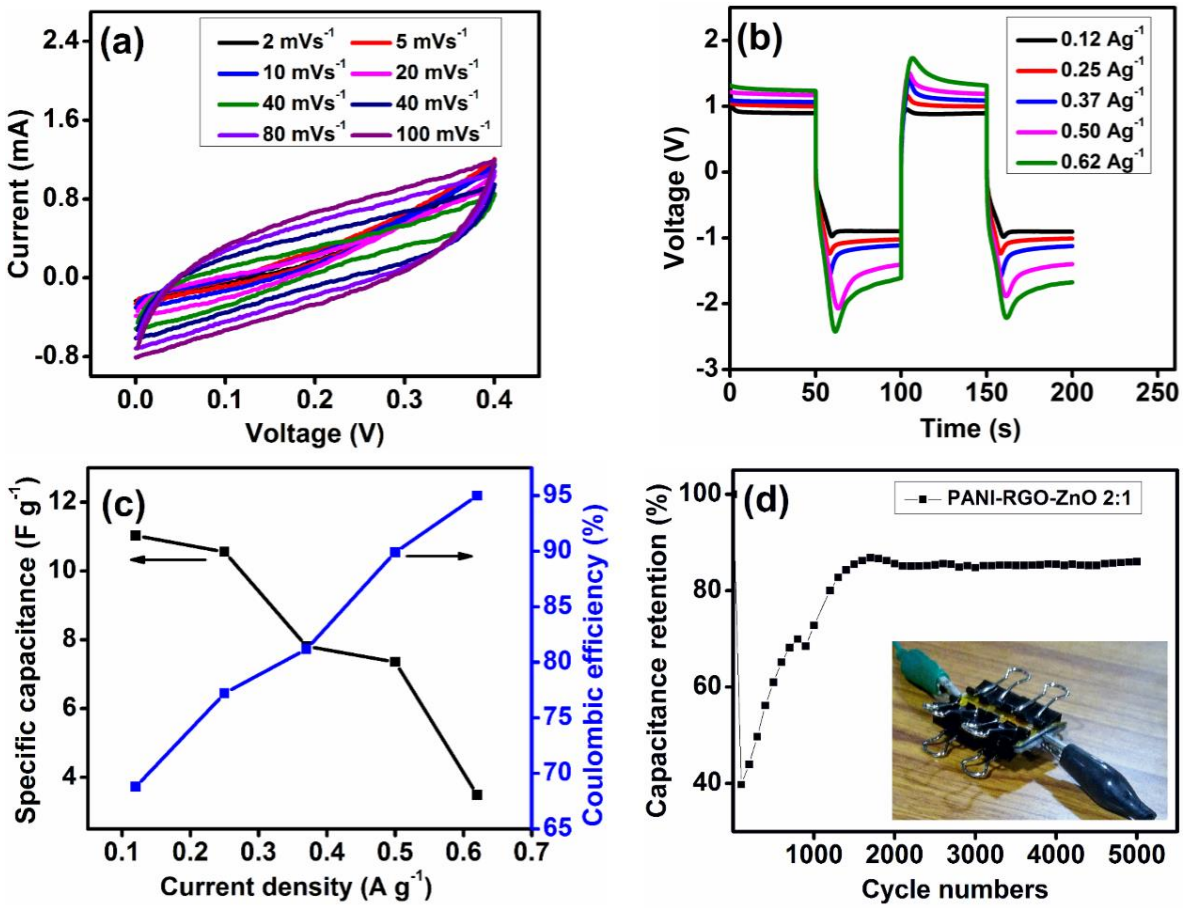

Figure 5.13. Two-electrode measurements of the PANI-RGO-ZnO 2:1 based symmetric supercapacitor device: (a) CV profile at various scan rates, (b) cyclic charge-discharge (CCD) measurements at various current densities, (c) specific capacitance and columbic efficiency against current densities, and (d) cyclic stability analysis.

It is noticed that the 2:1 nanocomposite would contribute to a significant ion transport due to the lower R_{ct} value. Therefore, EIS measurements have shown good electrocatalytic behavior of the PANI-RGO-ZnO 2:1, leading to improved C_s (Figure 5.11c). The ionic diffusional capacitance correlated to Warburg impedance that can be viewed in the low-frequency region by the inclined curves at ~ 45° [31], shows that 2:1 composite has a higher slope, which is attributed to an excellent capacitance response. An inset of Figure 5.11d, reveals an equivalent circuit diagram of the 2:1 nanocomposite. The characteristic measurements, as discussed above, conclude that PANI-RGO-ZnO 2:1 nanocomposite is a promising candidate for the supercapacitor applications. The CV profile of each nanocomposite at various scan rates (Figure 5.12) shows that PANI-RGO-ZnO 2:1 nanocomposite retains the maximum charge. Thus, the CV profile of the 2:1 nanocomposite shows maximum current (Figure 5.12a), and exhibits maximum region of the CV curve without redox peaks, indicating maximum specific

capacitance (C_s), ascribed to the synergistic effect between RGO layers, ZnO petals, and PANI chains [6,59].

Subsequently, two-electrode measurements of SSC device fabricated based on PANI-RGO-ZnO 2:1 nanocomposite are investigated. Figure 5.13a shows CV performance of SSC at various scan rates of 2 to 100 mV s^{-1} in the voltage range of 0 – 0.4 V. The symmetrical CV curves at a scan rate of up to 100 mV s^{-1}, are close to a rectangular shape without any deviation indicating high power capability of the SSC. The ionic diffusion has considerably been reduced in between the active electrode materials at higher scan rate [60]. Therefore, equal coordination is obtained between symmetric electrodes of PANI-RGO-ZnO 2:1 nanocomposite. The CCD graphs of SSC have been shown in Figure 5.13b at different current densities in the voltage range of ~ - 2 to ~ 1 V. These nonlinear characteristics responses are nearly square, exhibiting the pseudocapacitive performance of the PANI-RGO-ZnO 2:1 nanocomposite.

The estimated C_s of the SSC cell is ~ 11 F g^{-1} at a current density of 0.12 A g^{-1} (Figure 5.13c), which is significantly higher than the reported works such as, hierarchical nanosheets of $Ni(OH)_2$ derived from the Nickel Hexacyanoferrate (10.2 F g^{-1} at 25 mA) [61], carbon nanoballoon-based EDLCs (~ 7.5 F g^{-1} at 1 A g^{-1}) [62], and $Ni(OH)_2$ and $Fe_2O_3/RGO/Fe_3O_4$ supported ASC device (6.3 F g^{-1} at 20 mA cm^{-2}) [63]. The trend of specific capacitance (C_s) and columbic efficiency with current density (Figure 5.13c) shows good reversibility of the SSC device. Furthermore, a small voltage drop of the PANI-RGO-ZnO 2:1 electrode shows a satisfactory performance even at a higher current density, which is attributed to an excellent rate capability of the SSC device. The PANI-RGO-ZnO 2:1 electrode shows excellent cyclic performance and possesses high capacitance retention of ~ 85 % of the maximum capacity even after 5000 cycles (Figure 5.13d). An inset of Figure 5.13d shows a fabricated SSC device connected with two electrode network. We observe that C_s is being stabilized over the ~ 1000^{th} cycle, which is attributed to a superior lifespan and stability of the PANI-RGO-ZnO 2:1 electrode. There is no significant voltage drop (Figure 5.14) in the CCD graphs, denoting a low internal resistance (~ 80 Ω), and equivalent series resistance (ESR ~ 0.7 Ω) of the SSC device. A slightly negative region in the potential window may be due to a long discharging process and higher charge polarization.

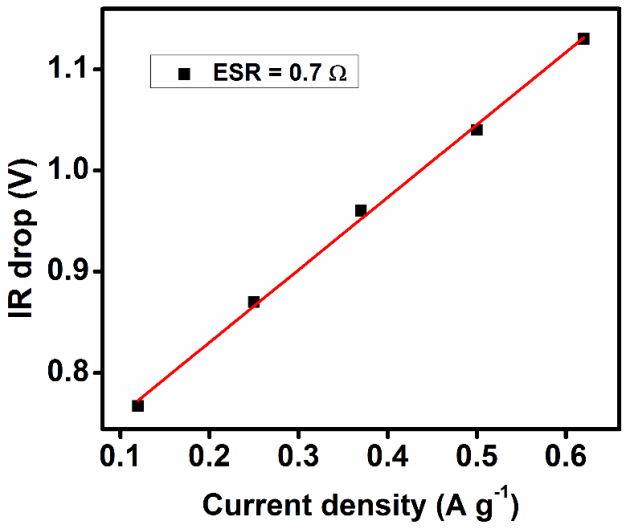

Figure 5.14. Analysis of IR drops during the charging-discharging of the supercapacitor based on PANI-RGO-ZnO 2:1 nanocomposite.

The EIS measurements based on an open circuit voltage provides the Nyquist plot of the first and last cycle of the PANI-RGO-ZnO 2:1 electrode in the frequency range of 0.1 Hz to 1 MHz (Figure 5.15a). The R_{ct} between symmetric electrodes is equivalent to the diameter of the semicircles. The SSC device shows more resistance at the first cycle than the last cycle, exhibiting an excellent performance of the supercapacitor. At the end of the cyclic process, a decrease in the electrode resistance strongly evidences the rapid charge transfer and a fast charging-discharging with an enhanced life cycle of the supercapacitor. In the last cycle, we observe that the Warburg line narrowly deviates towards the imaginary (– Z") axis, indicating that the PANI-RGO-ZnO 2:1 possesses a superior supercapacitance [6]. Following this, the equivalent circuit diagram (inset of Figure 5.15a) has been constructed, which explores the series resistance (R_1), charge transfer resistance (R_2), and Warburg impedance (W). The magnitudes of R_1, R_2, and W are contributed by the diffusional capacitance and double-layered pseudocapacitance. The estimated numerical values of all the electrical parameters are shown in Table 5.2. The minimum value of R_2 may be correlated with the substantial charge transport over the PANI-RGO-ZnO 2:1 electrode surface due to a high surface to volume ratio (see Table 5.1, BET measurements). Figure 5.15b shows the bode plot of the SSC device. In the high-frequency region (~ 100 kHz), the measured phase angle at ~ 62° (first cycle) and ~ 32° (last cycle) during cyclic stability are moving towards 90°, indicating an excellent capacitance behavior.

Table 5.2: Fitted electrical parameters of equivalent circuit diagrams during EIS measurements of cyclic stability.

Characteristic parameters	Last cycle	Fist cycle
R_1 (Ω)	14.86	4.307
R_2 (Ω)	14.74	57.13
CPE $_{constant}$	0.001233	0.0156
R_3 (Ω)	48.27	59.41
C_d (Farad)	0.0001381	0.004591
W $_{constant}$	0.04946	Not exist

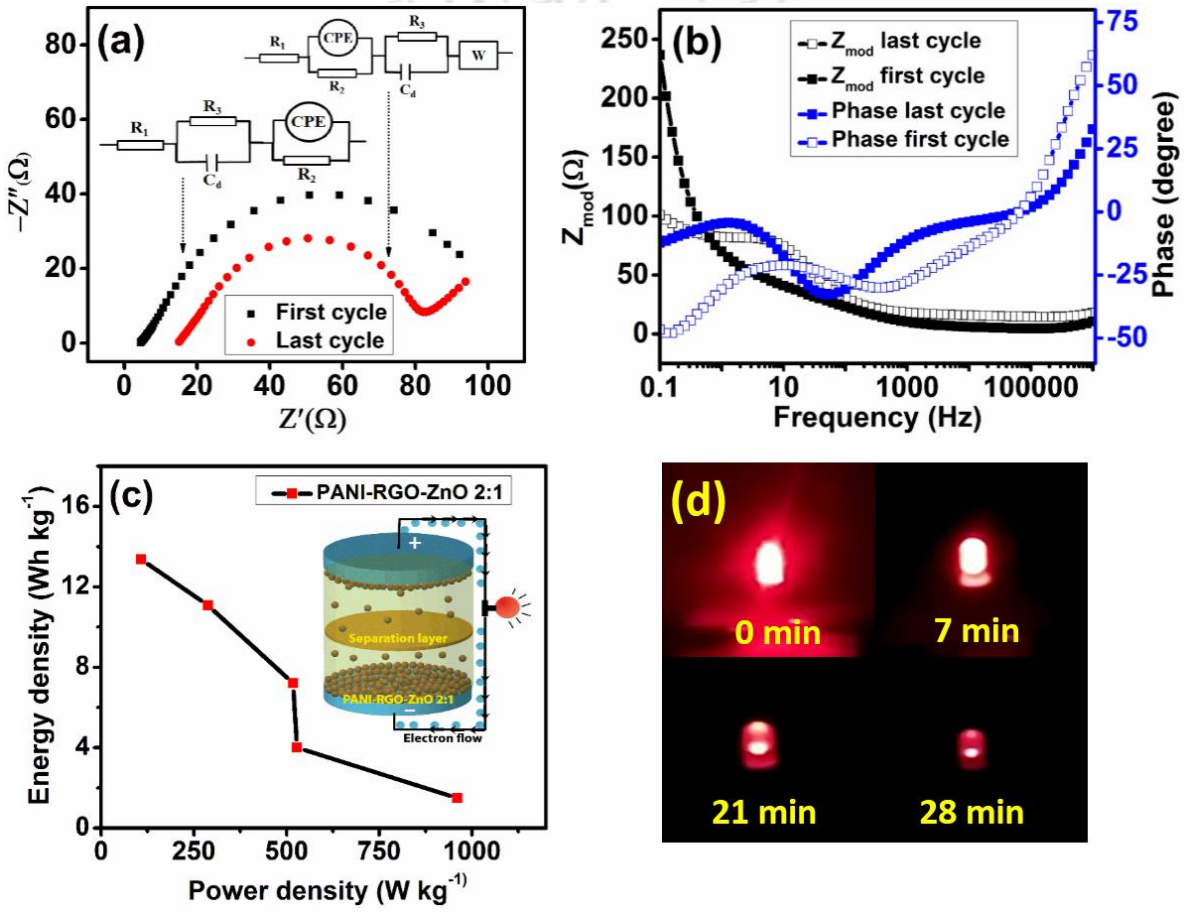

Figure 5.15. The symmetric devices of PANI-RGO-ZnO 2:1 electrode show (a) EIS spectra with equivalent circuit diagrams, (b) bode plots, (c) Ragone plot, and the inset shows a schematic diagram of symmetric device, and (d) powering of a LED.

At this frequency, the corresponding time constant ($\tau_0 = \frac{1}{f_0}$) for both the phase angles is ~ 0.01 ms, which is smaller than τ_0 reported by Taberna et al. [64]. The smaller τ_0 demonstrates a fast discharge process of the SSC device, which is attributed to the high power density. In contrast,

the maximum slope of the graphs in the low-frequency domain (< 10 Hz) corresponds to the Warburg response due to the rapid diffusion of charge carriers across the electrode surface. Therefore, an additional capacitance is ascribed in enhancing the overall capacitance. In the low-frequency region, phase angles are ~ -50° (at 2 Hz) and ~ -10° (at 10 Hz) for the before and after cyclic stability (Figure 5.15b), respectively, suggesting that the device could be functional as an ideal capacitor [65]. Further, slightly larger τ_0 (0.5 s and 0.1 s) at low frequency can be correlated to the long discharging time of the SSC, indicating a high energy density. We have estimated the overall τ_0 for the first and last cycles as 0.26 s and 0.06 ms, respectively. The decrease of the time constant with the number of cycles represents a rapid charging-discharging behaviour with a long lifespan of the SSC device. The impedance at each cycle gradually decreases with the increasing frequency, indicating excellent pseudocapacitive behaviour. The practical applications of the SSC device can be assessed based on the specific energy density (ED) and specific power density (PD). The specific energy and power densities are plotted in the Ragone plot, as shown in Figure 5.15c. The inset of Figure 5.15c shows a schematic arrangement of SSC device, glow an LED with an operating voltage of ~ 4 V. The calculations have been done by using equations 5.2 and 5.3 (see Method section for details).

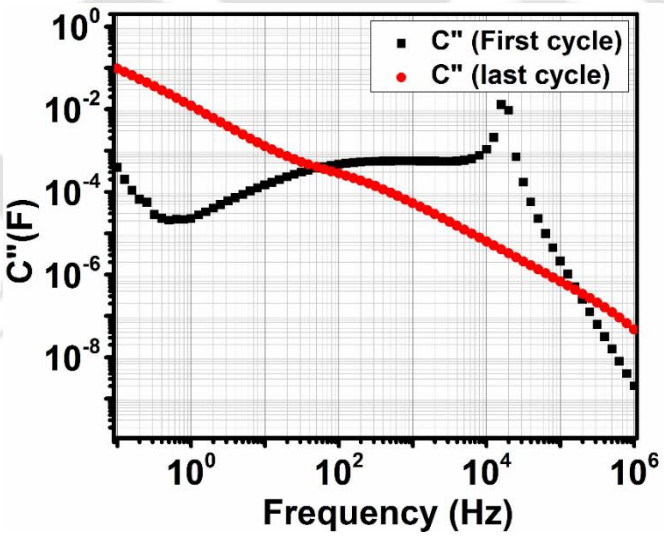

Figure 5.16. The graph of capacitance (C") against the frequency of the SSC device of PANI-RGO-ZnO 2:1.

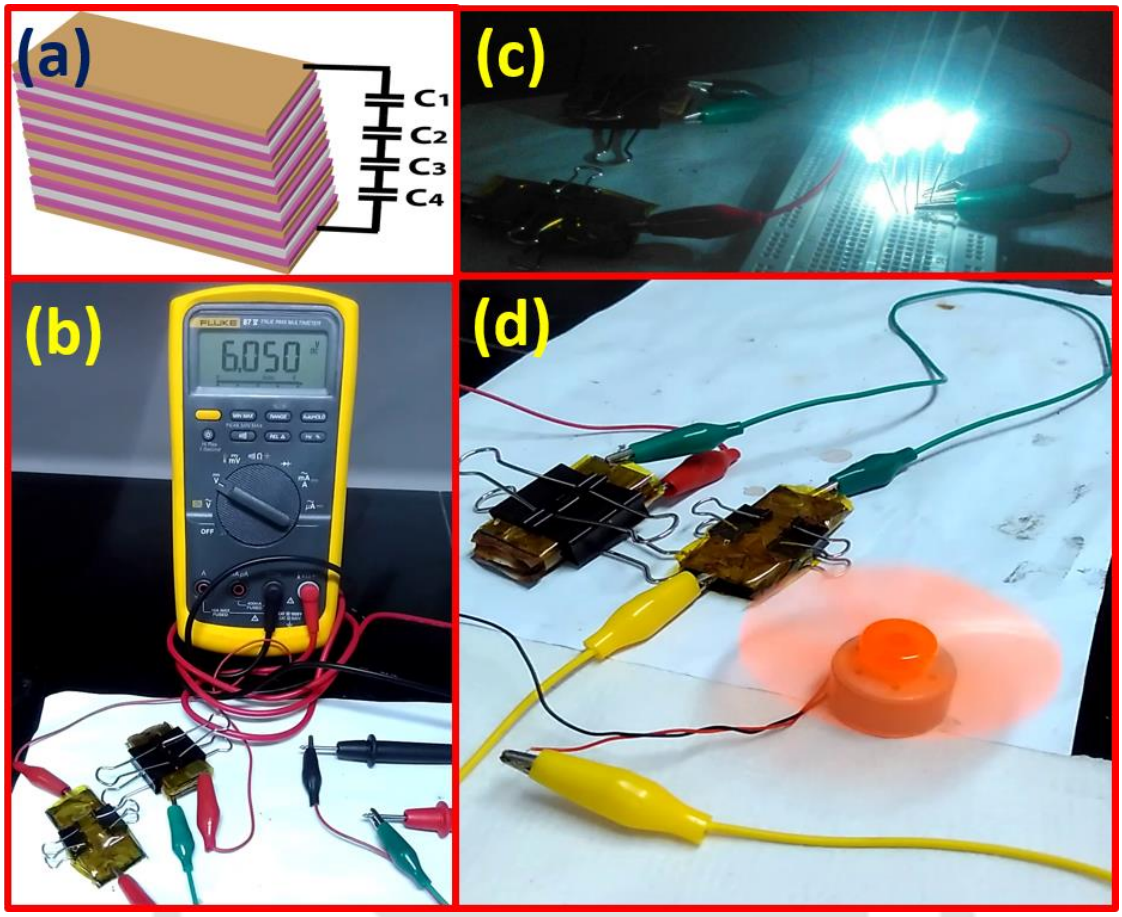

Figure 5.17. Photographs of (a) schematic diagram of STSC, (b) real-time monitoring of output voltage, (c) glowing a pair of LEDs, and (d) operation of a DC motor.

The SSC device provides a maximum ED and PD of 13.36 Wh kg^{-1} and 108 W kg^{-1}, respectively, at a current density of 0.12 A g^{-1}, and minimum ED and PD of 1.5 Wh kg^{-1} and 961 W kg^{-1}, respectively, at a current density of 0.62 A g^{-1}. The ability of energy storage in terms of ED and PD is well comparable to the other reported devices. For example, the ASC device by Marappan and Kaipannan et al. have shown ED and PD as 7.7 Wh kg^{-1} and 10.8 W kg^{-1} [61], respectively. Graphene-PANI mesoporous electrode materials prepared by Wang et al. have shown 11.3 Wh kg^{-1} (ED) and 106.7 W kg^{-1} (PD) [66]. Nitrogen and boron co-doped porous carbon electrode materials developed by Guo and Gao et al. have shown 3.8 Wh kg^{-1} (ED) and 165 W kg^{-1} (PD) [67]. The solid-state supercapacitor device by Wu et al. have shown 4.1Wh kg^{-1} (ED) and 400 W kg^{-1} (PD) [68]. The practical application of the SSC has been demonstrated by glowing a red LED and recorded the total time of the discharging process. Subsequently, an assembly of three SSC devices was made in series and charged for five minutes. After charging, the assembly took ~ 30 minutes to discharge completely, which

showed an excellent efficiency as an energy storage device (Figure 5.15d. The imaginary portion of the capacitance (C", F), a crucial parameter that provides details on energy losses in the SSC device through the respective irreversible processes (see Figure 5.16), is described using the following relation [69].

$$C''=\frac{Z'(\omega)}{\omega\times|Z(\omega)|^2} \qquad (5.5)$$

where, $Z'(\omega)$ is the real impedance, ω is the frequency of the AC signals, and $|Z(\omega)|^2$ is the modulus of the real and imaginary impedances, during impedance measurements. The SSC device could be applied in other applications too. To validate the operations, the SSC device has further been demonstrated by designing a separate tandem structure of the supercapacitors. In this system, four SSC devices are arranged in a compact layer-by-layer arrangement that appears to be equivalent to a solid dry battery (Figure 5.17a). The resultant STSC device structure is charged for ~ 5 min and obtained a wide expressive voltage of ~ 6.0 V (Figure 5.17b). As results, we have glowed a bunch of white LEDs having an operating voltage of ~ 6.0 V (Figure 5.17c) and observed that the STSC device exhibits excellent performance. We have also operated a DC motor at ~ 5.0 V for more than 10 s (Figure 5.17d). We have summarized our research output in a short abstract in Figure 5.18, demonstrating multiple applications. These applications substantiate that the PANI-RGO-ZnO 2:1 nanocomposite shows extraordinary supercapacitive applications with high power and energy density.

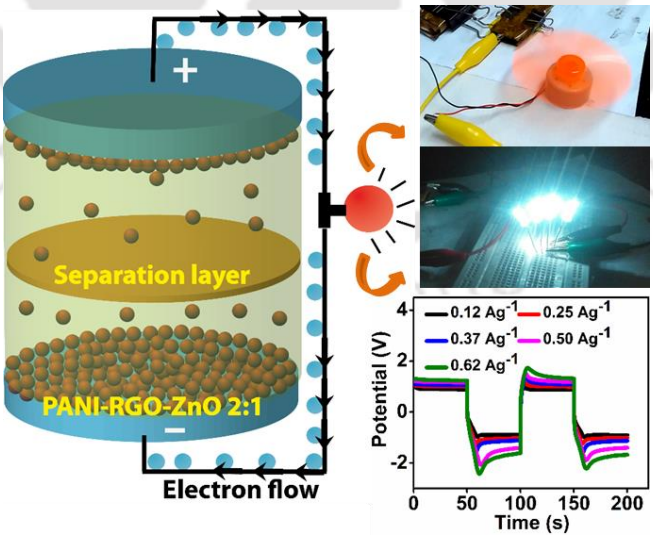

Figure 5.18. Fabricated SSC device with the characteristics applications.

5.4. Conclusions

A judicious choice of nanofillers can primarily enhance the electrochemical properties of a polymer nanocomposite comprising of conducting polymer. An adequate proportion and uniform mixing of nanofillers into the polymer matrix largely dictate the property enhancement of the nanocomposite. In this work, we report the preparation of ternary nanocomposites of PANI, RGO, and ZnO by varying the ratio of PANI and ZnO, keeping RGO fixed. The in-situ polymerization method of PANI ensures the formation of a well-mixed, homogenous composite. The presence of RGO and ZnO significantly enhances the electrochemical properties of the composites. The combination of PANI (p-type) and ZnO (n-type) yields a synergistic effect in the presence of RGO, which further facilitates the charge storage property. Therefore, the ternary nanocomposite appears to be an excellent material for supercapacitor. The detailed morphological studies show the presence of polycrystalline structures, which are responsible for the easy charge transport. Among all the nanocomposite, the PANI-RGO-ZnO 2:1 exhibits the superior electrochemical activities, high cyclic stability, and highest specific capacitance, including fast charge-discharge performance. The PANI nanorods with a flower-shaped morphology are intercalated by RGO and ZnO (with a high band gap, ~ 3.3 eV), resulting in an excellent material for energy storage. The fabricated SSC and STSC devices based on PANI-RGO-ZnO 2:1 nanocomposite exhibit an enhanced energy density and power density. We have observed an exceptional charge storage behavior of the SSC device, which may be due to a short diffusion length of electronic charge carriers in the PANI-RGO-ZnO 2:1 nanocomposite. The STSC device exhibits an improved energy storage behavior by glowing LED lights for ~ 30 minutes for a charging time of 5 minutes.

References:

[1] L. Liu, Y. Yu, C. Yan, K. Li, Z. Zheng, *Nat. Commun.* **2015**, *6*, 7260.

[2] H. Xu, X. Hu, H. Yang, Y. Sun, C. Hu, Y. Huang, *Adv. Energy Mater.* **2015**, *5*, 1401882.

[3] X. Chen, H. Lin, J. Deng, Y. Zhang, X. Sun, P. Chen, X. Fang, Z. Zhang, G. Guan, H. Peng, *Adv. Mater.* **2014**, *26*, 8126.

[4] L. Smith, B. Dunn, *Science* **2015**, *350*, 918.

[5] J. Jiang, Y. Li, J. Liu, X. Huang, C. Yuan, X. W. (David) Lou, *Adv. Mater.* **2012**, *24*, 5166.

[6] S. Palsaniya, H. B. Nemade, A. K. Dasmahapatra, *Polymer* **2018**, *150*, 150.

[7] J. Ji, L. L. Zhang, H. Ji, Y. Li, X. Zhao, X. Bai, X. Fan, F. Zhang, R. S. Ruoff, *ACS Nano* **2013**, *7*, 6237.

[8] K. Nomura, H. Nishihara, N. Kobayashi, T. Asada, T. Kyotani, *Energy Environ. Sci.* **2019**, *12*, 1542.

[9] K. Krishnan, P. Jayaraman, S. Balasubramanian, U. Mani, *J. Mater. Chem. A* **2018**, *6*, 23650.

[10] Y. Wang, Y. Song, Y. Xia, *Chem. Soc. Rev.* **2016**, *45*, 5925.

[11] Y. Zhu, S. Murali, M. D. Stoller, K. J. Ganesh, W. Cai, P. J. Ferreira, A. Pirkle, R. M. Wallace, K. A. Cychosz, M. Thommes, D. Su, E. A. Stach, R. S. Ruoff, *Science* **2011**, *332*, 1537.

[12] L. Manjakkal, C. G. Núñez, W. Dang, R. Dahiya, *Nano Energy* **2018**, *51*, 604.

[13] S. Zhang, N. Pan, *Adv. Energy Mater.* **2015**, *5*, 1401401.

[14] Z. Zhang, K. Chi, F. Xiao, S. Wang, *J. Mater. Chem. A* **2015**, *3*, 12828.

[15] X. Li, C. Zhang, S. Xin, Z. Yang, Y. Li, D. Zhang, P. Yao, *ACS Appl. Mater. Interfaces* **2016**, *8*, 21373.

[16] G. Han, Y. Liu, L. Zhang, E. Kan, S. Zhang, J. Tang, W. Tang, *Sci. Rep.* **2014**, *4*, 4824.

[17] X. Lu, M. Yu, G. Wang, T. Zhai, S. Xie, Y. Ling, Y. Tong, Y. Li, *Adv. Mater.* **2013**, *25*, 267.

[18] A. B. Djurišić, X. Chen, Y. H. Leung, A. M. C. Ng, *J. Mater. Chem.* **2012**, *22*, 6526.

[19] L. S. Aravinda, K. K. Nagaraja, H. S. Nagaraja, K. U. Bhat, B. R. Bhat, *Electrochimica Acta* **2013**, *95*, 119.

[20] X.-M. Cao, Z.-B. Han, *Chem. Commun.* **2019**, *55*, 1746.

[21] A. Mekki, Z. Ait-Touchente, S. Samanta, A. Singh, R. Mahmoud, M. M. Chehimi, D. K. Aswal, *Macromol. Chem. Phys.* **2016**, *217*, 1136.

[22] R. Karthik, S. Thambidurai, *J. Mater. Sci. Mater. Electron.* **2017**, *28*, 9836.

[23] S. Bera, A. Naskar, M. Pal, S. Jana, *RSC Adv.* **2016**, *6*, 40854.

[24] W. K. Chee, H. N. Lim, N. M. Huang, *Int. J. Energy Res.* **2015**, *39*, 111.

[25] K. Ghanbari, M. Moloudi, *Anal. Biochem.* **2016**, *512*, 91.

[26] H. Wu, S. Lin, C. Chen, W. Liang, X. Liu, H. Yang, *Mater. Res. Bull.* **2016**, *83*, 434.

[27] X. Zhang, J. Wu, G. Meng, X. Guo, C. Liu, Z. Liu, *Appl. Surf. Sci.* **2016**, *366*, 486.

[28] D. C. Marcano, D. V. Kosynkin, J. M. Berlin, A. Sinitskii, Z. Sun, A. Slesarev, L. B. Alemany, W. Lu, J. M. Tour, *ACS Nano* **2010**, *4*, 4806.

[29] S. Cho, M. Kim, J. S. Lee, J. Jang, *ACS Appl. Mater. Interfaces* **2015**, *7*, 22301.

[30] R. A. Talib, M. J. Abdullah, N. M. Ahmed, S. M. Mohammad, M. Bououdina, *Appl. Phys. A* **2016**, *122*, 540.

[31] R. Karthik, S. Thambidurai, *J. Mater. Sci. Mater. Electron.* **2017**, *28*, 9836.

[32] V. Sahu, S. Goel, R. K. Sharma, G. Singh, *Nanoscale* **2015**, *7*, 20642.

[33] M. Kim, C. Lee, J. Jang, *Adv. Funct. Mater.* **2014**, *24*, 2489.

[34] M. Cochet, G. Louarn, S. Quillard, J. P. Buisson, S. Lefrant, *J. Raman Spectrosc.* **2000**, *31*, 1041.

[35] Y. Zhang, J. Liu, Y. Zhang, J. Liu, Y. Duan, *RSC Adv.* **2017**, *7*, 54031.

[36] S. Chatterjee, R. K. Layek, A. K. Nandi, *Carbon* **2013**, *52*, 509.

[37] H. Zhang, R. Zong, Y. Zhu, *J. Phys. Chem. C* **2009**, *113*, 4605.

[38] S. Bera, M. Ghosh, M. Pal, N. Das, S. Saha, S. K. Dutta, S. Jana, *RSC Adv.* **2014**, *4*, 37479.

[39] S. Palsaniya, H. B. Nemade, A. K. Dasmahapatra, *ACS Appl. Polym. Mater.* **2019**, *1*, 647.

[40] U. Rana, S. Malik, *Chem. Commun.* **2012**, *48*, 10862.

[41] A. Mostafaei, A. Zolriasatein, *Prog. Nat. Sci. Mater. Int.* **2012**, *22*, 273.

[42] Y. Xia, J. M. Wiesinger, A. G. MacDiarmid, A. J. Epstein, *Chem. Mater.* **1995**, *7*, 443.

[43] M. P. Lavin-Lopez, J. L. Valverde, M. C. Cuevas, A. Garrido, L. Sanchez-Silva, P. Martinez, A. Romero-Izquierdo, *Phys. Chem. Chem. Phys.* **2014**, *16*, 2962.

[44] S. B. Rana, R. P. P. Singh, S. Arya, *J. Mater. Sci. Mater. Electron.* **2017**, *28*, 2660.

[45] Y.-L. Chen, Z.-A. Hu, Y.-Q. Chang, H.-W. Wang, Z.-Y. Zhang, Y.-Y. Yang, H.-Y. Wu, *J. Phys. Chem. C* **2011**, *115*, 2563.

[46] Q. Yao, Q. Wang, L. Wang, Y. Wang, J. Sun, H. Zeng, Z. Jin, X. Huang, L. Chen, *J. Mater. Chem. A* **2014**, *2*, 2634.

[47] M. Fathy, A. Gomaa, F. A. Taher, M. M. El-Fass, A. E.-H. B. Kashyout, *J. Mater. Sci.* **2016**, *51*, 5664.

[48] V. Sahu, S. Goel, R. K. Sharma, G. Singh, *Nanoscale* **2015**, *7*, 20642.

[49] N. J. Al-Thani, J. Bhadra, D. Abdulmalik, I. Al-Qaradawi, A. Alashraf, N. K. Madi, *Desalination Water Treat.* **2016**, *57*, 27374.

[50] A. K. Das, M. Srivastav, R. K. Layek, M. E. Uddin, D. Jung, N. H. Kim, J. H. Lee, *J. Mater. Chem. A* **2013**, *2*, 1332.

[51] N. Senthilkumar, E. Nandhakumar, P. Priya, D. Soni, M. Vimalan, I. V. Potheher, *New J. Chem.* **2017**, *41*, 10347.

[52] Kh. Ghanbari, M. Moloudi, *Anal. Biochem.* **2016**, *512*, 91.

[53] P. V. Kamat, *J. Phys. Chem. Lett.* **2010**, *1*, 520.

[54] M. M. Elmahdy, K. Chrissopoulou, A. Afratis, G. Floudas, S. H. Anastasiadis, *Macromolecules* **2006**, *39*, 5170.

[55] N. Li, G. Liu, C. Zhen, F. Li, L. Zhang, H.-M. Cheng, *Adv. Funct. Mater.* **2011**, *21*, 1717.

[56] Z.-F. Li, H. Zhang, Q. Liu, L. Sun, L. Stanciu, J. Xie, *ACS Appl. Mater. Interfaces* **2013**, *5*, 2685.

[57] X. Hong, B. Zhang, E. Murphy, J. Zou, F. Kim, *J. Power Sources* **2017**, *343*, 60.

[58] Y. Jiang, J. Liu, *ENERGY Environ. Mater.* **2019**, *2*, 30.

[59] C. Chen, G. Xu, X. Wei, L. Yang, *J. Mater. Chem. A* **2016**, *4*, 9900.

[60] Q. Lv, K. Chi, Y. Zhang, F. Xiao, J. Xiao, S. Wang, K. P. Loh, *J. Mater. Chem. A* **2017**, *5*, 2759.

[61] S. Kaipannan, S. Marappan, *Sci. Rep.* **2019**, *9*, 1104.

[62] Y. Suda, A. Mizutani, T. Harigai, H. Takikawa, H. Ue, Y. Umeda, *AIP Conf. Proc.* **2017**, *1807*, 020022.

[63] C. Zhao, X. Shao, Y. Zhang, X. Qian, *ACS Appl. Mater. Interfaces* **2016**, *8*, 30133.

[64] P. L. Taberna, P. Simon, J. F. Fauvarque, *J. Electrochem. Soc.* **2003**, *150*, A292.

[65] M. F. El-Kady, V. Strong, S. Dubin, R. B. Kaner, *Science* **2012**, *335*, 1326.

[66] Q. Wang, J. Yan, Z. Fan, T. Wei, M. Zhang, X. Jing, *J. Power Sources* **2014**, *247*, 197.

[67] H. Guo, Q. Gao, *J. Power Sources* **2009**, *186*, 551.

[68] Z.-S. Wu, A. Winter, L. Chen, Y. Sun, A. Turchanin, X. Feng, K. Müllen, *Adv. Mater.* **2012**, *24*, 5130.

[69] A. V. Radhamani, K. M. Shareef, M. S. R. Rao, *ACS Appl. Mater. Interfaces* **2016**, *8*, 30531.

Chapter-6

Heterostructured Layer Growth of Polyaniline by Vacuum Thermal Evaporation and Fabrication of Thin-Film Capacitors

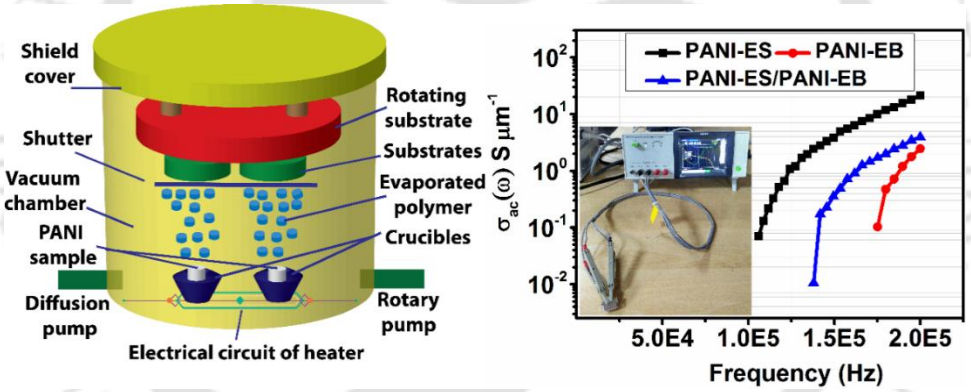

S. Palsaniya, H.B. Nemade, A.K. Dasmahapatra, Heterostructured Layer Growth of Polyaniline by Vacuum Thermal Evaporation and Fabrication of Thin-Film Capacitors, *J. Phys. Chem. C.* 123 (2019) 27959–27968.

6.1. Introduction

Thin film deposition of polymers finds manifold pioneering applications in electronics, optical, clinical and chemical devices [1–4]. Numerous deposition techniques such as dip coating, spin coating, L-B (Langmuir-Blodgett) technique, vacuum thermal evaporation [5,6], laser ablation [7,8], and chemical vapour deposition [9] have been adapted to prepare polymer thin films. The development in polymer thin film technology has been employed to meet the demand of novel applications in the field of data recording, beam splitters, transmitters and receivers, information mixers, wave harmonic generators and optical sensors [10]. In majority of the applications, the thickness of the thin film is usually maintained in the range of a few nanometers [4,11] and micrometers in some cases [3]. In the rapid development of nanotechnology, components with smaller size would be more beneficial. For example, reducing the transistor size in microelectronics, results in increased speed of the microprocessor. As a result, the developed electronic devices assure a smooth operation that promotes the manufacturing of miniaturized electronic components based on thin film technology [12].

It is reported that the fabrication of polymer thin films by evaporation (chemical or physical) is essentially thermal degradation of polymer chains in vacuum followed by evaporation and re-polymerization at the substrate [10]. The degraded components of the polymer chain orient randomly during repolymerization mechanism to re-build the polymer chains [13,14]. The obtained structures are chemically similar to the bulk polymer units. The thickness of the thin film is largely dictated by the deposition time [15], while the degradation of polymer chains substantially depends on the heating rate. Vacuum evaporation method for the deposition of polymer thin film offers significant advantages over other methods. For example, Li et al. [16] have reported the oxidative chemical vapour deposition technique to produce a porous PANI layer over a nonporous carbon nanofiber for its potential application in supercapacitors. This vacuum deposition method avoids several liquid phase methods that involves secondary materials to develop a porous surface. Nishio et al. [8] have explored the fabrication of polyacrylonitrile (PAN) thin films employing laser ablation via excimer laser beams in the UV region at various wavelengths (viz., 308, 248 and 193 nm). They have observed that the final structure depends on the ablation wavelength. The nitrile groups are eliminated at a lower wavelength (193 nm), cyclization of nitrile groups at a higher wavelength (248 nm), while at 308 nm the original structure was preserved. Inayoshi et al.[17], have deposited a thin film of polytetraflouroethylene (PTFE) by applying synchrotron radiation (SR) ablation method. The

surface morphology was quite distinct rough at lower (~20 ºC) temperature while smooth at higher (~200 ºC) temperature. It is believed that the movement of macromolecular chains is facilitated at higher temperature resulting in the formation of a relatively smooth surface.

Conducting polymers have been emerging as a state-of-the-art material to play a substantial role into the fabrication of solid state devices with diverse applications, such as, in chemical sensors [18,19], organic light emitting diodes [20,21], solar cells [22,23] and energy storage [24,25], and biosensors [26,27]. A thin film of conducting polymers must preserve a highly stable structure with an excellent ordered morphology to deliver desired property. Thin films with a geometrically arranged structure are quite responsive for easy charge transport that can successfully be utilized in energy storage applications [28–30]. In particular, PANI is a favourable candidate for thin film deposition via thermal evaporation, as acid doped PANI exhibits good electrical conductivity, environmental stability and light weight [31,32]. Lee et al. [33] have deposited a thin film of PANI-ES on Ag (1 1 0) with the help of thermal evaporation. At high resolution, electron energy loss spectroscopy has revealed the presence of PANI oligomers adsorbed over the substrate and occurrence of polymerization in thicker films. The resultant polymer showed conducting behaviour upon protonation. Agbor et al. [34] have deposited a thin film of PANI by employing vacuum evaporation, spinning, and Langmuir–Blodgett techniques, fabricated chemiresistors and employed for H_2S and NO_2 sensing. Li et al. [35] have deposited polycrystalline thin films of polyaniline/7,7,8,8-tetracyanoquino-dimethane (PANI-TCNQ) using a vacuum evaporation method. The charge transfer and optical properties were significantly different compared to the intrinsic PANI and TCNQ films. Ren et al. [36], by employing the pulsed excimer laser ablation (KrF) method, have successfully deposited a thin film of PANI with good electrical and structural properties. Furthermore, Lim and Choi [37] have explored the electrical properties, structure, and morphology of the PANI thin film produced by neutral and ionized cluster beam deposition (NCBD and ICBD) methods and pulsed laser deposition (PLD) technique. The thin film prepared by PLD method has shown higher electrical conductivity compared to others. Recently, Abdul-Manaf et al. [38] have prepared PANI thin films using electrodeposition process. In this work, PANI thin films via anodic deposition showed fully oxidized (an amorphous surface) material with a wide band gap (3.90 – 4.08 eV), while the cathodic deposition showed a complete reduction with a narrow band gap (1.05 – 1.20 eV). Most of the research work have explored the fabrication of single layer thin film of either PANI-ES or PANI-EB for sensing applications. The application of PANI-EB is relatively more than PANI-ES, in spite of the higher conductivity of the later compared to the former. PANI-EB deposited film shows a higher surface roughness than

PANI-ES, which is attributed to the relatively facile deposition of chain fragment of PANI-EB compared to PANI-ES. Therefore, PANI-EB have been mostly selected as a preferred material, specifically for the vacuum evaporation process [39–44].

Herein, we report the successful preparation of bilayer film of PANI-ES and PANI-EB along with the individual single layer film by vacuum evaporation method. The deposited films exhibit a stable morphology as revealed by Spectroscopic Ellipsometry (SE), XRD, FESEM, and AFM analysis. The measurement of optical band gap (1.7 – 2.2 eV) establishes that the fabricated thin films possess semiconducting behaviour. Fabricated thin film capacitors (on a glass substrate) show excellent charge transport properties, which is attributed to the good storage permittivity and capacitance. The characteristics measurements of current density, frequency dependent AC conductivities, and electrostatic charge densities establishes PANI thin films as an excellent high-density energy material.

6.2. Experimental Section

6.2.1. Materials

All chemicals were of analytical grade and utilized as received without further purifications. Aniline (Emparta grade ≥ 99%), Acetone (Emparta grade 99.5%), H_2O_2 (Emplura grade 50%) and Ammonia solution (Emplura grade, assay ≥ 25%) were purchased from Merck Millipore. Ammonium persulfate (99%) was purchased from Sisco Research Laboratories. Hydrochloric acid (assay 35-37%) and Sulfuric acid (assay 97%) was purchased from Fisher Scientific.

6.2.2. Synthesis of PANI-ES and PANI-EB

Polyaniline emeraldine salt (PANI-ES) and Polyaniline emeraldine base (PANI-EB) have been prepared following *in-situ* chemical oxidative polymerization of aniline, as reported previously [45,46]. A solution of 3.0 g aniline in 40 ml of 1.0 M HCl was mixed with a solution of 9.0 g ammonium persulfate (APS) in 40 ml of 1.0 M HCl, at ~ 0 ºC temperature. The resultant solution began to form a dark green precipitate. The solution was allowed to rest for 48 h at 0 – 4 ºC to complete the polymerization. Following this, the solution was filtered, and successively washed with DI water and 1.0 M HCl to obtain PANI-ES. A portion of PANI-ES was treated with 1.0 M NH_4OH solution to prepare PANI-EB, a bluish-gray precipitate, which was further filtered and washed. The PANI samples, viz. PANI-ES and PANI-EB, were vacuum dried for 24 h at 60 ºC and collected in the form of dry powder.

6.2.3. Thin film deposition

PANI-ES and PANI-EB thin films were deposited separately on microscopic glass slides and n-type silicon wafers, with the help of a vacuum organic evaporator (Hind Hivac, BC-300). Initially, glass slides (~1 mm thick) were cut into 3 × 3 cm^2 size and cleaned thoroughly - first sonicated in acetone for 30 minutes and washed with DI water, then treated with a piranha solution (3:1 ratio of H_2SO_4 : H_2O_2) to remove organic residues, and further washed with DI water. The glass substrates were subsequently treated with nitrogen gas purging to remove oxide impurities, and dried in a clean room. In the vacuum evaporator, the distance of the substrate holder from the target was 21 cm; the size of the target holder was 27×12 mm^2 with an inner diameter of 9 mm. The setup of the vacuum deposition system has been illustrated in Figure 6.1a. A measured quantity of target powder was kept in the target holder and deposited over the substrates at a temperature above the glass transition temperature. Based on the thermogravimetric (TGA) measurements (Figure 6.1b), the temperature for the deposition was kept at ~ 300 ºC and ~ 500 ºC for PANI-ES and PANI-EB, respectively. The deposition chamber was kept under vacuum with a pressure of ~1.3×10^{-6} Torr. The heating rate of the filament was fixed at 12 ºC per minute. Once the required temperature was reached, the shutter was opened, and deposition was allowed for 20 minutes to obtain a continuous thin film. To prepare the composite film (viz., bilayer film of PANI-ES and PANI-EB), we have followed a two-step process: first, a layer of PANI-ES was deposited as described above, and then by changing the target, the second layer of PANI-EB was deposited at an appropriate temperature.

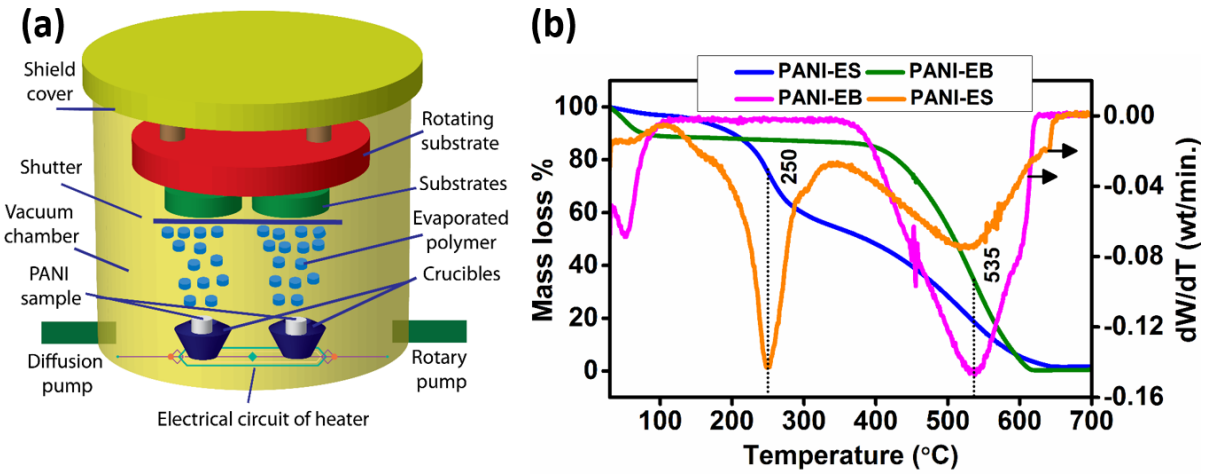

Figure 6.1. (a) Schematic illustration of the organic vacuum evaporation chamber, (b) thermogravimetric analysis of the PANI-ES and PANI-EB.

6.2.4. Characterization and measurements

Raman spectroscopy (HORIBA LabRam HR Evolution, He-Ne laser at an excitation of 633 nm) was recorded for an acquisition time of 10 s. X-Ray diffraction (XRD) (Bruker, D8 Advance with Cu-Kα-Kβ radiations at λ = 1.54 Aº, 40 kV, 40 mA) patterns were acquired in the range of 10 – 60º at a scan rate of 1º per minute. The reflectance spectra of the thin film samples were measured with a double beam UV/VIS/NIR spectrometer (PerkinElmer, Lambda 950) equipped with an integrating sphere in the wavelength range of 200–800 nm. Surface morphology and compositions were explored by FESEM at accelerating voltage of 2 kV (Zeiss, Gemini-300) and EDX (Zeiss, Sigma). Topography scans in the tapping mode were done at room temperature by the atomic force microscopy (Innova SPM). Variable angle spectroscopic ellipsometry (VASE, Semilab SOPICA, Model: GES5E) measurements were performed at the angle of incidences of 60º, 65º, and 70º. The I–V characteristics were measured using Keithley parameter analyzer (4200 SCS) at room temperature. AC conductivities, dielectric, and electrostatic properties of the fabricated devices were investigated with the help of impedance analyzer (IM7581, HIOKI) in the frequency range of 1 kHz to 200 kHz, at room temperature.

6.3. Result and discussion

6.3.1. Structure and morphology

PANI thin films in single and bilayer form were deposited over the n-type silicon wafer with palette colours, as shown in Figure 6.2a. The thickness of all the three films is in the range of 50 to 100 nm, measured by a profilometer. As shown in Figure 6.2a, the images (1), (2), and (3) represent PANI-ES (light greenish), PANI-EB (bluish) and PANI-ES/PANI-EB (partial bluish and greenish). The appearance of the PANI thin films with different colours depending on the oxidation states have also shown by Abdul-Manaf et al. [38]. In the PANI-ES thin film (Figure 6.2b), agglomeration and stretching of PANI chains resulted in “broccoli shaped” structure. This agglomerated structure of PANI-ES would provide an excellent electrostatic charge capability because closely bonded chains would facilitate an easy charge delocalization throughout the surface. Therefore, the overall high charge transfer proficiency would enhance the electrostatic charge storage capability. However, the presence of strong hydrogen bonding between amine and imine sites makes the emeraldine base (EB) relatively stronger than PANI-ES units [47]. Hence, PANI-EB units could not be dissociated readily during vacuum evaporation, and results in equally distributed arrays of PANI chains as seen in FESEM image of PANI-EB sample (Figure 6.2c).

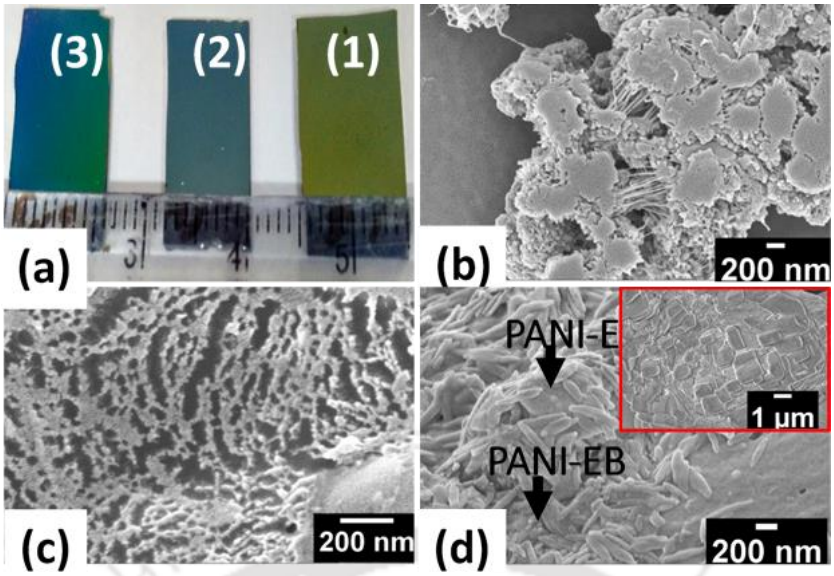

Figure 6.2. (a) Digital images of (1) PANI-ES, (2) PANI-EB, and (3) PANI-ES/PANI-EB. FESEM images of (b) PANI-ES thin film at 25 KX, (c) PANI-EB thin film at 75 KX, and (d) PANI-ES/PANI-EB heterostructure at 30 KX magnifications; the inset of (d) shows the FESEM image at the lower resolution.

The uniformity of the coating is largely attributed to the vapour deposition method adopted to prepare the thin films [16]. Figure 6.2d represents the image of the composite structure of PANI-ES/PANI-EB. The layer-by-layer deposition shows a distinctly different morphology compared to the PANI-ES and PANI-EB films. Here, PANI-ES could be ionically active due to polaron and bipolaron excitations consisting of $C=N^+$ and C–H bonding, which interacts with the amine (reduced) and imine (oxidized) nitrogen units of PANI-EB chains [48]. Thus, the resultant morphology appears to be a collection of tiny islands on the entire surface due to the agglomerated PANI-ES (inset of Figure 6.2d at lower magnification). The elemental compositions of the thin film of PANI-ES were investigated via EDX measurement. In a finite region at 2.5-micron resolution (Figure 6.3a), the elemental composition (wt%) of C, N and O are 61.2, 20.7 and 18.1, respectively, which strongly suggest the formation of PANI chains during re-polymerization. An appropriate amount of each element signifies their corresponding atomic arrangement throughout the PANI backbone. The C element is a prominent unit of PANI backbone. Therefore, it has the maximum wt%; the fractional amount of O is due to the oxidizing agent (viz., ammonium persulfate) and N is due to the anilinium ions during polymerization, as shown in Figure 6.3b–d.

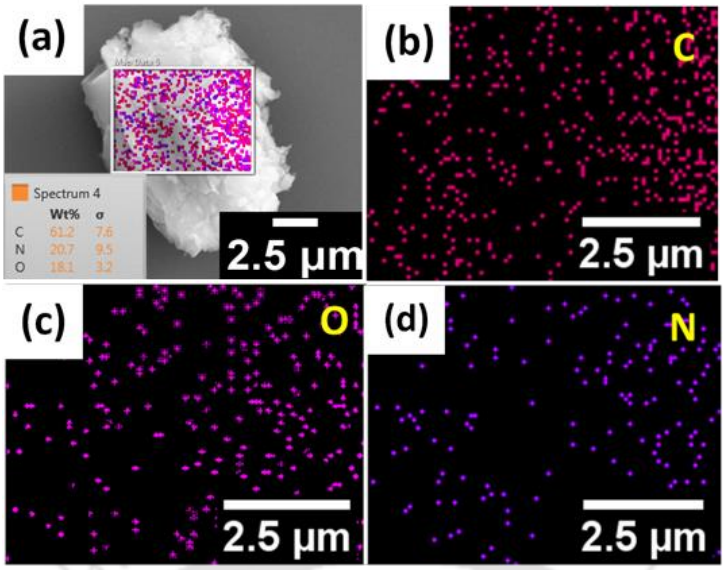

Figure 6.3. Elemental analysis using EDX mapping of the PANI-ES thin film: (a) selected a finite region using FESEM image to investigate the present elements, (b) carbon (61.2 wt %), (c) oxygen (18.1 wt %), and (d) nitrogen (20.7 wt %).

The AFM topographic images (scan area of 5µm×5µm) of vacuum evaporated PANI samples are shown in Figure 6.4. The average surface roughness (R_a) estimated from AFM measurement of PANI-ES, PANI-EB, and PANI-ES/PANI-EB is 4.67, 9.33, and 7.55 nm, respectively. The characteristics of surface roughness reveal that the surface is significantly rough. Figure 6.4a, corresponds to the PANI-ES, indicating an overall homogeneous growth, resulted from a well-distributed deposition over the substrate. PANI-EB (Figure 6.4b) shows a flower shape surface topography, with a higher roughness compared to the PANI-ES. This flower shape morphology is attributed to the rough surface, which appears initially from the oxidant residue and oligomers during vacuum deposition. The AFM image of the composite bilayer (Figure 6.4c) is attributed to both the oxidation states of PANI, as observed with the FESEM image too (Figure 6.2d). The bilayer surface is relatively rough in comparison with PANI-ES film. The roughness in our thin films is significantly less compared to the work reported by Li et al. [16] (~16 nm) and Cena et al. [49] (~ 100 nm). It can be concluded that the vacuum evaporation method successfully produces much smoother films of PANI compared to chemical processes.

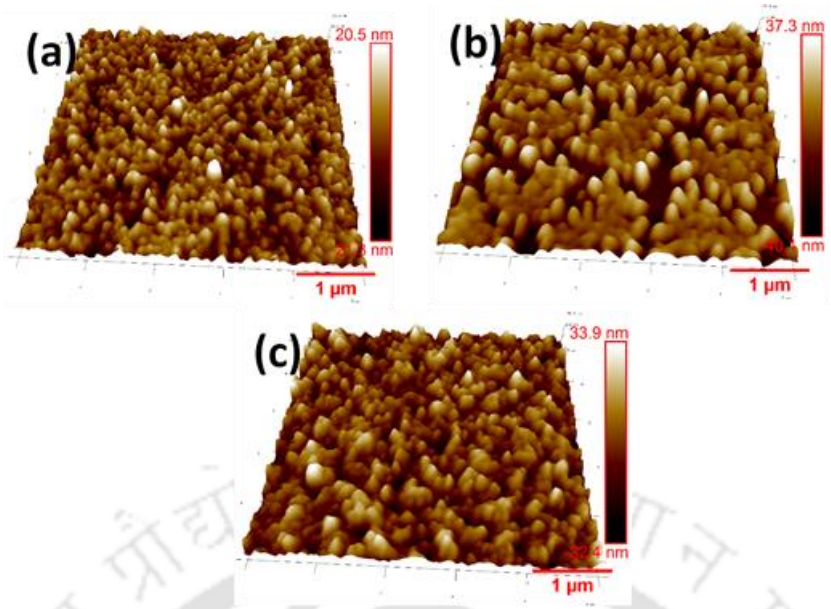

Figure 6.4. Topography analysis using AFM of the thin films at a scan area of 5 µm ×5 µm: (a) PANI-ES, (b) PANI-EB and (c) composite film of PANI-ES/PANI-EB.

The Raman spectra of deposited PANI thin films (viz., PANI-ES, PANI-EB, and PANI-ES/PANI-EB) is shown in Figure 6.5a. The obtained sharp peak at 520 cm^{-1} belongs to the Si substrate. The peak range of 597 to 623 cm^{-1} is related to $C=N^{+}$ bond vibrations of quinonoid rings due to phenoxazine analogous units and sulfate anions, respectively. The peak at 741 cm^{-1} is associated with the deformation of amine, corresponding to bipolaron structure of emeraldine salt, and the peak at 813 cm^{-1} is attributed to the deformation of benzene rings [50–53]. The peak at 741 cm^{-1} is also associated with the C–H outer plane vibration of in-phase bending of benzene rings, as reported by Varsanyi and Gyorgy [54]. The C–H bending vibrations at 1146 cm^{-1} correspond to semi-quinonoid rings. The band at 1334 cm^{-1} indicates the delocalized polaron structure of $C–N^{+\bullet}$ vibrations. The peak vibrations at 1406 cm^{-1} corresponds to phenazine shape [55], weak intensity at 1523 cm^{-1} represents the band vibrations of N–H deformations, and strong band vibrations at 1568 cm^{-1} denotes the C=C stretching of quinonoid units. The peak at 1623 cm^{-1} [51,56,57] represents the C–C ring stretching vibration of the benzenoid unit, which was also reported by Furukawa et al. [53]. The overall spectrum of the PANI-ES shows higher intensity as compared to the PANI-EB, which is attributed to an extensive charge delocalization due to polaron and bipolaron species, exhibiting a semiconducting behaviour. It is also observed that the bilayer structure of PANI-ES/PANI-EB is slightly blue shifted, possibly due to an enhanced chain segment along with quinonoid backbones of PANI structures.

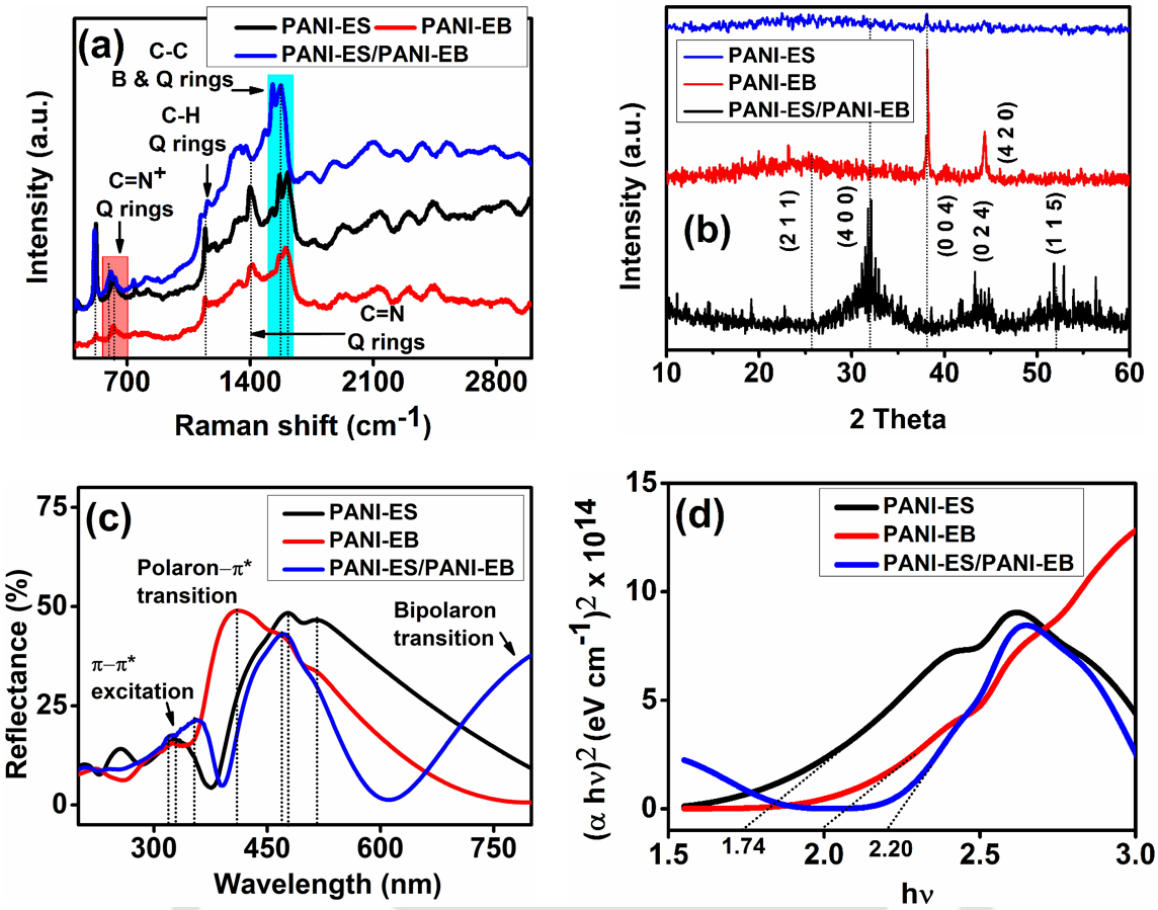

Figure 6.5. Structural confirmation was estimated using (a) Raman spectra, (b) X-Ray diffractions, (c) UV-Visible reflectance spectra, and (d) optical band energies of the PANI thin films.

X-Ray diffraction patterns of the thin film samples are shown in Figure 6.5b. The diffraction angles including interplanar spacings of the PANI samples at 25.6º (3.44 Å), 31.9º (2.79 Å), 38.2º (2.35 Å), 44.4º (2.03 Å) and 52º (1.75 Å) are related to crystallographic planes of (2 1 1), (4 0 0), (0 0 4), (4 2 0) and (1 1 5), respectively. This observation is well-matched with the work reported by Ren et al. [36]. The diffraction peaks at 31.9º and 38.2º correspond to PANI-ES/PANI-EB and PANI-EB, respectively, appears to be strong and sharp diffraction pattern, indicating a semicrystalline phase. However, PANI-ES and PANI-EB show a relatively broad peak around 25.6º, suggesting the formation of the isomorphous structure of PANI chains, which also corroborates with the FESEM analysis (Figure 6.2). The amorphous phase of PANI-ES would facilitate high electronic charge polarization that would be useful for electrostatic energy storage applications. A relatively broad peak for PANI-ES and PANI-EB at 25.6º with an interplanar spacing of 3.44 Å, suggests a regular arrangement of perpendicular and parallel PANI segments [45,58]. It is noted that the planes at 44.4º (4 2 0) in PANI-EB and at 43.3º (0 2

4) in the composite film indicate a plane orientation. The diffraction angle 44.4° arising in both PANI-EB and composite films that could be originated by the quinoid rings [38].

The optical reflectance spectra of the PANI thin films obtained from UV Visible spectroscopy is shown in Figure 6.5c. The reflectance spectra of PANI-EB and bilayer PANI-ES/PANI-EB are blue shifted compared to PANI-ES, at the maximum characteristic band reflectance of 408 and 470 and 477 nm, respectively. This blue shift reveals the presence of shorter PANI chains [59] and quinoid units. Since PANI-ES/PANI-EB possesses high crystalline peak as compared to others as shown in XRD analysis (Figure 6.4b), a fast decaying reflectance spectrum is obtained in PANI-ES/PANI-EB [24].

The reflectance spectra in the range of 220 to 255 nm may be correlated to π–π* electron transition within *para*-substituted benzenoid units [60,61]. The π–π* excitations corresponding to the conjugated PANI chains (viz., benzenoid ring) of PANI-ES, PANI-EB, and PANI-ES/PANI-EB are observed at 318, 328 and 353 nm, respectively [5,60]. The peaks in the reflectance spectra at 409, 472, and 477 nm are associated with the polaron-π* transition of the PANI samples [62]. Further, the reflectance peak at ~ 513 nm is contributed by bipolaron transition of benzenoid π and quinoid π* rings of PANI films [60,63]. A broad region between 500 to 600 nm represents characteristic polaron transition, while transition at 750 nm shows that the electrons are delocalized [5,64]. Furthermore, the optical band edge is determined using the tauc plot equation [24] as follows;

$$(\alpha h\nu)^{\frac{1}{n}} = A\left(h\nu - E_g\right) \qquad (6.1)$$

where A is an arbitrary constant, E_g is the band edge of the deposited material and n is an index related to the effective band transition. For instance, n = 0.5, 2, 1.5 and 3 correspond to direct, indirect, forbidden direct and forbidden indirect transitions, respectively. The calculated band energies are ~1.74, ~2.0 and ~2.20 eV for PANI-ES, PANI-EB and PANI-ES/PANI-EB, respectively, based on n = 0.5 (direct band edge) (Figure 6.5d). The band edge of vacuum evaporated PANI-ES (1.74 eV) thin film is close to that of bulk PANI-ES (1.8 eV) [65]. Uvdal et al. [66] reported that the band edge of conventional PANI-EB is around 2.0 eV, while 2.5 eV for vapour deposited film. It is observed that the combination of both layers provides a band edge of ~ 2.2 eV. The excellent optical properties signify that PANI thin films are promising candidates for electrostatic charge storage application due to the presence of direct charge transfer between energy bands. Therefore, the fabricated electronic devices would assure a smooth operation to promote the miniaturization based on thin film technology [67,68].

6.3.2. Ellipsometric analysis

The spectroscopic ellipsometry (SE) measurement is done to re-affirm the optical properties of thin films on a glass substrate [69–71]. In our case, SE measurements have been employed to validate film thickness and optical constants. The heterostructured thin film of PANI-ES and PANI-EB shows the optical constants close to the individual layers. This information on the optical constants will be essential for the device fabrication based on either single or bilayer films. Figure 6.6a shows a schematic illustration of SE measurements for estimation of the individual optical constants.

Spectroscopic ellipsometry allows in-situ monitoring and indispensable analysis of nanostructured thin films. The SE measurements are capable to quantize the morphology, composition, interlayer diffusion, and surface interaction of thin films. The refractive index and film thickness are key parameters to reproduce the scientific results for various applications, especially for thin film devices. Thus, maintaining a film thickness is highly necessary to investigate the physical parameters, such as complex refractive index and dielectric constants, etc. The complex reflectance ratio (ρ) of parallel (P) and perpendicular (S) plane polarized light waves defined as R_p/R_s, where, R_p and R_s are coefficients of reflection. The reflected light characterized by two distinct angles of Ψ and Δ are correlated as follows [72–74];

$$\tan(\Psi)e^{i\Delta} = \frac{R_p}{R_s} \tag{6.2}$$

where, Ψ is an amplitude ratio of the parallel plane incidence and perpendicular polarizations, and Δ is the phase difference. These parameters are strongly rely on film thickness. A two-layer model was used to evaluate thin films. The refractive index (n), and extinction coefficient (k) were extracted from the measured ψ and Δ following the Tauc-Lorentz fitting model. This model is valid for amorphous-semiconductor interface The finest fitting of the experimental values is identified by minimizing the root mean square error (RMSE) as follows [75];

$$\mathrm{RMSE} = \sqrt{\frac{1}{2N-M_i}\sum_{i=1}^{N}\left[\left(\frac{\psi_i^{Mod}-\psi_i^{Exp}}{\sigma_{\psi,i}^{Exp}}\right)^2+\left(\frac{\Delta_i^{Mod}-\Delta_i^{Exp}}{\sigma_{\Delta,i}^{Exp}}\right)^2\right]} \tag{6.3}$$

where, (ψ, Δ) is sum of 'N' experimental values, M signifies variable parameters, σ is the standard deviation, Mod and Exp in superscript are attributed to modeled/or fitted and experimental values, respectively. We report variable angle SE measurements in the visible range using the rotating analyzer. The SE measurements of single-layered PANI-ES (96.5 nm), PANI-EB (68.8 nm) and PANI-ES/PANI-EB heterostructure (49.4 nm) thin films were

performed on glass substrates. We have recorded variable thickness due to a slight deviation in heating rate and deposition time. Thin film samples longitudinally mounted fixing three angles of incidences (60º, 65º and 70º) at the room temperature and RH% 65. The values of Δ and Ψ are fitted maintaining a minimum value of the RMSE. A fractional deviation between measured and fitted data, is attributed to the interfacial region [73,76] between PANI layers and substrate. Similarly, using the fitted optical constants, we have observed complex dielectric function (real and imaginary) for the PANI thin films.

The parameters of the polymer thin films can be fitted into the SE curve by Tauc-Lorentz model [77]. The complex refractive index N = (n + ik)of thin films were plotted with the photon energy (hν, eV), where, n is refractive index, and k is an extinction coefficient [78]. The higher value of n represents higher absorption, whereas k = 0 manifests a complete transmittance of photon energy [79]. The trend of n and k with photon energy in Figure 6.6b and 6.6c show the characteristics of PANI-ES and PANI-EB, respectively, typical characteristics feature of semiconducting thin films. Jellison and Modine [80] reported the optical parameters of the amorphous semiconductors using the Lorentz model. The (n, k) response of the PANI-ES film (Figure 6.6b) is attributed to the presence of a porous semiconducting region, which would readily facilitate charge transport. It is observed that the refractive index of PANI-EB film shows an opposite behaviour of optical parameters (Figure 6.6c) relative to PANI-ES that can be associated to distinct oxidation states of PANI. The Ellipsometric study of Si-O-C-H films and PET substrate have been reported by Stehle and Piel [81] showed a similar trend of (n, k) to that of the PANI-EB film, suggesting the low *k* dielectric surface. The SE plots of PANI-ES/PANI-EB in Figure 6.6d shows the presence of both PANI-ES and PANI-EB thin films, signifying the formation of a heterostructure of PANI-ES and PANI-EB. Heterostructure films exhibit separate phases with distinct optical constants, such as n_1, k_1 (PANI-EB) and n_2, k_2 (PANI-ES) (Figure 6.6a). The plots of the ratio of parallel and perpendicular plane polarizations (ψ), and phase difference (Δ) against energy have been shown in Figure 6.7. The trend in ψ and Δ is typical to the PANI-ES and PANI-EB, as shown in Figure 6.7a, 6.7b, and 6.7d, 6.7e, respectively. The characteristic feature of the composite film shows the combined features of both PANI-ES and PANI-EB, as shown in Figure 6.7c and 6.7f for ψ and Δ, respectively.

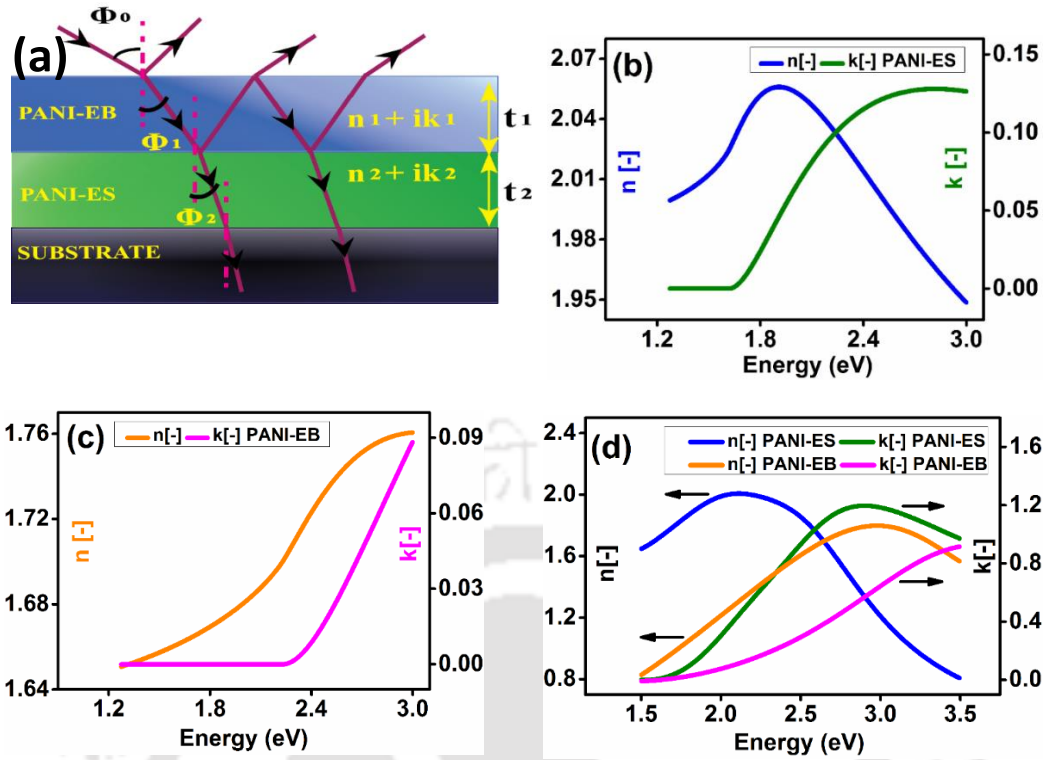

Figure 6.6. (a) Schematic diagram of heterostructured thin films. The optical constants (n,k) of (b) PANI-ES, (c) PANI-EB and (d) PANI-ES/PANI-EB composite.

The dielectric constants ($\varepsilon = \varepsilon_1 - i\varepsilon_2$) [80,82] were estimated from multiple reflections of ψ and Δ. We have estimated optical dielectric constants (ε_1), as shown in Figure 6.8 (a-c) and optical dielectric losses (ε_2), as shown in Figure 6.8 (d-f) of PANI films. The angular dependency study shows that the values of dielectric constants remain almost unchanged with a variation in incident angle by 5° (viz; 60°, 65°, and 70°) during the ellipsometry study. The measured optical dielectric constants further can be corroborated with the electrostatic dielectric constants measured by impedance analyser.

The magnitude of ε_1 for PANI-ES in Figure 6.8a shows a decreasing trend with increasing energy, from ~ 1.3 eV to 3.0 eV, while that of for PANI-EB (Figure 6.8b) shows an increasing trend. The composite films capture the trends of both films (Figure 6.8c) with multiple reflections. The decreasing trend of ε_1 of PANI-ES with photon energy can be attributed to its good dielectric strength. The ε_2 of dielectric functions is attributed to the optical

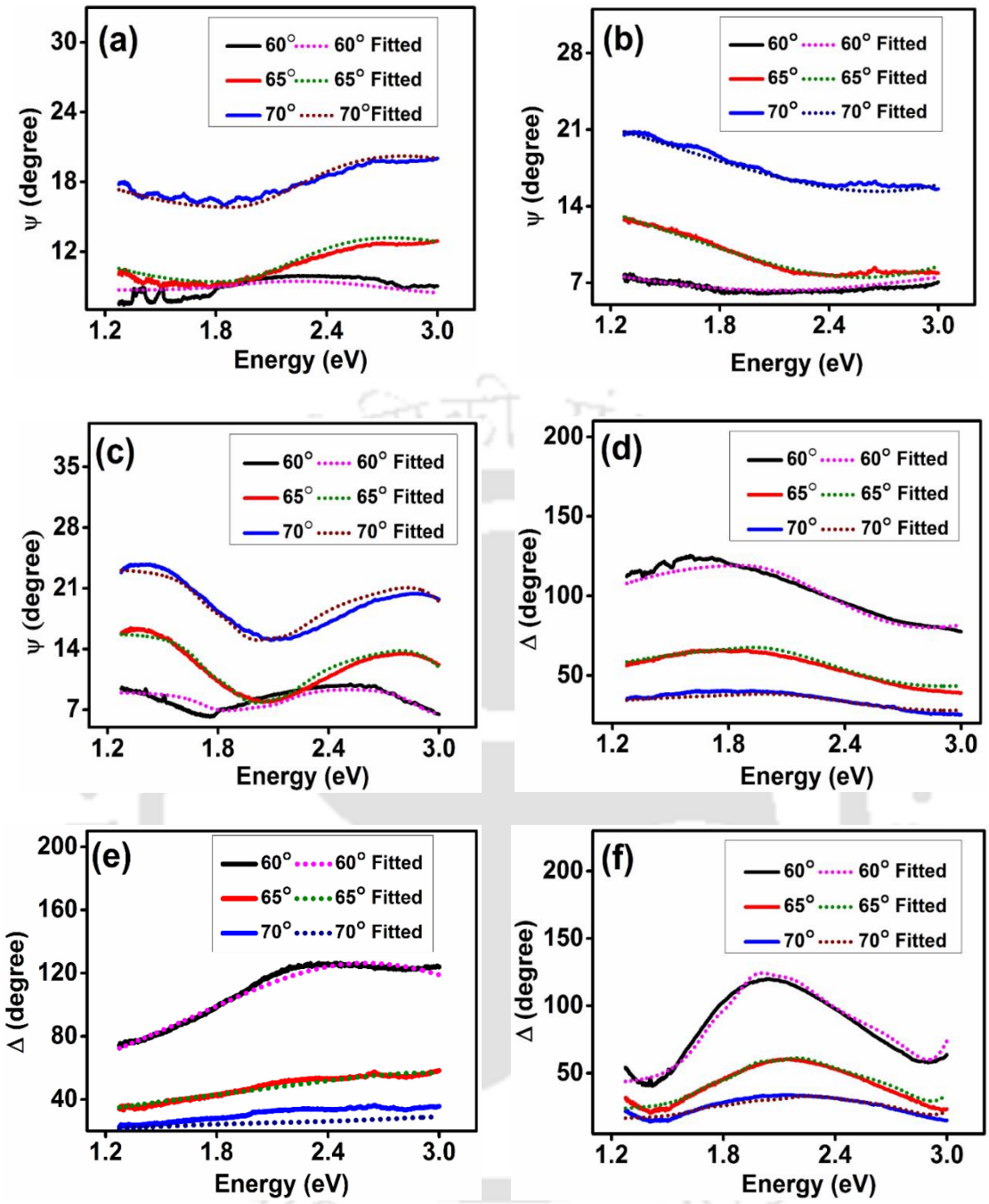

Figure 6.7. Spectroscopic Ellipsometry analysis of ψ for (a) PANI-ES, (b) PANI-EB, and (c) PANI-ES/PANI-EB thin films. Similarly, Δ for (d) PANI-ES, (e) PANI-EB, and (f) PANI-ES/PANI-EB thin films. Thick and dotted lines are associated to measured and fitted graphs, respectively.

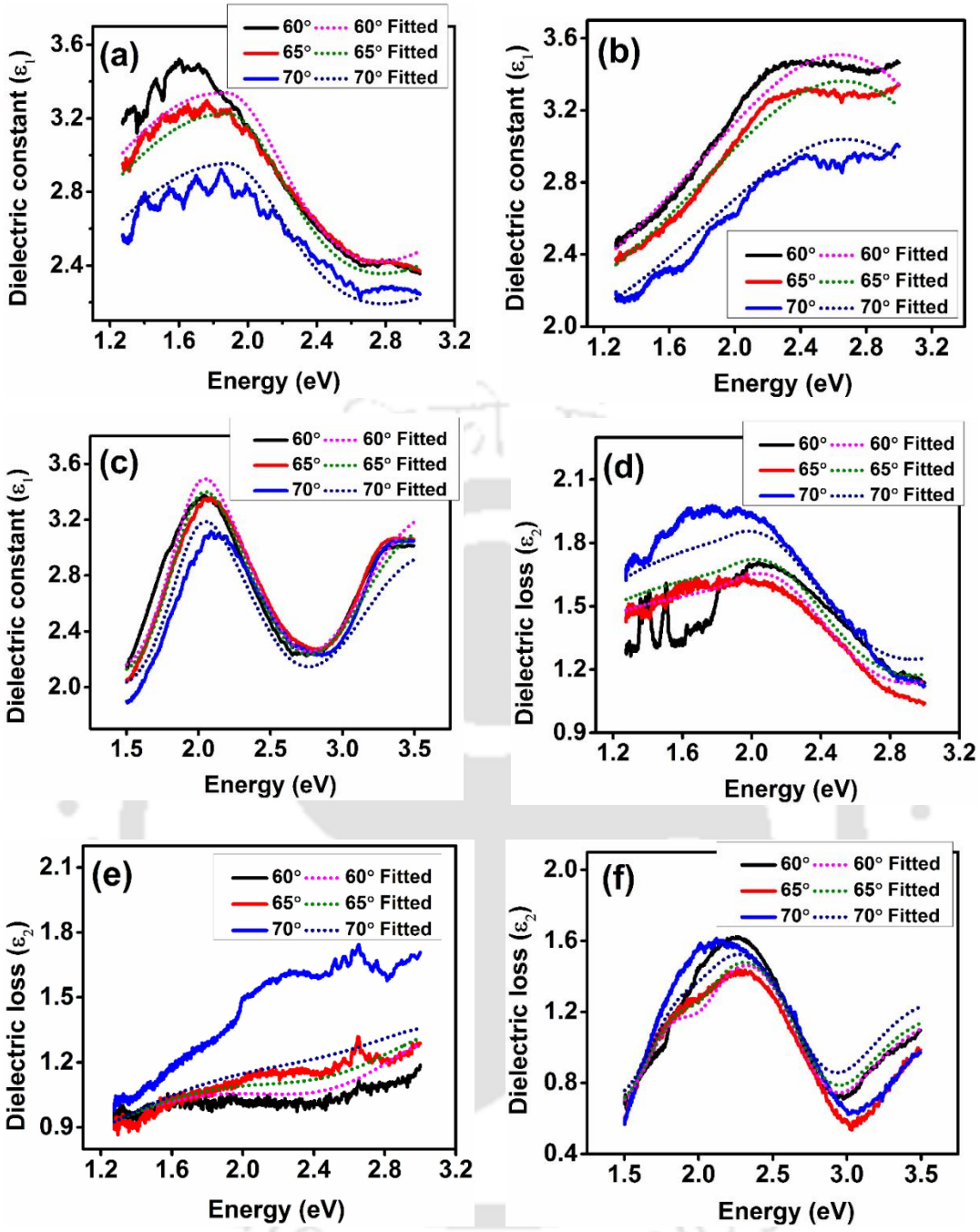

Figure 6.8. The real function of dielectric permittivity (ε_1) for (a) PANI-ES, (b) PANI-EB, and (c) PANI-ES/PANI-EB thin films. Similarly, imaginary function of dielectric losses (ε_2) for (d) PANI-ES, (e) PANI-EB, and (f) PANI-ES/PANI-EB are plotted with the photon energies. Thick and dotted lines are corresponding to measured and fitted graphs, respectively.

Table 6.1: Comparative study of various parameters of the PANI thin films. Heterostructure has two phases (viz., layers) excluding substrate. The band gap has been estimated separately for each layer during the spectroscopic ellipsometry (SE) analysis.

Sample name	Band gap (eV) E_g	Film thickness (nm)	Real ε_1	Imaginary ε_2	RMSE
PANI-ES	1.61	96.5	3.50	1.55	0.663
PANI-EB	3.89	66.8	3.46	1.18	0.015
PANI-ES/PANI-EB	3.82	49.4	3.37	1.63	0.029

absorption in PANI films. Hence, ε_2 tends to decrease against optical energy with increasing the film thickness [83]. Table 6.1 illustrates the analyzed ellipsometric parameters, particularly, film thickness and energy band gap (E_g) closely match with the measurements via profilometer and UV visible absorbance, respectively. A slight deviation in the band gap of the composite film in comparison to the PANI-ES and PANI-EB films is attributed to the variation in film thickness [84].

6.3.3. Fabrication of thin film capacitors

The deposition process of thin films of all the three samples has been discussed in section 2.3. Several planer capacitors were fabricated with thin film as the dielectric medium (Figure 6.9) and depositing an array of parallel aluminium electrodes having thickness ~50 nm, and width 2 cm and gap 1.5 mm using a stainless steel mask. We fabricated capacitors with three different types of thin films, viz. PANI-ES, PANI-EB, and PANI-ES/PANI-EB. The following characterization is based on the fabricated thin film capacitors.

6.3.4. Electrical and dielectric properties

I-V characteristics of the deposited thin films were measured using Parameter Analyzer with the help of fabricated electrodes over the thin films. I-V characteristics of all the samples obey an ohmic response closely. It is well reported that PANI-ES being a protonated form, shows the highest electrical conductivity as compared to the deprotonated form of PANI-EB, as shown in Figure 6.10a. However, the acid-doped PANI-ES shows a current of ~ 63 nA for the applied maximum potential of 12 V, due to the surface charge accumulation, facilitated by the aggregated structure as revealed by XRD analysis (Figure 6.5b). It is observed that current is negligible up to a bias voltage of ~ 2 V, and after that it rises rapidly, which is well agreed by the work reported Li et al.[35] on polyaniline/7,7,8,8-tetracyanoquino-dimethane (PANI–TCNQ) complex thin films.

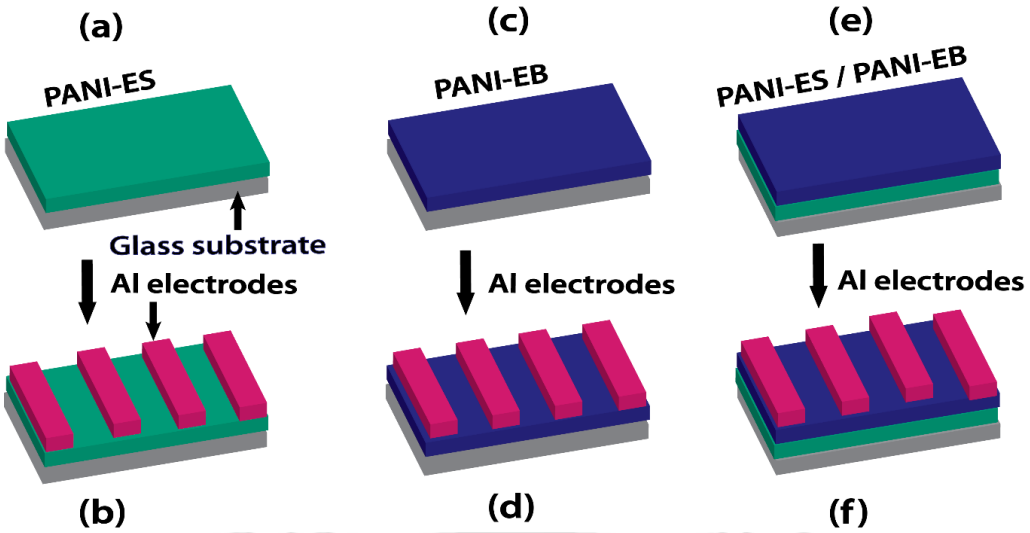

Figure 6.9. Schematic diagram of the fabrication process of an array of thin film capacitors: (a) PANI-ES, (b) Al (Aluminum) electrodes fabrication, (c) PANI-EB, (d) Al electrodes fabrication, (e) heterostructured film of PANI-ES/PANI-EB, and (f) Al electrodes fabrication at the periodic intervals.

A similar effect has also been reported by Hümmelgen et al. [85], based on the Fowler–Nordheim tunneling current measurements. The dielectric constants (ε') (storage permittivity) for the three PANI thin films were calculated using $\varepsilon' = \frac{C\,d}{\epsilon_0 A}$ [86], where C is capacitance (F), d is film thickness (nm), ϵ_0 is vacuum permittivity (8.85×10^{-12} F m^{-1}) and A is the area (m^2) of thin film between two electrodes, and plotted against frequency in Figure 6.10b. An isotropic effect of air ($\varepsilon_0 \approx 1.0005$) does not affect to the ε′ of thin films. Each thin film shows a consistent frequency response of ε', due to the seamless surface texture. The relatively high value of ε' in the range of 10^{-2} to 3.6×10^{-3} F m^{-1} is attributed to the significant agglomeration of the PANI-ES chains, as shown in the FESEM image (Figure 6.2b). Since PANI-ES is a semiconducting film, the charge can move throughout the surface and cause a high charge localization. In contrast, the composite thin film (viz., PANI-ES/PANI-EB) shows the lowest value of ε', in the range of 2.2×10^{-3} to 1.6×10^{-3} F m^{-1} due to the limited surface charge with low surface area, as is evidenced by XRD patterns (Figure 6.5b), suggesting the formation of a uniformly distributed surface (Figure 2d). The PANI-EB, shows a relatively extended curve of ε' with increasing frequency [87–89], suggesting a weak semi-conductor as compared to PANI-ES.

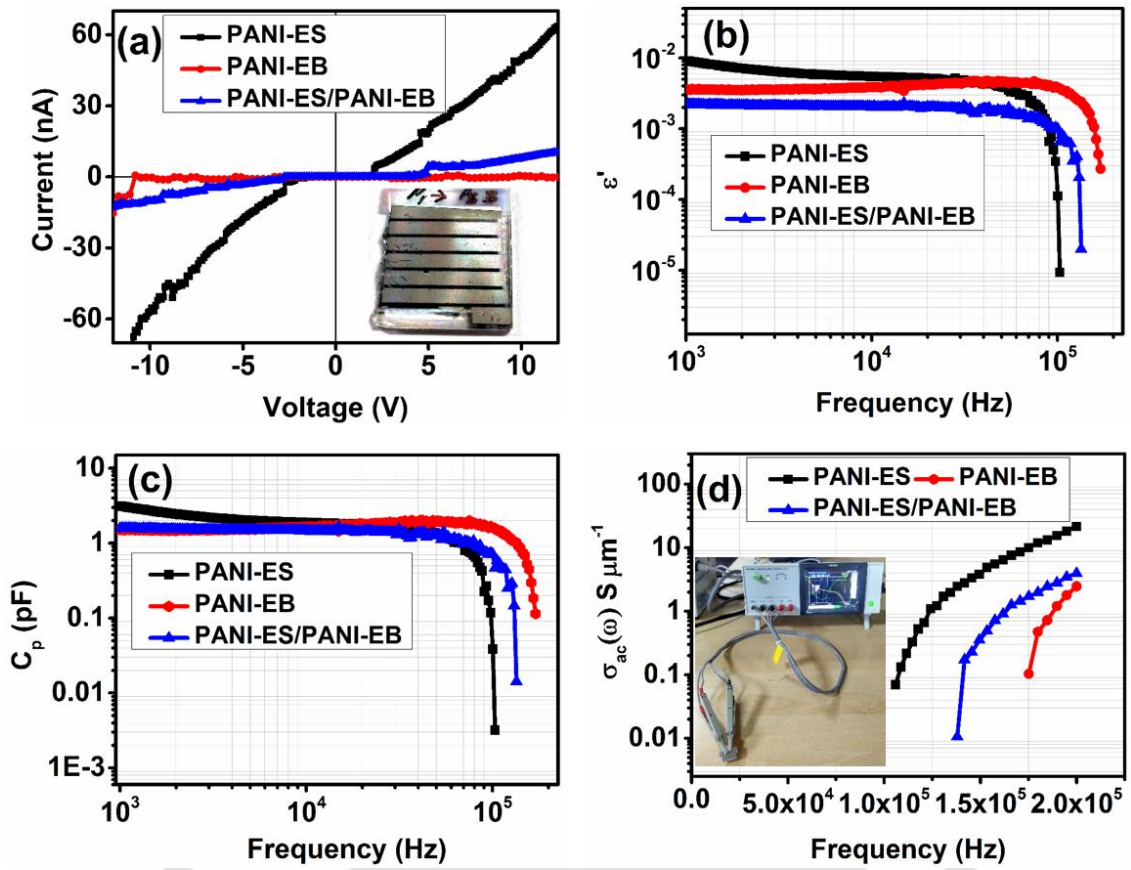

Figure 6.10. (a) I-V characteristics of all the thin films. Measurements of various physical properties as a function of frequency: (b) dielectric permittivity, (c) capacitance, and (d) AC conductivity of the thin films.

Therefore, PANI-EB surface revealed higher ε' as compared to the PANI-ES/PANI-EB thin film. It is to be noted that the storage permittivity of the thin films is comparatively low as compared to the bulk PANI materials, owing to the thin layered surface [90]. At the lowest frequency (viz., 1 kHz) the maximum capacitance of the fabricated thin film capacitors were ~ 3.5, ~ 1.8 and ~ 1.54 pF for PANI-ES, PANI-EB and PANI-ES/PANI-EB, respectively (Figure 6.10c). PANI-ES thin film capacitors exhibit a better charge storage property due to the maximum current carrying capability (Figure 6.10a) as compared to other thin film materials. PANI-EB is also relatively more stable at a higher frequency compared to the composite film. The frequency dependent AC conductivity (σ_{ac}) was estimated by using the following relation: $\sigma_{ac} = \omega\, \varepsilon_0\, \varepsilon' \tan(\delta)$ [86], where ε_0 is permittivity of vacuum, ε' is dielectric constant, ω is applied frequency and $\tan(\delta)$ is the loss tangent. Figure 6.10d represents the variation of AC conductivity with the applied frequency; inset shows the experimental setup of the fabricated thin film capacitors. The AC conductivities exhibit an increasing trend with increasing the applied frequency for the thin films (Figure 6.10d). The estimated values of AC conductivities were ~ 23.75, ~ 4.10, and ~ 2.47 S μm^{-1}, for PANI-ES, PANI-ES/PANI-EB and PANI-EB,

respectively. PANI-ES appears to be more conductive than PANI-EB due to the availability of π–π* conjugations and polaron–π* transitions. Consequently, the composite film of PANI-ES and PANI-EB shows a conductivity, intermediate between PANI-ES and PANI-EB. The linear behaviour of AC conductivity below 10^5 Hz is attributed to the DC conductivity. Therefore, the charge transport phenomenon is based on the total conductivity (viz., $\sigma_{total}=\sigma_{ac}+\sigma_{dc}$), as has been demonstrated by Yakut et al. [91] for thin film capacitors.

6.3.5. Electrostatic charge storage properties

The above dielectric properties of PANI thin films meet to high-density energy materials that could be favourable for thin film capacitors. These properties further investigated corresponding to induced electric field (Figure 6.11a – d).We have carried out impedance measurement to assess the resistive and charge transfer property of the fabricated materials. The real impedance (Z) exhibits a decreasing trend with increasing frequency for all the thin

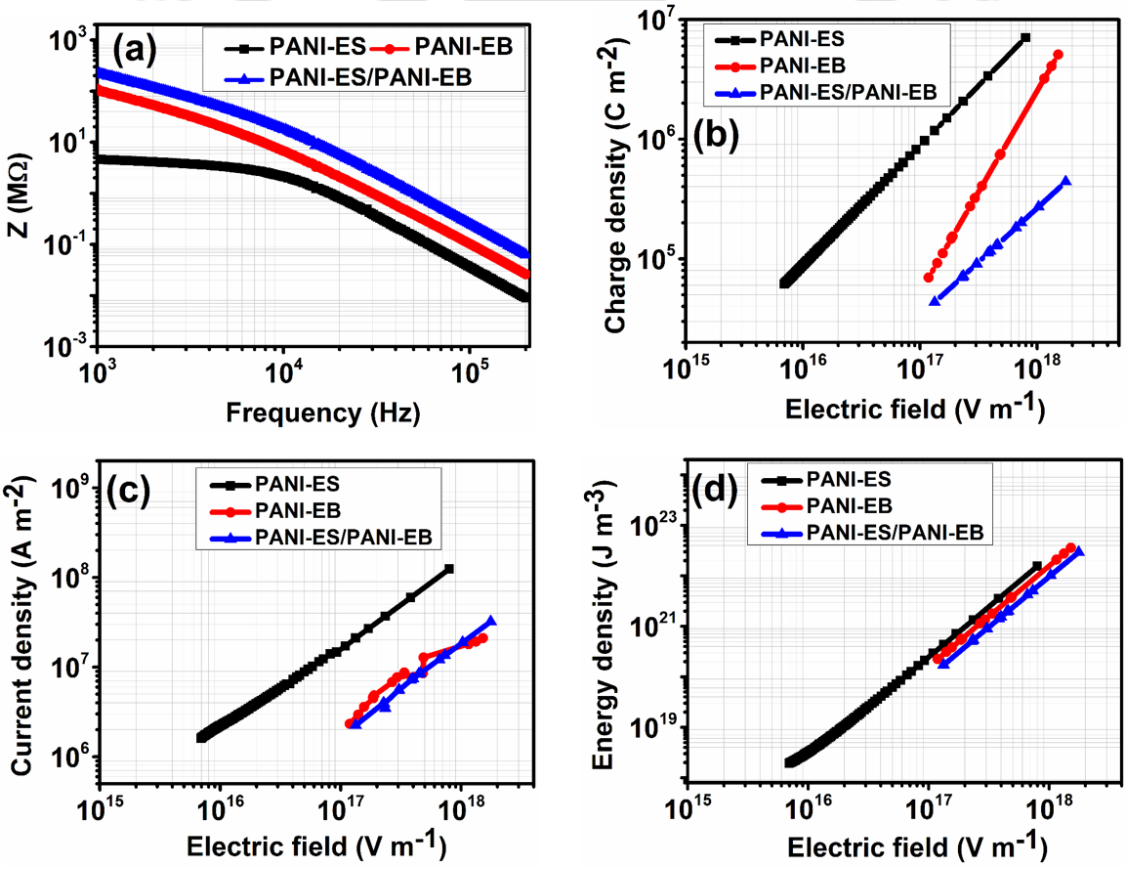

Figure 6.11. (a) Impedance-frequency response for the thin film capacitors. Change in (b) surface charge density, (c) current density, and (d) energy density with electric field, for all the thin film capacitors.

film capacitors (Figure 6.11a). The existence of a relaxation frequency (~10^4 Hz) is due to the injection barrier in the interfacial region [92,93]. The PANI-ES shows the lowest Z (~ 4.68 MΩ at 1 kHz), followed by PANI-EB and PANI-ES/PANI-EB thin films. The lowest value of Z of PANI-ES is well corroborated with the higher AC conductivity, as shown in Figure 6.10d. Therefore, a stable charge transfer proficiency will be highest in PANI-ES with minimum frequency-dependent losses. The variation of the Z with the frequency of each thin film can be correlated with the physical parameters such as the molecular structure of π–conjugate, and uniformity of the thin film.

PANI thin films possess surface charge accumulation driven by an induced electric field. The surface charge density (σ_s, C m^{-2}) of each thin film was evaluated using the relation: $\sigma_s = \frac{Q}{A}$ C m^{-2}, where, Q is the induced electrostatic charge due to the applied voltage (V), and A is the surface area of thin film (m^2) [94]. The electric field (E, V m^{-1}) was determined using the relation: $E = \frac{\sigma_s}{2\,\varepsilon_0}$; which is derived in as follows:

The PANI thin film is equivalent to thin sheet having uniform surface charge density (σ_s), as schematically shown in Figure 6.12. Electric field lines passes through PANI film based on the electric field ($\vec{E}$) can be analyzed as follows [95]:

As shown thin film region is considered to be a rectangular Gaussian surface. It is clearly seen that two faces with unit vector î would be alongside $\vec{E}$. Hence, $\vec{E}$ is perpendicular to the thin film throughout the surface area (A). The charge flux across the film is $\vec{E}$. î A. The net flux of the Gaussian surface from –X to +X directions is equivalent to that would be sum of 2EA, which is enclosed by the surface charge q. In another, $q = \sigma_s \times A$, where σ_s (C m^{-2}) is the surface charge density. Therefore,

$$2EA = \frac{q}{\varepsilon_0} = \frac{\sigma_s A}{\varepsilon_0} \qquad (6.4)$$

Accordingly, the electric field intensity will be as follows:

$$E = \frac{\sigma_s}{2\varepsilon_0}\ \text{V m}^{-1} \qquad (6.5)$$

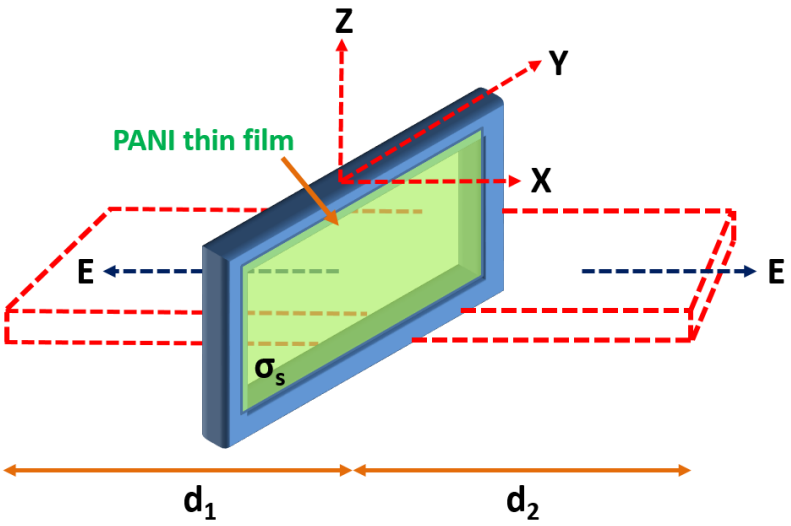

Figure 6.12. Schematic illustration of the electric field direction due to surface charge density of the PANI thin films.

Here, σ_s (Coulomb × m^{-2}) and ε_0(Farad × m^{-1}). For the electric field E is $\frac{\text{Coulomb}}{\text{Farad}}$ m^{-1}, and we know that 1 Farad = 1 coulomb per volt. After estimation we have electric field in volt per meter.

It has been observed that PANI-ES possesses the highest surface charge density (~7.07×10^6 C m^{-2}), as compared to the PANI-EB (5.09×10^6 C m^{-2}), and PANI-ES/PANI-EB (~4.41×10^5 C m^{-2}) thin film capacitors (Figure 6.11b). The PANI-ES has rapid columbic charge dispersion over the film surface in the presence of an electric field (~ 6.51×10^{15} V m^{-1}). The charge distributions for other films is responsive only at an electric field higher than ~ 10^{17} V m^{-1}, suggesting that the materials are less electrically active with small capacitance behaviour as shown in Figure 6.10c. The higher surface charge density of PANI-ES is attributed to the availability of free electrons on the PANI-ES surface, which facilitates an easy charge transfer with an enhanced charge density. On the other hand, relatively less-conducting PANI-EB film due to lack of free charge carriers exhibits an enhanced charge holding proficiency. As a result, to achieve a uniform polarization of electrostatic charge, a higher threshold (more than ~10^{17} V m^{-1}) is needed. It may be concluded that PANI-ES-based thin film capacitor is fast responsive at a low threshold and stable against electric field breakdown.

Current densities (J, A m^{-2}) of the thin film capacitors were measured and plotted in Figure 6.11c. The current density of each thin film shows an increasing trend with increasing electric field. The PANI-ES based capacitor exhibits the highest value of J (~ 1.4×10^8 A m^{-2}) at an

electric field of ~ 8.66×10^{17} V m^{-1}. The corresponding values for PANI-EB and PANI-ES/PANI-EB composite films are ~ 2.27×10^{7} A m^{-2} at ~ 1.59×10^{18} V m^{-1} and ~ 3.22×10^{7} A m^{-2} at ~ 1.78×10^{18} V m^{-1}, respectively. It is noted that the PANI-ES capacitor shows a high value of J with a low breakdown strength, which is attributed to the well-organized nanostructure (Figure 2b) of the thin film with a higher film thickness [96,97], making the surface conductive.

The energy density (U_e, J m^{-3}) of the fabricated thin film capacitors shows an increasing trend with the applied electric field (Figure 6.11d). The analysis of volumetric energy density ($U_e = \frac{1}{2}\varepsilon_r\varepsilon_0 E^2$ J m^{-3}) [98,99], revealed that PANI-ES based capacitors are fast responsive and store electrostatic energy of ~ 1.57×10^{18} J m^{-3} at an electric field of ~ 6.59×10^{15} V m^{-1}. PANI-EB and PANI-ES/PANI-EB capacitors show the response at a higher electric field breakdown. PANI-EB thin film due to the non-conducting phase, a higher threshold is needed to polarize the electrostatic charge carriers. As a result, the energy density of PANI-EB capacitor appears to be ~ 2.01×10^{20} J m^{-3} at the breakdown strength of electric field ~ 1.15×10^{17} V m^{-1}, while the composite thin film capacitors is responsive at an energy density of ~ 1.13×10^{20} J m^{-3} with a breakdown strength of ~ 1.30×10^{17} V m^{-1}.

6.4. Conclusion

Preparation of thin film of conducting polymer is essential to develop materials for advanced applications, such as in optoelectronics, energy harvesting and storage, and solar energy, etc. The conventional methods, such as spin coating, dip coating have limited applicability to the materials, which is brittle in nature, difficult to cast a smooth thin and flexible film. The vacuum thermal deposition method offers a promising method to overcome these limitations and to prepare PANI thin films. In this work, we have presented a comprehensive study on the preparation of PANI thin film and fabrication of PANI-based capacitor. Detailed morphological analysis, including spectroscopic ellipsometry, shows the formation of a thin film of PANI-ES, PANI-EB and composite film consisting of both with thickness ≤ 100 nm. As expected, the acid doped PANI-ES shows a higher conductivity than PANI-EB, while, the composite film is in between of these two. The excellent dielectric performance in the range of 1 kHz to 200 kHz frequency of the fabricated thin film capacitors is attributed to the random orientation of the polymer chain segments during the preparation of the thin film. We have shown that preparation of multi-layer thin film is possible to achieve by this method, which is otherwise difficult to achieve by other modes of thin film preparation. Layer-by-layer deposition by thermal evaporation may be a facile and feasible approach to fabricate thin films

with organic and inorganic moiety as well to bring the necessary structural heterogeneity for specific applications. The successful preparation of composite film and its application as a capacitor opens up the avenue to explore the preparation of multi-layered thin film with diverse applications in large area flexible devices such as, non-volatile memories, smart cards, and driver circuits of organic display. We believe that our findings will be extremely useful in device fabrication, where more than one layer of thin films with different doping level would be needed. It would also be possible to deposit an inorganic moiety into the PANI layer, if required, by following the same method as discussed.

References:

[1] N. Chen, D. H. Kim, P. Kovacik, H. Sojoudi, M. Wang, K. K. Gleason, *Annu. Rev. Chem. Biomol. Eng.* **2016**, *7*, 373.

[2] J. Lewis, *Mater. Today* **2006**, *9*, 38.

[3] X. Li, X. Yu, Y. Han, *J. Mater. Chem. C* **2013**, *1*, 2266.

[4] K. Park, D. Choi, J. Hong, *Sci. Rep.* **2018**, *8*, 3365.

[5] D. Boyne, N. Menegazzo, R. C. Pupillo, J. Rosenthal, K. S. Booksh, *J. Vac. Sci. Technol. A* **2015**, *33*, 031510.

[6] D. M. Taylor, *Semicond. Sci. Technol.* **2015**, *30*, 054002.

[7] S. Nishio, T. Chiba, A. Matsuzaki, H. Sato, *J. Appl. Phys.* **1996**, *79*, 7198.

[8] S. Nishio, T. Chiba, A. Matsuzaki, H. Sato, *Appl. Surf. Sci.* **1996**, *106*, 132.

[9] J. McElvain, S. Tatsuura, F. Wudl, A. J. Heeger, *Synth. Met.* **1998**, *95*, 101.

[10] K. P. Gritsenko, A. M. Krasovsky, *Chem. Rev.* **2003**, *103*, 3607.

[11] Y. Huang, D. R. Paul, *Macromolecules* **2006**, *39*, 1554.

[12] C. T. Black, K. W. Guarini, K. R. Milkove, S. M. Baker, T. P. Russell, M. T. Tuominen, *Appl. Phys. Lett.* **2001**, *79*, 409.

[13] E. M. Anderson, I. Ericsson, *J. Anal. Appl. Pyrolysis* **1981**, *3*, 35.

[14] S. L. Madorsky, *Thermal degradation of organic polymers*; Interscience Publishers, 1964.

[15] W. P. M. Willems, P. L. J. Welten, F. W. Marland, R. A. C. M. M. van Swaaij, *J. Electrochem. Soc.* **1995**, *142*, 1615.

[16] X. Li, A. Rafie, Y. Y. Smolin, S. Simotwo, V. Kalra, K. K. S. Lau, *Chem. Eng. Sci.* **2019**, *194*, 156.

[17] M. Inayoshi, M. Ito, M. Hori, T. Goto, M. Hiramatsu, *J. Vac. Sci. Technol. B Microelectron. Nanometer Struct. Process. Meas. Phenom.* **1999**, *17*, 949.

[18] D. Nicolas-Debarnot, F. Poncin-Epaillard, *Anal. Chim. Acta* **2003**, *475*, 1.

[19] C. Dhand, M. Das, M. Datta, B. D. Malhotra, *Biosens. Bioelectron.* **2011**, *26*, 2811.

[20] G. Gustafsson, G. M. Treacy, Y. Cao, F. Klavetter, N. Colaneri, A. J. Heeger, *Synth. Met.* **1993**, *57*, 4123.

[21] H. L. Wang, A. G. MacDiarmid, Y. Z. Wang, D. D. Gebier, A. J. Epstein, *Synth. Met.* **1996**, *78*, 33.

[22] H. Bejbouji, L. Vignau, J. L. Miane, M.-T. Dang, E. M. Oualim, M. Harmouchi, A. Mouhsen, *Sol. Energy Mater. Sol. Cells* **2010**, *94*, 176.

[23] Z. Liu, J. Zhou, H. Xue, L. Shen, H. Zang, W. Chen, *Synth. Met.* **2006**, *156*, 721.

[24] K. L. Bhowmik, K. Deb, A. Bera, R. K. Nath, B. Saha, *J. Phys. Chem. C* **2016**, *120*, 5855.

[25] J.-W. Jeon, J. O'Neal, L. Shao, J. L. Lutkenhaus, *ACS Appl. Mater. Interfaces* **2013**, *5*, 10127.

[26] S. Palsaniya, H. B. Nemade, A. K. Dasmahapatra, *ACS Appl. Polym. Mater.* **2019**, *1*, 647.

[27] F. Zhao, Y. Shi, L. Pan, G. Yu, *Acc. Chem. Res.* **2017**, *50*, 1734.

[28] Y. Liu, T. Cui, K. Varahramyan, *Solid-State Electron.* **2003**, *47*, 811.

[29] M. Irimia-Vladu, N. Marjanovic, A. Vlad, A. M. Ramil, G. Hernandez-Sosa, R. Schwoödiauer, S. Bauer, N. S. Sariciftci, *Adv. Mater.* **2008**, *20*, 3887.

[30] Y. Y. Smolin, K. L. V. Aken, M. Boota, M. Soroush, Y. Gogotsi, K. K. S. Lau, *Adv. Mater. Interfaces* **2017**, *4*, 1601201.

[31] V. J. Babu, S. Vempati, S. Ramakrishna, *Mater. Sci. Appl.* **2013**, *04*, 1.

[32] M. Wan, *Macromol. Rapid Commun.* **2009**, *30*, 963.

[33] K. K. Lee, J. M. Vohs, N. J. DiNardo, *Surf. Sci.* **1999**, *420*, L115.

[34] N. E. Agbor, M. C. Petty, A. P. Monkman, *Sens. Actuators B Chem.* **1995**, *28*, 173.

[35] J. C. Li, Z. Q. Xue, Y. Zeng, W. M. Liu, Q. D. Wu, Y. L. Song, L. Jiang, *Thin Solid Films* **2000**, *374*, 59.

[36] Z. M. Ren, Z. H. Mai, S. C. Ng, P. Miao, S. I. Pang, J. P. Wang, T. C. Chong, Y. F. Lu, *Surf. Coat. Technol.* **2000**, *125*, 388.

[37] H. Lim, J.-H. Choi, *J. Chem. Phys.* **2006**, *124*, 014710.

[38] N. A. Abdul-Manaf, W. Y. W. Yusoff, S. Z. N. Demon, N. A. Shaari, A. Shamshuddin, N. S. Mohamed, *Mater. Res. Express* **2019**, *6*, 096453.

[39] M. M. Ayad, G. El-Hefnawey, N. L. Torad, *J. Hazard. Mater.* **2009**, *168*, 85.

[40] H. L. Wang, A. G. MacDiarmid, Y. Z. Wang, D. D. Gebier, A. J. Epstein, *Synth. Met.* **1996**, *78*, 33.

[41] V. F. Ivanov, A. A. Nekrasov, O. L. Gribkova, A. V. Vannikov, *Synth. Met.* **1996**, *83*, 249.

[42] N. E. Agbor, M. C. Petty, A. P. Monkman, *Sens. Actuators B Chem.* **1995**, *28*, 173.

[43] T. L. Porter, *Surf. Sci.* **1993**, *293*, 81.

[44] D. Boyne, N. Menegazzo, R. C. Pupillo, J. Rosenthal, K. S. Booksh, *J. Vac. Sci. Technol. A* **2015**, *33*, 031510.

[45] S. Palsaniya, H. B. Nemade, A. K. Dasmahapatra, *Polymer* **2018**, *150*, 150.

[46] G. E. Asturias, A. G. MacDiarmid, R. P. McCall, A. J. Epstein, *Synth. Met.* **1989**, *29*, 157.

[47] W. Zheng, M. Angelopoulos, A. J. Epstein, A. G. MacDiarmid, *Macromolecules* **1997**, *30*, 2953.

[48] M. Canales, J. Torras, G. Fabregat, A. Meneguzzi, C. Alemán, *J. Phys. Chem. B* **2014**, *118*, 11552.

[49] C. R. Cena, L. F. Malmonge, J. A. Malmonge, *J. Polym. Res.* **2016**, *24*, 9.

[50] H. J. Salavagione, J. Arias, P. Garcés, E. Morallón, C. Barbero, J. L. Vázquez, *J. Electroanal. Chem.* **2004**, *565*, 375.

[51] Z. Rozlívková, M. Trchová, I. Šeděnková, M. Špírková, J. Stejskal, *Thin Solid Films* **2011**, *519*, 5933.

[52] M. Trchová, Z. Morávková, M. Bláha, J. Stejskal, *Electrochimica Acta* **2014**, *122*, 28.

[53] Y. Furukawa, F. Ueda, Y. Hyodo, I. Harada, T. Nakajima, T. Kawagoe, *Macromolecules* **1988**, *21*, 1297.

[54] G. Varsányi, S. Szöke, *Vibrational spectra of benzene derivatives*; New York : Academic Press, 1969.

[55] G. M. do Nascimento, M. L. A. Temperini, *J. Raman Spectrosc.* **2008**, *39*, 772.

[56] G. Ćirić-Marjanović, M. Trchová, J. Stejskal, *J. Raman Spectrosc.* **2008**, *39*, 1375.

[57] I. Šeděnková, M. Trchová, J. Stejskal, *Polym. Degrad. Stab.* **2008**, *93*, 2147.

[58] H. Baniasadi, A. Ramazani S.A., S. Mashayekhan, F. Ghaderinezhad, *Synth. Met.* **2014**, *196*, 199.

[59] A. A. Nekrasov, V. F. Ivanov, O. L. Gribkova, A. V. Vannikov, *Electrochimica Acta* **1999**, *44*, 2317.

[60] T.-F. Wu, J.-D. Hong, *RSC Adv.* **2016**, *6*, 96935.

[61] J. Stejskal, M. Trchová, *Polym. Int.* **2012**, *61*, 240.

[62] R. Sainz, W. R. Small, N. A. Young, C. Vallés, A. M. Benito, W. K. Maser, M. in het Panhuis, *Macromolecules* **2006**, *39*, 7324.

[63] C.-C. Han, M.-Y. Bai, K.-F. Yang, Y.-S. Lee, C.-W. Lin, *J. Mater. Chem.* **2008**, *18*, 3918.

[64] J. Stejskal, P. Kratochvíl, N. Radhakrishnan, *Synth. Met.* **1993**, *61*, 225.

[65] O. Kwon, M. L. McKee, *J. Phys. Chem. B* **2000**, *104*, 1686.

[66] K. Uvdal, M. Lögdlund, P. Dannetun, L. Bertilsson, S. Stafström, W. R. Salaneck, A. G. MacDiarmid, A. Ray, E. M. Scherr, T. Hjertberg, A. J. Epstein, *Synth. Met.* **1989**, *29*, 451.

[67] C. Constantinescu, A. Rotaru, A. Nedelcea, M. Dinescu, *Mater. Sci. Semicond. Process.* **2015**, *30*, 242.

[68] M. Akhtar, H. A. Weakliem, R. M. Paiste, K. Gaughan, *Synth. Met.* **1988**, *26*, 203.

[69] T. R. Dillingham, D. M. Cornelison, E. Bullock, *J. Vac. Sci. Technol. A* **1994**, *12*, 2436.

[70] H. A. Al-Attar, Q. H. Al-Alawina, A. P. Monkman, *Thin Solid Films* **2003**, *429*, 286.

[71] J. B. de Lima Filho, Á. A. Hidalgo, *Synth. Met.* **2017**, *223*, 80.

[72] M. Losurdo, M. Bergmair, G. Bruno, D. Cattelan, C. Cobet, A. de Martino, K. Fleischer, Z. Dohcevic-Mitrovic, N. Esser, M. Galliet, R. Gajic, D. Hemzal, K. Hingerl, J. Humlicek, R. Ossikovski, Z. V. Popovic, O. Saxl, *J. Nanoparticle Res.* **2009**, *11*, 1521.

[73] K. Hinrichs, M. Gensch, N. Nikonenko, J. Pionteck, K.-J. Eichhorn, *Macromol. Symp.* **2005**, *230*, 26.

[74] W. Ogieglo, H. Wormeester, K.-J. Eichhorn, M. Wessling, N. E. Benes, *Prog. Polym. Sci.* **2015**, *42*, 42.

[75] S. M. Sirard, P. F. Green, K. P. Johnston, *J. Phys. Chem. B* **2001**, *105*, 766.

[76] W. Ogieglo, H. Wormeester, M. Wessling, N. E. Benes, *ACS Appl. Mater. Interfaces* **2012**, *4*, 935.

[77] H. Fujiwara, *Spectroscopic Ellipsometry: Principles and Applications*; John Wiley & Sons, 2007.

[78] W. Ogieglo, H. Wormeester, K.-J. Eichhorn, M. Wessling, N. E. Benes, *Prog. Polym. Sci.* **2015**, *42*, 42.

[79] C. Yim, M. O'Brien, N. McEvoy, S. Winters, I. Mirza, J. G. Lunney, G. S. Duesberg, *Appl. Phys. Lett.* **2014**, *104*, 103114.

[80] G. E. Jellison, F. A. Modine, *Appl. Phys. Lett.* **1996**, *69*, 371.

[81] J. L. Stehle, J. P. Piel, *Appl. Surf. Sci.* **2009**, *256*, S72.

[82] A. R. Forouhi, I. Bloomer, *Phys. Rev. B* **1986**, *34*, 7018.

[83] D. I. Yakubovsky, A. V. Arsenin, Y. V. Stebunov, D. Y. Fedyanin, V. S. Volkov, *Opt. Express* **2017**, *25*, 25574.

[84] A. E. Abdelrahman, W. M. M. Yunus, A. K. Arof, *J. Non-Cryst. Solids* **2012**, *358*, 1447.

[85] I. A. Hümmelgen, L. S. Roman, F. C. Nart, L. O. Péres, E. L. de Sá, *Appl. Phys. Lett.* **1996**, *68*, 3194.

[86] D. Deger, K. Ulutaş, Ş. Yakut, H. Kara, *Mater. Sci. Semicond. Process.* **2015**, *38*, 1.

[87] X. B. Lu, G. H. Shi, J. F. Webb, Z. G. Liu, *Appl. Phys. A* **2003**, *77*, 481.

[88] H. M. E. Ghanem, H. Attar, H. S. Ahmad, S. Abduljawad, *Int. J. Polym. Mater. Polym. Biomater.* **2006**, *55*, 663.

[89] L. Wang, F. Gao, J. Xu, K. Zhang, J. Kong, M. Reece, H. Yan, *Compos. Sci. Technol.* **2018**, *158*, 112.

[90] V. J. Babu, S. Vempati, S. Ramakrishna, *Mater. Sci. Appl.* **2013**, *04*, 1.

[91] S. Yakut, K. Ulutas, D. Deger, *Thin Solid Films* **2018**, *645*, 269.

[92] D. A. Ahn, S. Lee, J. Chung, Y. Park, M. C. Suh, *ACS Appl. Mater. Interfaces* **2017**, *9*, 22748.

[93] S. K. Pradhan, A. Kumar, P. Kour, R. Pandey, P. Kumar, M. Kar, A. N. Sinha, *J. Mater. Sci. Mater. Electron.* **2018**, *29*, 16842.

[94] B. Wang, W. Huang, L. Chi, M. Al-Hashimi, T. J. Marks, A. Facchetti, *Chem. Rev.* **2018**, *118*, 5690.

[95] L. Eskola, In *Geophysical Interpretation using Integral Equations*; Eskola, L., Ed.; Springer Netherlands: Dordrecht, 1992; pp. 9–20.

[96] G. X. Liu, A. Liu, Y. Meng, F. K. Shan, B. C. Shin, W. J. Lee, C. R. Cho, *J. Nanosci. Nanotechnol.* **2015**, *15*, 2185.

[97] B.-G. Son, S. Y. Je, H. J. Kim, C.-K. Lee, C.-K. Lee, A. Y. Hwang, J. Y. Won, J. H. Song, R. Choi, J. K. Jeong, *Phys. Status Solidi RRL – Rapid Res. Lett.* **2013**, *7*, 485.

[98] B. Chu, X. Zhou, K. Ren, B. Neese, M. Lin, Q. Wang, F. Bauer, Q. M. Zhang, *Science* **2006**, *313*, 334.

[99] S. Palsaniya, H. B. Nemade, A. K. Dasmahapatra, *Carbon* **2019**, *150*, 179.

Chapter-7

Mixed Surfactant Mediated Synthesis of Hierarchical PANI Nanorods for Enzymatic Glucose Biosensor

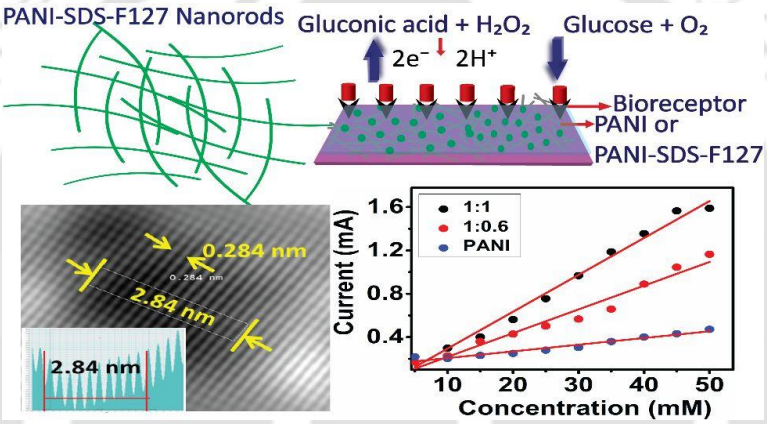

S. Palsaniya, H.B. Nemade, A.K. Dasmahapatra, Mixed Surfactant-Mediated Synthesis of Hierarchical PANI Nanorods for an Enzymatic Glucose Biosensor, *ACS Appl. Polym. Mater*. 1 (2019) 647–656.

7.1. Introduction

The functional nanomaterials are promising candidates for various potential applications, such as in microelectronics [1], biomedical [2,3], sensors [4,5], solar energy[6,7], energy storage devices as supercapacitors [8,9], batteries [10,11], photo catalytic[12], photonic devices [13] and electromagnetic interference (EMI) shielding [14]. The properties of the nanomaterials can be tailored by controlling their size and shape. For example, a nanorod (1D) would behave distinctly different from a nanosphere (3D) or a nanoflake (2D). Out of the several methods, the application of structure directing agents (SDAs) in preparing well-shaped nano materials is quite promising, as the SDA-mediated materials exhibit unique properties, especially, in pore size, surface geometry and crystalline frameworks [15,16]. The SDAs are typically molecular network structures, which guide the formation of nanomaterials, to the desired size and shape, for a specific application. Thus, they are also called as template. The templates are classified largely in two categories: hard and soft [17]. The hard templates are usually based on inorganic compounds and have been used to prepare a varieties of porous complex structures, such as, γ-alumina [18,19], zeolites [20–22] and ordered alumina molecular sieves by CMK-3 [23]. The soft templates are typically organic species, such as organic amines, tetramethylammonium cation, polyethylene glycol (PEG), cetyl trimethylammonium bromide (CTAB), sodium dodecylsulfate (SDS) [24,25] and polymers (triblock copolymers).

Although the exact mechanism of SDA is not properly understood, it has been postulated that the atomic framework and geometric configuration of the template is the key route for the structure directing phenomenon [22,26]. Therefore, it is possible to get an enhanced crystallinity of a crystalline material in the presence of SDA [27]. It is believed that the SDA molecules accelerates the rate of nucleation in the crystallization process, leading to a high crystalline material. The A-B-A triblock copolymers (viz. Pluronic P123, Pluronic F127) have extensively been used as SDAs due to their amphiphilic character. Bagshaw and Pinnavaia [28], have reported the first study on the preparation of mesoporous alumina using nonionic alkyl polyoxyethylene ether in the presence of Pluronics 64L (BASF) and $(PEO)_{13}(PPO)_{30}(PEO)_{13}$ as SDAs. Cai et al. [29] have synthesized a highly ordered mesoporous alumina with excellent absorption and structural properties employing a varieties of SDAs, including pluronic F108, P123 and F127. Out of these, the pluronic F108 exhibited the most promising results when aluminium isopropoxide was used as the aluminium precursor. Liang et al. [25] have developed an urchin-like γ-Al_2O_3 hollow microsphere in the presence of Pluronic P123 as a SDA. Dacquin

et al. [30] have reported a facile method to achieve a well-organized bimodal porous alumina structure by using the Pluronic P123.

One-dimensional nano-structure, especially with conjugated polymers are gaining much attention due to their excellent physical and chemical properties, suitable for sensing applications. Among the conjugated polymers, polyaniline (PANI) is one of the most promising candidate due to its excellent environmental stability, and tunable electrical properties by controlling the oxidation states. It is believed that, intrinsic PANI in an acidic medium show a semi-crystalline behavior, results limited surface area [31]. A wide range of nanostructures of PANI such as, nanofibers [32,33], hollow nano-capsules, hollow sphere [34,35], nano ribbons [36] and one-dimensional (1D) nanorods[37] have been synthesized with the help of structure directing agents. Among these nanostructures, 1D PANI nanorods has been shown to have numerous applications due to their remarkable physical, chemical and electrical properties [37,38].

The combination of anionic and non-ionic surfactants usually produce tailored made mesoporous structures with superior properties [39,40]. For example, presence of anionic surfactant, sodium dodecyl sulfate (SDS) and non-ionic surfactant, nonylphenol ethoxylate (NP-9) as the SDAs was shown to be a facile route to produce PANI nanoparticles with controlled size [41]. However, in some cases, the nonionic surfactants outperforms the anionic surfactants due to the presence of a long hydrophobic part, which facilitates the formation of well-organized structure [42]. Recently, Anu Prathap et al. [43], has prepared mesostructured PANI by self-assembly facilitated by mixed surfactants of anionic surfactant (sodium dodecyl sulfate, SDS) and nonionic co-surfactant (polyoxyethylene lauryl ether or Brij-35, polyethylene glycol-4000 or PEG, pluronic P123). The presence of both the surfactants has played a crucial role in dictating an enhanced surface area with increased conductivity, which is helpful in the use as H_2O_2 and glucose sensor. The PANI/SDS/P123/GOx have exhibited good reception of enzymes for the glucose bio-sensing with a sensitivity of 2.27 µA/mM. The increase in conductivity of PANI with a wide range of morphology has been reported by Yang et al. [27], in the presence of PEO and its triblock co-polymers (viz., P123 and F127). Hang et al. [44] explored a facile and cost effective process to produce a periodic array of nanoparticles, Au@MIL-100(Fe), which has subsequently been utilized for glucose sensing via surface plasmon resonance. The sensor showed an excellent sensing behavior in the range of 0–12 mM. Electrochemical polymerization exhibits numerous advantages over the chemical process. Hoang and Holze et al. [45] developed a facile method to prepare the nanocomposite of anilinium-MMT and thin film deposition over the electrodes surface using potentiostatic

electropolymerization that can be attributed to enhanced electrochemical activities. Hang et al. [46] have fabricated arrays of micro/nanostructures based on Cu coated by reduced graphene oxide (rGO), following the principle of formation of monolayer colloidal crystal leading to the formation of copper nanospheres. The rGO coated Cu nanospheres appears to be a core–shell structure that exhibits an excellent electrocatalytic performance to reduce the 4–nitrophenol to 4–aminophenol.

This work reports preparation of PANI-SDS-F127 nanocomposite via *in-situ* polymerization method of aniline monomers in the presence of aqueous solution of SDS and F127 (mixed surfactants as SDA). We have prepared a series of nanocomposites with varying ratios of PANI and F127 for a fixed amount of SDS. We have observed that the morphology of the resultant composites strongly depends on the ratio of PANI:F127. For the composite with 1:1 ratio of PANI:F127, we have observed the formation of nanorods with remarkably high electrical properties, suitable for sensing application. We have demonstrated the applicability of the resultant nanocomposites for enzymatic glucose biosensing.

7.2. Experimental

7.2.1. Materials

All chemicals and reagents were of laboratory grade and used without further purification. Aniline (Mol wt. 93.13 g/mol, Emparta grade, ≥99%), Sodium dodecylsulfate (SDS Mol. wt. 288.37 g/mol, Emplura grade ≥90%) was purchased from Merck Life Science Pvt. Ltd. Hydrochloric acid (HCl, Mol wt. 36.46 g/mol, assay 35- 37 wt %) purchased from fisher scientific. Ammonium per sulphate (APS Mol. wt. 228.19 g/mol, ≥99%) purchased from Sisco Research Laboratory. Glutaraldehyde solution 25% (Mol.wt. 100.12 g/mol), Phosphate buffer capsules (PBS, pH 7.0 ±0.05), dimethyl sulfoxide (DMSO Mol wt. 78.13 g/mol, ≥99.5%) were purchased from Merck Specialities Pvt. Ltd. Pluronic® F-127, Glucose Oxidase (Type II-s Aspergillus niger), nafion and glucose were purchased from Sigma Aldrich. DI water from Bio-age system at resistivity 18.3 MΩ per cm was used in the synthesis.

7.2.2. Synthesis of polyaniline and its functionalized derivatives

Preparation of PANI: PANI has been synthesized following the IUPAC technical report [47]. Aniline monomer (2.0 g) was added in an acidic medium (to enhance electron conduction) 50 ml of 1M HCl, to form aniline hydrochloride solution by stirring for 30 minutes. A solution of 4 g of ammonium persulfate (APS) was prepared in 50 ml of 1M HCl, and then added into the aniline hydrochloride solution, dropwise maintaining a temperature of 0 °C under constant stirring. Initially, the mixture was colorless, the color turned into bluish to dark green few minutes later, indicating the formation of polyaniline emeraldine salt (PANI-ES). After the

completion of APS addition, the solution incubated at 0 to 4 °C up to 24 hours for complete polymerization. The PANI precipitate was filtered and successively washed with 1 M HCl, followed by acetone, and again with 1 M HCl. The precipitate collected in a glass beaker, vacuum dried at 60°C for 24 hours.

Preparation of PANI-SDS-F127 composites: Reportedly, synthesis of PANI nanomaterials in the presence of both anionic and nonionic surfactants, exhibit micellar structure [39,41]. As shown in Figure 7.1, PANI chains grow inside the micellar structures. Aniline (2.0 g) was first dissolved in 50 ml of 1 M HCl solution at constant stirring for 30 min. Further, 2.5 g of SDS (anionic surfactant) and 2.0 g of Pluronic F-127 (nonionic co-surfactant) were mixed, and poured under stirring into the aniline hydrochloride solution for homogeneous dispersion. Finally, previously prepared APS in HCl solution (9 g of APS in 50 ml of 1M HCl) was added drop by drop into the above solution maintaining the temperature ~0°C. Initially, the light bluish color was visible; later on, the color was changed into greenish, indicating the completion of the polymerization of aniline monomers, mediated by the surfactants. Subsequently, precipitate of PANI-SDS-F-127 at 1:1 was allowed to filter and successively washed with DI water, acetone and 1 M HCl. Finally, the product is dried in vacuum at 60°C for 24 hrs. Following the similar protocol, a series of composites with varying weight ratio of PANI and pluronic F127, such as 1:0.6, 1:0.7 and 1:0.9, were synthesized, keeping the amount of SDS fixed.

7.2.3. Characterization and measurement

The Raman spectra of the samples were recorded using HORIBA LabRam HR Evolution with He-Ne laser, at an excitation wavelength of 633 nm. The UV-Visible absorption spectra were recorded by the Shimadzu (model no. UV-2600 230V EN) spectrophotometer. The FTIR spectra were recorded from Perkin Elmer, USA/Spectrum Two in the range of 4000-400 cm^{-1}. FTIR scanning were performed using KBr mixed pellets of powder nanomaterials. The X-ray diffraction (XRD) patterns were recorded in the range of 5-60° at a scan rate of 1° per minute, using powder XRD Bruker model no. D8 Advance using Cu-Kα-Kβ radiations at λ=1.54 A°, 40 kV, 40 mA.

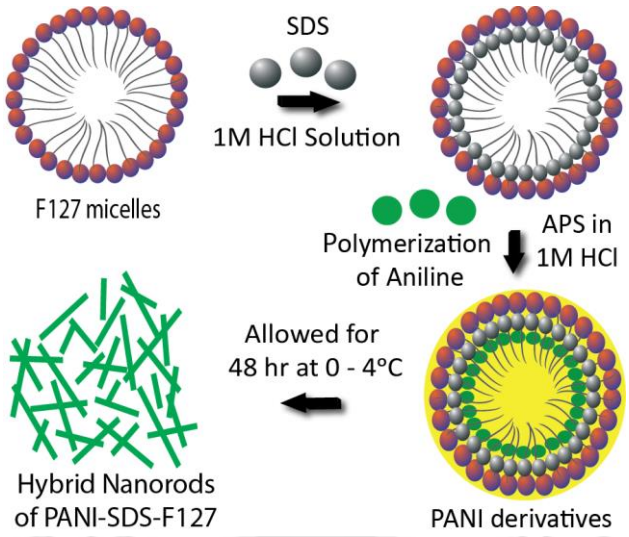

Figure 7.1. Schematic diagram of synthesized nanomaterials. The polymerization of PANI in the presence of SDS and F127 as structure directing agents (SDAs).

Surface morphology and structure were carried out by the Field Emission Scanning Electron Microscopy at accelerating voltage of 10 kV (FESEM) JEOL model no. JSM-7610F. The Field Emission Transmission Electron Microscopy (FETEM) images and elemental mapping were recorded by JEOL model JEM 2100 at the acceleration voltage of 200 kV. PerkinElmer TGA-4000 Thermogravimetric analyzer was used to record the thermal stability of the samples. Surface area and pore size measurements were carried by the BET analyzer (model no. micromeritics TriStar II). Further, the I–V characteristics were carried out using Keithley parameter analyzer, 4200 SCS, within a potential range of –1V to +1V at room temperature. The AC electrical measurements and dielectric properties were analyzed using Solartron LCR meter (model no. SI1260). The cyclic voltammetry (CV) and chronoamperometric based electrochemical measurements were carried out on Metrohm Autolab model 128N electrochemical workstation.

7.2.4. Electrode fabrication for electrochemical measurements

Three electrodes were arranged during experiments with bare glassy carbon electrode (GCE) (3 mm diameter) as a working electrode, Ag/AgCl as a reference electrode and Pt wire as a counter electrode. Before performing experiments, GCE was first cleaned using a diamond pad, then with alumina paste. Further, it was washed with ethanol before drying in air. For preparing working electrode, a 20 mg/ml suspension of PANI-SDS-F127 based samples were prepared in dimethyl sulfoxide followed by ultrasonication. Furthermore, 5 µL of the prepared solution was dropcasted on GCE and dried in air. For enzyme immobilization, modified electrode by polymeric nanomaterials was dipped into 1% glutaraldehyde solution for 10 min. Glutaraldehyde-processed electrode was immersed in GOx (10 mg/ml of PBS to maintain pH 7 approximately) solution for

1.5 h to stick the enzyme on the electrode for glucose sensing. Consequently, 5 µL of 1% Nafion solution was prepared in methanol and dropped upon the PANI-SDS-F127/GOx/Glucose modified GCE to precisely bind the deposited materials for an easy electron transport during measurements.

7.3. Results and discussion

We begin with a detailed description on microstructures of PANI-SDS-F127 ternary composites with varying ratio of PANI and F127. Following this, we discuss the electrochemical behavior of all the materials, including the application of the composite in glucose sensing.

7.3.1. Structure and morphology

The Raman spectra (Figure 7.2a) represents the symmetric stretching of phonon vibrations and polar bonds of PANI in the prepared composites. The peaks of pure PANI at 1091 cm^{-1} and 1224 cm^{-1} corresponds to C–H benzenoid bending and C–N bond stretching, respectively. Furthermore, the peak at 1323 cm^{-1}, 1387 cm^{-1} and 1606 cm^{-1} represent the quinoid free radical stretching vibration of $C–N^{\bullet+}$, quinoid stretching and benzenoid stretching, respectively [9,48]. The C–C bond deformation of benzene quinoid rings at 1606 cm^{-1} confirmed the HCl doped PANI, revealing the polaron-polaron protonation. The peak at 1510 cm^{-1} corresponds to N–H deformations, associated with the quinoid stretching [49]. Therefore, the synthesized materials possess a greater charge accumulation owing to the conjugate anilinium ions, driven by N–H and $C–N^{\bullet+}$ quinoid stretching. These quinoid stretching of the composites 1:0.6 to 1:1 remains unchanged, which confirm that the charge hopping mechanism does not affect to the vibrational deformations [50]. Figure 7.2b represents the XRD patterns of PANI and all the composites at the varying ratio of PANI and F127. The characteristic peaks at 20.3º and 25.3º correspond to the crystallographic planes of (0 4 1) and (1 6 0), respectively. These peaks are attributed to the PANI and their periodic vertical positioning, revealing an amorphous nature of PANI chains [51], with an inter-planar spacing of 0.436 nm and 0.350 nm, respectively. Further, the presence of sharp peak for 1:0.6, 1:0.7 and 1:0.9 composites is an indication of the crystalline phase. The intensity of the peaks increases with increasing the quantity of F127. However, the sample with 1:1 composition shows a lower peak intensity as the amount of F127 is beyond the critical micelle concentration (viz., 1:0.9). The presence of a broad shape of the diffraction pattern for 1:1 composite suggests a closely packed, randomly oriented polycrystalline structure with smaller particle size, resulted from the self-assembly of PANI nanorods mediated by the SDA.

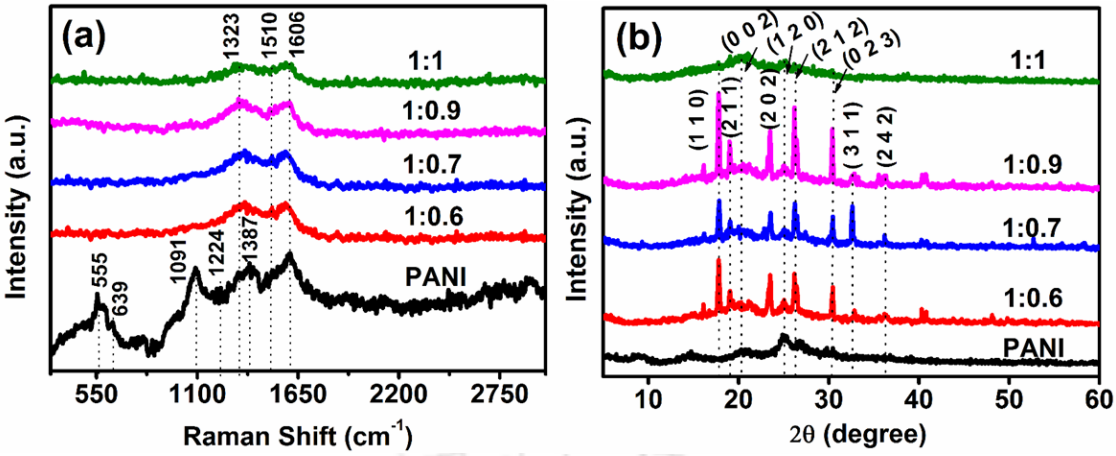

Figure 7.2. (a) Raman Spectra and (b) XRD patterns of pure PANI and PANI-SDS-F127 composite materials with varying ratio of PANI and F127.

In addition, the observed planes for all the PANI-SDS-F127 composites are (1 1 0), (2 1 1), (2 0 2), (2 1 2), (0 2 3) and (3 1 1) corresponding to an inter-planar spacing, d (nm) of 0.495 (17.9°), 0.465 (19.03°), 0.373 (23.42°), 0.393 (26.28°), 0.293 (30.4°) and 0.274 (32.67°), respectively. It has been noticed that the intensities of the diffraction peaks are varying in the same plane configuration, suggesting the polycrystalline nature of the composite materials. FTIR spectra (Figure 7.3) were recorded to verify the presence of PANI bond formation and structural representation of PANI with SDS and F127. The oxidation state of pure PANI at 1643 cm^{-1} and 1458 cm^{-1} are attributed to C=C bond stretching of quinoid rings and benzenoid rings, respectively [52].

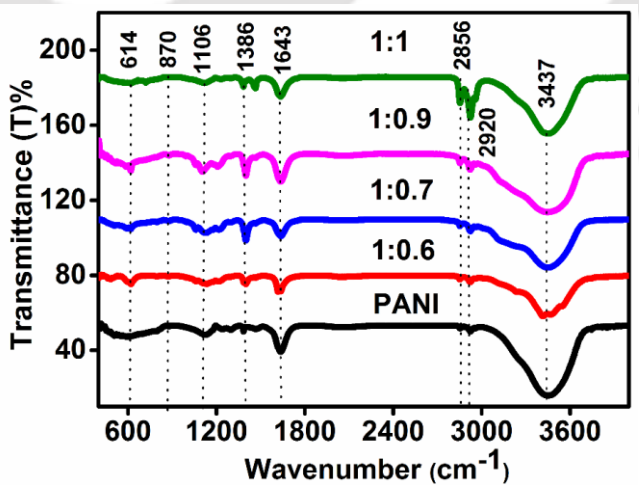

Figure 7.3. FTIR spectra of PANI and PANI-SDS-F127 composites at varying composition of PANI and F127.

There is a weak absorption in the range of 3000–3500 cm^{-1}, which represents the C–H and N–H bond stretching of PANI backbone. Additionally, the peak shown in the range of 1106 cm^{-1} and 1386 cm^{-1}, indicates about the quinoid-benzenoid-quinoid units and benzenoid unit, respectively. Furthermore, the absorption at 614 cm^{-1} and 1063 cm^{-1} represents the C–H in-plain bending mode of vibrations of benzenoid and quinoid rings, suggesting the formation of polyaniline emeraldine salt [53]. The characteristics peak at 1063 cm^{-1} in PANI-SDS-F127 corresponds to the acidic level. During washing, some amount of SDS was washed out, as maximum amount was retained and contributed towards the formation of hierarchical nanostructures. As a result, the characteristic peaks of mesoporous structure in the range of 870 cm^{-1} to 1063 cm^{-1} corresponds to small amount of stretching by virtue of the appearance of di-substitute of benzene groups. As such, peak at 1223 cm^{-1} suggests the existence of –S=O at the lower absorption, and below the 614 cm^{-1} spectral intensity confirm the moderate stretching of S–O group [54].

The characteristic absorption bands of PANI and PANI composites are shown in Figure 7.4a. Absorption in the range of 270 to 308 nm, corresponds to the π-π* electronic transition into benzenoid units. The absorption peak at 449 nm corresponds to polaron transition. Compared to the ternary composites, pure PANI shows a minimum absorbance, in the range of 219 to 260 nm, which is attributed to the $\pi - \pi^*$ [55] transition. Redox behaviour in an acidic medium provides protonated anilinium ions [56,57], enhanced characteristic absorbance. The 1:1 sample shows the maximum absorbance due to excess electronic transitions. In accordance, partial protonation is being observed in PANI backbone, with an absorbance band at 480 to 610 nm. This indicates that the polaron and bipolaron transitions of aniline to anilinium conversion took place during the polymerization process. The optical band gap was determined (Figure 7.4b) by the classical tauc plot method using by the following equation [58].

$$(\alpha h\nu)^{\frac{1}{n}} = k(h\nu - E_g) \qquad (7.1)$$

where, the band gap is E_g, k is the materials constant, ν is the frequency of the incidence photon energy (hν), h is Planck's constant and α being the absorption coefficient of corresponding materials. The band absorbance $(\alpha h\nu)^{\frac{1}{n}}$ has been plotted against photon energy at n = 1/2 for the direct transition. An intercept of the tangent drawn on the real axis gives the band gap of the concerned materials. The corresponding band energies of pure PANI and ternary composites are 2.02, 2.35, 2.35, 2.42 and 2.25 eV for PANI, 1:0.6, 1:0.7, 1:0.9 and 1:1, respectively.

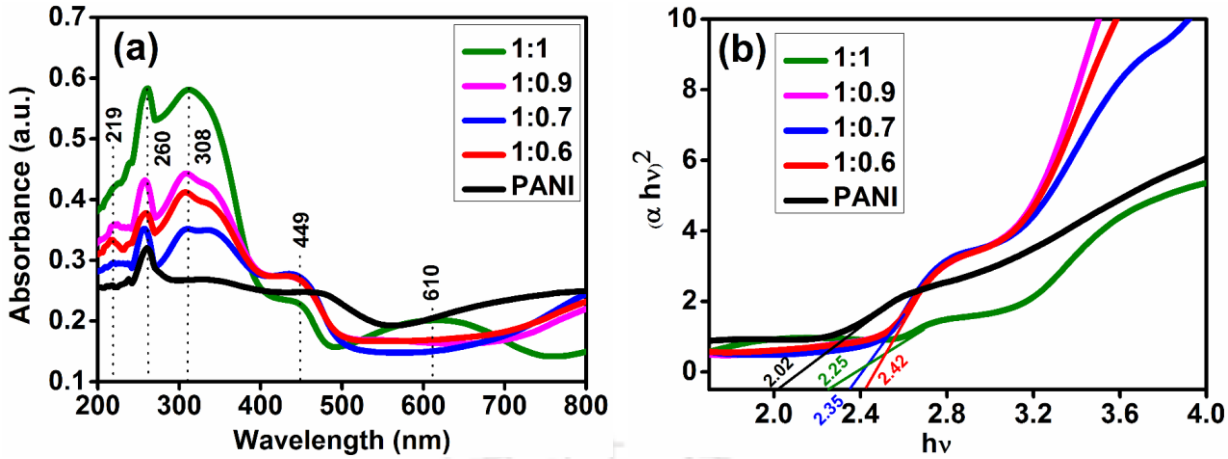

Figure 7.4. (a) UV Visible absorption spectra, (b) calculated optical band gap energies of the nanocomposite samples.

The FESEM image (Figure 7.5a) of PANI-SDS-F127 at 1:1 exhibits unidirectional symmetric nanorods with an average length and diameter of 2.9 µm and 173 nm, respectively. Further, the FETEM image (Figure 7.5b) closely corroborates with the FESEM result, exhibiting uniformly distributed nanorods. The inset of Figure 7.5b reveals a flower shape arrangement of micro-rods throughout the crystal structure, at a low magnification. The presence of ordered, symmetrical and inter cross-linked nanorods are attributed to the specific concentration ratio of PANI:F127, leading to the formation of mesoporous materials. As discussed before, the XRD pattern revealed the formation of a polycrystalline structure for the sample with 1:1 (Figure 8.2b) composition, while the other samples showed a semi-crystalline nature. The short penetration depth of the nanorods (due to small diameter) would provide a direct path for the electron movement that would readily detect the target analytes as compared to other nanostructures [59]. The HRTEM images (Figure 7.5c – d) exhibit a crystalline phase with an inter-planer spacing of 0.284 nm. The selected area electron diffraction (SAED) pattern (inset of Figure 7.5c), shows the polycrystalline character due to the inclusion of pluronic F127. The ordered controlled surface structure may be attributed to the hydrogen bonding between anilinium ions and amphiphilic polymers at the time of polymerization. An elemental mapping via FETEM of a specific region (Figure 7.5e) shows that the relevant elements (viz., O, S, Cl, C and N) are uniformly distributed throughout the matrix (Figure 7.5f – j).

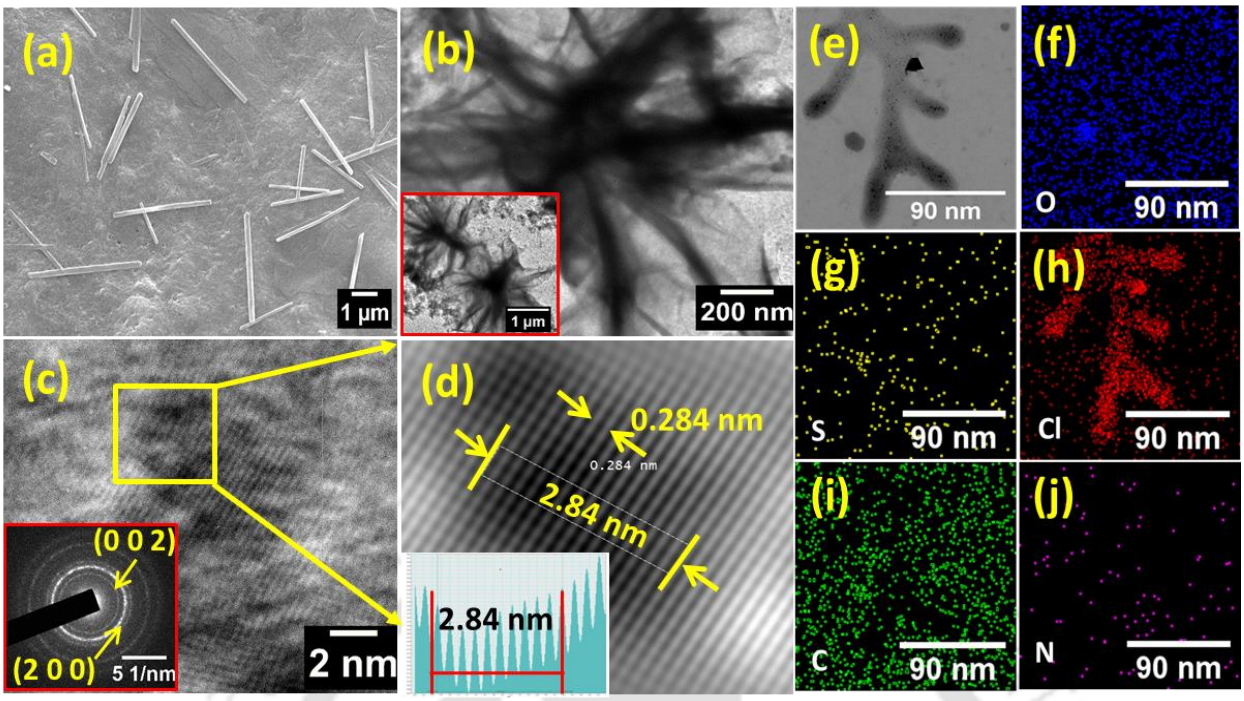

Figure 7.5. Electron microscopy images of PANI-SDS-F127 at 1:1 ratio of PANI and F127: (a) FESEM image; (b) FETEM image shows a star shape arrangement of nanorods, inset image is at high magnification (1µm); (c) HRTEM image and inset is a SAED pattern; (d) signal processed HRTEM image of the d-spacing at a finite region, inset diagram show the distribution of planer distance; (e) FETEM image of a selected region and (f – j) shows the corresponding elemental mapping, confirming the arrangement of different elements.

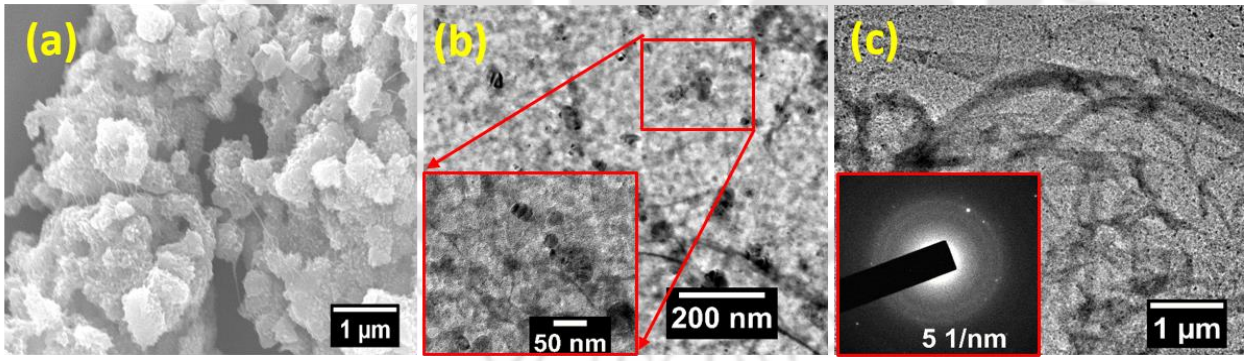

Figure 7.6. Surface morphology of the pure PANI sample.

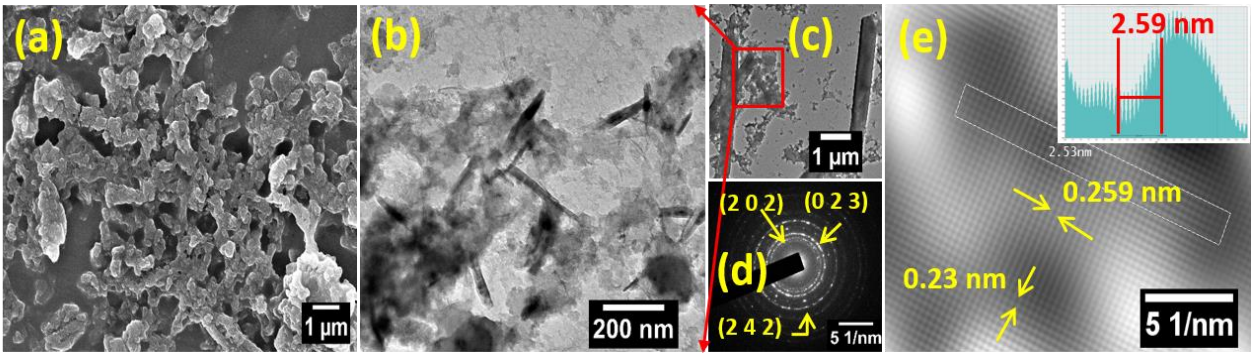

Figure 7.7. Surface morphology of the PANI-SDS-F127 1:0.6.

Morphological analysis for the remaining samples (viz., pure PANI 1:0.6, 1:0.7 and 1:0.9) are presented in Figure 7.6 to 7.9. As shown in Figure 7.6a, FESEM image of pure PANI as long nanofibers analogous to rod like structure, agglomerated and turned into spherical particles (average diameter 419 nm). FETEM images, (Figure 7.6b) at higher (200 nm), inset at 50 nm, and (Figure 7.6c) at lower (1 µm) magnifications. The uniform distribution of PANI nanofibers unveiled an amorphous behaviour as shown by the SAED pattern, inset of (Figure 7.6c). The FESEM image of the PANI-SDS-F127 at 1:0.6 ratio shows (Figure 8.7a) rod shape mesoporous structure with an average diameter of 473 nm. The FETEM images are indicating a combination of nanorods (Figure 7.7b) at higher (200 nm) and (Figure 7.7c) lower magnifications (1 µm). An evidence of polycrystalline behaviour at different planes of composite materials shown by SAED pattern (Figure 7.7d).

HRTEM image (Figure 7.7e) showing moire patterns with distinct interplanar spacing, results a combination of two lattice planes is (interplanar distances are 0.259 and 0.230 nm) clearly visible due to the high crystallinity [60]. The planner spacing at 0.259 nm correspond to the semicrystalline nature of the PANI backbone chains. An inset of Figure 7.7e is a distribution of planner distances in the range of 2.59 nm, indicating a mesophase. The FESEM image of PANI-SDS-F127 at 1:0.7 ratio (Figure 7.8a), an inter-crosslinked crystalline layers are consisting a mesoporous structure at their mean dimension of 596 nm. FETEM images, (Figure 7.8b) at higher (200 nm) magnification shows the growth of nano capsules and (Figure 7.8c) at lower (0.5 µm) magnification nano capsules looks an integral part of PANI backbone. Therefore, an interfacial area being changed due to the combination of two different templates at varied amount of F127. The SAED pattern (Figure 7.8d), a configurations of multiple planes confirm a polycrystalline behaviour. HRTEM (Figure 7.8e) reveals about fringes of crystalline behaviour with lattice spacing d (0.305 nm), as inset show a distribution of the inter-planer spacing.

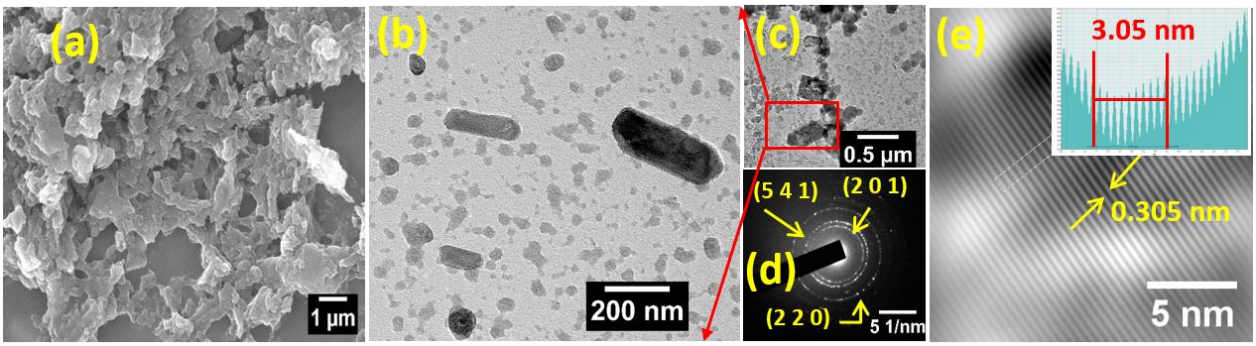

Figure 7.8. Surface morphology of the PANI-SDS-F127 1:0.7.

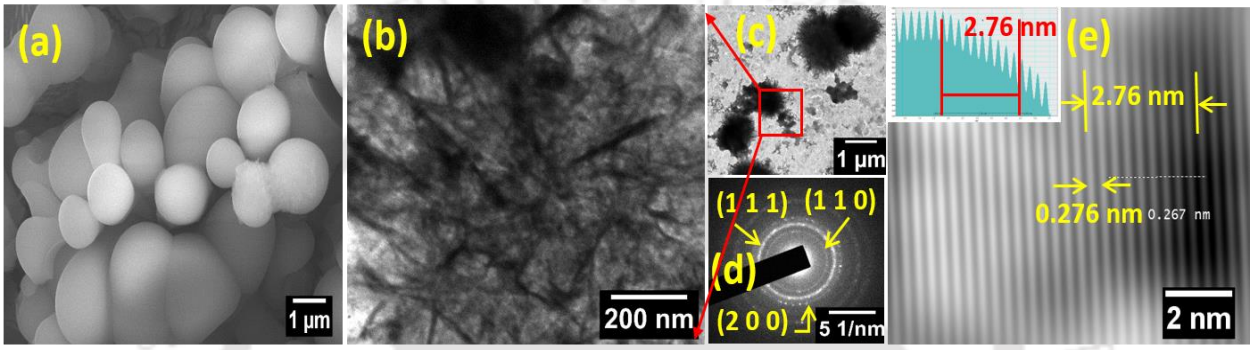

Figure 7.9. Surface morphology of the PANI-SDS-F127 1:0.9.

FESEM micrograph (Figure 7.9a) of the PANI-SDS-F127 at 1:0.9 ratio is due to the swollen nature of PANI backbone chain, at an increased weight of F127. The average diameter is 1 µm with the high interfacial area. It is noted that an ordered mesoporous structures governed by the additive templates. FETEM image (Figure 7.9b) at higher magnification (200 nm) and (Figure 7.9c) at lower magnification (1 µm) unveiled about the symmetric distribution of the flower shape nanorods. Polycrystalline SAED pattern (Figure 7.9d) at (1 1 1) plane is attributed to PANI with high charge transport due to symmetric alignment of nanorods. The (1 1 0) and (2 0 0) planes are corresponding to a relatively lower interfacial area. Following this, two dissimilar fibers and rod shape structures have been observed, as shown in (Figure 7.9b). HRTEM image (Figure 7.9e) shows a d spacing of 0.276 nm, and inset diagram shows the distribution of interplanar spacing, suggesting a mesoporous structure. Effective surface area of a porous material is an important property as far as the application is concerned. To estimate the surface area of the prepared composite materials, we have used the BET (Brunauer, Emmett, Teller) surface area analyzer [61].

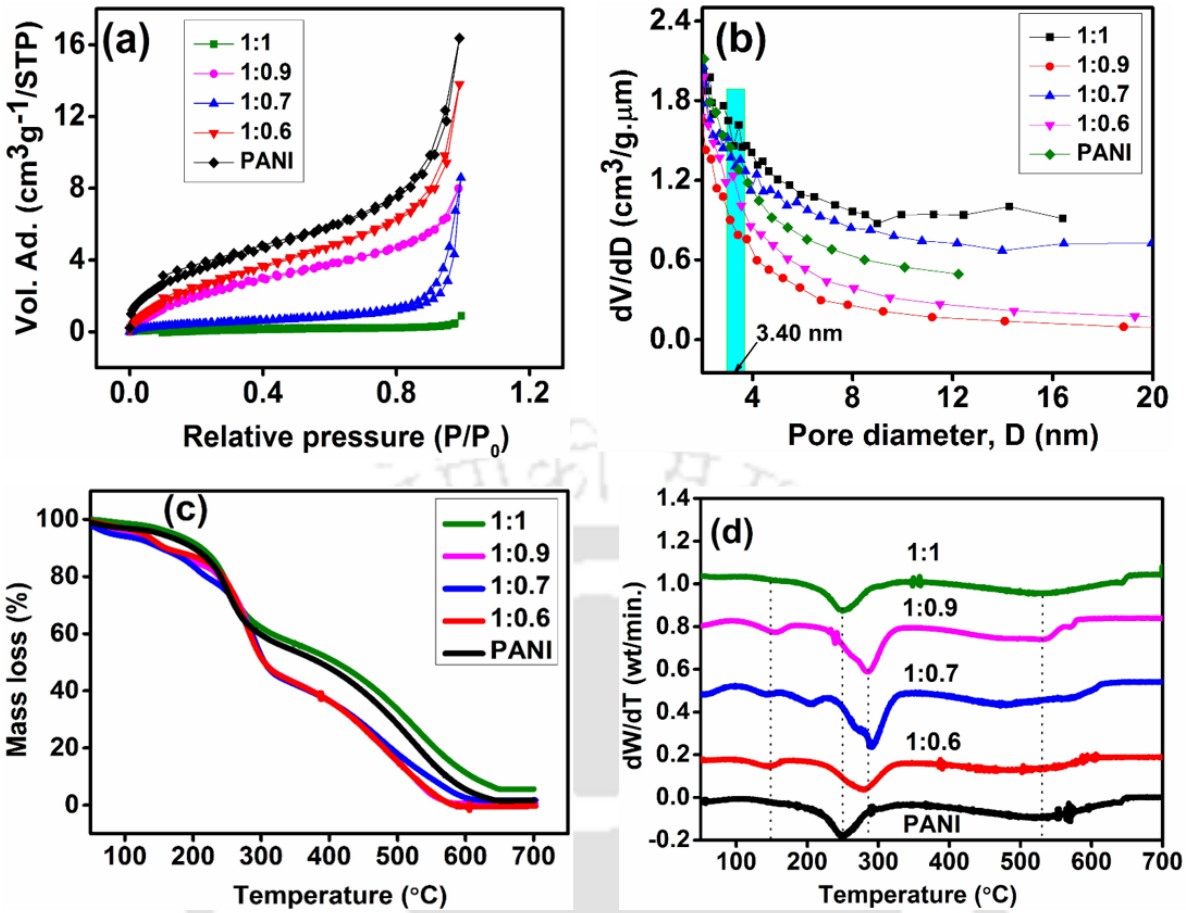

Figure 7.10. (a) N_2 adsorption and desorption isotherms and (b) Pore volume distribution of the mesoporous materials, (c) thermal stability, and (d) differential thermogravimetric analysis of pure PANI and PANI-SDS-F127 composites with varying ratio of PANI and F127.

Table 7.1. The illustration of the BET surface area, BJH pore size distribution and pore volume of all the composites, including pure PANI.

Materials	BET surface area (m^2 g^{-1})	Total area (m^2 g^{-1})	BJH adsorption avg. pore diameter (nm)	BJH adsorption pores volume (cm^3 g^{-1})
PANI	13.377	22.488	8.917	0.02255
PANI-SDS-F127 (1:0.6)	11.072	38.766	8.738	0.01932
PANI-SDS-F127 (1:0.7)	6.844	67.337	14.801	0.05681
PANI-SDS-F127 (1:0.9)	9.485	21.696	6.452	0.01023
PANI-SDS-F127 (1:1)	0.751	1.065	6.446	0.00114

Figure 7.10a, shows the N_2 adsorption and desorption isotherms of all the composites with reference to the pure PANI. The adsorption- desorption pattern shows a type IV isotherm with a narrow hysteresis loop, measured at relative pressure (P/P_0) of 0.1 to 1.0 [62], exhibiting mesoporous structures. The electron micrograph results are in close agreement with the surface area analyzer leading to the conclusion that the composite have mesoporous structures. The

Barrett-Joyner-Halenda (BJH) pore size distribution is shown in Figure 7.10b. The BET surface area, and BJH adsorption pore diameter, and pore volume have been presented in Table 7.1. The incorporation of F127 (viz., increasing the amount of F127) has a distinct effect on the well-organized size and shape of the mesoporous structure of PANI-SDS-F127 composites. Out of all the samples, pure PANI shows a maximum porosity with a highest surface area. An increasing amount of F127, the porosity (and hence the surface area) shows a decreasing trend, which is attributed to the presence of the polycrystalline structures as is shown in SAED patterns (Figure 7.5c for 1:1, and Figure 7.7, 7.8 and 7.9 for 1:0.6, 1:0.7 and 1:0.9 composites, respectively). The PANI-SDS-F127 at 1:1 ratio has maximum crystallinity (based on BET surface area measurement), which would be suitable for readily transportation of charge carriers. It has been noticed that, XRD diffraction patterns of 1:1 (Figure 7.2b) composite shows a relatively broader peak, which suggests that the material possesses an ensemble of smaller size crystalline domains with random orientation (viz., polycrystalline structure). The gradual decrease in pore size corresponds to good interconnection of PANI chains, leading to a higher crystalline surface, as confirmed by the FESEM images of all the samples.

Based on the above structural details, we propose the formation of the ternary composite with the following mechanism (Figure 7.1). F127, being a triblock copolymer with PEO (hydrophilic) and PPO (hydrophobic) block, form micelles with a hydrated outer part of PEO block as corona, and PPO block as an inner core region. SDS being more compatible with the PPO blocks, diffuses into the core region of the micelle [63]. When aniline is added into the solution (in the presence of micellar structure of F127 and SDS), it diffuses through the core region and is polymerized, upon successive addition of HCl and APS. Thus, PANI chains grow inside the core of the core-shell structure of micelle. The size and shape of the PANI chains are dictated by the relative composition of PANI and F127, for a given amount of SDS [64,65]. The SDS has a significant role in balancing the electrostatic charge, which is produced by protonated Anilinium ions. The SDS amount was fixed, because of excess SDS could be responsible for high negative charge localization, and would result in excessive leakage current. We believe that the varying ratio of F127 with PANI for a given amount of SDS is the key factor in producing the ordered microstructures.

7.3.2. Thermal analysis

To get a comprehensive estimate on the thermal stability (Figure 7.10c) of the materials, thermogravimetric analysis (TGA) was carried out for all the composites, including pure PANI. The first mass loss of 6% ~ 120 °C is due to the evaporation of water present in the composites [66,67]. The second mass loss of ~10% at ~ 210 °C is attributed to the decomposition of SDS present

in the composites. All the samples show a mass loss of 28% at ~ 260 °C, which corresponds to the decomposition of PANI [68]. The mass loss of 1:0.6 and 1:0.7 samples was slightly higher than the rest of the samples. However, a synergistic effect has been observed in the sample with 1:1 composite, which exhibits distinctly higher thermal stability, arises from the higher crystallinity. The overall maximum 37% mass loss of the samples was recorded by the differential thermogravimetric (DTG) analysis in the range of 250-285 °C (Figure 7.10d). Temperature above 447 °C, TGA curve shows the 44% residue, with a complete decomposition at 600 °C, as recorded by time dependent decomposition of nanocomposites by the DTG [69]. The maximum rate of mass decomposition per minute exhibit at a certain temperature, as the ternary nanocomposite samples have different rate of mass loss.

7.3.3. Electrical and dielectric properties

One dimensional nanorods (cf, Figure 7.5a), offer a superior electronic performance. These nanorods would play an important role in directing electron transfer that can be employed as an active electrode material, specifically for electrochemical activities. As discussed before, the SDA-mediated nanomaterials are capable of retaining the crystalline phase and provides a regular surface texture, with an improved electrical conductivity, which can easily be explored as a promising nanomaterial for the sensing applications [70]. We have estimated both ac and dc conductivities for all the samples. The dc conductivity, $\sigma_0(t)$, is ascribed to the band transition, whereas, the ac conductivity, $\sigma(\omega, t)$, is attributed to the electron hopping mechanism. In addition to this, since ac conductivity is frequency dependent, the conductivity increases with increasing frequency. The overall conductivity of the materials was analyzed as $\sigma_{total} = \sigma_0(t) + \sigma(\omega, t)$ [71,72], and detailed calculations are shown below as follows. The samples were palletized using palate maker at 10 MPa pressure for two minutes and then silver paste was polished on the pallets to form the conductive electrodes. The measurements were carried out at 1 kHz to 20 MHz at room temperature. In this experiment, frequency dependent losses were measured by the dissipated energy (ε'') and dissipation factor along with the generated capacitance. During measurements, the silver paste polished both surfaces of the pellet establish a capacitive environment, and pellet was considered as dielectric medium. The dielectric constant (ε') was calculated using the following equation [73].

$$\varepsilon' = \frac{Cd}{\epsilon_0 A} \qquad (7.2)$$

The parameters ε_0, d and A are the free space permittivity, pellet thickness and cross sectional area of the pellet, respectively. Following this, the capacitance (C) corresponding to the dielectric

constant can be correlated. Dielectric loss of energy in form of dissipation was determined using following equation [74].

$$\varepsilon'' = \varepsilon' \tan\delta \quad (7.3)$$

The dielectric loss factor, tan δ was obtained from the instrument during measurements, which is proportional to the energy losses caused by the applied field. The AC conductivity (σ_{ac}) was calculated by using the following equation [9,75].

$$\sigma_{ac} = \varepsilon' \varepsilon_0 \omega \tan\delta \quad (7.4)$$

Thus, ac conductivity is proportional to the applied frequency (f) as: ω =2πf. Hence, with increasing frequency, the ac conductivity will also increase. The dc conductivity of nanomaterials was measured on the compressed pallets by using the silver paste contacts as output terminals. The electrical resistivity ρ_{dc} was calculated using following equations [72].

$$P_{dc} = \frac{\Delta V}{t} \times \frac{A}{I} \quad (7.5)$$

where, I is the series current, V is the applied voltage, A is the area of circular pellets and t is the thickness of pellets, considered as a distance between the contact electrodes.

The dielectric constant (ϵ') and dielectric losses (ϵ") were characterized as shown in Figure 7.11a and Figure 7.11b, respectively. In all the samples, we have observed that the dielectric properties show a decreasing trend with increasing frequency. However, at the higher frequency (viz., $\log_{10}(\omega)$, ~ 10^7 Hz), the moving charge localization gets perturbed resulting a non-monotonic behavior. It has been observed that the magnitude of both ϵ' and ϵ" decreases with increasing the amount of F-127. PANI shows maximum ϵ' as compared to the prepared ternary composites, while, the composite with 1:1 ratio exhibits the lowest value for ϵ' and ϵ". The measurement of ac conductivity, σ (ω, t) with frequency shows a non-monotonic (viz., increasing and then decreasing) trend for all the ternary composites (Figure 7.11c). Furthermore, at the higher frequency range, the ac conductivity rapidly enhances, indicating that the prepared samples are quite responsive at the high frequency.

Table 7.2. The DC electrical conductivity of the pure PANI and mesoporous networks.

Name of Sample	PANI	PANI-SDS-F127 1:0.6	PANI-SDS-F127 1:0.7	PANI-SDS-F127 1:0.9	PANI-SDS-F127 1:1
Conductivity (S/m)	0.0234	0.0363	0.0552	0.0676	0.0835

It has been noticed that ac conductivities of the ternary composites are relatively higher than that of pure PANI, and with increasing the quantity of F127, the magnitude of ac conductivity increases. The prepared materials demonstrate the applicability within a certain range of frequency, which may have expected from a polymer composite. At high frequency (viz., $\log_{10}(\omega)$ ~ 10^7 Hz), the non-monotonic behavior is attributed to the resonance effect, which arises due to the presence of polar groups of polymeric chains, contributing towards the electric field induced dipole polarization [76]. To estimate total conductivity (viz., dc), we have measured the I-V characteristics (Figure 7.11d) of all the samples. It appears that the materials possess a good dc conductivity as is evidenced from a linear ohmic behavior of the I-V characteristics, as shown in Table 7.2. The charge carriers are easily transported through the adjacent nanorods by a tunneling type mechanism [77], facilitated by anionic and protonated ions in the mesoporous networks, and enhanced the overall charge conduction.

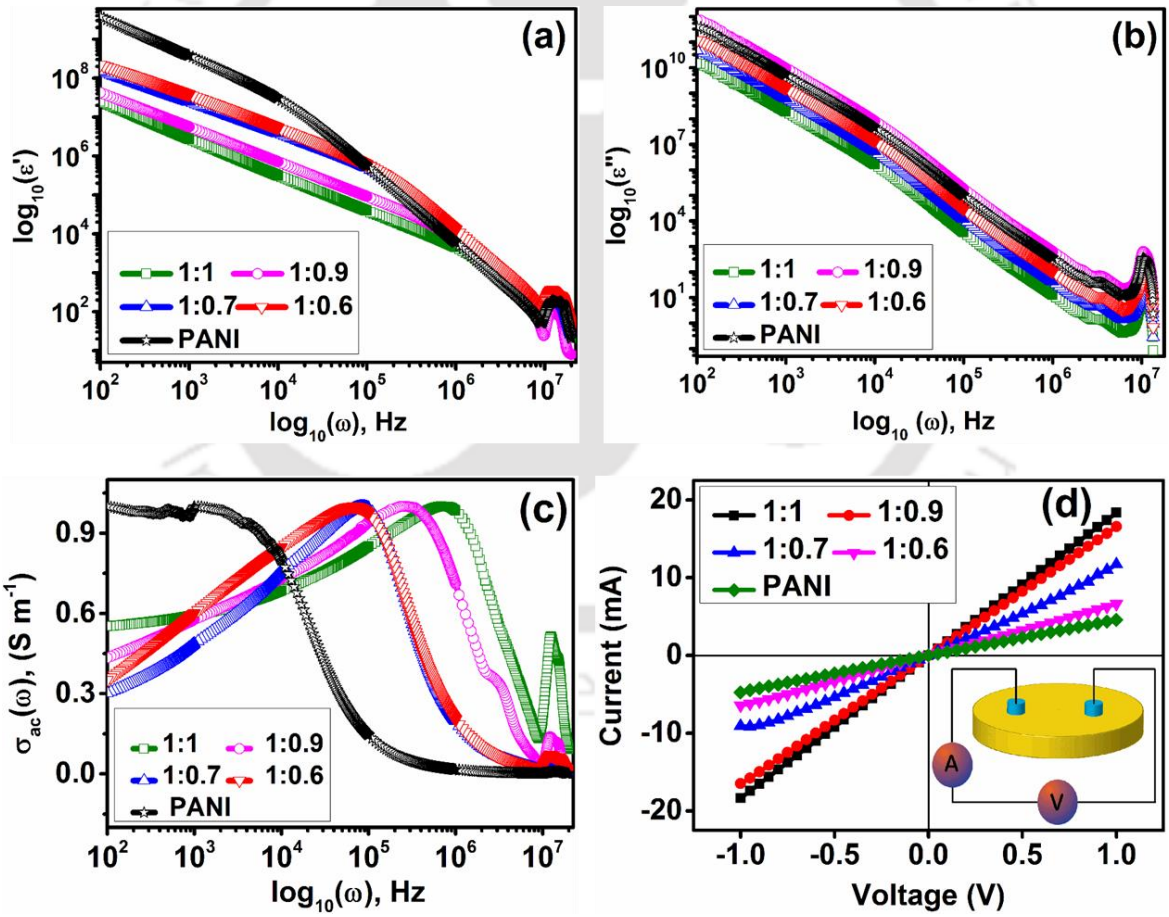

Figure 7.11. Dielectric properties from low to high frequency range measured at room temperature: (a) dielectric constant ϵ'(ω), (b) dielectric loss ϵ"(ω), (c) ac conductivity $\sigma_{ac}(\omega)$ and (d) I-V characteristics of pure PANI and PANI-SDS-F127 composites with varying ratio of PANI and F127. The inset of (d) shows the measurement procedure followed.

From the above analysis, it may be inferred that the *in-situ* polymerization method produced a well-dispersed composite structure to exhibit such electrical properties. In addition, continuous increasing of nonionic surfactant F127 could overlapped and produce a thick layer over the PANI, which may act as electronic charge barrier, correspond to reduced electrical conductivity. It can be estimated that after a certain amount of F127 may decrease the overall charge transport properties, attributed to reduced sensitivity.

7.3.4. Electrochemical performance of glucose biosensor

The electrochemical performance of the composite materials was investigated using three electrode setup. In comparison, PANI-SDS-F127 samples were correlated with pure PANI for the glucose sensing performance. The schematic diagram in Figure 7.12a represents the electrode fabrication process (for detailed description, see section 7.2.4). The enzyme, glucose oxidase (GOx), being an easily adsorbable material, is immobilized on the active electrode material, and used in glucose sensing. Below, we present our detailed analysis on the sensing behavior of 1:1 sample, in comparison with 1:0.6 and pure PANI (Figure 7.12b – c). The cyclic voltammogram was recorded for the various glucose concentrations at a scan rate of 50 mV s^{-1} and a potential window of ±1 V in 0.1 M phosphate buffer solution (PBS). Pure PANI shows the lowest current, whereas, 1:1 sample (Figure 7.12d) shows the highest. It may be perceived that the electrostatic interaction of electrode material's surface is likely to be stronger with increasing the amount of F127. On addition of glucose, oxidation is initiated over the modified electrode's surface at ~ 0.4 V and the reaction peak exhibited at ~ 0.56 V. Consequently, the observed glucose sensing peaks for oxidation are slowly declining with increasing glucose concentration, due to the decrease in anodic current. In contrast, an increasing order of cathodic current is observed during the glucose reduction. The PANI-SDS-F127 derivatives have high interfacial area; therefore, the electron transfer rate enhances with increasing glucose concentrations, varying from 0 mM to 10 mM. As such, the current and potential characteristics clearly show a catalytic behavior above 0.56 V. Ternary nanocomposites exhibits balanced charge accumulation, evidenced a rapid charge transport following the oxidation and reduction behaviour. Thus, in case of pure PANI reduction peaks were not obvious. The sensing mechanism of glucose is depicted schematically in Figure 7.13a. The linear detection range and sensitivity have been investigated by the chronoamperometry measurements, recorded at 0.56 V. A rapid response of current with time is obtained by the successive addition of glucose (Figure 7.13b), and after a certain amount no more sensing is noticed. The amperometry profile were carried out repeatedly at an interval of 30 seconds. The linear calibration range of sensing performance is analyzed from 5 to 50 mM at an

interval of 5 mM glucose concentration (Figure 7.13c). The highest sensitivity was found to be 485.787 μA cm^{-2} mM^{-1} for 1:1 sample, with a limit of detection of 3.202 μM. The detailed calculations of sensitivity (S) and limit of detection (LOD) are presented below in section 7.3.5. The data for sensitivity, correlation coefficient and limit of detection for all the three samples are presented in Table 7.3. The present sensor based on PANI-SDS-F127 with 1:1 ratio of PANI and F127 exhibits a superior sensing characteristic compared to the PANI-SDS-P123 [43] based sensor, which showed a sensitivity of 2.27 μA/mM with a linear response up to 20 mM. The rapid response of the biosensor is principally attributed to the mesoporous structure of the PANI-SDS-F127 composite that readily diffuse the glucose. The composite with 1:1 composition has a crystalline phase of nanorods, which provides an enhanced charge transport ability with an improved sensitivity.

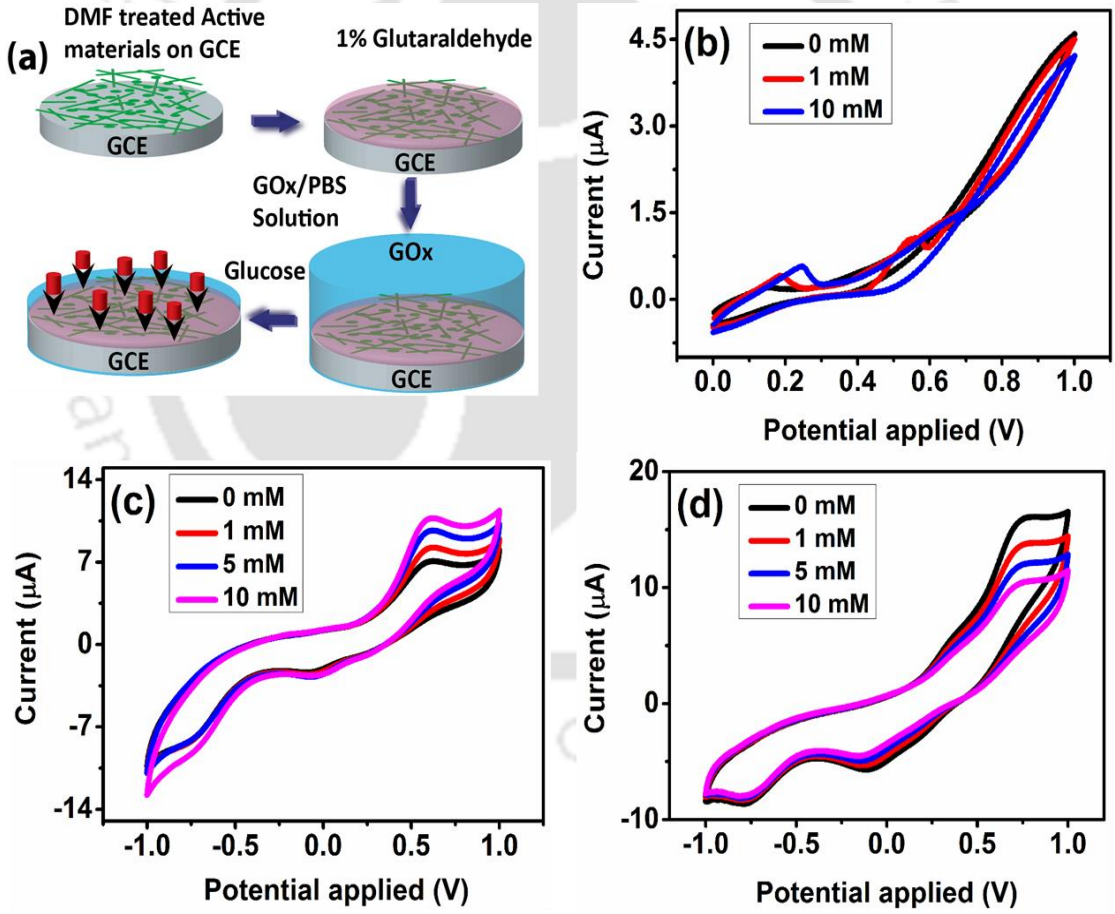

Figure 7.12. (a) Schematic diagram of the electrode fabrication to measure the electrocatalytic activities of the electrode materials. Cyclic voltammetry (CV) response for (b) pure PANI, (c) PANI-SDS-F127 at 1:0.6 and (d) PANI-SDS-F127 at 1:1, respectively.

Table 7.3. Sensing parameters (viz., sensitivity, correlation coefficient and limit of detection) of PANI, and PANI-SDS-F127 composites with 1:0.06 and 1:1 ratio of PANI and F127.

Active Materials ratio	Sensitivity ($\frac{\mu A}{cm^2 mM}$)	Correlation coefficient (r)	LOD (µM)
PANI	329.25	0.9633	3.299
PANI-SDS-F127 1:0.6	312.634	0.9827	3.670
PANI-SDS-F127 1:1	485.787	0.9775	3.202

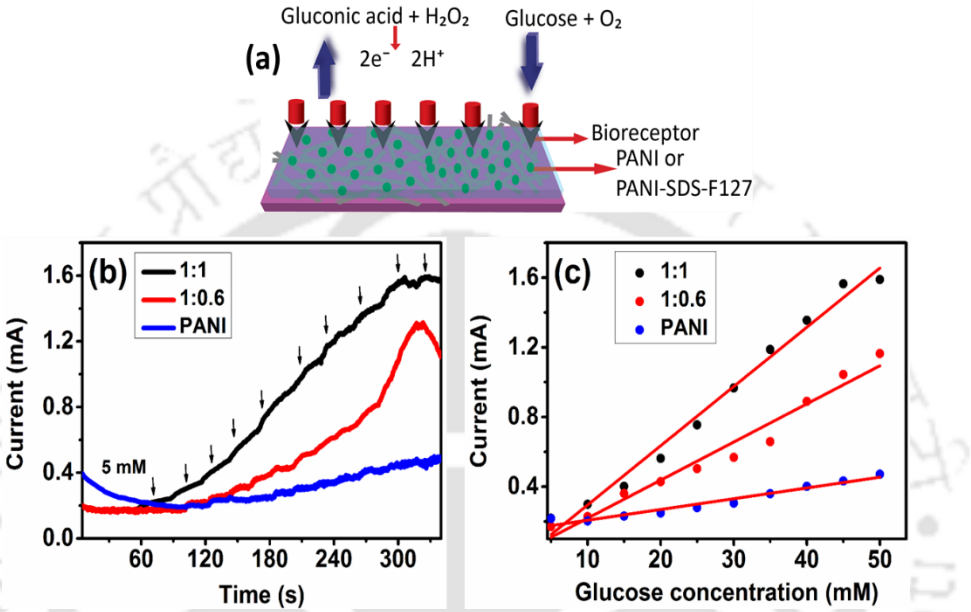

Figure 7.13. (a) Schematic diagram of reaction and glucose sensing mechanism, (b) linear sensing behavior of chronoamperometry profile, (c) linear calibration curves during successive addition of the glucose concentration for the samples of pure PANI, PANI-SDS-F127 at 1:0.6 and PANI-SDS-F127 at 1:1.

The sensitivity depends on the rate of electron transfer, which is largely governed by the redox behavior of glucose in the presence of PANI-SDS-F127/GOx modified electrodes. The glucose is catalyzed by GOx into gluconic acid and hydrogen peroxide as follows: $H_2O_2 \rightarrow 2H^+ + O_2 + 2e^-$. Following this, an oxidation driven by H_2O_2 form a conducting medium via free electrons in 0.1 M PBS. In the present study, as mentioned before, the 1:1 composite exhibits an excellent sensitivity (~ 486 µA cm^{-2} mM^{-1}) in comparison with the reported glucose biosensors. For example, Miao et al.[78] have reported 9.62 µA cm^{-2} mM^{-1} sensitivity for Nafion/GOx/AuNP-PVP-PANI modified glass carbon electrode. In their report, Au nanoparticles with polyvinylpyrrolidone over PANI surface was prepared as a flower shape structure via electropolymerization. Similarly, GOx immobilized zirconium phosphate-carbon aerogel (ZrP-

CA) composite showed a sensitivity of 5.56 µA mM^{-1} cm^{-2} [79]; and GOx immobilized Au nanoparticle decorated titanate nanotubes (GNP/TNT) [80] showed a sensitivity of 5.1 µA mM^{-1}.

7.3.5. Calculation of sensing parameters: Sensitivity (S) calculations were based on the following equation [81]. The slope of the linear calibration curve in the finite concentration range of glucose, considered as the measure of sensitivity.

$$S = \frac{\text{Slope of calibration curve}}{\text{Electrode area}} \frac{\mu A}{mM\ cm^2} \quad (7.6)$$

$$S_{PANI} = \frac{23.047}{0.070} = 329.25$$

$$S_{1:0.6} = \frac{21.884}{0.070} = 312.634$$

$$S_{1:1} = \frac{34.005}{0.070} = 485.787$$

Limit of detection (LOD) was analyzed using the following relation [82,83]:

$$LOD = \frac{k \times SD}{S} \quad (7.7)$$

$$LOD_{PANI}(M) = \frac{3.0 \times 3.62173 \times 10^{-4}}{329.25} = 3.299 \times 10^{-6}$$

$$LOD_{1:0.6}(M) = \frac{3.0 \times 3.82486 \times 10^{-4}}{312.634} = 3.67 \times 10^{-6} \quad (7.8)$$

$$LOD_{1:1}(M) = \frac{3.0 \times 5.18512 \times 10^{-4}}{485.787} = 3.202 \times 10^{-6} \quad (7.9)$$

For the LOD calculations above, “k” is constant and taken as 3.0; SD is the standard deviation of the sensing measurements and “m” is slope of the linear calibration curve. The signal to noise ratio (S/N) for an instrument during measurements always should be in the range of $10 \geq S/N \geq 3$. Since, 10 blank electrode response were taken without an analyte, based upon the standard deviation of 10 blank electrodes, k is taken as 3.0.

7.4. Conclusion

The macroscopic property enhancement is largely governed by the microscopic structural arrangement of the constituent components. A homogeneously dispersed system would offer a superior property to that of a non-homogeneous one. In this report, we have shown the application of SDAs in preparing well-dispersed ternary composites of PANI, SDS and F127, via *in-situ* polymerization. The morphological and structural analysis established the formation of a hierarchical structure with an improved property. We have prepared a series of ternary composite with varying the ratio of PANI and F127 for a given amount of SDS. Among all the samples, the 1:1 samples have exhibited an excellent electrochemical property. The microscopic analysis along

with the XRD data and BET surface area measurements revealed that the sample is polycrystalline in nature with a collection of smaller size crystals. This enhanced crystalline domain contributes significantly in facilitating electron movement, leading to a higher electrical conductivity and superior electrochemical property. The application in glucose sensing with a remarkably high sensitivity (~486 μA/cm^2 mM) with a lower detection limit of ~4 μM, is attributed to the synergistic effect of all the components present in the composite in an orderly manner. This work offers a facile approach towards the development of affordable future glucose biosensors.

References

[1] B. B. Y. Hsu, E. B. Namdas, J. D. Yuen, S. Cho, I. D. W. Samuel, A. J. Heeger, *Adv. Mater.* **2010**, *22*, 4649.

[2] N. Yi, M. R. Abidian, In *Biosynthetic Polymers for Medical Applications*; Poole-Warren, L.; Martens, P.; Green, R., Eds.; Woodhead Publishing Series in Biomaterials; Woodhead Publishing, 2016; pp. 243–276.

[3] R. Balint, N. J. Cassidy, S. H. Cartmell, *Acta Biomater.* **2014**, *10*, 2341.

[4] J. Huang, S. Virji, B. H. Weiller, R. B. Kaner, *J. Am. Chem. Soc.* **2003**, *125*, 314.

[5] S. Bibi, H. Ullah, S. M. Ahmad, A.-H. Ali Shah, S. Bilal, A. A. Tahir, K. Ayub, *J. Phys. Chem. C* **2015**, *119*, 15994.

[6] J. Liu, Y. Xue, M. Zhang, L. Dai, *MRS Bull.* **2012**, *37*, 1265.

[7] L. Kavan, J.-H. Yum, M. K. Nazeeruddin, M. Grätzel, *ACS Nano* **2011**, *5*, 9171.

[8] L. Ding, B. Su, *J. Electroanal. Chem.* **2015**, *736*, 83.

[9] A. K. Das, S. Maiti, B. B. Khatua, *J. Electroanal. Chem.* **2015**, *739*, 10.

[10] R. Liu, Y. Ren, Y. Shi, F. Zhang, L. Zhang, B. Tu, D. Zhao, *Chem. Mater.* **2008**, *20*, 1140.

[11] M. C. Orilall, U. Wiesner, *Chem. Soc. Rev.* **2011**, *40*, 520.

[12] H.-S. Yun, K. Miyazawa, H. S. Zhou, I. Honma, M. Kuwabara, *Adv. Mater.* **2001**, *13*, 1377.

[13] Y. Xu, F. Zhang, X. Feng, *Small* **2011**, *7*, 1338.

[14] T. Mäkelä, S. Pienimaa, T. Taka, S. Jussila, H. Isotalo, *Synth. Met.* **1997**, *85*, 1335.

[15] X. Qi, T. Balankura, Y. Zhou, K. A. Fichthorn, *Nano Lett.* **2015**, *15*, 7711.

[16] W. He, Y. Yang, J. Li, L. Long, K. Zhang, Y. Xiang, S. Qin, J. Yu, *Colloids Surf. Physicochem. Eng. Asp.* **2016**, *509*, 583.

[17] A. Thomas, F. Goettmann, M. Antonietti, *Chem. Mater.* **2008**, *20*, 738.

[18] Q. Yuan, A.-X. Yin, C. Luo, L.-D. Sun, Y.-W. Zhang, W.-T. Duan, H.-C. Liu, C.-H. Yan, *J. Am. Chem. Soc.* **2008**, *130*, 3465.

[19] H. Cao, C. Tie, Z. Xu, J. Hong, H. Sang, *Appl. Phys. Lett.* **2001**, *78*, 1592.

[20] T. T. Trinh, K.-Q. Tran, X.-Q. Zhang, R. A. van Santen, E. J. Meijer, *Phys. Chem. Chem. Phys.* **2015**, *17*, 21810.

[21] T. J. Daou, J. Dhainaut, A. Chappaz, N. Bats, B. Harbuzaru, H. Chaumeil, A. Defoin, L. Rouleau, J. Patarin, *Oil Gas Sci. Technol. – Rev. D'IFP Energ. Nouv.* **2015**, *70*, 447.

[22] L. Xin, H. Sun, R. Xu, W. Yan, *Sci. Rep.* **2015**, *5*, 14940.

[23] Q. Liu, A. Wang, X. Wang, T. Zhang, *Chem. Mater.* **2006**, *18*, 5153.

[24] C. Márquez-Alvarez, N. Žilková, J. Pérez-Pariente, J. Čejka, *Catal. Rev.* **2008**, *50*, 222.

[25] Q. Liang, X. Guo, T. Quan, F. Meng, *J. Adv. Ceram.* **2016**, *5*, 225.

[26] A. P.-Z. Clark, K.-F. Shen, Y. F. Rubin, S. H. Tolbert, *Nano Lett.* **2005**, *5*, 1647.

[27] L. Yang, W. Wu, Y. Ohki, Y. Feng, S. Li, *J. Appl. Polym. Sci.* **2017**, *134*, 45547.

[28] S. A. Bagshaw, T. J. Pinnavaia, *Angew. Chem. Int. Ed. Engl.* **2003**, *35*, 1102.

[29] W. Cai, J. Yu, M. Jaroniec, *J. Mater. Chem.* **2011**, *21*, 9066.

[30] J.-P. Dacquin, J. Dhainaut, D. Duprez, S. Royer, A. F. Lee, K. Wilson, *J. Am. Chem. Soc.* **2009**, *131*, 12896.

[31] N. Parveen, M. O. Ansari, M. H. Cho, *Ind. Eng. Chem. Res.* **2016**, *55*, 116.

[32] J. Huang, R. B. Kaner, *J. Am. Chem. Soc.* **2004**, *126*, 851.

[33] I. D. Norris, M. M. Shaker, F. K. Ko, A. G. MacDiarmid, *Synth. Met.* **2000**, *114*, 109.

[34] W. Yang, Z. Gao, N. Song, Y. Zhang, Y. Yang, J. Wang, *J. Power Sources* **2014**, *272*, 915.

[35] W. Dai, L. Ma, M. Gan, S. Wang, X. Sun, H. Wang, H. Wang, T. Zhou, *Mater. Res. Bull.* **2016**, *76*, 344.

[36] W. Hou, Y. Xiao, G. Han, D. Fu, R. Wu, *J. Power Sources* **2016**, *322*, 155.

[37] U. Rana, S. Mondal, J. Sannigrahi, P. Kumar Sukul, M. Asif Amin, S. Majumdar, S. Malik, *J. Mater. Chem. C* **2014**, *2*, 3382.

[38] F. Zeng, Z. Qin, B. Liang, T. Li, N. Liu, M. Zhu, *Prog. Nat. Sci. Mater. Int.* **2015**, *25*, 512.

[39] M. Nandi, R. Gangopadhyay, A. Bhaumik, *Microporous Mesoporous Mater.* **2008**, *109*, 239.

[40] D. Zhao, J. Feng, Q. Huo, N. Melosh, G. H. Fredrickson, B. F. Chmelka, G. D. Stucky, *Science* **1998**, *279*, 548.

[41] B.-J. Kim, S.-G. Oh, M.-G. Han, S.-S. Im, *Langmuir* **2000**, *16*, 5841.

[42] A. Kuczynska, A. Uygun, A. Kaim, H. Wilczura-Wachnik, A. G. Yavuz, M. Aldissi, *Polym. Int.* **2010**, *59*, 1650.

[43] M. U. A. Prathap, B. Thakur, S. N. Sawant, R. Srivastava, *Colloids Surf. B Biointerfaces* **2012**, *89*, 108.

[44] L. Hang, F. Zhou, D. Men, H. Li, X. Li, H. Zhang, G. Liu, W. Cai, C. Li, Y. Li, *Nano Res.* **2017**, *10*, 2257.

[45] H. Van Hoang, R. Holze, *Chem. Mater.* **2006**, *18*, 1976.

[46] L. Hang, Y. Zhao, H. Zhang, G. Liu, W. Cai, Y. Li, L. Qu, *Acta Mater.* **2016**, *105*, 59.

[47] J. Stejskal, R. G. Gilbert, *Pure Appl. Chem.* **2002**, *74*, 857.

[48] M. Tagowska, B. Pałys, K. Jackowska, *Synth. Met.* **2004**, *142*, 223.

[49] M. Trchová, Z. Morávková, M. Bláha, J. Stejskal, *Electrochimica Acta* **2014**, *122*, 28.

[50] A. K. Das, S. Maiti, B. B. Khatua, *J. Electroanal. Chem.* **2015**, *739*, 10.

[51] Z. Zhang, Z. Wei, M. Wan, *Macromolecules* **2002**, *35*, 5937.

[52] A. G. Macdiarmid, J. C. Chiang, A. F. Richter, A. J. Epstein, *Synth. Met.* **1987**, *18*, 285.

[53] J. Stejskal, P. Kratochvíl, N. Radhakrishnan, *Synth. Met.* **1993**, *61*, 225.

[54] H. Liu, X. B. Hu, J. Y. Wang, R. I. Boughton, *Macromolecules* **2002**, *35*, 9414.

[55] M. D. A. Khan, A. Akhtar, S. A. Nabi, *New J. Chem.* **2015**, *39*, 3728.

[56] Q. Zhang, K. Zhang, D. Xu, G. Yang, H. Huang, F. Nie, C. Liu, S. Yang, *Prog. Mater. Sci.* **2014**, *60*, 208.

[57] Z. Lei, Z. Chen, X. S. Zhao, *J. Phys. Chem. C* **2010**, *114*, 19867.

[58] W.-S. Huang, B. D. Humphrey, A. G. MacDiarmid, *J. Chem. Soc., Faraday Trans. 1* **1986**, *82*, 2385.

[59] S. Yang, Y. Liu, W. Chen, W. Jin, J. Zhou, H. Zhang, G. S. Zakharova, *Sens. Actuators B Chem.* **2016**, *226*, 478.

[60] P. Singla, N. Goel, V. kumar, S. Singhal, *Ceram. Int.* **2015**, *41*, 10565.

[61] G. Fagerlund, *Matér. Constr.* **1973**, *6*, 239.

[62] W. Ma, S. Chen, S. Yang, W. Chen, Y. Cheng, Y. Guo, S. Peng, S. Ramakrishna, M. Zhu, *J. Power Sources* **2016**, *306*, 481.

[63] A. Pitto-Barry, N. P. E. Barry, *Polym. Chem.* **2014**, *5*, 3291.

[64] W. Leng, S. Zhou, G. Gu, L. Wu, *J. Colloid Interface Sci.* **2012**, *369*, 411.

[65] J. Swain, A. K. Mishra, *Photochem. Photobiol. Sci.* **2016**, *15*, 1400.

[66] V. J. Babu, S. Vempati, S. Ramakrishna, *Mater. Sci. Appl.* **2013**, *04*, 1.

[67] F. Yan, G. Xue, *J. Mater. Chem.* **1999**, *9*, 3035.

[68] A. Kumar, A. Mishra, K. Awasthi, V. Kumar, *Macromol. Symp.* **2015**, *357*, 168.

[69] S. Bhandari, N. K. Singha, D. Khastgir, *J. Appl. Polym. Sci.* **2013**, *129*, 1264.

[70] L. Tang, Y. Fang, Y. Pang, G. Zeng, J. Wang, Y. Zhou, Y. Deng, G. Yang, Y. Cai, J. Chen, *Chem. Eng. J.* **2014**, *254*, 302.

[71] B. E. Kilbride, J. N. Coleman, J. Fraysse, P. Fournet, M. Cadek, A. Drury, S. Hutzler, S. Roth, W. J. Blau, *J. Appl. Phys.* **2002**, *92*, 4024.

[72] A. R. Blythe, *Polym. Test.* **1984**, *4*, 195.

[73] T. b. Adams, D. c. Sinclair, A. r. West, *Adv. Mater.* **2002**, *14*, 1321.

[74] C. Wu, X. Huang, X. Wu, L. Xie, K. Yang, P. Jiang, *Nanoscale* **2013**, *5*, 3847.

[75] M. S. Aziz, H. M. El-Mallah, *Int. J. Polym. Mater. Polym. Biomater.* **2005**, *54*, 1157.

[76] M. Wan, A. K. Srivastava, P. K. Dhawan, R. R. Yadav, S. B. Sant, R. Kripal, J.-H. Lee, *RSC Adv.* **2015**, *5*, 48421.

[77] L. He, S. C. Tjong, *Nanoscale Res. Lett.* **2013**, *8*, 132.

[78] Z. Miao, P. Wang, A. Zhong, M. Yang, Q. Xu, S. Hao, X. Hu, *J. Electroanal. Chem.* **2015**, *756*, 153.

[79] Z. Yu, Y. Kou, Y. Dai, X. Wang, H. Wei, D. Xia, *Electrocatalysis* **2015**, *6*, 341.

[80] R. Zhao, X. Liu, J. Zhang, J. Zhu, D. K. Y. Wong, *Electrochimica Acta* **2015**, *163*, 64.

[81] S. R. Balakrishnan, U. Hashim, G. R. Letchumanan, M. Kashif, A. R. Ruslinda, W. W. Liu, P. Veeradasan, R. Haarindra Prasad, K. L. Foo, P. Poopalan, *Sens. Actuators Phys.* **2014**, *220*, 101.

[82] M. Stoytcheva, R. Zlatev, G. Montero, Z. Velkova, V. Gochev, *Biotechnol. Biotechnol. Equip.* **2018**, *32*, 213.

[83] H.-P. Loock, P. D. Wentzell, *Sens. Actuators B Chem.* **2012**, *173*, 157.

Chapter-8

Summary and Future Scope

8.1. Summary of the research work

The property enhancement in polymer nanocomposite strongly depends on the distribution of nanofillers within the polymer matrix. An evenly dispersed polymer nanocomposite would definitely yield a superior property over the one with uneven distribution. In thesis work, **chapter-2** attributed to various binary and ternary nanocomposites, among them PANI-G-MoS_2 exhibits an excellent electrochemical activity and enhanced cyclic stability with improved performance as a supercapacitor electrode compared to the pure PANI and PANI-G binary composites. **Chapter-3** is associated to the graphene oxide, reduced graphene oxide, and α–MnO_2 based PANI functionalized binary and ternary nanocomposites. Among all the nanocomposites, PANI-RGO-MnO_2 have appeared an excellent candidate for high–density energy storage material with excellent dielectric strength. In the **chapter-4** we prepared a series of the binary and ternary nanocomposites of PA6, rGO, and PANI components, and studied comparatively. We observed that PA6-rGO-PANI 1:2 show an excellent electrochemical performance with improved cyclic stability, as compared to other binary and ternary composites. Further, fabricated symmetric supercapacitor device also have shown an outstanding performance by glowing the LED. C**hapter 5**, shows ZnO (transition metal oxide) and RGO based PANI functionalized binary and ternary nanocomposites. Among them PANI-RGO-ZnO 2:1 composite exhibits superior performance as an electrode material compared to others. In **chapter-6,** the emeraldine salt and base form of pure PANI have been deposited on a glass and n–type Si wafer using vacuum evaporation technique. We observed that PANI-EB is readily deposited with unfolded chains as compared to PANI-ES. In contrast, PANI-ES thin film shows a good electrical conductivity. Hence, fabricated thin film capacitors also have shown remarkable current density and energy density at high percolation threshold. C**hapter-7** shows the hierarchical order of PANI nanostructures with the application of structure directing agents (SDAs). The application of PANI nanorods for glucose sensing exhibit high sensitivity (~ 486 μA cm^{-2} mM^{-1}) with lower detection limit of ~ 4 μM, attributed to the synergistic effect of all the components present in the composite in an orderly manner.

8.2. Future scope of the research work

C**hapter 8** summarizes the overall work with a few future studies: (i) in vivo experiments for targeted drug delivery, (ii) high density energy materials in power sector and stealth environment, (iii) miniaturized electronics component for nano-electronics devices, (iv) development of flexible energy storage devices and hybrid batteries; (v) miniaturization of

PANI nanorods can be utilized for life saving drugs and fabrication of biosensors as well as immuno sensors of the same for clinically diagnostic devices.

8.3. Research output

Patents

1. **Shatrudhan Palsaniya**, Harshal B. Nemade, Ashok Kumar Dasmahapatra "Ternary composites comprising hierarchical nanostructures and system thereof" Indian Patent filed, App. no: TEMP/E-1/51329/2019-KOL.
2. **Shatrudhan Palsaniya**, Harshal B. Nemade, Ashok Kumar Dasmahapatra "Development of PA6/rGO/PANI Nanocomposites and Applied for Electrochemical Energy storage via Symmetric Supercapacitors" Indian Patent filed, App. no: TEMP/E-1/56448/2019-KOL.

Journal publications

1. **S. Palsaniya**, H.B. Nemade, A.K. Dasmahapatra, "Synthesis of polyaniline/graphene/MoS_2 nanocomposite for high performance supercapacitor electrode", Polymer. 150 (2018) 150–158.
2. **S. Palsaniya**, H.B. Nemade, A.K. Dasmahapatra, "Mixed Surfactant-Mediated Synthesis of Hierarchical PANI Nanorods for an Enzymatic Glucose Biosensor", ACS Appl. Polym. Mater. 1 (2019) 647–656.
3. **S. Palsaniya**, H.B. Nemade, A.K. Dasmahapatra, "Graphene based PANI/MnO_2 nanocomposites with enhanced dielectric properties for high energy density materials", Carbon. 150 (2019) 179–190.
4. **S. Palsaniya**, H.B. Nemade, A.K. Dasmahapatra, "Heterostructured Layer Growth of Polyaniline by Vacuum Thermal Evaporation and Fabrication of Thin-Film Capacitors", J. Phys. Chem. C. 123 (2019) 27959–27968.
5. **S. Palsaniya**, H.B.Nemade, A.K. Dasmahapatra, "Fabrication of symmetric supercapacitor based on hierarchical ordered PA6/rGO/PANI nanocomposites for energy storage applications". **(Communicated).**
6. **S. Palsaniya**, H.B.Nemade, A.K. Dasmahapatra, "PANI/RGO/ZnO Ternary Nanocomposites for High Performance Symmetric Tandem Supercapacitor". **(Communicated).**
7. **S. Palsaniya**, H.B.Nemade, A.K. Dasmahapatra, Fabrication of triboelectric Nanogenerator using the ultrafast laser micromachining. **(Under processing).**

Publication with collaboration

8. J. Singh, S. Juneja, **S. Palsaniya**, Ashis.K. Manna, R.K. Soni, J. Bhattacharya "Evidence of oxygen defects mediated enhanced photocatalytic and antibacterial performance of ZnO nanorods" Colloids Surf. B Biointerfaces. 184 (2019) 110541.

Conferences publication

9. **S. Palsaniya**, H.B. Nemade, A.K. Dasmahapatra, Size dependent triboelectric nanogenerator and effect of temperature, in: IEEE, ICMAP 2018: pp. 1–2.

Conferences:

1. **Shatrudhan Palsaniya**, Harshal B. Nemade, Ashok Kumar Dasmahapatra "Preparation of Surfactant-Assisted Hierarchical PANI Nanorods for Enzymatic Glucose Biosensor" 2019 Fall Meeting & Exhibit, Boston, Massachusetts, USA, Dec. 1-6, 2019.
2. **Shatrudhan Palsaniya**, Harshal B. Nemade, Ashok Kumar Dasmahapatra, "MnO_2 Nanorods Functionalized RGO/PANI Nanocomposites for High Performance Density Energy Storage Materials" Oral Presentation, ICANN 2019, IIT Guwahati, India, Dec. 18-21, 2019.
3. **Shatrudhan Palsaniya**, Harshal B. Nemade, Ashok Kumar Dasmahapatra, "Graphene-based PANI/MnO_2 Nanocomposites with Enhanced Dielectric Properties for High Energy Density Materials" Oral Presentation, Reflux 7.0, IIT Guwahati, India, Sept. 28-29, 2019.
4. **Shatrudhan Palsaniya,** Harshal B. Nemade, Ashok Kumar Dasamhapatra, "Synthesis of Polyaniline/Graphene/MoS_2 Nanocomposite for High Performance Supercapacitor Electrode" Research Conclave 2019, IIT Guwahati, India, March 14-17, 2019.
5. **Shatrudhan Palsaniya**, Harshal B. Nemade, Ashok Kumar Dasmahapatra, "Synthesis of Polyaniline/Graphene/MoS_2 Nanocomposite Electrode Materials for high Performance Asymmetric Supercapacitor," COMPFLU-2018, IIT Roorkee, India, Dec. 6–9, 2018.
6. **Shatrudhan Palsaniya**, Harshal B. Nemade, Ashok Kumar Dasmahapatra, "Preparation and Characterization of MnO_2/rGO/PANI Nanocomposite and Application of Symmetric Supercapacitor" ICSM-2018, MNIT Jaipur, India, Dec. 9–14, 2018.
7. **Shatrudhan Palsaniya**, Harshal B. Nemade, Ashok Kumar Dasmahapatra, "*In-Situ* Polymerization of Aniline with GO/RGO using Exfoliated MnO_2 dispersion based Nanocomposites for the Fabrication of Supercapacitors" Research Conclave 2018, IIT Guwahati, India, March 8 – 11, 2018.

8. **Shatrudhan Palsaniya**, Harshal B. Nemade, Ashok Kumar Dasmahapatra, Size Dependent Triboelectric Nanogenerator and Effect of Temperature, Oral Presentation, ICMAP-2018, IIT (ISM) Dhanbad, India, Feb. 9 – 11, 2018.
9. **Shatrudhan Palsaniya**, Harshal B. Nemade, Ashok Kumar Dasmahapatra, Fabrication of PANI/RGO/MnO_2 nanocomposites using *in-situ* polymerization for the application of Supercapacitor, ICANN-2017, IIT Guwahati, India, Dec. 18 – 21, 2017.
10. **Shatrudhan Palsaniya**, Sunny Kumar, Harshal B. Nemade, Ashok Kumar Dasmahapatra, Highly Flexible Paper based Triboelectric Nanogenerator for Energy Harvesting and Sensing Application, Oral Presentation, NANOfim-2017, GBU Noida, India, Nov. 16 – 17, 2017.
11. **Shatrudhan Palsaniya**, Harshal B. Nemade, Ashok kumar Dasamahapatra, "Graphene growth over Cu film using liquid hydrocarbon" Research Conclave 2017, IIT Guwahati, India, March 16 – 19, 2017.
12. Jaspal Singh, **Shatrudhan Palsaniya**, and R.K. Soni, pH dependent hydrothermal synthesis of ZnO nanorods for the application in sun light induced Photocatalytic activity, ICNSMD-2018, University of Delhi, India, Dec. 17– 20, 2018.
13. Pankaj Kumar, **Shatrudhan Palsaniya**, "Structural and Characterization Study of Silica-Gel at Variable Particle Size" Reflux 7.0, IIT Guwahati, India, Sept. 28-29, 2019.
14. Pankaj Kumar, **Shatrudhan Palsaniya**, "Study of temperature dependent properties of silica gel at variable particle size" ICANN2019, IIT Guwahati, India, Dec. 18-21, 2019.

Fellowship and awards

1. 2nd prize in Research Conclave 2019, IIT Guwahati. (Poster)
2. 1st prize in Reflux 7.0 2019, IIT Guwahati. (Oral)
3. Travel fellowship by DST Govt. of India, 2019.